Analysis of the wear of oil wells drill bits

By

Rafid Kadhim Abbas

Submitted in accordance with the requirements for the degree of

Doctor of Philosophy

The University of Leeds

School of Chemical and Process Engineering

November 2015

The candidate confirms that the work submitted is his own, except where work which has formed part of jointly authored publications has been included. The contribution of the candidate and the other authors to this work has been explicitly indicated below. The candidate confirms that appropriate credit has been given within the thesis where reference has been made to the work of others.

Section 3.1 of chapter three of this thesis has already been published in Onepetro website (Abbas *et al.,* 2014). The analyses, discussions and conclusions were all done by Rafid Abbas. Other authors of this publication provided feedback and guidance.

Abbas, R. K., Hassanpour, A., Hare, C., & Ghadiri, M. (2014, November 12). Instantaneous Monitoring of Drill Bit Wear and Specific Energy as a Criteria for the Appropriate Time for Pulling Out Worn Bits. Society of Petroleum Engineers. doi:10.2118/172269-MS.

Acknowledgments

First of all I would like to thank my supervisors, Dr. Ali Hassanpour, Colin Hare and Professor Mojtaba Ghadiri for their support as well as kindly providing me valuable feedback and information. I would like to express my gratitude to Mr Stuart Micklethwaite for his kind help and notes regarding using the facilities of the scanning electron macrograph in Lemas at the University of Leeds.

I must here express my deep thanks and appreciation to my sponsor (The Ministry of Higher Education and Scientific research in Iraq) for granting the opportunity to do my PhD at the University of Leeds. A special word of thanks is given to Mr. Adrian Eagles for helping me to use the instruments of surface profilemeter at the Institute of Medical and Biological Engineering. Great acknowledgment is given to my colleagues from the Institute of Particle Science and Engineering, especially Jabbar Gardy, Ahmed Al-Saadi, Ali Mohammed, Mohammad Afkhami, Sandra, Rodrigo, Akinola, Amin, Dr. Faiz Mahdi (Postdoc.) and Mohammadreza. Special word of thanks is given to Dr. Umair Zafar (Postdoc.) in Ghadiri group for his assistance in carrying out nano-scratch tests. Furthermore, I must not forget the precious information given by Prof. Ben Beake (Micromaterials, UK) for his help regarding the nano-scratch test.

I am indebted to my beloved parents for their support and encouragement during my whole life and specifically throughout my study. I would like to mention the immeasurable support from my wife and from my children Younis, Zainab, Fatima and my adorable daughter Ghadir.

Finally, I have to thank members of Ghadiri group who gave me valuable feedback during my presentations and I extend my compliments to all who participated in this work that I forgot to mention his or her name.

This work is dedicated to my loving parents and my beloved family

For their infinite support and always being with me

Abstract

Predicting the wear of drill bits is essential for all oil companies to maximise drilling efficiency and reduce loss in money and time. Typically, this problem has been dealt with by evaluating the specific energy of the drill bits at drilling formation intervals. Although this technique sometimes provides a good indication of the bit tooth wear, a number of phenomena such as bit balling and high vibration of the drill bit might give misleading results that affect the reliability of these techniques. Therefore, it is necessary to develop an effective predictive tool for the bit tooth wear rate by both experimental and theoretical approaches.

A case study is presented for the evaluation of the specific energy combined with dimensionless drilling parameters method as indicating tools for monitoring the wear of the roller-cone bits. The results were compared with the qualitative tooth wear index of the bits and an agreement was found for limited cases. The case study did not include the mechanical properties of the materials that form the bit, therefore a wear model was needed to combine the drilling parameters with the mechanical properties of the materials forming the bit under the phenomena of three body abrasion where the drill bits are in reality facing this effect. The new formula for quantifying the bit tooth wear is presented and compared with the qualitative bit tooth wear index, where close matching was obtained.

Experimental studies were carried out on polycrystalline diamond compact cutters from two manufacturers. The mechanical properties were determined by micro-indentation as well as nano-indentation testing on the diamond and the substrate layers of the cutters. Microstructural properties of the materials forming the PDC cutters found to be effective on the mechanical properties and consequently on the amount of wear. The volume of wear for the PDC cutters was determined experimentally using micro and nano-scratch tests of PDC cutters. The experimental wear was compared with the predicted wear based on current approaches in the literature. The results show that the wear of both layers of PDC cutters in this work can be predicted by the material mechanical properties and the applied load on the indenter. The analytical study based on various scanning electron microscopy techniques revealed that the main dominant wear mechanism for the substrate and the diamond layers is abrasive wear in the format of ploughing and cutting.

Keywords: bit tooth wear; PDC bits; roller-cone bits; micro-scratch testing; nano-scratch testing.

Table of Contents

List of Figures

List of Tables

Nomenclature

Latin Characters

A	projected indentation area (nm^2)
A_b	cross- sectional area of the tooth, (m^2)
A_{bit}	surface area of the bit (in^2)
$A_{circular\ sector}$	area of the circular sector (μm^2)
A_p	area of the particle (μm^2)
$A_{segment}$	area of the circular segment (μm^2)
$A_{triangle}$	area of the triangle (μm^2)
AETT	acoustical emissions toughness test
a	half length of the diagonal indent (m)
a_1	empirical constant
a_2	empirical constant
ac	chord length (μm)
BSE	back scattered electrons
b	width of the scratch (μm)
DC	double cemented tungsten carbide
DEI	diamond enhanced inserts
DEM	discrete element method
d , d_b	bit diameter (in)
d_a	average length of the indent diagonals (mm)
d_l	length of the longest indent diagonal (μm)
C	crack length (m)
C	Carbon (diamond phase)
CED	circular equivalent diameter (μm)
Co	cobalt (binder)
CTL	composite-transition layer
E	Young's modulus (N/m^2, mN/nm^2, GPa)

EF	correction efficiency factor (-)
E_n	energy
E_r	reduced modulus (mN/nm^2, GPa)
E_D	bit drilling efficiency (-)
EDS	energy dispersive spectroscopy
EDX	energy dispersive x-ray
F	applied load (mN, N)
F(A)	function of load , sliding distance and hardness
F_D	dimensionless tooth flatness (-)
FEA	finite element analysis
G-ratio	grinding ratio (-)
H	hardness of the material (N/m^2, mN/nm^2, GPa)
H_a	hardness of the abrasive body (N/m^2, GPa)
(H_a/H_m)	ratio of the abrasive hardness to the material hardness (-)
H_w	hardness of the abraded body (N/m^2, GPa)
HK	Knoop hardness (GPa)
HPHT	high pressure and high temperature
HV	Vvickers hardness number
h	height of the volume removed , depth of the scratch (µm , m)
h_b	height of the worn insert (m)
h_p	projected depth (nm)
IADC	international association of drilling contractors
i	referring to the indenter
JSA	available junk slot area of the bit (in^2)
K	constant for the system or wear coefficient (-)
K_{IC}	fracture toughness of the material ($MPa.m^{1/2}$)
L	interval being drilled or sliding distance (ft, µm ,m)
MAPE	mean absolute percentage error (%)

MSE	mechanical specific energy (psi)
MSE_{adj}	adjusted mechanical specific energy (psi)
N,N_b	speed rotation of the bit (rpm)
N_{cone}	speed rotation of the cone of the bit (rpm)
N_{leg}	speed rotation of the leg of the bit (rpm)
NbC	niobium carbide
$NSPDC$	new steel polycrystalline diamond compact bit
n	power of the ratio (H_R/H_b) or index of incremental area and sliding distance (dimensionless)
PDC	polycrystalline diamond compact
P_{max}	maximum applied load (mN)
PR	rate of penetration (ft/hr), (m/hr)
PR_D	dimensionless rate of penetration
R_a	average surface roughness (µm)
R_c	radius of the circle (µm)
R_{Ku}	kurtosis roughness (-)
R_q	root mean square roughness (µm)
R_{sk}	surface skewness (-)
RS	raman spectroscopy
r	bit radius (mm), (in.), (m)
r_{cone}	radius of the cone of the bit (in), (m)
r_i	radius of the insert (m), (cm)
r_{leg}	radius of the leg of the bit (in), (m)
r_t	height of the triangle (µm)
S	stiffness of the material (mN/nm)
Sa	arc length of the sector (µm)
S_m	stiffness of the machine without the sample (N/mm)
S_{net}	net stiffness of the sample (mN/nm)

S_{total}	stiffness of the sample plus the stiffness of the machine (N/mm)
s	referring to the sample
SE	specific energy (psi)
$SE_{avg.}$	average specific energy (psi)
SEM	scanning electron microscope
SEI	secondary electron image
SHN	scratch hardness number (GPa)
SiC	silicon carbide
T	measured torque (lb.ft)
T_D	dimensionless torque
TaC	tantalum carbide
TC	tungsten-carbide
TCI	tungsten carbide inserts
TSDC	thermally stable diamond composites
TSPD	thermostable polycrystalline diamond compact
UCS	unconfined compressive strength (MPa, psi)
V_b , V_w	volume of material removed from the bit or the material (μm^3, mm^3, m^3)
V_{cone}	linear velocity of the cone of the bit (m/min)
V_i	volume of the material removed from the insert, (m^3)
V_{leg}	linear velocity of the lege of the bit (m/min)
V_R	volume of the of rock removed (m^3)
V_{wt}	total volume of nanowear (μm^3), (mm^3)
VTL	vertical turret lathe
VV	bit face void volume (in^3)
W	weight on bit (lb , Kg.)
W_D	dimensionless weight on bit
W_H	wear resistant coefficient (-)
WC	tungsten carbide

WCo-B	ternary borides
w_s	scratch width (μm)
X	sliding distance (μm)
XRD	x-ray diffraction

Greek Characters

α_p	half angle of the abrasive particles (degree)
Δx	distance change in Hook's law (mm, µm)
θ	abrasion angle or the angle opposing the segment of the circle (degree)
θ_c , α	attack angle (degree)
μ	bit coefficient of friction (-)
v	Poisson's ratio (dimensionless)
ω	angular velocity (rpm)

Chapter 1 Introduction

1.1 Wear of oil and gas drill bits

Drilling for oil and gas is still very demanding in many areas around the world. Rotary drilling is the most common technique for drilling oil and gas and since the invention of rotary drilling two types of drill bits have been used: roller-cone and Polycrystalline Diamond Compact (PDC) bits. Roller cone bits or tricone bits have three rotating cones with each one rotating on its own axis during drilling, while PDC bits are fixed cutter bits with no moving parts. Drilling occurs due to the compression and rotation of the drill string. Tricone bits are used in general to drill a wide variety of rocks, from soft to extremely hard. PDC bits are used to drill various sorts of formations, especially at harsh environments (formations of high pressure and high temperature). Since the wear of drill bits is considered an intrinsic cost, significant savings can be achieved by effective control and minimisation of bit wear. Real-time monitoring of the status of the bit wear is crucially important to increase the rate of penetration and determining the right time to pull out the bit due to its wear. Drilling with worn bits might cause losing the bit and consequently bit fishing is required that would add additional cost beside the overall drilling costs as well as delaying the drilling operations.

1.2 Objectives of the thesis

1- The overall aim of this PhD is to develop a new original wear model for predicting the bit tooth wear for drill bits. Theoretical and experimental work were carried out to obtain a wear model using state of the art technologies for wear testing such as micro-indentation and micro-scratch test along with nano-indentation and nano-scratch tests.

2- The literature survey presented in Chapter 2 demonstrates the main failure modes and wear mechanisms of oil drill bits and studying the destructive and non-destructive bit testing techniques. Previous models for wear quantification are presented and described individually.

3- Predicting the real-time bit tooth wear using a combination of specific energy and dimensionless drilling parameters. Developing a new theoretical model for bit wear monitoring based on three body abrasion. A case study is presented to show the implication of the new model (Chapter 3).

4- Experimental work includes nano and microindentation testing carried out on Polycrystalline Diamond Compact (PDC) inserts from different sources to measure the mechanical properties of the materials forming these inserts. These properties include hardness, Young's modulus and fracture toughness (chapter 4).

5- Using state of the art technology for wear testing experimentally (micro and nano-scratch testing). The aim of these tests is determine the volume of wear of the PDC samples based on the geometry of the removed material. An original proposed formula was presented to quantify the wear of the PDC specimens. Analytical study carried out in the experimental work using SEM, BSE, EDX and 2-D surface roughness measurements to investigate the mechanism of wear of the PDC cutters (chapter 5).

A general work plan is summarised in Figure 1.1 to illustrate the stages of the research process.

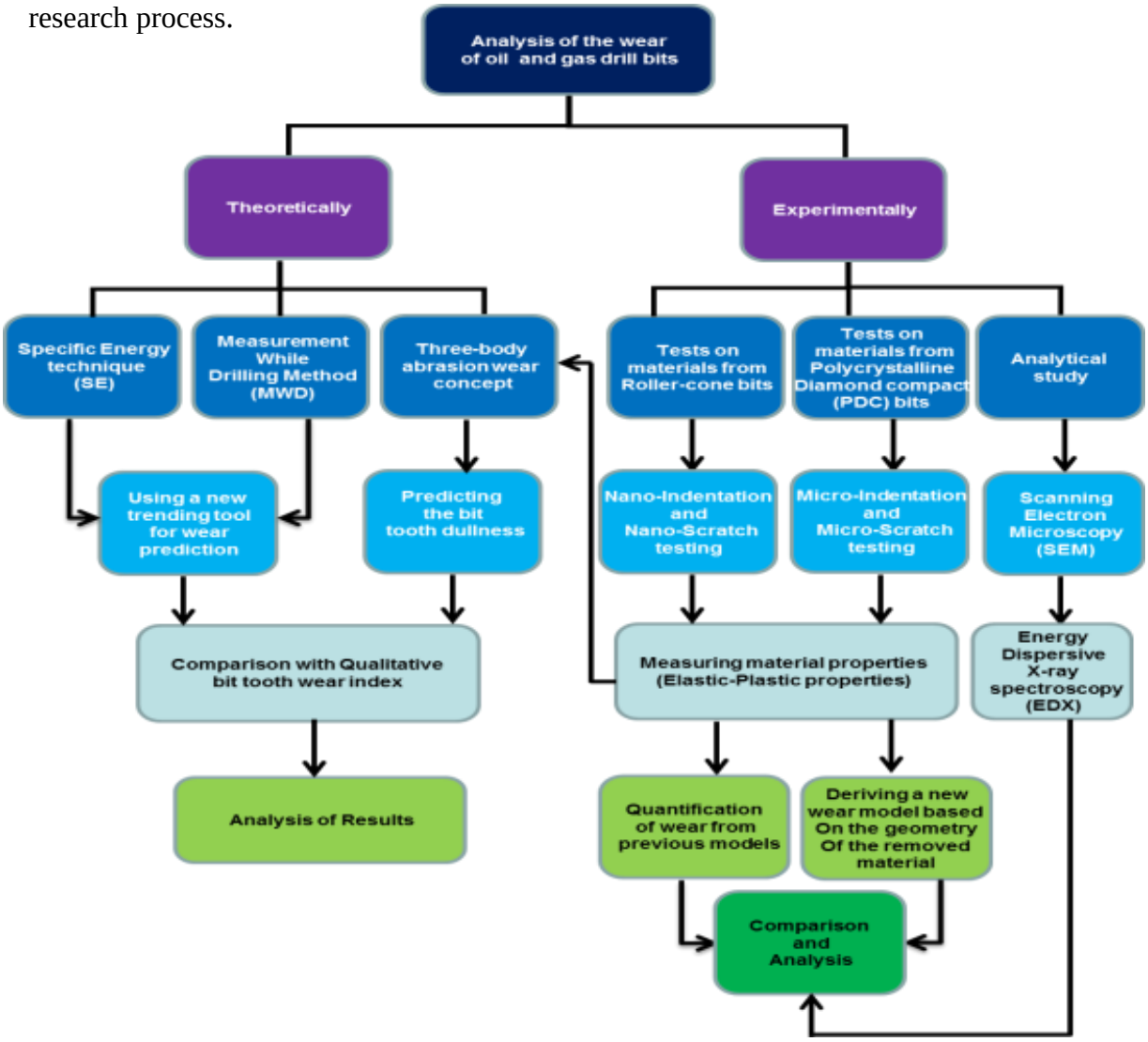

Figure 1.1 Shematic diagram of the work plan

Chapter 2 Literature Review on Oil and Gas Drill Bit Wear

This chapter deals with assessing wear analysis methods for drill bits, where bit wear mechanisms have been clarified to give a better understanding of the failure modes of roller-cone and PDC bits. In addition, state of the art of manufacturing processes of synthesising manufacture oil drill bits is reviewed. The wear mechanisms were explained by applying various laboratory tests. Abrasion and scratch tests are applied on roller-cone bits, whereas destructive and non-destructive tests are used for PDC bits. Micro-ploughing and micro-cutting behaviour in roller-cone and PDC bits were the dominant format of abrasive wear, however further scratch test analysis is needed for PDC bits for further clarification. Wear in drill bits is influenced by many factors related to drilling and rock properties, as well as the properties of materials that form the bit. The type and amount of wear is dependent on several complicated factors that need to be considered in anticipating the rates of wear in field and laboratory conditions such as the geometry of the bit as well as the drilling parameters along with the mechanical properties of the materials forming the drill bit.

Numerous quantification technologies of bit wear have been described. Each method depends on the available measured data and on wise interpretation to estimate the bit wear condition. Furthermore, each approach has assumptions that limit its applicability. However, diverse quantification techniques have been applied for understanding the bit performance of the bit and when to pull out the bit due to the wear, they should be used in conjunction with the conventional techniques of wear detection like bit records and well logging methods. Modelling and simulation are advanced approaches to give a better understanding of the bit behaviour and its design, which consequently leads to the optimum bit performance as well as predicting the wear rate of drill bits.

The main objective of this review is to investigate the wear mechanisms of the oil drill bits. Furthermore, previous methods for wear quantification were discussed and also apply a suggested approach for estimating the torque of the bit which consequently can be used for calculating dimensionless drilling parameters, to be used as indications for monitoring bit wear.

2.1 An overview of wear mechanisms of oil and gas drill bits

2.1.1 Wear mechanisms of roller-cone bits

Wear of drill bits is defined as macroscopic or microscopic removal or fracture of material, particularly at the cutter surface, or more general as, any degradation that reduces bit life. Mouritz and Hutchings (1991) investigated the wear rates of the materials used in the teeth of the rotary drill bits and the abrasive wear mechanisms of these materials. The teeth of the rotary drill bits contain three layers. The external layer consists of a WC-Co hardfacing layer, the second layer is made from high-carbon martensitic steel and the third layer is the core of the tooth that consists of low-carbon martensitic steel. Small cylindrical specimens manufactured from materials similar to those used in the teeth of rotary drill bits were used in the investigation by Mouritz and Hutchings (1991). The abrasive rocks like sandstones and non-abrasive rocks such as limestone, representing the most common rock formations encountered in oil drilling were used in the tests.

When the specimens of low and high carbon steel were scratched with a diamond stylus, the wear damage caused by the process of micro-ploughing and micro-cutting as shown in Figures 2.1 and 2.2 respectively. In micro-ploughing, the material is displaced to the sides of the wear groove and the material is not removed from the surface, while in cutting a chip is formed at the end of the groove and the material is removed from the surface (Kopeliovich ,2015).

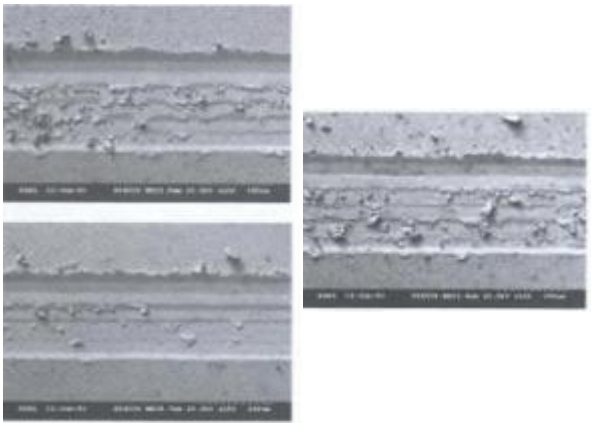

Figure 2.1 SEM images of wear scars formed by the process of micro-ploughing **(**Sinha, 2006)

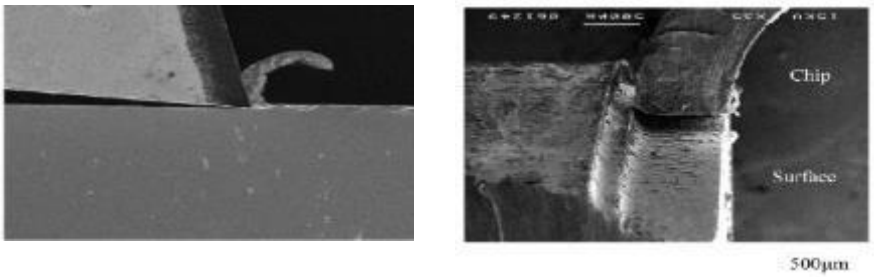

Figure 2.2 SEM images for large wear particle formed by micro-cutting (Fujiwara, 2012)

Mouritz and Hutchings (1991) observed that abrasion against limestone causes small wear by the mechanism of ploughing for low and high carbon steel, while no evidence of severe damage to the hardfacing layer of WC-Co was observed due to the high hardness of the hardfacing layer compared to low hardness of limestone rocks.

Osburn (1969) and Perrott (1979) illustrated the strong influence of rock hardness on the wear of the rotary drill bit tools made of tungsten-carbide with cobalt as a binder. Abrasion was found to be worse under high temperatures (hot abrasion) causing thermal fatigue. Osburn (1969) also added that the WC grains during the manufacturing of the roller-cone insert bits must be structured perfectly to gain maximum fracture resistance. Larsen-Basse (1973) explained that the main modes of failure for roller-cone insert drill bits are as the follows:

1- impact fracturing, 2- thermal fatigue, 3- abrasive wear and 4- mechanical fatigue due to overloads.

Reshetnyak, and Kuybarsepp (1994) studied the abrasive erosion of hard metals such as WC-Co alloys that form the roller-cone insert bits. The extent of wear was evaluated and indicated, that the hardness of the material cannot be the only dominant property causing the abrasive erosion wear. The wear is attributed to other properties, such as the compressive strength and the fracture toughness.

2.1.2 Wear mechanism of PDC bits

Polycrystalline Diamond drill bits are known to be more efficient than conventional roller cone bits, especially in soft rock formations. For a better understanding of bit efficiency, bit-rock interaction of the worn tool should be studied in detail. It has been deduced that more than 50% of the energy of drilling by PDC bits is dissipated by the wear of cutters under normal drilling conditions, when assuming a

steady- motion, and avoiding excessive heating, therefore studying the wear mechanism of PDC is highly essential (Geoffroy, 1999).

Ortega and Glowka (1984) illustrated the main categories of PDC cutters failure as: 1- delaminiation near the interface of the diamond and the substrate layers 2- plastic deformation of the diamond and table and the substrate 3- chipping at the edge of cutting and 4-chipping at the diamond table and dislodging of the diamond grains 5- abrasive wear and 6- thermal fatigue.

Dunn and Lee (1979) believed that the main reason of the PDC failure is due to the tensile stresses arising after the sintering process inducing cracks, which propagate throughout the diamond table and substrate. PDC bits in general suffer from several additional problems which including: (1) chipping of the diamond layer, (2) bit balling, (3) stud breakage in hard rocks, (4) abrasive wear, (5) poor hydraulics, (6) insufficient cleaning efficiency,. (7) deflection of the bit when applying high weight on bit, (8) scratching the composite layer of the cutters due to poor bonding of tungsten carbide stud, (9) distribution of cutters on the bit and (10) thermal failure. The improvements of synthesising manufacture methods of PDC bits to withstand both failure and impact have been investigated by many researchers (Fang *et al.* 2001). However, an important step for the improvement is to understand the failure mechanisms and modes of PDC bits. Fang *et al.* (2001) illustrated the main failure modes of PDC cutters are due to frictional heat and the high abrasiveness of the rock, as shown in Figure 2.3.

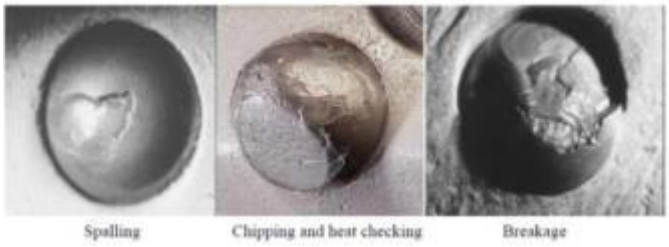

Figure 2.3 Typical failure modes of PDC inserts for rock drill bit
(Fang *et al.*, 2001)

Tze-Pin *et al.* (1992) and Zacny (2012) postulated four primary failure modes of PDC cutters according to the type of wear mechanism:

1- smooth wear 2- microchipping 3- gross fracturing or (spalling) and 4- delamination.

Tze-Pin *et al.* (1992) and Zacny (2012) attributed smooth wear to the individual diamond crystals being polished away due to mechanical and thermal loads. This type of failure is less significant than other failure mechanisms, because the wear is not severe and the material removal of the PDC cutters is trivial (Figure 2.4).

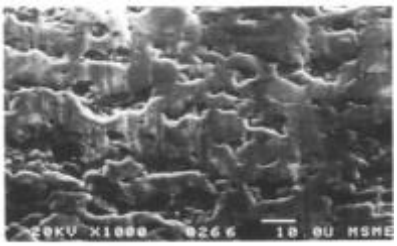

Figure 2.4 Smooth wear on the diamond layer (after Tze-Pin *et al.,* 1992)

Microchipping failure occurs along the edge of the diamond table of the PDC cutter or insert. The main reason of this failure is due to the action of the bit cutting forces besides thermomechanical fatigue (Figures 2.5 and 2.6).

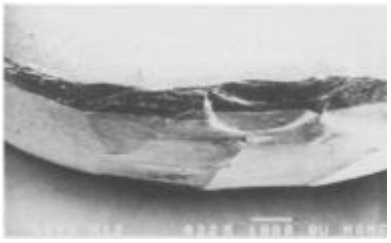

Figure 2.5 Microchipping damage at the edge of the PDC insert
(Tze-Pin *et al.,* 1992)

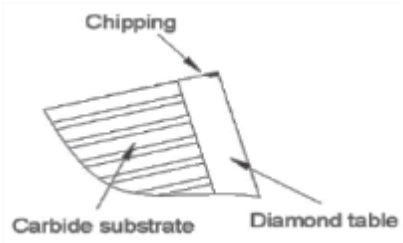

Figure 2.6 Schematic image of the microchipping failure of the PDC cutter
(Zacny, 2012)

Gross fracturing, or fatigue represents the most severe type of failure causing the damage of PDC cutters and subsequently, reducing the bit life. This failure is attributed to the impact load of the drill bit on the bottom of the wellbore. This failure usually occurs in hard formations with high hardness, causing greater stress on the PDC cutters.

Delamination of both diamond and WC layers is attributed to the mismatch between the thermal expansion coefficients of the two layers. Tze-Pin *et al.* (1992) stated that this type of failure is caused by the high impact loading of the bit on the bottomhole. Figure 2.7 shows delamination failure mode, indicated by dark arrows.

Figure 2.7 Delamination failure mode of PDC cutter (Tze-Pin *et al.*, 1992)

Zacny (2012) divided fracturing in general into four categories according to the dimensions, shape, size and distribution of the occurred fractures as follows: Microfracturing, Macrofracturing , Gross fracturing , and Ultimate fracturing.

In microfracturing, the fractures are very thin having a thickness of a few micrometers. For this category the fractures are parallel to the diamond table and the width and length of the individual fracture planes does not exceed 3 mm. Figures 2.8 and 2.9 illustrate a schematic and SEM micrographs of microfracturing under SEM, respectively.

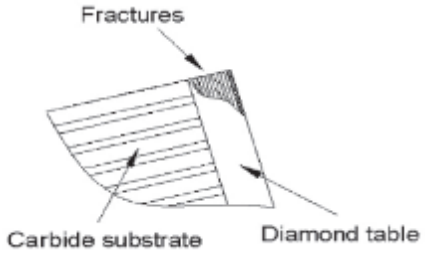

Figure 2.8 Schematic image of the microfracturing failure (Zacny, 2012)

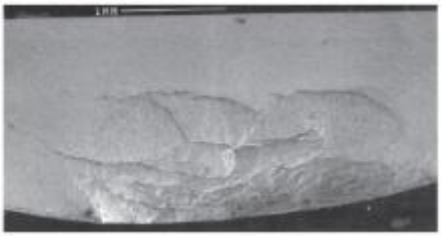

Figure 2.9 An example of microfracturing failure (Zacny, 2012)

In macrofracturing, the thickness of the fractures is greater than 0.1 mm. The length and width of the fracture are about 5 mm and 8 mm respectively. The fractures are parallel

to the diamond table and do not extend to the WC substrate. Figures 2.10 and 2.11 show a schematic and a SEM images of macrofracturing mode, respectively.

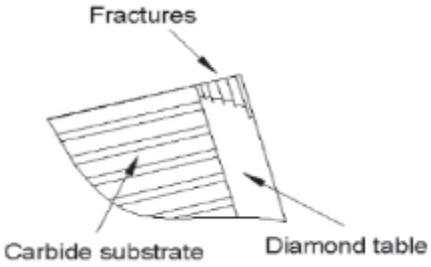

Figure 2.10 Schematic image of the macrofracturing failure (Zacny, 2012)

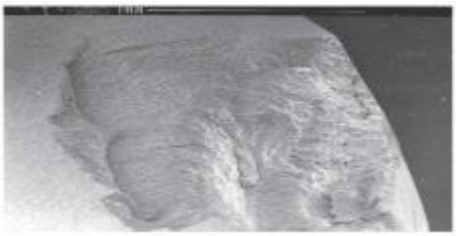

Figure 2.11 An example of macrofracturing failure of the PDC cutter (Zacny, 2012)

In gross fracturing (spalling), the fractures are thick and extend into the WC layer, with a length of about 8mm and a width up to 12 mm. Hence, this type of failure is severe and causes the removal of large parts of the diamond table as shown in 2.12 and 2.13.

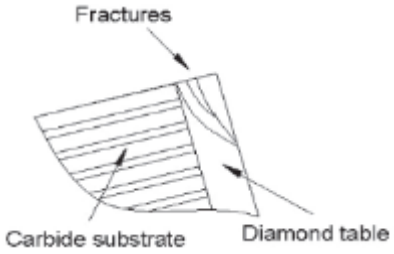

Figure 2.12 Schematic image of gross fracturing failure mode (Zacny, 2012)

Figure 2.13 Gross fracturing failure of the PDC insert (Zacny, 2012)

Ultimate fracturing is the most detrimental, because spalls can include more than half of the diamond table with a considerable part of the WC layer as shown in Figures 2.14 and 2.15.

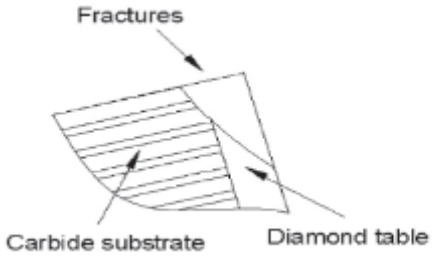

Figure 2.14 Schematic image of ultimate fracturing failure mode (Zacny, 2012)

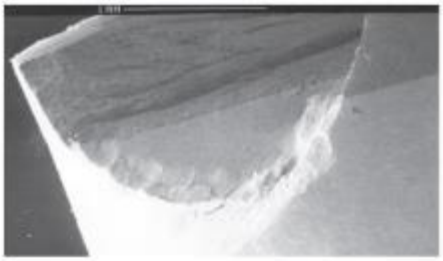

Figure 2.15 Ultimate fracturing in PDC cutter (Zacny, 2012)

It is worth mentioning that, other kinds of wear such as adhesive wear has minor effect on oil drill bits, while impact wear affect the drill bits, especially when applying excessive loads on the bits as mentioned by Wirojanupatump and Shipway (1999). In drill bits, when fluids are present, the influence of corrosion is considered negligible when compared to the wear where the material forming the drill bit is being physically removed. The corroding effect is neglected since the abrasive wear take action on the surface of the material forming the drill bit before oxidization.

2.2 Drill bit testing

2.2.1 Roller-cone bit testing

Two types of tests were performed within the studying of the wear mechanisms by Mouritz and Hutchings (1991):-

***2.2.1.1 Abrasion testing*:** the specimens of the teeth materials were abraded against sandstone and limestone disks for a total period time of 300 seconds. Mass loss measurements illustrated that the materials used in the cutting teeth of roller-cone bits suffered wear rates almost 140 times more when abraded against sandstone as compared to limestone. Figures 2.16 and 2.17 demonstrate the difference in the mass loss of the bit materials with time, or sliding distance when abraded with sandstone and limestone respectively.

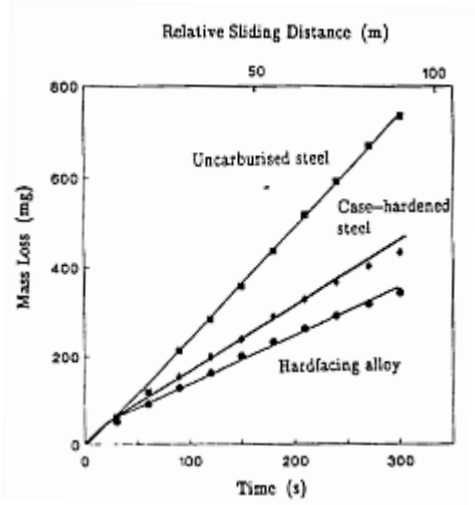

Figure 2.16 Mass loss of bit materials when abraded against sandstone (Mouritz and Hutchings, 1991)

Mouritz and Hutchings (1991) concluded that the hardness of the metal samples increased as the following order: Low-carbon steel < high-carbon steel < WC-Co alloy. The above conclusion comes from the principle that abrasive wear rate of any material depends on the ratio of its hardness (H_m) to the hardness of the abrasive (H_a).

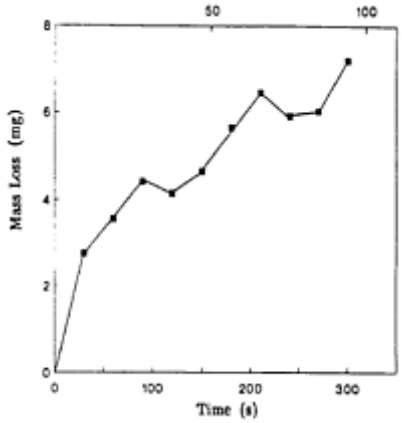

Figure 2.17 Mass loss of bit materials when abraded against limestone (Mouritz and Hutchings, 1991)

When $H_a/H_m < 1$, this means that the abrasive cannot easily scratch the material and the wear rate is extremely low. However, when $(H_a/H_m) > 1.2$, the abrasive is much more capable of scratching the material and hence causes high wear rates (Richardson 1968). The hardness values of the three materials used in the test were: - 460 HV, 700 HV and 1320 HV for low-carbon steel, high-carbon steel and WC-Co alloy, respectively.

Table 2.1 shows the mineral composition and expected hardness values for the sandstone. It can be seen that most of the minerals in the sandstone are considered hard, while the limestone is mainly consists of calcite with a hardness of 110 HV which is less than the hardness of the specimens.

Abrasion tests of the specimens against limestone disk showed that wear resistance increased with hardness. Therefore, it is safe to say that during drilling sandstone formations, the WC-Co alloy of the bit teeth external layer will wear away slowly due to its high hardness , however when this layer is damaged the teeth will face severe wear.

Table 2.1 Composition of minerals and anticipated values of hardness for sandstone (Mourtiz and Hutchings, 1991)

Mineral	Content	Hardness (HV)
Quartz	41%	~ 1,100
Rock Fragments	27%	~ 950
Feldspars	3%	~ 875
Fossils	3%	~ 110
Mica	Trace	~ 110
Heavy minerals	Trace	~ 1,200
Quartz-bearing clay	Trace	~ 1,100

***2.2.1.2 Scratch testing*:** This test is carried out to simulate the types of wear obtained by a hard mineral particle as it slides over a drill bit. This test is performed by sliding a sharp diamond stylus across polished bit materials. The attack angle (θ_c) defined as the angle between cutting face of the stylus and surface of specimen. Various attack angles are chosen during the abrasion. The selected attack angles in Mouritz and Hutchings' (1991) work, ranged from 6 to 86°. The scratched surfaces of the specimens were examined by a scanning electron microscope (SEM).

2.2.2 Testing of PDC bits

Various tests have been carried out on PDC bits to assess their performance and applicability in diverse drilling conditions including harsh environments such as high

bottom hole temperature conditions. The tests are broadly divided into, destructive and non-destructive methods (Bellin *et al*., 2010 a).

2.2.2.1 Destructive testing

In these tests the cutters of the bit are destroyed without possibility of reusing. The aim of this test is to simulate downhole conditions in order to assess the behaviour of the cutters under these conditions. Two types of destructive tests are implemented by the companies providing PDC cutters and PDC bits, namely abrasion and impact tests.

A- Abrasion test: Abrasion resistance is the capability of the cutter to survive when abraded against abrasive rocks. The abrasion resistance depends mainly on the hardness of the minerals in the rock. Highly abrasive rocks like granite or hard sandstone are normally considered for the test.

The Vertical Turret Lathe (VTL) abrasion test is mainly implemented by the PDC cutter manufacturers (Figure 2.18). In this method the cutter is fixed on a VTL with a rock sample placed beneath the cutter. The rock sample is rotated at fixed rotational velocity as the cutter indents the rock sample at a certain depth, usually less than 1 mm, and is moved laterally from the outer circumference of the rock to the axis in a spiral mode. A range of rotation rates are possible. Modern VTLs are computerised to control the applied slide velocity.

During a dry VTL test, the cutter is not cooled and consequently most of the frictional heat enters the cutter and the transformation process of diamond to graphite is accelerated. The test assesses the stability of PDC cutters under elevated temperatures and the durability of these cutters against wear. The cutter is tested until the wear progresses into the WC substrate or the test is terminated at the point when the graphitisation occurs, as indicated by a black ring left on the rock.

Figure 2.18 Abrasion testing of a PDC cutter using a vertical lathe (Bellin *et al.*, 2010 b)

At atmospheric pressure, the conversion of diamond to graphite starts at 1000°C. (Evans and James, 1964). However, when PDC cutters used to drill abrasive and hard rocks, the performance of these cutters decreased at near 750°C as it is believed that the diamond layer of the PDC cutter converts to graphite due to the frictional heat. When temperature increases, this transformation of diamond to graphite accelerates.

As PDC cutters have cobalt as a binding material, the presence of this binder accelerates the transformation of diamond to graphite. The acceleration of the graphitisation phenomena is occurred due to the significant difference of the thermal expansion coefficients between cobalt and diamond that led to the breakage of the strong bonds between the diamond to diamond grain that give the diamond high hardness forming hexagonal sheets of carbon atoms. This is the reason that PDC converts to graphite more quickly than diamond that has no binder. When facing elevated temperature, the graphitisation of polycrystalline diamond embedded in cobalt becomes the main dominant mechanism (Bellin *et al*., 2010 b). Graphitisation of diamond to graphite causes the deterioration (wear) of the PDC cutters which is attributed to the allotropic (crystal structure) convert from the diamond to the non-diamond (graphite) phase with the presence of frictional heat.

The cooled or wet VTL test (with air or water) is conducted to evaluate the life of the cutters under moderate temperatures. In this case the abrasion wear occurred will be mainly due to the abrasiveness of the rock as thermal effects are minimised. In this method wear is measured by the weight loss of the cutter.

The intrinsic goal of the VTL test is to study the resistance of diamond grains against micro-chipping and gouging when abraded against hard rock such as granite or hard sandstone.

The grinding ratio (G-ratio): G-ratio is an industrial term defined as the dimensionless number that represents the volume of rock removal per unit wear volume of the cutter. A large, G-ratio means a greater amount of rock will be removed for a certain amount of volumetric wear of the PDC cutter, and is therefore desirable. The G-ratios have been increased from 1 for the first PDC cutter generation to 15 for the most recent ones, which indicate the substantial improvements of abrasion resistance of recent PDC cutters.

B- Impact test: In this test, the cutter is impacted at a given inclined angle varying from 15° to 25° from a given height. At least ten samples of cutters are tested under different heights, giving varying impact energies up to 100J. Each cutter sample is dropped three to seven times at a given energy level. Figure 2.19 illustrates the comparison of damage due to impact for different cutters under various energy levels.

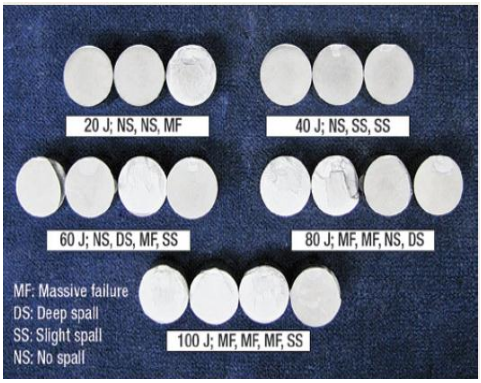

Figure 2.19 Spalled cutters after impact testing (Bellin *et al.*, 2010 b)

Figure 2.20 shows the results of 22 cutters tested under increments of impact energy varied from 20 J up to 100 J. Only six cutters survived and the test showed 0% spallation and the rest exhibited 60% to 80% spallation with an average overall spallation of 68%. For most cases, the acceptable spallation limit was < 30%, hence, the cutters failed to pass the test. However, the impact test measures the impact resistance under very low or zero vibration conditions, while in the drilling field the cutters are under a high level of vibration. Therefore, the impact test could have limitations since it does not replicate true process conditions (Bellin *et al.* 2010 b).

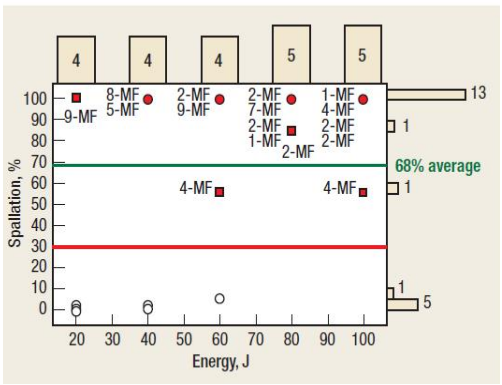

Figure 2.20 Spallation chart of impacted PDC inserts (Bellin *et al.*, 2010 b)

2.2.2 .2 Semi-destructive testing

Micro and nano-indentation tests as well as micro and nano-scratch tests on WC-Co ceramics , diamond and materials like diamond were investigated by many researchers

to measure the hardness and Young's modulus. However, there is limited work on micro and nano tests in the literature conducted on PDC samples, particularly those with WC-Co as a substrate coated with polycrystalline diamond embedded in cobalt as a binder. Further investigation of micro and nanoindentations as well as micro and nanoscratch testing is essential to measure the mechanical properties of the PDC cutters and to reveal the main wear mechanisms of the PDC inserts .

Ndlovu *et al.* (2007) performed micro and nanoindentation tests on different tungsten-carbides embedded in cobalt to measure the mechanical properties of WC-Co and to correlate the obtained results with the effect of the microstructure of the grains. The differences in the samples based on various cobalt content as well as different grain size of WC. The wear of the hard metal was investigated in microscratch testing, where various deformation mechanisms were observed. A smaller WC grain size produced a lower scratch width and depth; therefore, better scratch resistance compared to coarser WC grains.

Xie and Hawthrone (2006) investigated different WC-Co ceramics by using micro-scratch testing to monitor the plastic deformation and failure of such materials. The scratched areas were described and correlated the wear characteristics with a number of materials based on the material loss measurement .

Sawa and Tanaka (2002) carried out experiments on natural diamond indentation to measure the Young's modulus. The produced curves were showing high degree of elastic recovery. The obtained load-displacement curves were corrected for the effect of machine compliance to adjust the obtained results. The final recorded value of Young's modulus of the tested natural diamond was (1090-1217) GPa.

The hardness of the nano-polycrystalline diamond was measured by the microindentation method using mainly the Knoop indenter (Sumiya and Irifune, 2004). Vickers indenter was also used for the indentation test, while the nanoindentation test was also attempted with Berkovich probe, where a large amount of elastic recovery was observed. The wreckage of Vickers indenter during microindentation and Berkovich indenter during nanoindentation tests were encountered. Couvy *et al.* (2011) reported on the nanoindentation hardness and Young's modulus of hard materials: Nanopolycrystalline Diamond (NPD) ; Cubic Boron Nitrite (CBN) and Polycrystalline

Compact Diamond (PCD). The PCD sample consists of diamond grains in micron scale embedded in silicon-carbide as a binder with a volume of 25%. The obtained results of nanohardness of the PCD sample were (8-19) ± 2 GPa and Young's modulus was (86-168) ± 24 GPa. Figure 2.21 shows the nanoindentation curves for the samples investigated.

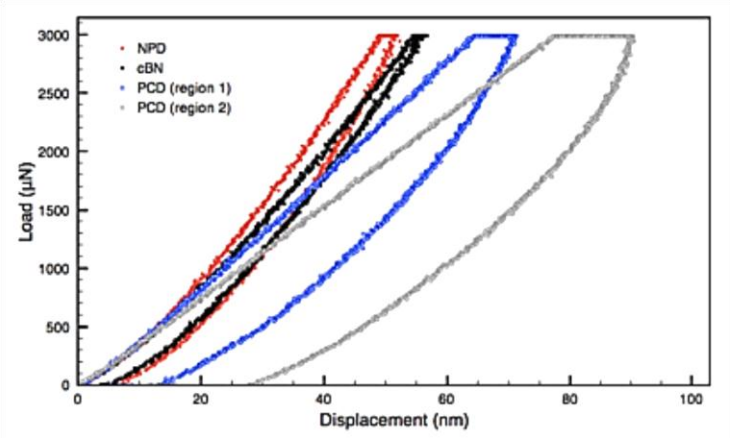

Figure 2.21 Load–displacement curves measured during nanoindentation of NPD, CBN and PCD samples (Couvy *et al.*, 2011)

Lu *et al.* (2012) performed micro-scratch testing on specimens made of WC-Co coated with a thin layer of diamond. The cobalt content of the substrate was 6% and the thickness of the diamond layer was around 4 μm. The micro-scratch test was conducted with a Rockwell diamond indenter with a tip radius of 50 μm. The micro-scratch test was carried out with various loads of 10, 15, 20, 25 and 30 N. The aim of the test was to investigate the delamination of diamond thin coatings on WC-Co materials. The delamination was noted to be more worse when increasing the load. The width of the diamond coating after delamination increases with increasing load. It was found that, the critical load for the tested diamond coatings was between 4 and 6 N. Figure 2.22 illustrates the microscratch test of the sample and the grooves obtained at various loads.

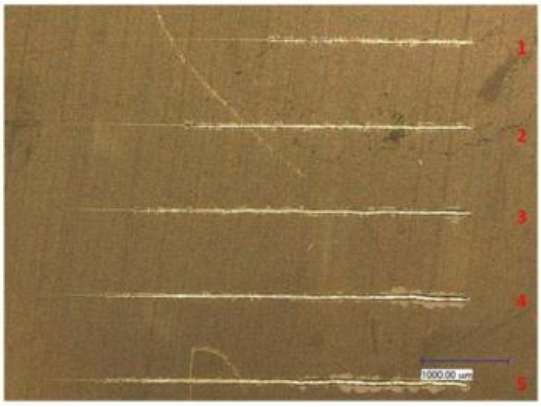

Figure 2.22 Microscopic image of the scratches produced by micro-scratch test (Lu *et al.*, 2012)

Semi-destructive testing using state of the art technologies opens the door for further study relevant to wear analysis and quantification rather than using traditional techniques that based on the measurement of the mass loss, especially with PDC samples that have cobalt or nickel as a binder. Micro and nano-scratch testing are the most approaches could this task.

2.2.2 .3 Non-destructive testing

In this method, a part of the cutter is examined in order to detect any voids and flaws, particularly at the interface of diamond to carbide. Visual and microscopic testing as well as C-scan techniques are the most common methods for detecting the flaws. The latter approach is used to detect delamination and voids in the diamond table by using ultrasonic waves ranging from 0.2 to 800 MHz (Bellin *et al.*, 2010 b). Small flaws and defects can be detected down to 5-10 μm and the determination of their location is also possible. The test is achieved by placing the cutter into a tank of water, which is scanned using an acoustic microscope. An image of the inner diamond table and the diamond to substrate interface is produced. This is useful when flaws, cavities voids cannot be detected by visual or microscopic examination (Bellin *et al.*, 2010 b). Figure 2.23a illustrates examples of the flaws discovered by C-scan test. Furthermore, the Acoustical Emissions Toughness Test (AETT) can be quantitatively applied to PDC cutters to evaluate the impact strength of the bonds between diamond - diamond grain created during the sintering process under High Pressure and High Temperature (HPHT). The test includes applying loads by a diamond indenter on the PDC inserts at constant rate. Meanwhile, acoustic emissions caused by micro-cracks are detected by special acoustic sensor and the crack length determined. As such this technique gives a measure of fracture toughness as shown in Figure 2.23b (Varel International, 2010).

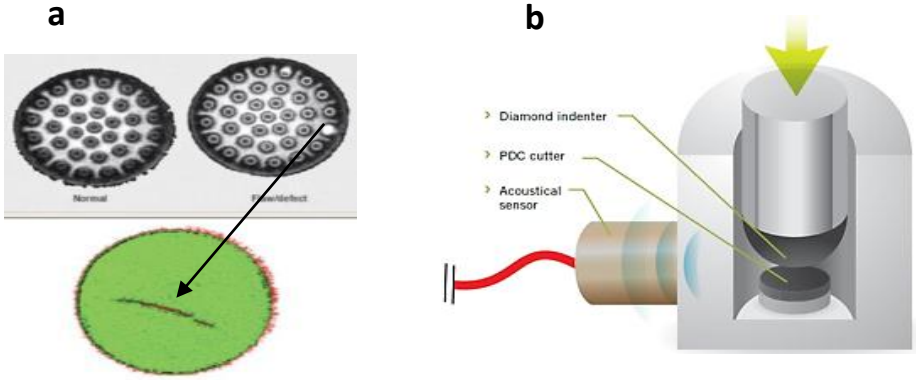

Figure 2.23 (a) C-scan test to detect flaws in the diamond of the PDC cutter (Bellin *et al.*, 2010 b) (b) Acoustical emissions toughness test (Varel International, 2010).

2.2.2.4 Analytical study

Boland and Lee (2010) showed the use of analytical techniques for studying the Thermally Stable Diamond Composites (TSDC) that are used widely in the manufacturing of Thermostable PDC bit cutters (explained in section 4.6). The analytical approaches include Scanning Electron Microscope (SEM), Energy Dispersive Spectroscopy (EDS), X-ray Diffraction (XRD) and Raman Spectroscopy (RS). The latter was used by Kromka *et al.* (2005) to distinguish between poor and good quality TSDC samples. This comparative study was based on the variation of Raman spectrums; where low wear resistance or poor quality TSDC samples, showed a broad peak between 1350 and 1550 cm^{-1}, which is related to graphite or non-diamond material (Figure 2.24). On the other hand, good quality TSDC inserts displayed a sharp unique peak close to 1332 cm^{-1}, which is characteristic of diamond, with no evidence of the graphite peak, as shown in Figure 2.25.

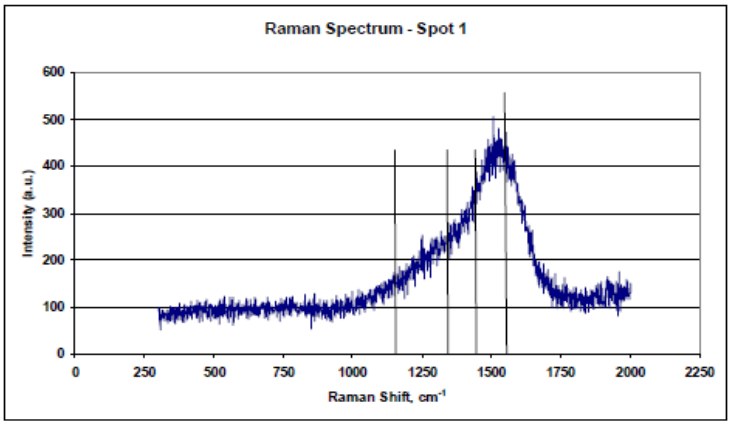

Figure 2.24 Raman shift of poor wear resistance of a TSDC sample (Boland and Lee, 2010)

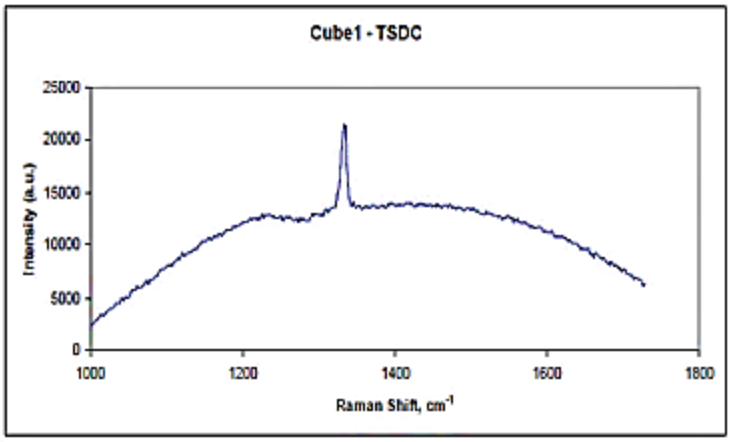

Figure 2.25 Raman spectrum of high wear resistance of a TSDC specimen (Boland and Lee, 2010)

Boland and Lee (2010) compared PDC cutters of various qualities using X-ray imaging. The study revealed the flaws within a projected image produced from X-ray source. The 3D X-ray images displayed the intrusions of the substrate (blue colour) into the diamond layer, forming cracks that some of which extend to the outer surface (Figure 2.26). The cracks were found to be generated during the manufacturing process of the PDC inserts. PDC samples that contain such cracks showed poor wear resistance compared to good wear resistance quality PDC cutters that showed fewer flaws (cracks).

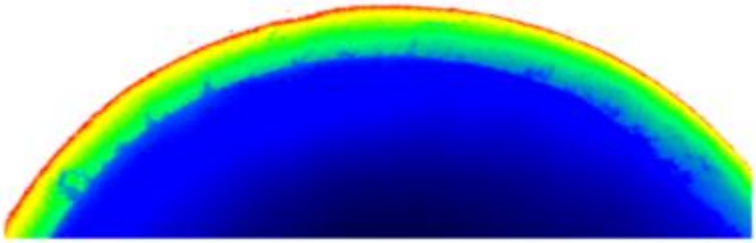

Figure 2.26 3D X-ray image of a poor wear resistance PDC cutter showing the intrusions of WC –substrate (blue colour) to the outer surface (Boland and Lee, 2010)

2.3 Theoretical background on wear quantification

Bit performance, defined as the service duration of bit tooth and the bearings, is affected by many factors according to the drilling operation. The effect of rotary speed on drill rate and bit performance has been widely studied, with most of the research dedicated to a better understanding of the parameters involved in bit performance. It has been illustrated that tooth wear increases with rotary speed and thus, allowing increasing of bearing revolutions that increase the possibility of bearing's failure. Increased the tooth wear negatively affects the drilling efficiency and consequently decreases the penetration rate**.**

2.3.1 The aim of the theoretical background

The objective of the theoretical background is to explain and describe empirical multi models developed by several researchers. The focus will be on the expressions, formulas and the applications.

2.3.2 Quantification methods of bit wear

2.3.2.1 Specific energy (SE) technique

Many authors aimed at finding the best optimum method to detect the wear of the drill bits to determine the life of the bit. Bit performance is intrinsically affected by wear, thus the efficiency of the drill bit could be determined by using the specific energy technique (*SE*).

Several attempts have been made to study the principle of specific energy, also referred to mechanical specific energy (*MSE*) and its effect on bit performance. Teale (1965) defined the concept of specific energy in rotary drilling as the energy required removing a unit volume of rock. Teale indicated that *SE* is inversely proportional to fragment size of rock excavated and as such minimum value of *SE* corresponds to the unconfined compressive strength of the rock, which is a fundamental property. Teale (1965) presented the following equation for the *MSE* determination:

$$MSE = \frac{Work\ done}{Volume\ of\ rock\ removed} = \frac{W}{A_{bit}} + 120\pi\frac{N.T}{A_{bit} * PR} \qquad (2-1)$$

where W is the weight on bit (lb) , A_{bit} is the surface area of the bit (in^2) , N is the rotary speed (rpm) , T is the torque at bit (lb.ft) and PR is the penetration rate (ft/hr). The unit of *MSE* in the above equation is in $lb.in/in^3$ or psi. The full derivation of Equation (2-1) is shown in Appendix A.A.

Pessier and Fear (1992) developed an energy balanced model for drilling under hydrostatic pressure rather than atmospheric pressure as used in previous models in order to make improvements more applicable to the drilling field. The output results were correlated with the field data and there was a close agreement. Two key indices were used for bit performance and bit monitoring: mechanical specific energy and bit coefficient of sliding friction. Both of these indices provide a good indication of bit performance, thus leading to optimum bit selection, diagnosis of failure of the teeth and bearing of the bit, as well as the real time monitoring of the drilling process. Another *SE* equation was introduced (2-2) depends on drilling parameters such as rate of penetration, weight on bit and torque at bit. Penetration rate is the distance (depth interval) being drilling in a certain period of time by the bit. It is obtained practically from dividing the interval being penetrated over the required time for this penetration.

When torque at bit is not measured while drilling, Pessier and Fear (1992) derived an empirical equation for the estimation of torque as follows:

$$T = \mu \frac{d.W}{36} \qquad (2-2)$$

where T is the measured torque (lb.ft) and μ is the bit coefficient of sliding friction (dimensionless number). μ values have been obtained from laboratory measurements and varied from 0.21 for roller-cone bits up to 0.84 for PDC bits, depending on the formation being drilled and the bit type.

Pessier and Fear (1992) reformulated Equation (2-1) as follows:

$$MSE = W \left(\frac{1}{A_{bit}} + \frac{13.33 \,.\mu\,.N}{d\,.PR}\right) \qquad (2-3)$$

A dramatic increase in *SE* values could be a warning indication of short bearing life and low *PR*. The same interpretation happens when μ values (bit coefficient) increase sharply from the normal increasing trend line.

MSE values obtained from Teale's equation could be used for lithology prediction as the specific energy corresponds to the uniaxial compressive strength of the rock. Dupriest and Koederitz (2005) found that during drilling, the highest efficiency the drill bit reaches is 30-40%, and consequently the *MSE* from Teale (1965) has to be corrected by multiplying with a factor ranging from 0.3 - 0.4 before it can be compared with the formation strength. The adjusted Mechanical Specific Energy MSE_{adj} is obtained as follows (Dupriest and Koederitz 2005):

$$MSE_{adj} = MSE * EF \qquad (2-4)$$

where *MSE* is the raw Mechanical Specific Energy (psi) from Teale's equation, *EF* is the correction Efficiency Factor (dimensionless) and $MSE_{adj.}$ is the corrected mechanical specific energy (psi).

In most petroleum drilling applications, 0.35 is used as an average value for *EF* regardless of drill bit type (Dupriest and Koederitz 2005). Figure 2.27 shows the mechanical efficiencies of the two main kinds of drill bits used in oil and gas drilling. It

illustrates that when the weight on bit (*W*) and the obtained depth of cut increase, the bit finally reaches its highest efficiency i.e. 35-40% for roller-cone (insert) bit and 30-35% for PDC bit. Efficiency is typically determined by comparing the actual energy consumed by the bit with the theoretical energy required to excavate a specific volume of rock. Bits in general tend to transport only 30-40% of their energy into the process of rock destruction, even when running at maximum performance. However, if depth of cut is insufficient, the performance of energy transport decreases even below 30-40% causing very low rate of penetration (*PR*).

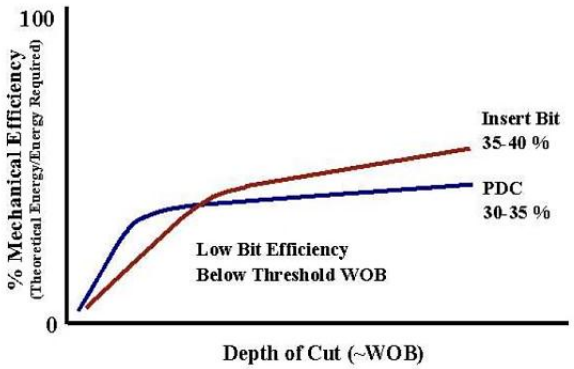

Figure 2.27 Drilling efficiencies of tungsten-carbide roller cone and PDC bits (Dupriest and Koederitz, 2005)

Waughman *et al.* (2002, 2003) described a methodology for measuring specific energy (*SE*) for every section drilled with checking the current formation type (lithology) with the benefit of gamma ray (*GR*) readings to indicate bit performance and wear. The main disadvantage of this technique is that it requires measuring the bit torque which it is not always measured during drilling. Consequently, many authors attempted to develop methods for computing *SE* without torque values.

Rabia (1982) and Rabia *et al.* (1986) simplified the specific energy equation of Teale so that torque was no longer included. The torque in Teale's equation was replaced by an approximation that torque is directly proportional to weight on bit and bit diameter. Rabia (1982), Rabia *et al.* (1986) and Farrelly and Rabia (1987) applied their modified specific energy formula on the actual field drilling as follows:

$$SE = 20\ \frac{W\,.N}{d\,.PR} \qquad (2-5)$$

where *W* is the weight on bit (lb) , d is the diameter of the bit (in) , *N* is the rotary speed (rpm), *PR* is the penetration rate (ft/hr) and *SE* is expressed in lb.in/in^3 or psi.

Equation (2-5) is used specially for roller-cone bits when drilling various rock formations as postulated by Rabia (1985). The derivation of Equation (2-5) is shown in Appendix A.A.

Farrelly and Rabia (1987) stated that when drilling a homogenous interval, the specific energy shows a gradual slow rise, an indication of continuous bit wear. However, dramatic increases of *SE* values correspond to severe bit wear, lithology change, drill string vibration or even sometimes due to bit balling which occurs when shale particles accumulate on the face of the drill bit. These multiple conditions could cause the specific energy to rise, due to a number of reasons, resulting misleading interpretation (Dupriest and Koederitz 2005).

SE values were calculated based on field data for different bits and for various formations. Farrelly and Rabia (1987) concluded that *SE* controls the bit performance, where the lowest values of *SE* refer to optimum bits to be used in drilling operation and consequently reduced drilling costs. *SE* values provide a reasonable indication of bit performance during drilling. *SE* depends on bit type, bit wear, cuttings removal, rock type and rock properties (Farrelly and Rabia 1987). Specific energy gives an indication of lithology changes and how to choose the optimum bit for drilling a certain formation. However, the *SE* technique is not totally reliable and should be used in conjunction with other methods during bit selection to give a better understanding of bit performance. The following approaches could be used in conjunction with *SE*:

1- Cost per foot assessment 2-Bit wear assessment 3-Bit records analysis 4- Coding of International Association of drilling contractors (IADC) 5- Well logs and geophysical analysis 6- Geological information.

2.3.2.2 Wear and Measurements While Drilling (MWD)

Measurement While Drilling (MWD) tools were introduced in 1981 to measure some of the important drilling parameters, particularly related to bit wear such as weight on bit, rotary speed, penetration rate and bit torque. The bit information can be obtained by computing parameters from the MWD. Warren (1984), Burgess (1985), Falconer and Normore (1987) as well as Kuru and Wojtanowicz (1992) investigated a torque model to show the effects of tooth wear on drilling. The method is based on a Mechanical

Efficiency Log (MEL) which used data of penetration rate, rotation speed and MWD values of torque and weight on bit.

The following dimensionless drilling equations were defined:

$$T_D = a_1 + a_2\sqrt{PR_D} \quad (2-6)$$

where T_D is the dimensionless torque, PR_D is the dimensionless penetration rate (see Equation 2-10), a_1 and a_2 are the drilling torque constants and they varied with lithology and bit wear. Wear of the bit affects mainly a_1 accordingly Equation (2-6) can be written as follows (Burgess 1985):

$$T_D = a_1 E_D + a_2\sqrt{PR_D} \quad (2-7)$$

where E_D is the bit drilling efficiency, which is a function of bit wear (dimensionless) and ranges from 1 for a new sharp bit to near zero for completed worn bit. When E_D equals 1, Equation (2-7) would be same as Equation (2-6). Rearranging Equation (2-7) leads to Equation (2-8):

$$E_D = (T_D - a_2\sqrt{PR_D})/a_1 \quad (2-8)$$

$$T_D = \frac{T}{W.d} \quad (2-9)$$

where T is the measured torque (lb.ft), W is the weight on bit (lb) and d is the bit diameter (in).

$$PR_D = \frac{PR}{N.d} \quad (2-10)$$

where PR_D is the dimensionless rate of penetration, PR is the rate of penetration (ft/hr), N is the bit rotary speed (rpm) and d is the diameter of the bit (in).

F_D is another dimensionless parameter representing flatness and can be determined from E_D values. Flatness of the bit tooth refers to the wear of the cutting parts of the bit (tooth for roller-cone bits or inserts for PDC bits).

$$F_D = W_D.(1 - E_D) \quad (2-11)$$

where W_D is the dimensionless weight on bit.

$$W_D = \frac{PR_D}{4\,.\,a_1 E_D} \qquad (2-12)$$

When applying this approach, calculations of the dimensionless drilling parameters i.e. Equations (2-7)-(2-12) should be done for each depth interval.

The values of drilling torque constants a_1 and a_2 could be determined by plotting T_D vs. square root of PR_D where a_1 being the intercept of the T_D axis and a_2 being the slope of the time through the plotted points.

By using this model, it could become possible to anticipate the wear of milled tooth bits in real time from MWD measurements. When wear occurs, E_D decreases from one to zero, while F_D values behave in a reverse way; F_D is equal to zero for a sharp new bit and when wear occurs F_D values start to increase.

In this case during the course of drilling, the bit could be pulled and replaced when the bit efficiency (E_D) falls sharply. With MWD technique, a drill bit could be used to the full extent of its useful life, and so maximize the drilling operation and decrease drilling costs.

2.3.2.3 Other quantification methods of wear

Abrasive wear is the dominant type of wear occurring in oil well drilling due to the drilling mechanism of the bit cutters against rock formation. This type of wear causes serious damage to the drill bit, therefore, many tribologists and lubrication engineers have assessed means of wear quantification to understand the materials resistance against it and how it can be minimised. Various wear models have been postulated, however most are only relevant for specific cases.

Rabinowicz (1996) developed an abrasive wear model to improve the quantification of the two body abrasive wear (Figure 2.28). This model describes the process of an abrasive grain sliding over a distance (X) while the grain is pressed upon a given surface with a force (F). Rabinowicz (1977) derived the following equation of wear through two body abrasive for soft rock formation:

$$V_w = \frac{F.\tan(\theta)\,.X}{\pi\, H_w} \qquad H_w < 0.8H_a \qquad (2-13)$$

where *Vw* is the volume of material removed, *F* is applied load (N), *X* is the sliding distance (m), θ is the abrasion angle (˚), H_a is the hardness of the abrasive material (N/m^2) and H_w is the hardness of the abraded material (N/m^2).

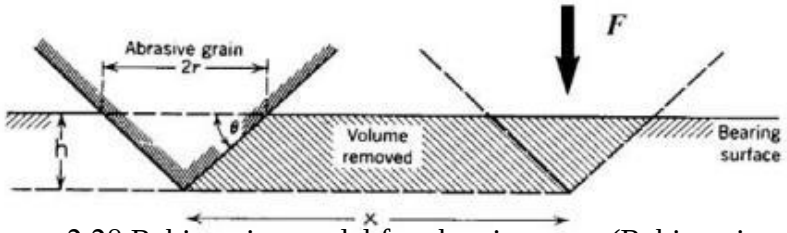

Figure 2.28 Rabinowicz model for abrasive wear (Rabinowicz, 1996)

However, application of Equation (2-13) is limited to soft rock formation, Rabinowicz postulated the following equation for wear determination against intermediate rock formations in the case of three body abrasive wear, where the hardness of the abrasive and the abraded material are included.

$$V_w = \frac{F.\tan(\theta).X}{5.3\,H_w}\left(\frac{H_a}{H_w}\right)^{2.5} \qquad 0.8H_a < H_w < 1.25H_a \qquad (2-14)$$

Hutchings (1992) also investigated abrasive wear involving the removal of material by plastic deformation. This model is based on assuming that the abrasive particle is represented as a cone of semiangle (α_p) being dragged across the surface of the material under indentation pressure. Hutchings (1992) suggested this abrasive wear model is as follows:

$$V_w = \frac{2\,F\,X}{\pi\,.H_w.\tan(\alpha_p)} \qquad (2-15)$$

where V_w is the volume of wear (m^3), *F* is the applied load (N), *X* is the sliding distance (m), H_w is the hardness of the abraded material (N/m^2) and α_p is the half angle of the abrasive particle (˚).

The main difference between Rabinowicz and Hutchings models is that Rabinowicz assumed that the projected area of the cone would be a whole circle, while Hutchings assumed that that the normal load is supported over only half of the circular projected area of the cone. In addition, the relation between the abrasive angle (θ) and the semiangle (α_p) that represents the half angle of the abrasive particle is as follows:

θ= 90- α_p , and $\tan(\theta) = 1/\tan(\alpha_p)$.

Accordingly, the expected wear volume values obtained from Hutchings would be double values of Rabinowicz.

Element six Ltd, one of the largest companies that manufacture PDC cutters, investigated an empirical formula of abrasive wear of polycrystalline diamond cutters developed by Dubrovinskaia *et al.* (2006), which is as follows:

$$W_H = K_{IC}^{0.5} . E^{-0.8} . H^{1.43} \qquad (2-16)$$

where W_H is wear resistant coefficient or the reciprocal of wear coefficient (dimensionless), K_{IC} is the fracture toughness (MPa .m$^{0.5}$), E is the Young's modulus (GPa) and H is the hardness (GPa). Equation (2-16) suggests that increasing the value of hardness or fracture toughness of the material makes it more resistant to wear. However,

since this equation is empirically derived, no mechanistic interpretation is offered to explain the proposed relationships with mechanical properties.

Table 2.2 shows mechanical properties and wear coefficients of various PDC products manufactured by different companies alongside natural diamond (PDC cutters manufactured by Element six Ltd. are referred to ADNRs). However, it is not clear how the mechanical properties were determined.

Table 2.2 Mechanical properties and wear coefficients of PDC and natural diamond (Dubrovinskaia *et al.*, 2006)

Property	Syndrill	Syndite	Sundax3	Natural Diamond	ADNRs
Fracture toughness (MPa.m$^{1/2}$)	9.8	8.8	6.9	3.40-5.0	11.1 ±1.2
Knoop hardness (GPa)	50	50	50	57-104	105 ±12
Young's modulus (GPa)	810	776	925	1140	1070 ±54
Wear resistant coefficient	3.97	3.89	2.99	2.14-5.49	10 ±2

Budinski (2007) demonstrated the implication of Archard wear model (1953) as shown in Equation (2-17):

$$V_w = \frac{K \,.\, F \,.\, X}{H} \qquad (2-17)$$

where K is a constant, or wear coefficient of the system which needs to be determined experimentally, F is the force pressing bodies together, X is the sliding distance and H is the hardness of the softer solid of the two interacting solid surfaces. Archard's equation suggests that wear increases with increased force (F) and sliding distance, while the wear decreases when the hardness of the material increases.

Budinski (2007) modified Archard equation by including the conical angle of the abrasive object:

$$V_w = \frac{K \,.\, F \,.\, X}{H \,.\, B} \qquad (2-18)$$

where B = 2.cot θ/π and θ represents the conical angle of the abrasive object. K is a constant. Equation (2-18) is used widely for erosive wear and functionalised for wear prediction by simulation.

Ning and Ghadiri (2006) developed a wear model for materials under shear loading. The surface damage in consideration here is the elastic-plastic damage by the propagation of lateral cracks as particles are loaded and slid against each other by shearing. The new developed model (Equation 2-19) shows that the fracture toughness has a stronger influence on the volume loss than the particle hardness.

$$V_w = \frac{0.07 \,.\, F^{\frac{5}{4}}}{K_c \,.\, \pi^{\frac{5}{4}} \,.\, H^{\frac{1}{4}}} \left(2X + \frac{\pi^{\frac{1}{4}} \,.\, H^{\frac{1}{4}} \,.\, F^{\frac{3}{4}}}{17.1 \,.\, K_c} \right) \qquad (2-19)$$

where V_w is the wear or the volume loss by surface damage assuming plastic deformation, F is the applied load, X is the sliding distance, H is the hardness and K_c is the fracture toughness of the particle. Ning and Ghadiri's equation is applied to semi-brittle materials. This model could be applied on tungsten-carbide ceramics and polycrystalline diamond as they have a brittle part which is diamond embedded in a ductile material (cobalt) and the same with WC (Ndlovu, 2009, Xu, 2008 and Donald, 2010). However, the equation includes the fracture toughness which is difficult to determine, especially for polycrystalline diamond (Lin *et al*., 1994). Determination of fracture toughness of the diamond layer experimentally was constrained when using

conventional approaches and there is limited work in the literature. Overall, Table 2.3 illustrates the main models used for wear quantification and the parameters required for the determination of wear.

Table 2.3 Bit wear quantification models

Wear Model	Applied Load	Hardness of the Abrasive Material	Hardness of the Abraded Material	Sliding Distance	Fracture Toughness	Angle of Abrasion	Young's Modulus
Rabinowicz (1996)	√	√	√	√	×	√	×
Hutchings (1992)	√	×	√	√	×	√	×
Ning & Ghadiri (2006)	√	×	√	√	√	×	×
Archard (1953)	√	×	√	√	×	√	×
Element six Ltd. (2006)	×	×	√	×	√	×	√

2.3.3 Wear quantification using simulation methods

2.3.3.1 Finite Element Analysis (FEA)

FEA can be defined as a process of computer simulation or modelling interactions between contacting surfaces by setting a two or three dimensional mesh on surfaces, taking into account all the relevant material properties (Budinski, 2007). FEA is useful for predicting the distribution of the stresses within contacting solids. Figure 2.29 shows a simple scheme of finite element modelling; indentation of a flat surface by a sphere, where the nodes of the mesh in the contacting area are deformed depending on parameters such as modulus of elasticity and Poisson's ratio. The distribution of stress or deflection map is shown in Figure 2.30. However, it should be noted that the accuracy of this approach depends on the accuracy and resolution of the mesh, and the material properties input into the mode.

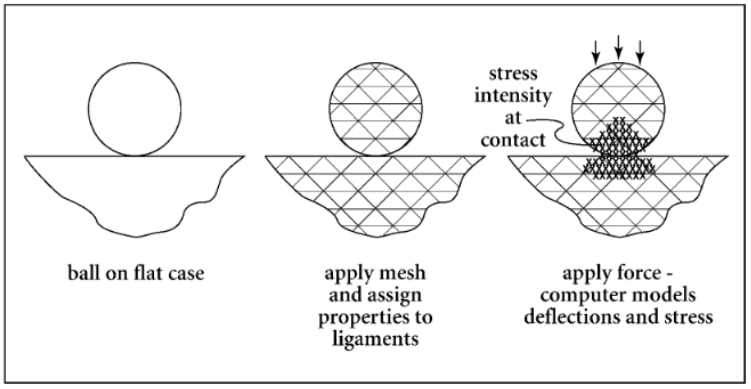

Figure 2.29 Simple scheme of finite element modelling (Budinski, 2007)

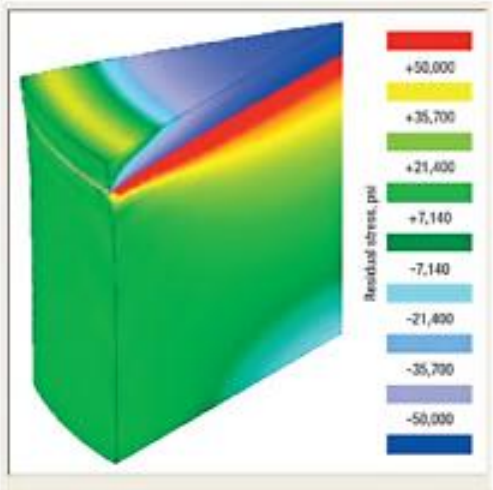

Figure 2.30 FEA simulation results showing the stress distribution at the diamond-to-substrate interface (Bellin *et al.,* 2010 b)

Furthermore, for modelling wear processes, plastic behaviour of the material should also be taken into account. Finite element modelling is considered a novel technique for analysing cutter behaviour and cutter advancements (Bellin *et al.,* 2010 b). FEA has been used for PDC bits and on virtual cutters to simulate the sintering conditions and to anticipate stress distribution in the diamond table and the diamond to substrate interface, in particular the residual tensile stress responsible for fragility in the diamond table, as shown in Figure 2.30. The use of FEA allows a numerical matrix solution, mapping the physical properties such as stress and strain of the material at different locations within the cutter which provides enough knowledge for minimising the wear of PDC cutters under various drilling circumstances. The stress and strain can then be optimised using certain design features built into the cutter. The use of FEA has allowed the advancement of new cutter technologies with improved performance. Further study is needed in this field to demonstrate how FEA can be used to quantify wear in drill bits and particularly for determining the optimum suitable model for wear quantification.

Many FEA models have been used in the design and determination of thermal behaviour of PDC bits. Continuous refinement of complex FEA models has led to the development of PDC bits, taking into account many factors that might affect the manufacturing of the PDC bits (Ziaja and Miska, 1982). However, several assumptions are typically applied, which limit the practical application of the simulation models to predicting the performance of PDC bits (Ziaja, 1985).

2.3.3.2 Discrete Element Method (DEM)

In the last decade the broad use of the discrete element method has progressed and been deployed widely for various applications. DEM considers a number of particles that move independently, following Newton's laws of motion, with particle contacts following a force-displacement law. Currently its application is mainly on various particle processing problems as a means of determining information that cannot be found experimentally. Favier (2007) suggested two issues that can limit the implementation of DEM:

1- The determination of the DEM model, i.e. the determination of the model parameters that must be included in the model and their values.

2- The limitations of the DEM model such as the assumed element size and numbers being used.

However, if the DEM model is chosen for the optimum solution of the problem, the real challenge is to determine the best model for the material with respect to the conditions within the process. DEM can be used to determine the loads exerted by granular material on various structures. The DEM model can be effectively combined with finite element analysis (FEA) to provide load information for structural analysis. DEM has been used to model the fracturing of rock and cemented materials (Favier 2007). The fracture features of the rock are controlled by the strength of the bonds between particles, the particle properties and size distribution of the particles (Favier 2007). Mendoza *et al.* (2010) employed DEM to model rock cutting as represented by laboratory scratch tests, showing a good agreement with experiments.

Figure 2.31 illustrates the cutter of a bit drilling through the bonded particle bed. The study shows that this approach could be applied to simulate the drilling of rock by drill bits to evaluate the wear of the materials that form the bit. Akbari *et al.* (2011) used DEM to simulate the loads affecting PDC cutters and their interaction with the rock formation. Boundary conditions such as pressure, temperature, velocity, humidity, friction coefficient, etc. were assumed in order to study the friction forces and the rate of penetration with the optimum weight on bit to gain maximum rock cutting as shown in Figure 2.32.

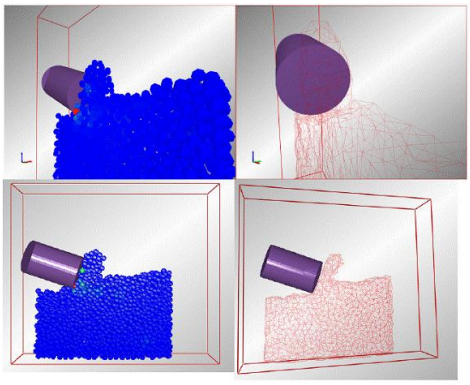

Figure 2.31 A simplified DEM model of a drill cutter removing a cutting by the means of breaking the bonds between the particles (Favier, 2007)

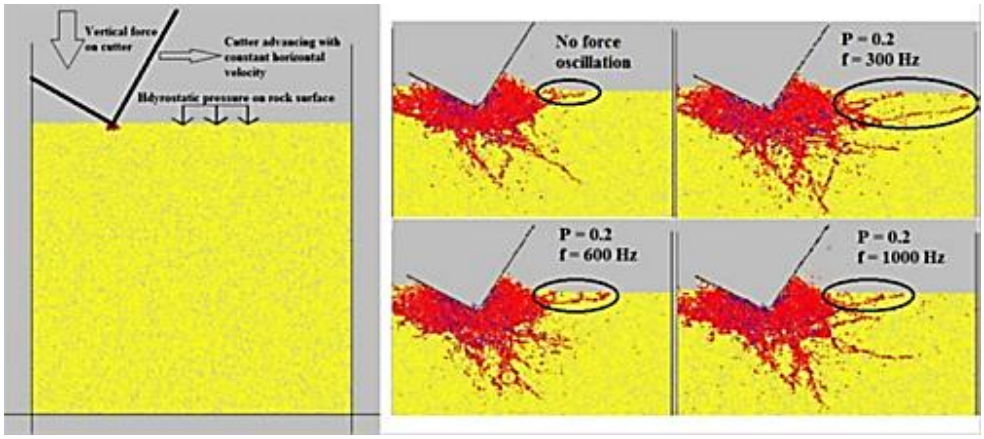

Figure 2.32 Rock cutting process using DEM model (Akbari *et al.*, 2011)

2.4 Novel methods for improving roller-cone and PDC drill bits

2.4.1 Enhanced inserts

Sneddon and Hall (1988) introduced a new technique of Composite-Transition Layer (CTL) to ameliorate PDC bits, to rectify the problematic drilling conditions against hard abrasive formations, such as granite and quartz. This new step of synthesising manufacture PDC bits provides better resistance to impact and wear damage. In this approach, the transition layers of the cutter consist of PDC and sintered WC-Co particles bonded with each other. The process is achieved by mixing individual crystals of man-made diamond and cemented carbide particles. This process is called High Pressure, High temperature (HPHT) technology for sintering PDC. Figure 2.33 shows the cross- section of an enhanced insert CTL technology (Sneddon and Hall, 1988). The outer layer of the insert cutter is completely PDC, then the concentration of WC-Co increases towards the inner layers until the last inner layer, which consists of 100%

WC-Co. According to the tests of the new enhanced PDC bits, several advantages appeared by using this technique. Firstly, each composite layer enhances the layer below it forming a great coat against abrasion. Secondly, manufacturing of Composite PDC-WC-Co layers leads to a rounded or curved shape of the cutters, thus allowing more impact resistance as compared to the planed conventional cutters. The rounded shapes provide improved toughness and reduced contact area.

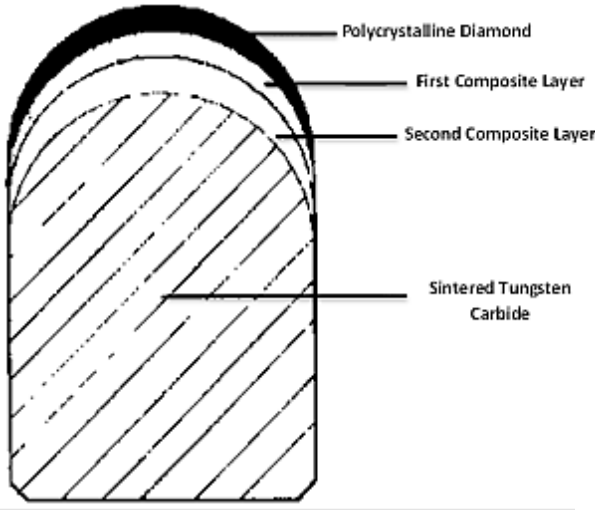

Figure 2.33 Cross section of enhanced inserts (Sneddon and Hall, 1988)

2.4.2 Co-Composition and various grain size graded cemented carbides

Mori *et al.* (2003) studied the development of materials that are highly resistant against wear and chipping to prolong the life of the roller cone insert bits during drilling hard abrasive rocks. Their design is Co-composition graded cemented carbides. First of all the efficiency of the inserts (cutters) could be ameliorated by manufacturing them in a conical shape. Test results showed that these manufactured insert samples achieved more than eight times the wear resistance of traditional inserts. The semi round design of the inserts achieved over twenty times the wear resistance of traditional ones. It is concluded that using cemented carbides with extra coarse WC grains (above 5 μm) gives a lower hardness and greater toughness, whereas using medium coarse grains of WC (2.1-3.4μm) provides better hardness and lower toughness (Sandvik Hard Material, 2009). A mixture of fine and coarse grains of WC provides a compromise of both hardness and toughness in the same material. Bellin *et al*. (2010b) showed that using sintered grains of fine diamond provide more resistance against abrasion and gives a lower wear rate, while coarse grains of this material have better toughness against impact and higher wear rate. Yahiaoui *et al.* (2013) confirmed that the PDC cutters that

have small diamond grains are the most abrasive resistant compared with coarse grain ones. Yahiaoui *et al.* (2015 a) concluded that when increasing the WC grain size led to increase the acoustic emission energy leads to rise the fracture toughness. Cobalt content has a great effect on the wear of the WC-Co alloys. Modulating the hardness when cobalt is used as a binder will add ductility to the WC which is brittle led to an improvement of WC-Co alloys against crack propagation.

2.4.3 Honeycomb structured polycrystalline diamond and Double Cemented tungsten carbide (DC)

Chipping breakage and wear are the primary signs of failure for the materials which formed the roller-cone bits. Chipping and fracture resistance could be mitigated, but on sacrificing wear resistance and hardness of bit materials. This problem halts the advancement of producing hard materials that can withstand both wear and chipping. Fang *et al.* (2001) described two methods to tackle the encountered challenges:

1- Honeycomb structured PDC: This approach appeared to address the previous difficulties by designing composite materials used in the manufacturing of the roller-cone bits. An example for this approach is a honeycomb structured composite of polycrystalline diamond (PDC) and WC-Co for the synthesising manufacture diamond enhanced inserts for roller-cone bits. The PDC/WC-Co composite exhibits improved with super wear resistance, because of the diamond, and simultaneously, ameliorates chipping and fracture resistance. Hence, PDC forms the core of the unit cell, whereas WC-Co constitutes the web cell boundaries, i.e. each single PDC cell is completely isolated by WC-Co. Figure 2.34 illustrates the microstructure of honeycomb PDC/WC-Co composite. The role of WC-Co boundary is to deflect and disrupt crack and fracture propagation processes due to the high toughness of the WC-Co as compared to the core of the cell (PDC). On the other hand, this design does not compromise the wear resistance, due to the high resistance of diamond against wear.

2- Double Cemented Tungsten Carbide (DC): it consist of very high amount of cobalt resulting in a fracture toughness about 50% greater than traditional cemented tungsten carbide, while maintaining wear resistance by using large, hard phase granules of tungsten carbide. Figure 2.35 demonstrates the microstructure of DC compared to conventional WC-Co materials.

The two designs of the tungsten carbide bits have been tested under both laboratory and field conditions (Fang *et al.*, 2001). It was found that no damage occurred to the inserts of honeycomb structural PDC of the bit. On the other hand, 57% of the standard PDC inserts were chipped or spalled on the outer layer of diamond and the WC substrate was also worn.

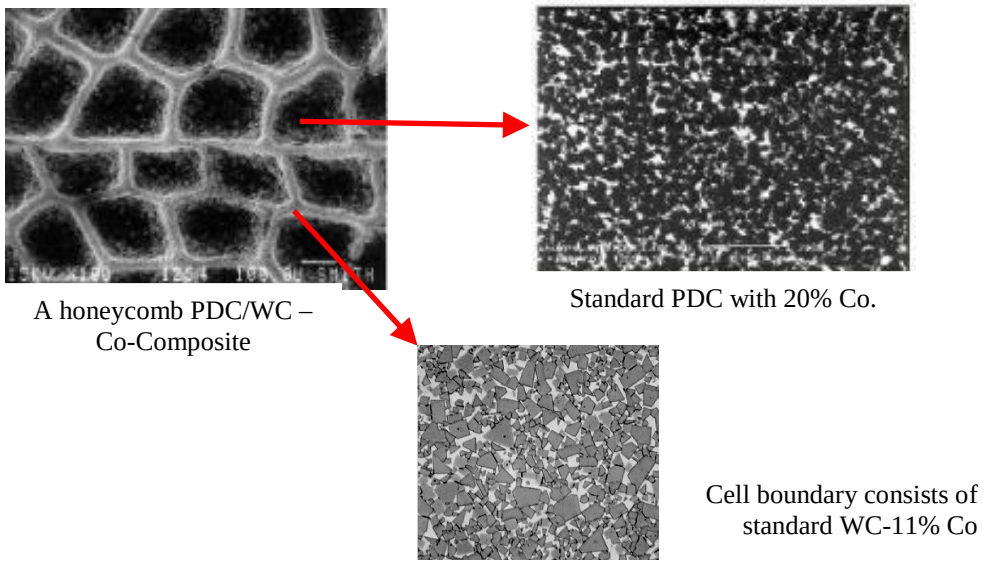

Figure 2.34 Honeycomb structured polycrystalline diamond (Fang *et al.*, 2001)

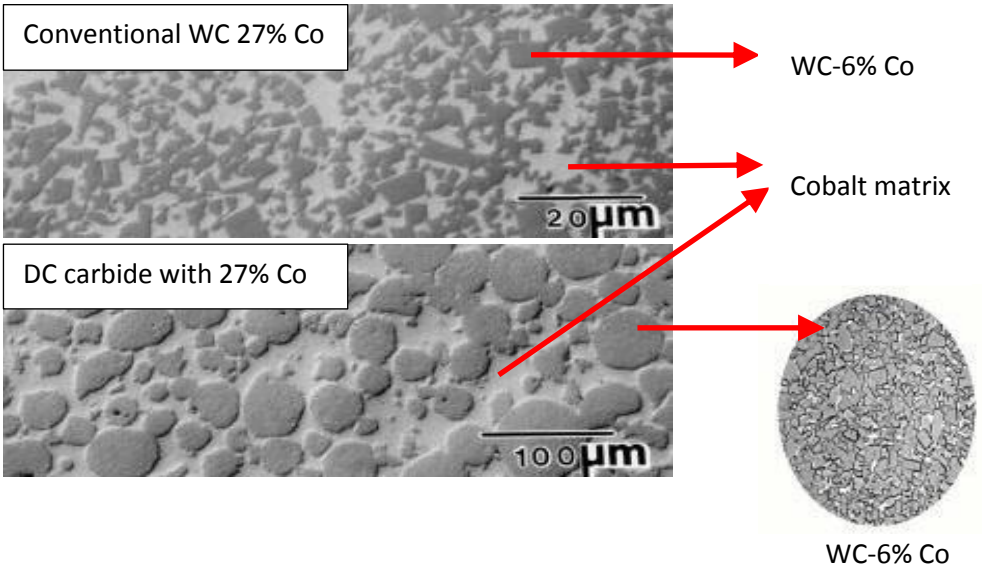

Figure 2.35 Optical micrograph image of conventional and DC carbides (Fang *et al.*, 2001)

Figure 2.36 shows the extent of chipping in honeycomb structured PDC/WC-Co composite inserts as compared to the standard ones. A DC carbide bit was also used in drilling hard dolomite formation at depths between 4700 and 5200 ft. The compressive strength of the dolomite formation ranges from 5000-30000 psi (34.47-206.85 MPa) , which led to insert breakage of the standard bits in this interval. However, the new DC bits drilled the total interval with no significant insert breakage. Figure 2.37 compares DC carbide inserts with the conventional-WC-Co-inserts.

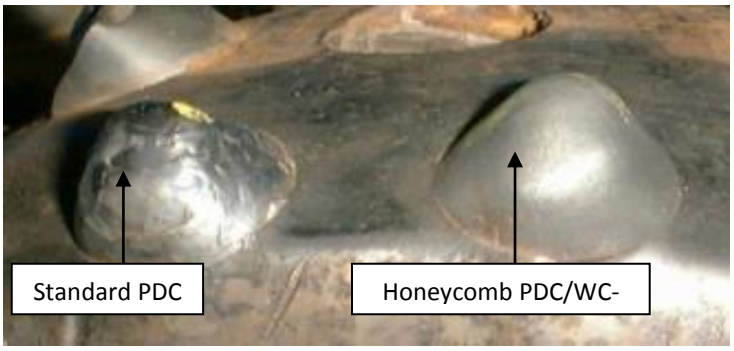

Figure 2.36 Chipping resistance and durability of a rock drill bit insert enhanced with the honeycomb structured PDC/WC-Co. (Fang *et al.*, 2001)

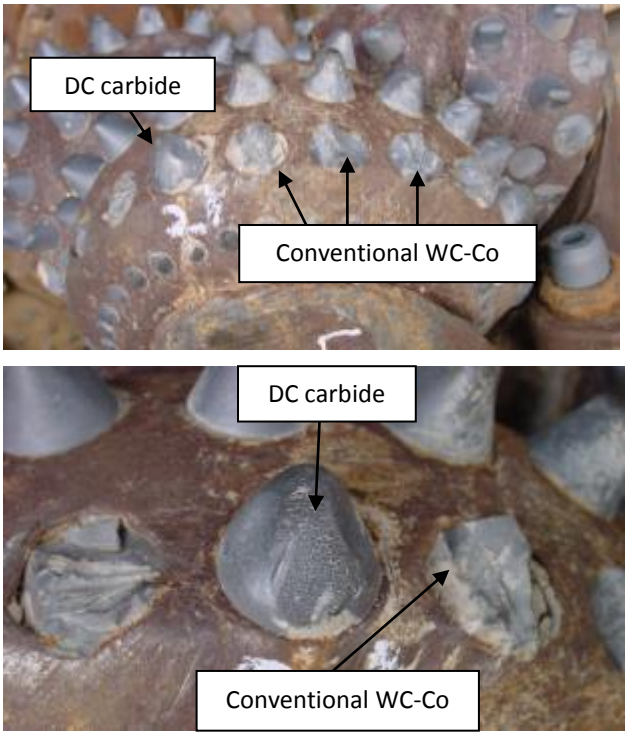

Figure 2.37 Comparison of rock bit inserts with DC carbide and conventional WC-Co. after field test (Fang *et al.*, 2001)

2.4.4 New Steel PDC bits (NSPDC)

Conventional matrix bodied PDC bits, made from multi-materials, including WC, have been used to drill hard and harsh formations , but the majority of the PDC bits were worn and many bit runs were required to complete the drilling particularly in gas wells (Beaton *et al.*, 2008). Due to poor rate of penetration and bit performance a new generation of PDC bits was needed to resolve the issue. Beaton *et al.* (2008) demonstrated new steel PDC bits with the ability to increase the rate of penetration and alleviate the drilling performance challenges while drilling hard abrasive steep formations with difficult drilling circumstances, such as high bottom hole pressure and high mud weight and viscosity. The new technology, New Steel Polycrystalline Diamond Compact bit (NSPDC) was based on its superior hydraulic configuration such as: blade shape and height, bit face Void Volume (VV), available Junk Slot Area (JSA), flexibility of total flow area and nozzle orientation. All of these features lead to improving bit performance and cleaning efficiency, thus increasing penetration rate and fulfilling the drilling operation successfully within a shorter time and with reduced cost. The new design and shape of NSPDC bits is shown in Figure 2.38, where using seven interchangeable nozzles are used to enhance hole cleaning efficiency and penetration rate (PR).

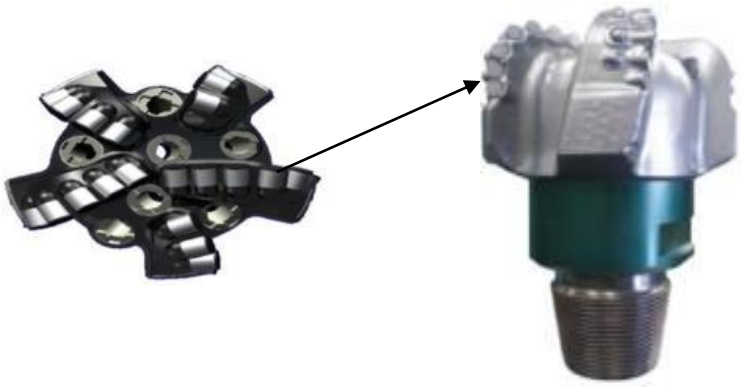

Figure 2.38 New Steel PDC (NSPDC) bit, (6-1/8") with 7 interchangeable nozzles (Beaton *et al.*, 2008)

Figure 2.39 demonstrates the condition of the NSPDC bit after a complete drilling interval without serious dullness or related problems. Dullness refers to the drill bit that has a severe grade of wear. It is clear that the hardfacing protection layer around the cutters which is made from stainless steel is not affected by wear, making NSPDC bits highly popular due to their superior performance and resistance against damage and wear, especially in severe drilling conditions and directed wells.

Figure 2.39 Dullness condition of the NSPDC bit after drilling the entire interval in one run (Beaton *et al.*, 2008)

2.4.5 Diamond Enhanced Inserts or Cutters (DEI)

Cobb *et al.* (2011) discussed the new technology of Diamond Enhanced Inserts (DEI), where the inserts are made from composite polycrystalline diamond, but applied for roller-cone bits. This technique has been tested in two case studies in abrasive and directional sections and the results were encouraging to alleviate bit wear during drilling harsh conditions. The diamond enhanced cutters have the following applications:

1- First generation of Diamond Enhanced Inserts (DEI):

In this generation heel inserts were used to enhance the protection of the bit against the remaining rock ridges that might wear the sealing area of the bit, as shown in Figure 2.40. Furthermore, this new generation of drill bits improves the rate of penetration and increases the durability of the bit using rounded bit inserts. This type of bits lead to three to four times more wear resistance compared to Tungsten Carbide Inserts (TCI). The first generation of DEI improved the drilling operation, however still it could not tackle all the encountered problems, such as the short durability of the inserts.

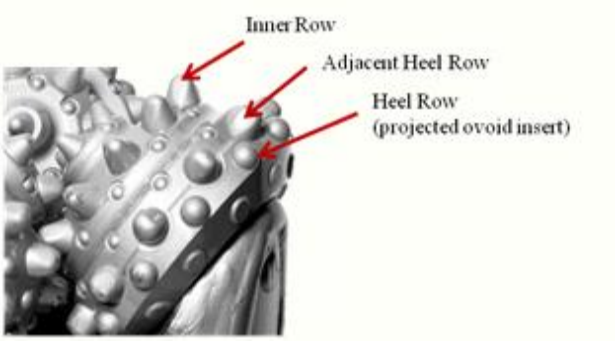

Figure 2.40 Using the technology of heel row inserts (Cobb *et al.*, 2011)

2- Second generation of the Diamond Enhanced Inserts (DEI):

Combination of DEI and TCI specifications led to the second generation of Diamond Enhanced Insert heels. This new design involves diamond inserts heels of curved shape. The new improvement reduced the overall wear and the inserts were more aggressive with moderate durability.

3- Third generation of the Diamond Enhanced Inserts (DEI):

During drilling abrasive and directional sections, the bits are prone to abrasive wear and impact. With the use of rounded heel inserts with high quality allows less frictional heat is produced at the contact area. However, abrasion resistance was increased, and impact durability was reduced; causing the inserts to lose the diamond layer. Figure 2.41 demonstrates the chipping problem in DEI, where the crack on the diamond's surface layer leads to the loss of diamond coating and consequently reduces effectiveness of inserts.

.

Figure 2.41 Progression of damages on diamond enhanced inserts
(Cobb *et al.*, 2011)

Several attempts have been made to remedy the difficulties of the second generation DEI bits. Cobb *et al.* (2011) developed a novel DEI bit by using a tougher diamond layer that could overcome the problems of the previous generations of DEI bits, i.e. chipping and diamond loss. Many bit runs were done with this new technique to test their performance and durability. Figure 2.42 illustrates the comparison among three generations of DEI used in three cones within the same bit.

Overall, this approach enabled the roller-cone bits with DEI in the heel row to be more durable against wear and impact as compared to conventional WC inserts. In addition, the new technique improved the bit life and consequently reduced costs and time for drilling abrasive and directional sections.

Figure 2.42 Comparison between 1st, 2nd and 3rd generations of diamond heels, where each generation has been applied in a cone within the same roller- bit (Cobb *et al.*, 2011)

2.4.6 Thermostable PDC (TSPD) cutters

The use of traditional PDC bits at elevated temperature conditions, particularly 700°C and higher, is not effective due to the occurrence of thermal and abrasive wear. For this purpose, Thermally Stable Polycrystalline Diamond (TSPD) cutters have been developed. The TSPD cutters consist of three layer composite materials. The upper layer consists of a diamond –silicon carbide (SiC) structure with a strong chemical bond in the interface between diamond and silicon carbide grains, while the middle layer is the sintered polycrystalline diamond and the lower one consists of a WC/Co-substrate.

The process of sintering is done under high pressure and high temperature (HPHT). Figure 2.43 shows this process (Osipov *et al.*, 2007).

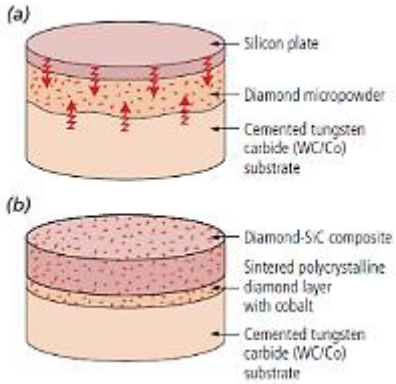

Figure 2.43 Starting and finishing stages of HPHT sintering process (Osipov *et al.*, 2007)

A comparison between conventional PDC and TSPD cutters is shown in Table 2.4, clearly showing better compressive strength and fracture toughness for PDC inserts, as compared to TSPD ones. However, the latter is distinguished with a combination of high wear resistance and high thermostability.

Table 2.4 Comparison of the mechanical properties between conventional PDC and TSPD cutters (Osipov *et al.*, 2007)

Property	Standard PDC inserts	Thermally stable PDC inserts	Synthetic monocrystalline diamond	Cemented tungsten-carbide (WC/15 mass.%Co)
Density, g/cm^3	3.90-4.10	3.42-3.46	3.51-3.52	13.80-14.10
Knoop microhardness, (GPa)	50-60	50-55	70-105	15-18
Compressive strength, (GPa)	7.5-8.5	4.0-5.5	7.0-9.0	12.0-14.0
Fracture toughness, MPa.m$^{1/2}$	9.0-10.0	7.0-8.0	3.0-4.0	11.0-12.0
Young's modulus, (GPa)	810-850	920-960	1000-1150	70-100
Thermal stability,˚C	700	1200	900	1400

TSPD cutters have been tested for their stability during drilling high abrasive rocks under high temperature conditions. The results showed increasing temperatures up to 800°C for 3 minutes gives a total deterioration or wear of the diamond layer for conventional PDC cutters, whereas heating up to 1100°C for 3 minutes leads to only a slight change in the diamond–SiC layer of the TSPD cutters. Two types of TSPD bits were run to drill certain formations. Figure 2.44 illustrates the two kinds of TSPD bits that were used throughout the test run (which are commercially known as ISM-AP-214, 3C type and ISM-AP-165, 1C type), however the properties of these bits are not disclosed.

The field test used various bits with conventional PDC and TSPD cutters to drill different formations. The results of the field test showed that the TSPD bit (ISM-AP-214, 3C) achieved a better performance than the traditional PDC cutters, especially when drilling moderate to hard formations, where a higher rate of penetration was achieved (0.98 m/hr) and the entire interval (406 m) was drilled using just one TSPD bit during (413) hours compared to other standard PDC bit that drilled the same well, but the interval being excavated was only 152 m and the penetration rate was (0.4 m/hr) at (380) working hours. TSPD bits show to be more effective than normal PDC bits when used for drilling moderate to hard formations.

Figure 2.44 Two types of TSPD bits used in the run test, ISM-AP-214, 3C type on the left and ISM-AP-165, 1C type on the right (Osipov *et al.*, 2007)

2.4.7 Selection of binder with additives

Katiyar *et al.* (2016) indicated that abrasive and erosive wear are the most modes of wear occurring in Tungsten-Carbide (TC) bits and they could overcome by lowering the content of the binder (cobalt or nickel) as well as using very fine grains of WC. This combination led to a substrate with high hardness high wear rate resistance. Using nickel as a binder for the WC alloy led to better corrosion resistance with more durability for the TC drill bits compared to cobalt binder. Adding some additives to the WC alloy such as tantalum carbide (TaC) and niobium carbide (NbC) lead to increase the softening temperature of the binder (cobalt or nickel) and consequently improve the thermal properties of the binder.

Yahiaoui *et al.* (2015 b) mentioned the new processes for manufacturing the WC-Co alloys (reactive coating, imbibition and reactive imbibition). Each process led to a special grade of WC-Co alloy. These new processing techniques control the migration of cobalt. Using boride (B) during the manufacturing processes led to the diffusion of boride into the WC-Co more deeper forming WCo-B (ternary borides) causing the reduction of the free cobalt left in the composite matrix. This improvement led to increase the hardness and the fracture toughness of the WC-Co inserts. The existence of the boride phase decreases the wear rate by strengthening the active surface and limiting the effect of cobalt content.

2.5 Discussion

Field rock samples should be used in abrasion tests in order to give a better representation of the encountered rocks while drilling for oil and gas, since otherwise

the testing rock samples may not show similar features to these of oil field. Impact laboratory tests for PDC bits are fulfilled under low vibrations, typically less than 1 Hz. In contrast, under drilling conditions, PDC bits exhibit axial vibrations with frequencies ranging from 2 to 6 Hz. As impact tests provide an indication of impact resistance. It is more useful for assessing the quality of the diamond and diamond-WC substrate, rather than impact resistance measurements that replicate the conditions experienced whilst drilling. Grinding ratio technique provides crucial information about the quality of the PDC and it could be used for the evaluation of PDC samples against wear as well as a quality index criterion.

The progress in PDC cutter technology which achieved by various famous manufacture companies led to the advancement of the testing instruments and techniques. Some of the current testing methods need significant time for completion. In addition, the current impact test which is used by many companies require a significant number of cutters to be tested for each run to gain reliable results. However, Varel International Company has recently developed the new technique of Acoustical Emission Toughness Testing (AETT).

Specific energy as well as all other wear quantification methods should be compared simultaneously with conventional bit record data and penetration rate logs to avoid any noise data or misleading interpretation produced from one or more of the wear quantification methods.

If theoretical wear models are applied to quantify the wear of the drill bits, comprehensive comparison between the qualitative bit wear and the theoretical predicted wear must be made in order to evaluate the reliability of the wear models .

Residual stress is the main cause of delamination of the PDC cutters. The big difference of the thermal expansion coefficient between the diamond and the binder (cobalt) as well as between the diamond layer and the substrate induces a significant internal stress that cause cracks in the diamond layer. The residual stress between the diamond layer and the substrate is increased in the PDC inserts upon cooling after sintering. The sintering process is performed at high pressure and high temperature (HPHT). The substrate tends to have tensile stress, while the diamond layer has compressive stress causing shear stress to be increased significantly near the edge at the interface between

the diamond and the substrate layer. The occurred shear stress is detrimental that leads to fracturing (crack propagation) within the diamond table causing chipping as well as delamination at the interface between the diamond and the substrate layer.

FEA simulation techniques should be used to analyse the residual stresses in roller-cone cutters and PDC cutters as well to provide a better understanding of the behaviour of the material during the sintering process and how to avoid the reported problems encountered within the synthesising manufacture. Furthermore, DEM simulations could be very useful for determining the torque, especially when torque data is missing, which is a crucial parameter for quantifying the bit dullness. The rapid progress of PDC will benefit from the deployment of numerical simulations for bit design. However, further work is needed to simulate the wear of PDC and roller-cone bits.

As described above, past research gave an understanding of the manufacturing methods of oil drill bits and how to improve the overall features of them.

2.6 Conclusions

It is concluded that abrasion wear is the dominant type of wear occurring in roller-cone bits, which is caused by the process of ploughing when the abrasive rocks are soft like limestone, while the process of micro-ploughing and micro-cutting are the main cause of abrasive wear of roller-cone bits when abraded against hard formations such as granite or hard sandstone.

The most common types of wear occurring in PDC bits during drilling are abrasion and impact. Abrasive wear is mainly caused by thermal degradation when PDC bits are used to drill in harsh environments of elevated temperature, causing the transformation of diamond to graphite (graphitisation).

Overall, the major cause of wear for drill bits is abrasion when the drill bit is mostly abraded against rock formations that are mainly consisting of silica (SiO_2) such as sandstone. However, another destructive form of wear occurring in oil drill bits is fatigue or gross fracturing. Fatigue occurs due to the repeated excessive drilling loads when impacting against rocks. The properties of the rock such as the particle size of the grains, the content of the cemented material and the abrasiveness of the grains influence the wear rate of the bit. Hence, studying the characteristics of rocks would be helpful to select the optimum drill parameters (rate of penetration, weight on bit, etc.) and to

choose the most appropriate type of drill bit for a certain rock formation and consequently this will prolong the bit life and reduce the drilling costs. Rocks that have a coarse grain size and contain larger angular particles cause increased wear rates. The wear rates of the materials forming the drill bit decrease as their hardness increases.

Using a combination of state of the art instruments for bit cutters testing (micro and nano-scratch) will give better knowledge of the durability of roller-cone teeth and PDC cutters under various drilling conditions. Chapters 4 and 5 in this thesis illustrate the application of state of the art technologies of micro and nano indentation and scratch testing which are available at the Institute of Particle Science and Engineering (IPSE) at the University of Leeds. PDC samples are imported from two different manufacturers for the above testing techniques.

Field tests on TSPD bits showed that these bits are highly resistant to wear, especially in elevated temperatures. In comparison, TSPD bits exhibit better performance than conventional PDC bits, especially when drilling intermediate to hard formations which represent the most difficult sections encountered during drilling.

Characterisation of the mechanical properties of the materials forming the bit such as hardness, Young's modulus and fracture toughness is crucially important to quantify the wear of the drill bits, as all wear models discussed here require the determination of these properties.

Wear models of Rabinowicz (1996), Hutchings (1992) and Ning and Ghadiri (2006) could be used for wear prediction of the drill bits and comparing their results with the proposed experimental wear model to verify the results, while Archards' (1953) technique is used for the determination of the coefficient of wear, while Element six Ltd. model is discarded as insufficient explanation was provided about the parameters used in this empirical model.

Developing a wear model which uses the concept of three body abrasion would be useful to improve the wear prediction of the drill bits as drill bits are susceptible to three abrasion wear rather than two abrasion wear.

Chapter 3 Case Study

3.1 Real-time monitoring of drill bit wear and specific energy as a criteria for the appropriate time for pulling out worn bits

3.1.1 Introduction

Current techniques for deciding when to pull out the worn bits are based on speculation rather than reliable engineered methods. Two concepts have been previously reported in the literature as shown in sections 2.3.2.1 and 2.3.2.2 to incorporate the effects of drilling parameters on forecasting the life of drill bits. Bit tooth flatness and specific energy approaches were used for assessing the bit tooth wear and predicting the rock formation and its properties being drilled (Pessier and Fear ,1992 and Burgess ,1985). However, drilling shale formations or encountering a surface of erosion especially unconformities as well as not taking into account the properties of the rocks and the bit, reduces the reliability of these methods.

In the following case study, recently drilled oil wells from southern Iraq are analysed for bit wear, where a modified technique based on specific energy and bit dullness is presented as mentioned in sections 2.3.2.1 and 2.3.2.2 and assessed as trending tools for determining the status of the drill bit in cases where drill torque data is unavailable. Estimated results of bit wear for each bit run are correlated with the qualitative bit tooth wear obtained from the field bit record. Detecting bit wear by monitoring real-time bit flatness (F_D) would be useful for obtaining information regarding tooth wear or tooth failure while drilling and when to decide appropriately to pull out the bit.

Literature values of unconfined compressive strength (UCS) of the drilled formations are compared with the computed Mechanical Specific Energy (*MSE*).

3.1.2 Objectives

During drilling in many producing oil wells in southern Iraq, the bit torque values were missing due to the lack of the measurement while drilling logs (MWDL) and tools. The application of the previous mentioned techniques for bit tooth wear prediction such as Specific Energy (*SE*) and dimensionless drilling parameters are not possible unless torque values are known. Using Equation (2-2) to calculate the torque is also unattainable as the coefficient of friction values (μ) were unknown. Torque measurements can be performed only by Measurements While Drilling Logs (MWDL), and these instruments are not always available during the drilling operation, or are not

used due to the high costs of such devices. There is no accurate equation for torque determination, except that developed empirical equation found by Warren (1984).

Warren (1984) suggested an equation for torque prediction based on laboratory studies. Warren (1984) obtained the following equation for torque determination:

$$T = \left(3.79 + 19.17\sqrt{\frac{PR}{N.d}}\right) d.W.\left[\frac{1}{1 + 0.00021\,.L}\right] \qquad (3-1)$$

where T is the torque (lb. ft), W is the weight on bit (lb) , d is the diameter of the bit (in) , N is the rotary speed (RPM) , PR is the penetration rate (ft/hr) and L is the interval drilled by the bit (ft).

In the present work Equation (3-1) is applied to obtain the dimensionless drilling torque (T_D) which is needed for the calculation of dimensionless tooth flatness (F_D) and also for the determination of the specific energy as shown in further calculations.

3.1.3 Data acquisition

The data used in further calculations of this case study were collected mainly from bit records of various wells in southern Iraq and are referred to as A_1, A_2, B_1, B_2 and B_3. All of these wells are located at the province of Basrah in southern Iraq. The selection of the wells being studied based upon the availability of the bit records, therefore five wells were chosen from two different oil fields that have the necessary data needed for the further calculations. Figure B.1 in Appendix-B shows a sample of a bit record obtained for a well being drilled in the South of Iraq, where drilling parameters are shown along the status of the bits used for drilling the well. Figure 3.1 illustrates the main largest oil field in southern Iraq. Lithology of the wells of interest is obtained from bit records, offset wells and from the study of Al-Ameri *et al.* (2011), as shown in Figure 3.2, which indicates the main rock formations being excavated.

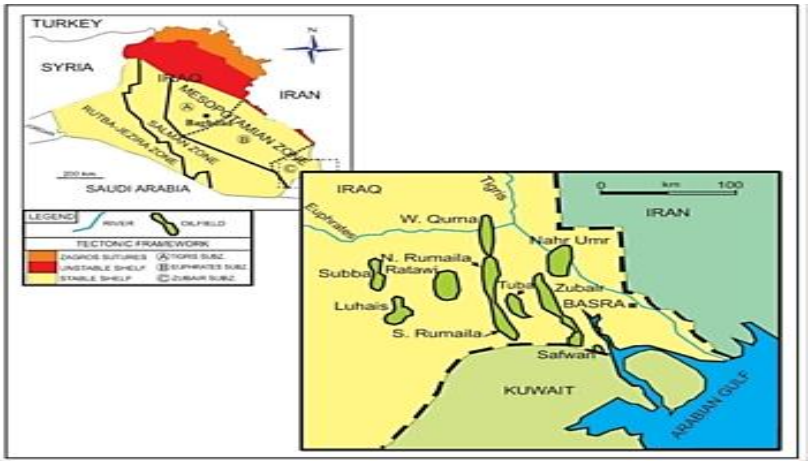

Figure 3.1 Location of main oil fields in southern Iraq (Abeed *et al.*, 2012)

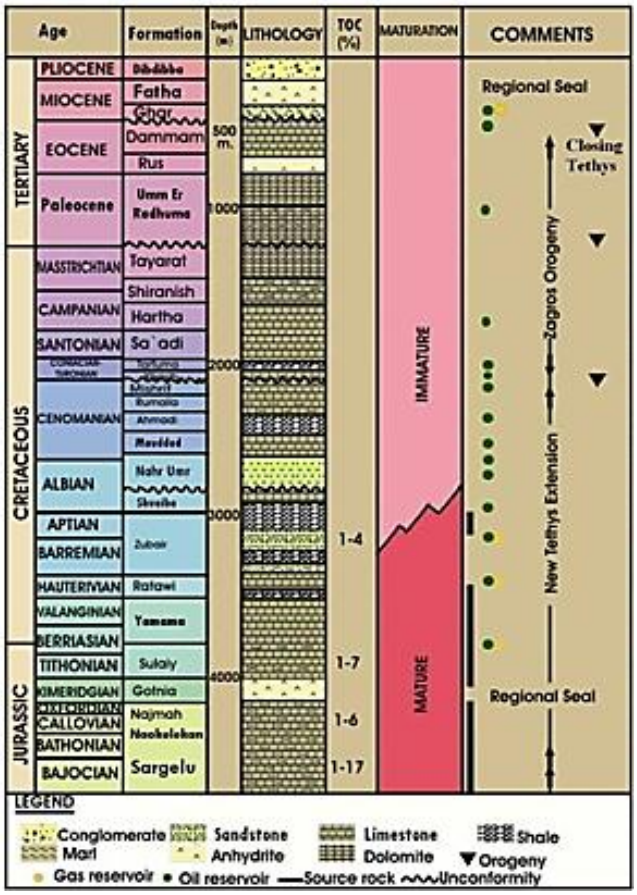

Figure 3.2 Southern Iraq Stratigraphic column for main oil fields in Basrah region (Al- Ameri *et al.*, 2011)

Qualitative bit tooth wear obtained from bit records. International Association of Drilling Contractors (IADC) classified the severity of the bit tooth wear or dullness of the PDC cutters as a fraction of 8. For instance,1/8, 2/8 up to 8/8 , where 1/8 refers to that just one part out of eight (overall length) of the teeth or insert is damaged. 8/8 or 1 means that the teeth or insert is completely worn.

3.1.4 Analysis of the results and discussion

Drilling data variables such as bit diameter, weight on bit, rotary speed, and penetration rate with respect to depth were used to calculate the Specific Energy (*SE*), Mechanical Specific Energy (*MSE*), average Specific Energy (SE_{avg}), and adjusted values of Mechanical Specific Energy (MSE_{adj}). *SE* values are computed using Equation (2-5), and since the provided bit records did not include the measured torque, therefore, the mechanical specific energy (*MSE*) (Equation 2-1) cannot be calculated. However, it should be pointed that torque values can be estimated using Warren's approach (Equation 3.1) that has uncertainty of about 10% of the real torque (Warren 1984). According to the study of Pessier and Fear (1992) it was observed that bit coefficient of friction (μ) values are within the range of 0.21 for roller-cone to 0.84 for PDC bits, and

in this work it was approximately 0.21, as all drill bits used in the five selected wells are roller-cone bits. *MSE* values are calculated by using Equation (2-1) based on the calculation of torque from Equation (3-1). SE_{avg} represents the average values of *MSE* and *SE* obtained from Equations (2-1) and (2-5) respectively, while MSE_{adj} is the adjusted value of *MSE* according to Equation (2-4). *SE*, *MSE*, SE_{avg} and MSE_{adj} values are plotted versus depth in Figures 3.3, 3.7, 3.9, 3.11and 3.13 respectively to observe their trends as compared with the qualitative tooth wear of the oil drill bit obtained from bit records.

The second part of the calculations is computing the dimensionless torque (T_D) and dimensionless rate of penetration (PR_D), using Equations (2-9) and (2-10), respectively. It is worth mentioning that, these calculations should be done for each depth interval being drilled to monitor the real-time parameters with depth. By plotting T_D versus PR_D and fitting the best linear trend line across the points, the intercept of the line a_1 and the slope a_2 of Equation (2-6) are determined. Next, the bit efficiency (E_D) is computed using Equation (2-8). Finally, Equations (2-12) and (2-11) are used to compute dimensionless weight on bit (W_D) and the bit tooth flatness (F_D), respectively. A comparison is needed between the anticipated tooth flatness trend (F_D) and the qualitative bit tooth wear to assess the reliability of this technique as an indicator for bit tooth wear. Bit records were provided with the bit tooth wear according to the International Association of Drilling Contractors (IADC) classification. Figure B.1 in Appendix- B illustrates an example of a bit record.

Well A_1

Well A_1 lies in one of the largest oil fields in southern Iraq along with many other oil producing wells nearby. A sample of bit record data is illustrated in the upper part of Table 3.1 which display that the well was drilled by various bits at different depth intervals. For instance, the first bit (SS5) drilled an interval of 38 m (i.e. from the surface till depth 38 m) and the second bit penetrates from depth 38 m to depth 660 m. The lower part of the table shows the calculation of the dimensionless parameters. Torque (T) is determined from Equation (3-1), while the mechanical coefficient of friction (μ) is calculated from Equation (2-4) and finally the dimensionless parameters are calculated through Equations (2-9) to (2-11). The obtained results are used later to produce Figures 3.3 to 3.6 for well A_1.

Table 3.1 Sample of bit record data and computations for well A_1 (Data are provided from bit records obtained from the section of Petroleum Engineering of South Oil Company)

Depth (m)	Bit Dia. (inch)	Drill bit Commercial Name (code)	Bit Area (inch^2)	WOB (ton)	Distance Drilled (m)	Rotary Speed(rpm)	ROP (m/hr)	ROP (ft/hr)
0-38	26	SS5	530.660	10	38	100	6.33	20.762
38-660	17 ½	R1	240.406	10	622	100	5.78	18.958
660-947	12 1/4	X3A	117.799	18	287	70	4.94	16.203
947-1440	12 1/4	MSS	117.799	18	493	75	6.36	20.861
1440-1530	12 1/4	M44NF	117.799	18	90	75	4.5	14.760
1530-1721	12 1/4	X3A	117.799	18	191	90	2.19	7.183
1721-1925	12 1/4	JD4	117.799	18	204	90	2.45	8.036
1925-2074	8 ½	J4	56.716	15	147	100	3.5	11.480
2074-2440	8 ½	S84F	56.716	15	366	60	3.5	11.480

Depth (m)	μ	Torque (lb.ft.)	T_D	T_D*10^3	R_D	Sq(R_D)*10^3	F_D	Bit tooth wear (0-8)
0-38	0.193	2788.605	0.064	64.352	0.002	39.964	-0.805	2
38-660	0.146	1417.530	0.049	48.601	0.002	46.548	3.194	4
660-947	0.193	2365.806	0.064	64.376	0.004	61.475	-0.416	2
947-1440	0.179	2198.652	0.060	59.827	0.005	67.388	2.311	4
1440-1530	0.211	2582.809	0.070	70.281	0.003	56.684	-2.209	2
1530-1721	0.170	2080.115	0.057	56.602	0.001	36.098	0.169	3
1721-1925	0.171	2098.304	0.057	57.097	0.001	38.181	0.180	3
1925-2074	0.197	1393.456	0.066	65.574	0.003	51.973	-1.069	4
2074-2440	0.192	1357.608	0.064	63.887	0.005	67.097	0.244	2

Figure 3.3 shows the specific energy plotted versus depth, while Figure 3.4 illustrates the observed qualitative bit tooth wear versus depth. It is clearly shown from Figure 3.3 that the specific energy values of all types are increased steadily with depth from the first bit run till a depth of 947 m, which could mean that the dullness or the wear of the teeth is rising gradually. However, Figure 3.4 shows a reduction in tooth wear values from a depth of 660 m to about 947 m, while the specific energy values at the same depth interval rose steadily. This contradiction is continued for further depths.

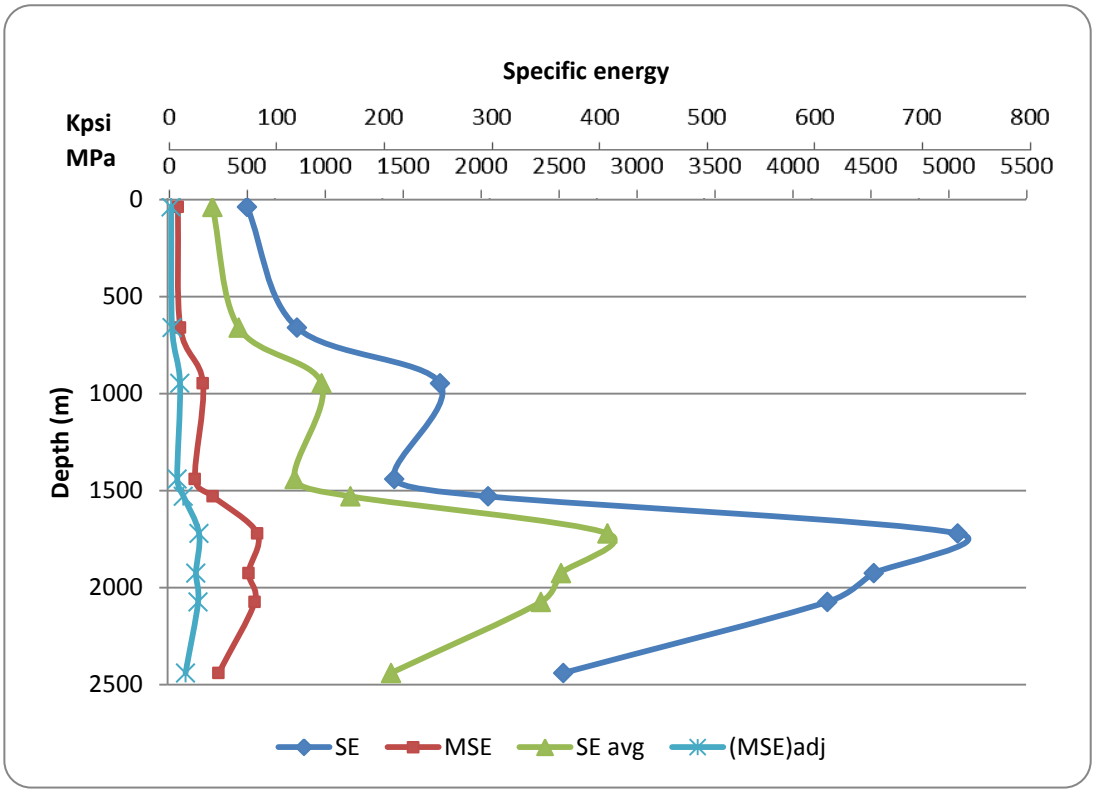

Figure 3.3 Specific energy vs. depth for well A_1

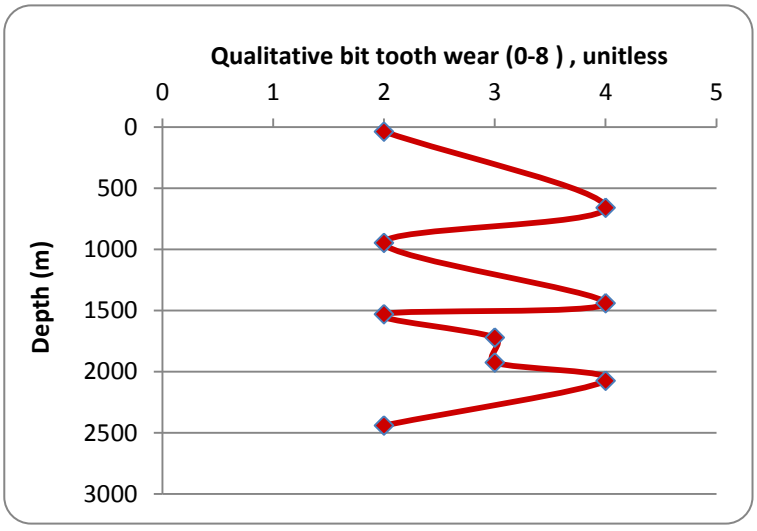

Figure 3.4 Qualitative tooth dullness vs. depth for well A_1 (Provided from bit records obtained from the section of Petroleum Engineering of South Oil Company)

From depth 1530 m to 1721m, the trend of specific energy matches the trend of the actual tooth dullness. Furthermore, from depth 1721 m to 1925 m both specific energy and the bit tooth wear are decreased. For further depths there is no agreement.

The second attempt for predicting the bit tooth wear is by using dimensionless drilling parameters, specifically the bit tooth flatness parameter (F_D) which is relevant to bit

wear. Dimensionless torque (T_D) and dimensionless rate of penetration (PR_D) can be calculated through Equations (2-9) and (2-10) for each depth interval. Due to the linear relation between square root of PR_D and T_D in Equation (2-7), a cross plot is drawn between $\sqrt{PR_D}$ and T_D for well A_1 to obtain the intercept and slope of the best fit line through the plotted points as shown in Figure 3.5.

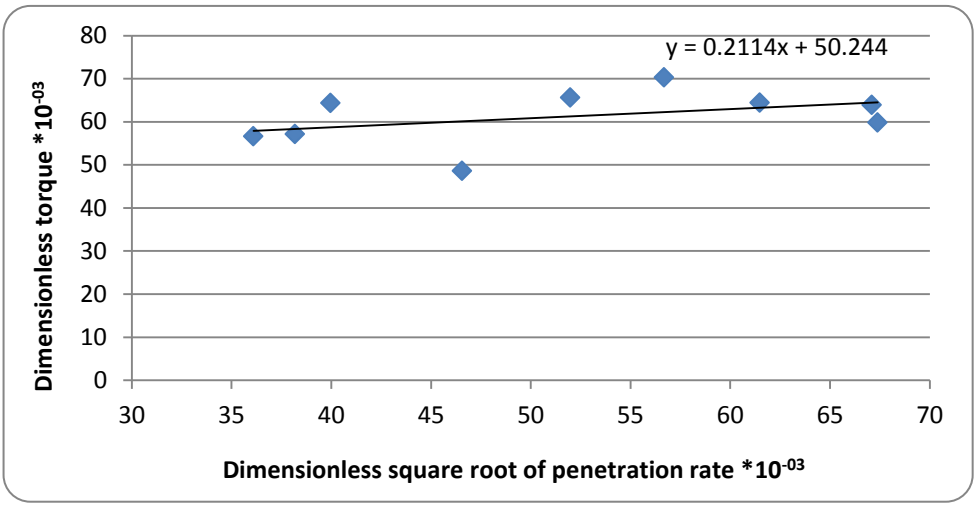

Figure 3.5 Cross plot of dimensionless torque (T_D) with dimensionless square root of penetration rate (R_D) for well A_1

The same cross plot is performed for the rest of the wells. Figures B.2-B.5 in Appendix-B show the same cross plot for wells B_1, B_2, A_2 and B_3 respectively. Table 3.2 illustrates the obtained values of the intercepts and the slopes for five wells in the south of Iraq.

Table 3.2 Intercepts and slopes obtained from the cross plot of the dimensionless torque with the dimensionless penetration rate for five wells in southern Iraq

Well Name	Intercept (a_1)	Slope (a_2)
A_1	50.244	0.211
B_1	46.503	0.311
B_2	39.161	0.468
A_2	48.28	0.407
B_3	55.243	0.11

The obtained values of a_1 and a_2 were used to calculate the dimensionless bit tooth flatness (F_D) by using Equations (2-8), (2-12) and (2-11). The predicted tooth flatness is compared to the actual bit tooth wear to assess its behaviour and trend. Both the predicted tooth flatness and the actual qualitative tooth dullness versus depth are plotted in Figure 3.6.

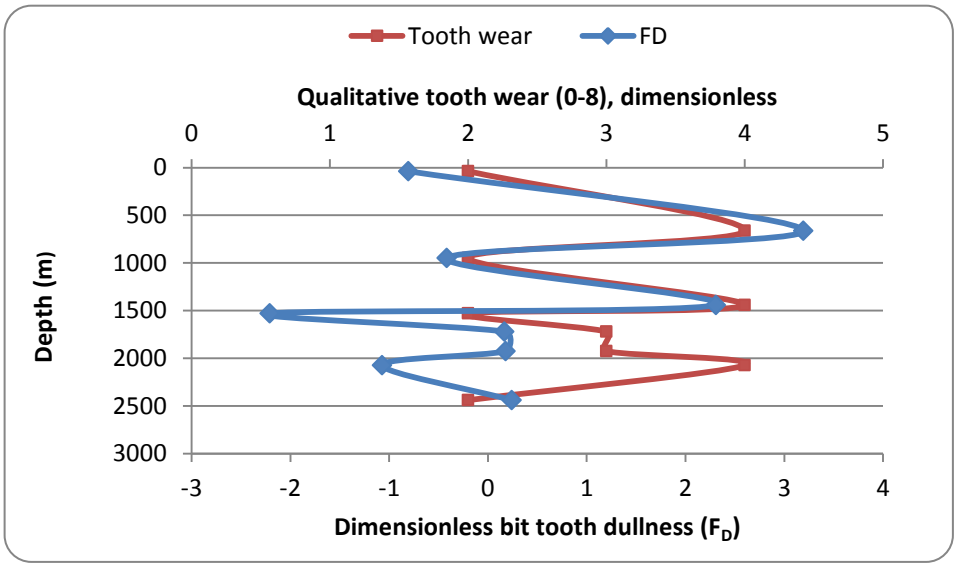

Figure 3.6 Comparison between dimensionless bit tooth flatness (F_D) and the actual tooth wear versus depth for well A_1

It was surprisingly observed that the two curves are matching from the first bit run at depth 38 m to depth 1925 m. In spite of the good agreement, divergence is revealed from depth 1925 m onwards.

The interpretation for this difference might be attributed to shale formations where bit balling could occur. This likelihood is confirmed with the lithology of most wells lies in Basrah oils fields which provided from the study of Al-Ameri *et al.* (2011) indicating that beyond a depth of 1925 m, shale formations are present as either the dominant or the second- most dominant formation as shown in Figure 3.2. Figure 3.6 illustrates the existence of shale formations at depths close to 1925 m which match the study of Al-Ameri *et al.* (2011). Bit tooth flatness method is likely to be more efficient predicting tool than the specific energy technique, thus it will be applied for another four wells to observe its efficiency and reliability as a trending tool for predicting the bit tooth dullness.

Well B_1

Well B_1 lies in a huge oil field that consists of many other wells being drilled for the

case of oil production. The same procedure of computations was performed for this well to make a clear understanding of bit tooth dullness while drilling. Figures 3.7 and 3.8 demonstrate this principal.

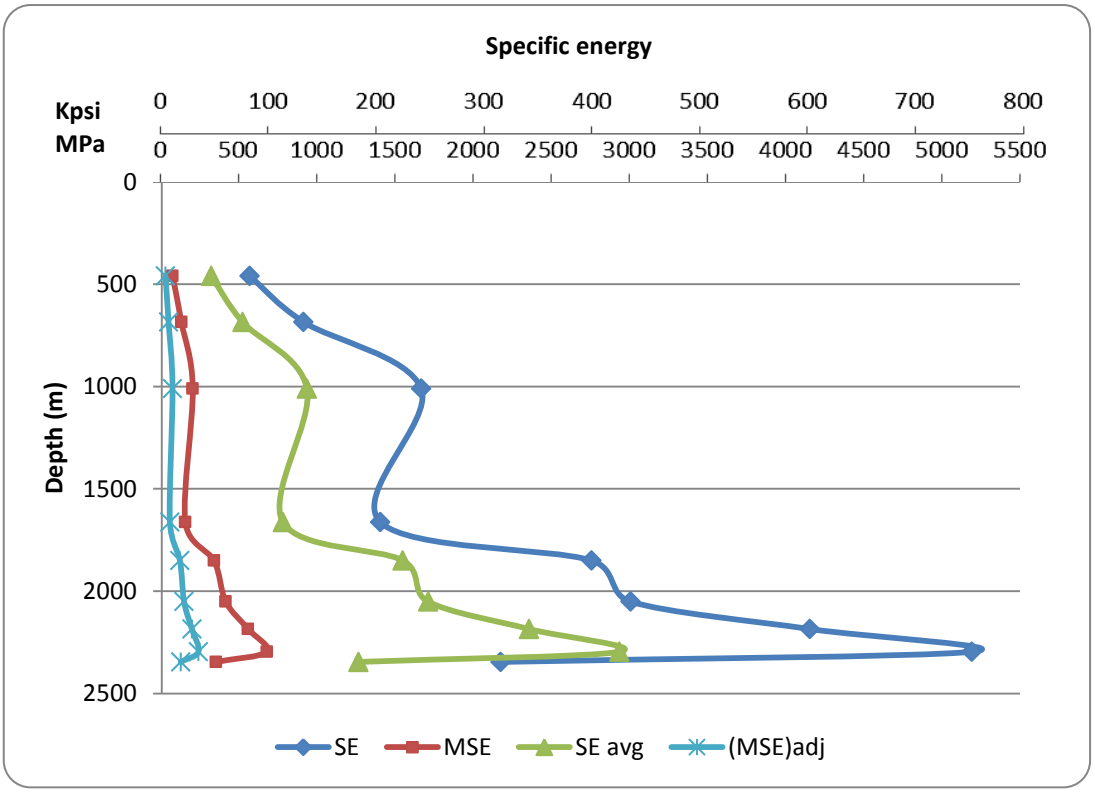

Figure 3.7 Specific energy vs. depth for well B_1

Again, specific energy seems to suggest that the teeth of the bit are beginning to wear from the first bit run, while the actual bit dullness is rather different (see Figure 3.7) where it shows a decreasing trend from a depth of 660 to 1000 m, after which it to rises again. The dramatic increase in the specific energy trend from the normal increasing line is clearly shown at a depth of 1850 m, which could indicate a sharp wear of the bit teeth. This agrees with the rising trend of the qualitative bit wear as shown as the red curve in Figure 3.8. Maximum bit wear occurred at a depth of 2051 m, while the highest peak of specific energy exists at depth 2296 m, which means that the approach of specific energy is not always a precise approach for predicting the bit tooth wear, therefore it should be applied in conjunction with other techniques such as gamma ray and sonic logs to avoid any misleading conclusions.

Figure 3.8 illustrates the matching in trends for dimensionless bit flatness and qualitative bit tooth wear from the first bit run till a depth of 2000 m, where the dimensionless bit tooth flatness is equal to 3.87 a depth 460 m and the corresponding qualitative bit tooth wear is 4 ,but from depth 2000 m onwards, there is an uncertainty

of the bit flatness technique. For example at depth 2051 m, the dimensionless flatness (F_D) is -0.887, whereas the corresponding qualitative bit tooth wear at that depth is 6. This discrepancy is a lot and after investigation of the lithology for this well at depth 2000 m onwards revealed that shale formations (and associated bit balling) exist and might cause the uncertainty from that depth onwards (Al-Ameri *et al.*, 2011). It is worth noting that it is not realistically possible to get a negative value for the dimensionless bit tooth flatness (F_D), however this parameter is used as a wear indicator of the bit. In general, the results emphasized the fact that dimensionless bit flatness approach is more applicable in forecasting the bit teeth wear as compared to the specific energy method. To confirm the reliability of this technique, all above computations are done for three other wells.

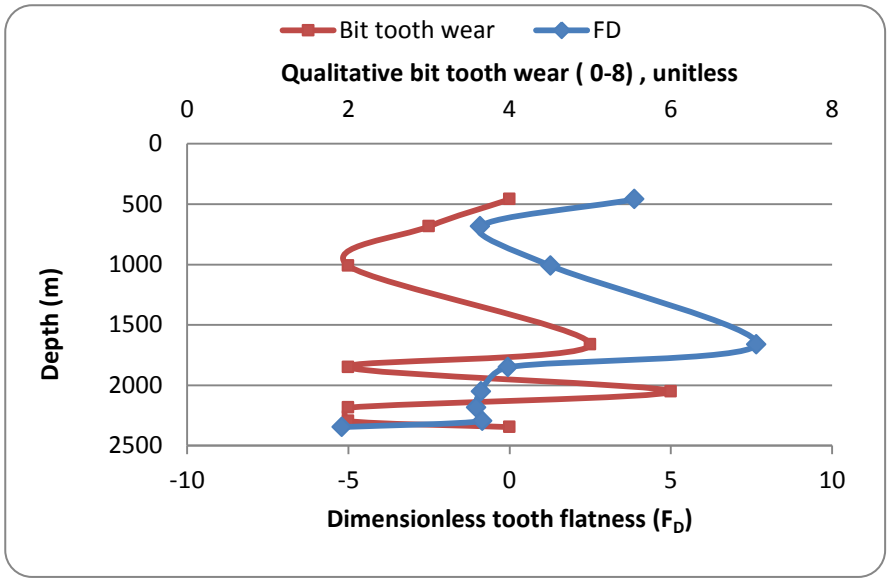

Figure 3.8 Bit tooth flatness (F_D) compared to the qualitative bit tooth wear for well B_1

Well B_2

In this well, as shown in Figure 3.9 the specific energy increased gradually from the first bit run till depth 1000 m which agreed with the qualitative bit tooth wear which shown as the red curve in Figure 3.10, however, from depth 1000 m till depth 1058 m, the qualitative bit tooth wear decreased dramatically from 6 to 2 and went back to 4 as seen from Figure 3.10, while the specific energy started to reduce sharply at depth 1058 m till depth 1756 m. The rest bit runs show similar behaviour for the specific energy compared to the actual tooth wear except at depth 2561 m where the specific energy increased rapidly and reached the peak, while the bit tooth wear increased sharply at depth 2722 m.

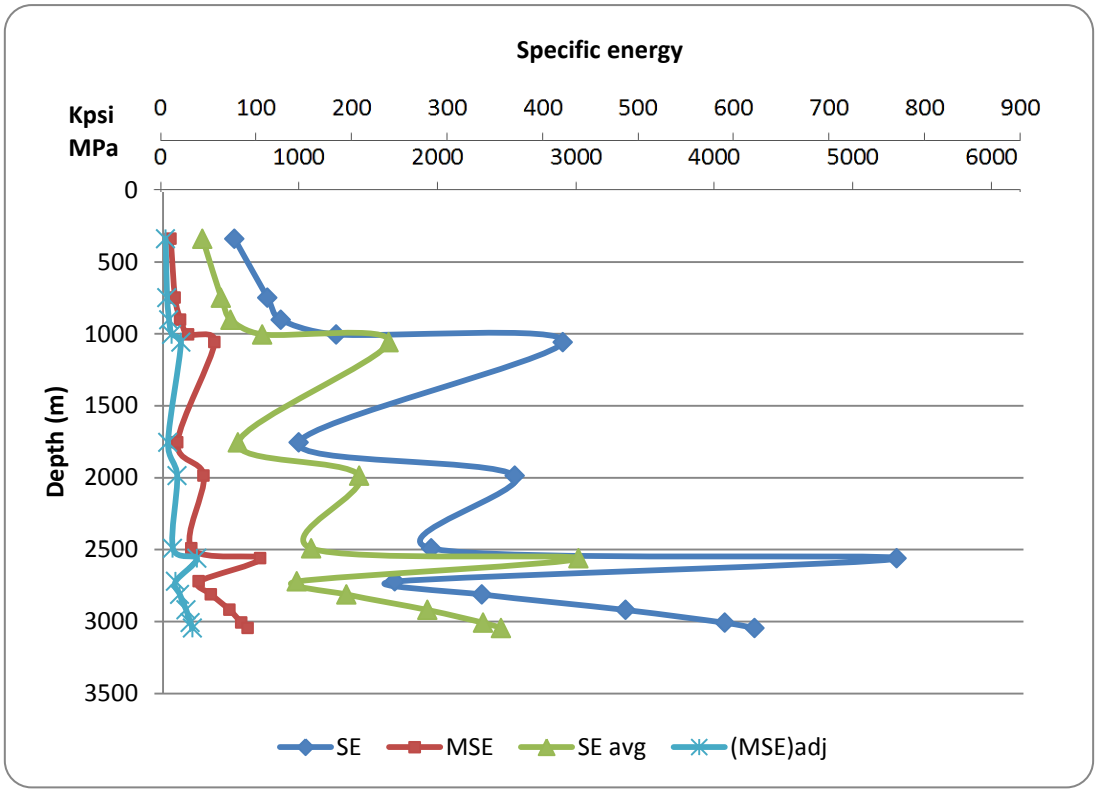

Figure 3.9 Specific energy vs. depth for well B_2

As a quick glance comparison between the trends of the specific energy and the qualitative bit tooth wear, it seems that there is a good agreement between the two. However, the escalation or reduction of the specific energy when compared to the qualitative bit tooth wear is not at the same depth. For example, from depth 340 m to depth 1004 m there is an increasing trend for the qualitative bit tooth wear and started to decrease after 1004 m, while specific energy increased from depth 340 m to depth 1058 m and after that depth the specific energy displayed reduction in trend. The same finding was found at the rest depths of this well. Therefore, another comparison technique is needed to overcome this issue.

Figure 3.10 illustrates that the predicted bit tooth flatness behaves similarly to the trend of the qualitative bit tooth wear in all bit runs except for slight insignificant discrepancy at some depths which means that tooth flatness approach shows the ability to forecast the wear status of the drill bits efficiently.

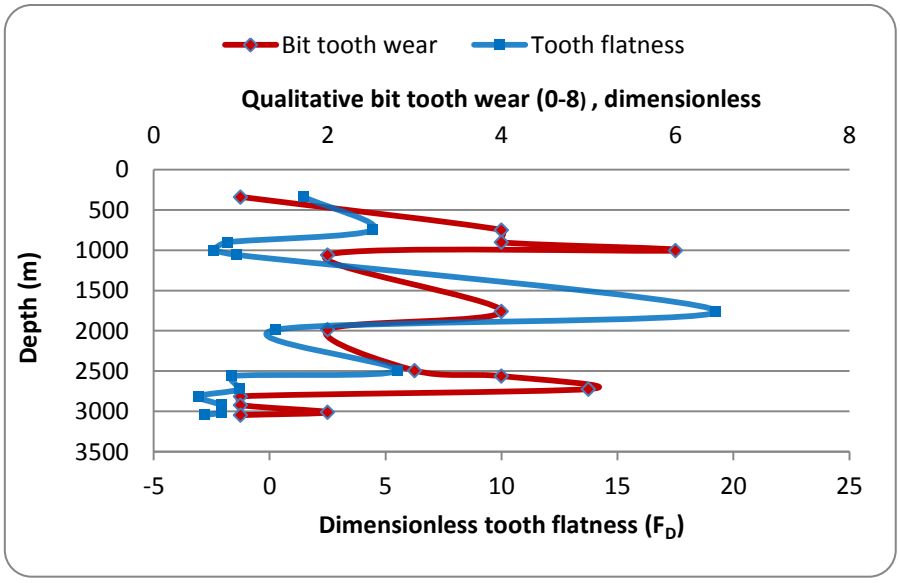

Figure 3.10 Bit tooth flatness and qualitative bit tooth wear versus depth for well B_2

Well A_2

Figure 3.11 demonstrates the gradual increase of the specific energy with depth from the first bit run till depth 1920 m., whereas the behaviour of the qualitative bit tooth dullness showed in Figure 3.12 is rather different, where it starts to decrease from the first bit run to depth 919 m and starts to rise afterwards to depth 1920 m. From depth 1920 m to 2220 m of the wellbore, there is a good agreement between the trend of the specific energy and the qualitative bit wear. However, Figure 3.12 shows the agreement in behaviour between the actual tooth wear and the predicted one (F_D) at most depths.

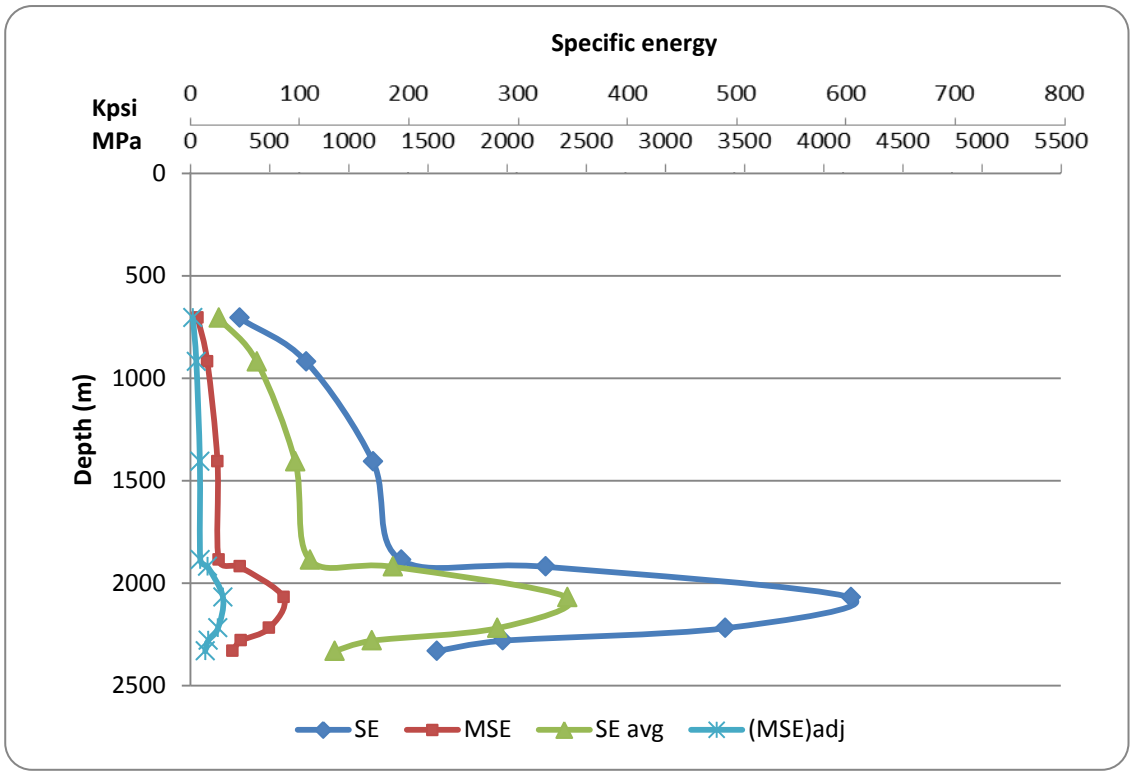

Figure 3.11 Specific energy vs. depth for well A_2

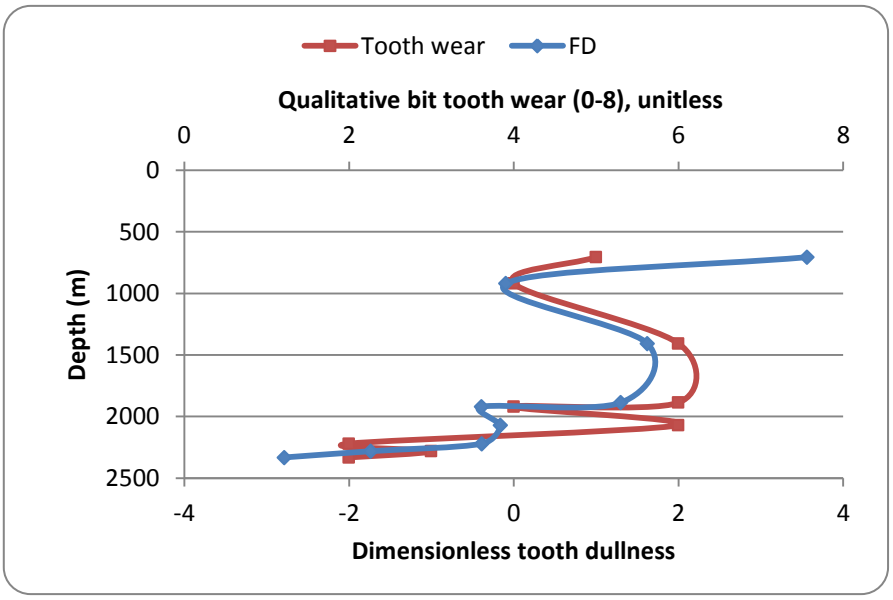

Figure 3.12 Comparison between tooth flatness (F_D) and qualitative tooth wear versus depth for well A_2

Well B_3

Figure 3.13 shows for well B_3, the specific energy method alone does not seem to indicate the bit wear efficiently when compared to the qualitative bit tooth wear shown in Figure 3.14, where there is a disagreement at many depths which reduces the reliability of the specific energy technique, whereas bit tooth flatness technique (F_D) agrees with the actual wear trend nicely at most depths as shown in Figure 3.14 and it is likely to be considered a reliable method to predict the tooth wear rather the traditional specific energy method.

In general, comparison of the dimensionless bit tooth flatness (F_D) and. the qualitative bit tooth wear versus depth for wells A_1 , B_1 and A_2 show that at depth 2000 m onward, there is an incompatibility between the predicted bit tooth flatness behaviour and the actual bit wear. After analysing the offset wells and the lithology at depth 2000 m onward, shale formation is encountered and that might affect the results of the predicted bit wear due to the influence of shale on the bit i.e. bit balling.

Furthermore, unconformities might occur at depth 2000 m for some wells between Khasib and Mishrif formations and at depth 2850 m between Nahr-Umr and Shuaiba formations as clearly seen from Figure 3.2 represented by a wavy line rather than straight lines.

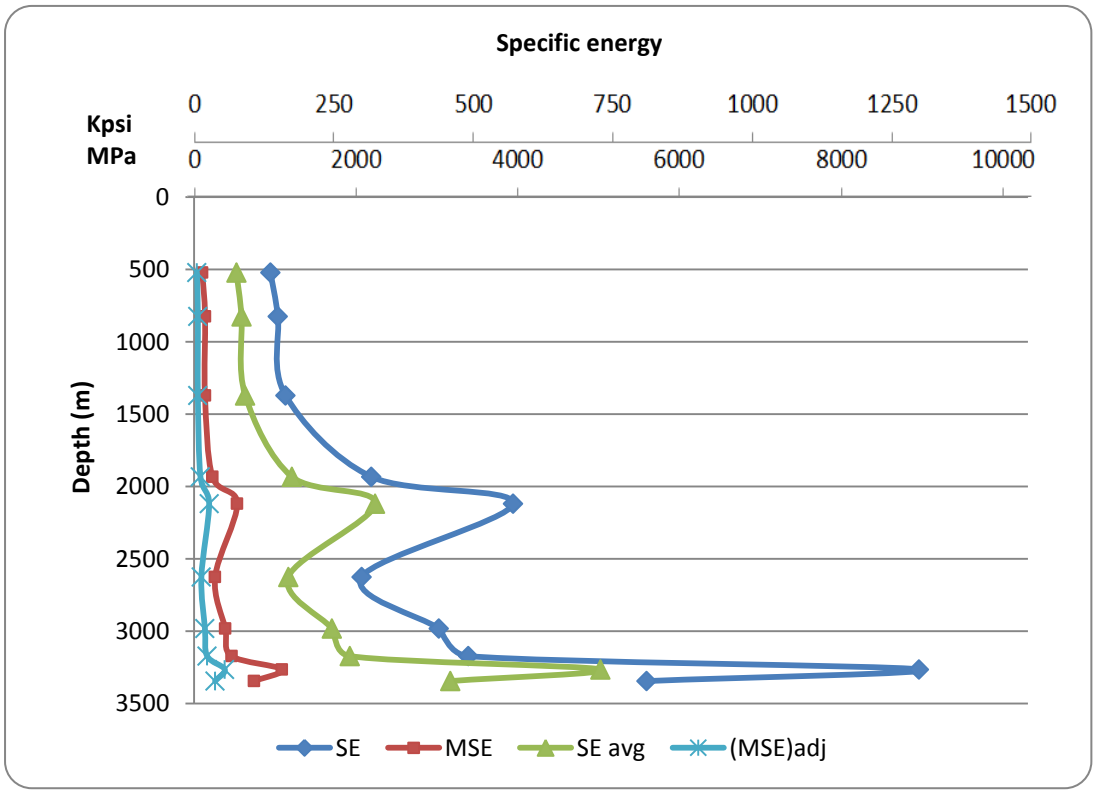

Figure 3.13 Specific energy vs. depth for well B_3

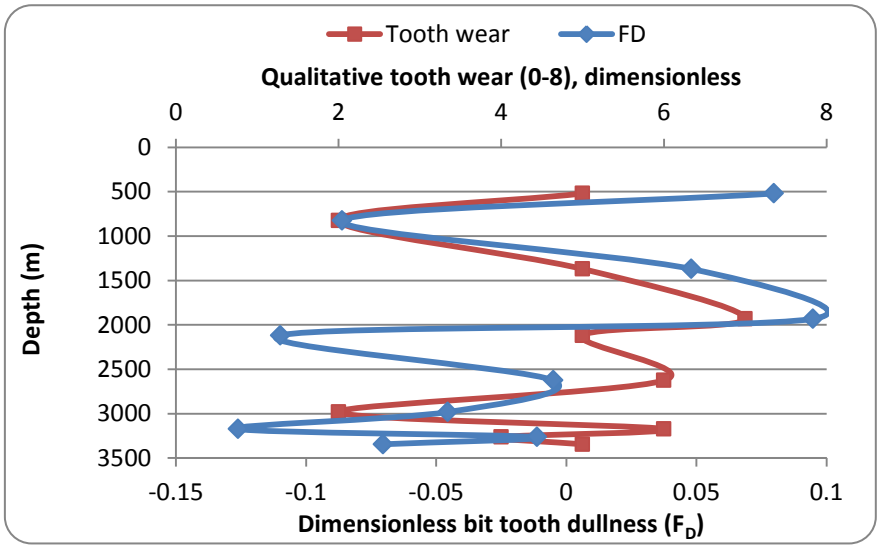

Figure 3.14 Tooth dullness compared to the qualitative bit tooth wear versus depth for well B_3

Analysis of the unconfined compressive strength (UCS) of the rock formation:

According to Teale (1965) the minimum specific energy values could be correlated with values of unconfined compressive strength (UCS). In this study, the adjusted mechanical specific energy MSE_{adj} using Equation (2-4) would give the minimum value for the specific energy which could correspond to the UCS values of the rock from the work of Zhao (2007). Tables 3.3 to 3.7 illustrate the calculated values of MSE_{adj} for five

wells in southern Iraq and the corresponding values of (UCS) according to the investigation of Zhao (2007). The lithology of the five selected wells is taken from the previous work of Al-Ameri *et al.* (2011) as shown in Figure 3.2, while other lithological information is taken from bit records and offset wells. It was observed that adjusted mechanical specific energy values were within the range of the estimated values of the unconfined compressive strength of the corresponded formations, except for a few cases where some formations are influenced by the occurrence of shale that cause bit balling phenomena.

Table 3.3 Calculated values of adjusted mechanical specific energy compared to the unconfined compressive formations for well A_1

Depth (m)	Rock formation	Mechanical specific energy (Eq. 2-3) (MSE) ,psi	Adjusted mechanical specific energy (Eq. 2-4) (MSE_{adj}) , psi	Adjusted mechanical specific energy (MSE_{adj}) , MPa	Unconfined compressive rock strength (UCS), MPa (After Zhao 2010)
0-38	Conglomer-ate	9572.13	3350.24	23.10	30-230 for Conglomerate.
38-660	Limestone	11799.41	4129.79	28.47	30-250 for Limestone.
660-947	Limestone	32989.73	11546.4	79.61	30-250 for Limestone.
947-1440	Dolomite	25583.87	8954.35	61.74	20-120 for Dolomite.
1440-1530	Limestone	42274.51	14796.08	102.02	30-250 for Limestone.
1530-1721	Shale +Lime.	83649.22	29277.23	201.86	30-250 for Lime. and 5-100 for Shale.
1721-1925	Limestone	75456.03	26409.61	182.09	30-250 for Limestone.
1925-2074	Shale+ bit of Lime.	81149.59	28402.36	195.83	5-100 for Shale.
2074-2440	Marl +Shale +Lime.	47656.9	16679.92	115.00	30-250 for Lime. and 5-100 for Shale

Table 3.4 Comparison of adjusted mechanical specific energy with unconfined compressive strength (UCS) for well B_1

Depth (m)	Rock formation	Adjusted mechanical specific energy (MSE_{adj}) , MPa	Unconfined compressive rock strength (UCS) , MPa (After Zhao 2010)
0-460	Anhydrite +Marl	24.81	30-250 for Limestone and 5-100 for Shale
460-684	Limestone	44.52	30-250 for Limestone.
684-1010	Dolomite	70.13	20-120 for Dolomite
1010-1662	Limestone + Marl	53.33	30-250 for Limestone
1662-1850	Limestone	117.75	30-250 for Limestone.
1850-2051	Limestone + bit of Shale	144.24	30-250 for Limestone and 5-100 for Shale
2051-2185	Limestone + Shale	194.62	30-250 for Limestone and 5-100 for Shale
2185-2296	Shale	236.87	5-100 for Shale
2296-2346	Marl +Shale +Limestone	122.57	30-250 for Lime. and 5-100 for Shale.

Table 3.5 Computed adjusted mechanical specific energy compared to the unconfined compressive strength (UCS) for well B_2

Depth (m)	Rock formation	Adjusted mechanical specific energy (MSE_{adj}) , MPa	Unconfined compressive rock strength (UCS) , MPa (After Zhao 2010)
0-340	Conglomerate.	21.99	30-230 for Conglomerate.
340-749	Anhydrite +Marl	34.02	5-100 for Shale and 30-250 for Lime.
749-902	Dolomite.	49.66	20-120 for Dolomite.
902-1004	Dolomite	71.41	20-120 for Dolomite.
1004-1058	Lime.+ Dol.	145.10	30-250 for Lime and 20-120 for Dolomite.
1058-1756	Lime.+ Dol.	41.13	50-150 for Dol. and Lime.
1756-1986	Limestone.	114.80	30-250 for Limestone
1986-2492	Shale +Limestone.	80.46	5-100 for Shale and 30-250 for Lime.
2492-2561	Limestone+ Shale	273.65	30-250 for Lime, and 5-100 for Shale
2561-2722	Sandstone + Limestone	101.79	20-170 for Sandstone and 30-250 for Limestone.
2722-2812	Lime. +Shale + Sandstone	135.97	30-250 for Lime. and 5-100 for Shale and 20-170 for Sandstone.
2812-2920	Sandstone + bit of Shale	187.21	20-170 for Sandstone and 5-100 for Shale
2920-3009	Shale	221.16	5-100 for Shale.
3009-3045	Shale +Lime.	238.62	5-100 for Shale and 30-250 for Limestone

Table 3.6 Adjusted mechanical specific energy compared to the unconfined compressive strength (UCS) for well A_2

Depth (m)	Rock formation	Adjusted mechanical specific energy (MSE_{adj}) , MPa	Unconfined compressive rock strength (UCS) , MPa (After Zhao 2010)
0-706	Limestone+ Anhydrite	16.39	30-250 for Limestone.
706-919	Dolomite	37.64	20-120 for Dolomite.
919-1407	Dolomite	60.12	20-120 for Dolomite.
1407-1887	Limestone	63.13	30-250 for Limestone.
1887-1920	Limestone	109.54	30-250 for Limestone.
1920-2070	Shale + bit of Limestone	206.86	5-100 for Shale and 30-250 for Lime.
2070-2220	Limestone +bit of Shale	174.61	5-100 for Shale and 30-250 for Lime.
2220-2281	Limestone +Marl	112.20	30-250 for Limestone.
2281-2332	Marl + Shale+ Limestone	93.81	5-100 for Shale and 30-250 for Lime.

Table 3.7 Adjusted mechanical specific energy and unconfined compressive strength (UCS) for well B_3

Depth (m)	Rock formation	Adjusted mechanical specific energy (MSE_{adj}) , MPa	Unconfined compressive rock strength (UCS) , MPa (After Zhao 2010)
0-520	Conglomerate+ Anhydrite +Lim.	35.94	30-230 for Conglomerate and 30-250 for Lime.
520-825	Anhydrite +Marl	48.01	----------
825-1370	Dolomite	47.57	20-120 for Dolomite
1370-1932	Limestone	79.57	30-250 for Lime.
1932-2118	Shale +Lime.	187.58	5-100 for Shale and 30-250 for Limestone.
2118-2626	Shale +Lime.	91.41	5-100 for Shale and 30-250 for Limestone.
2626-2982	Lime. +Shale	135.52	30-250 for Lime. and 5-100 for Shale.
2982-3172	Shale	162.99	5-100 for Shale.
3172-3264	Sandstone + Shale	381.54	20-170 for Sandstone and 5-100 for Shale.

Tables 3.3-3.7 show the comparison between the calculated unconfined compressive strength (UCS) from the mechanical specific energy equation with UCS from the

laboratory work of Zhao (2010) to predict the type of rock formation being excavated. The mentioned values of UCS after Zhaos' work show a range values and cannot represent the exact value of the corresponding rock formation, therefore, in order to obtain more reliable values of UCS. It is necessary to run experimental UCS tests on real rock samples collected from the field corresponded to the formation being studied.

3.1.5 Conclusions

Dimensionless parameters methods suggested by many researchers could be useful to quantify bit tooth wear, when only the measured values of torque are known. However, in most cases, the data of torque are not available. In this study an approach based on the dimensionless bit tooth flatness was used as a real-time monitoring "trending tool" of the dullness of the bit teeth. All studied wells in this research showed good agreement between trends of the qualitative bit wear and the predicted bit tooth wear, excluding the regions of shale accumulations. When drilling shale formations, the drill bit will suffer from the phenomena of bit balling, which means that the sticky shale particles will accumulate at the face of the bit, thus causing high values of torque and consequently high value of specific energy, so special care is needed when using the specific energy technique during drilling shale formations.

Unconformities within the rock formations also cause misleading results, hence specific energy and dimensionless drilling parameter techniques cannot always be reliable tools for monitoring the wear of the teeth unless other methods are used simultaneously such as well logs combined with geological information.

The predicted values of the Unconfined Compressive Strength of the rock (UCS) were determined from the adjusted mechanical specific energy values based on the study of Teale (1965) as the minimum specific energy is corresponded to the unconfined compressive strength (UCS). The calculated adjusted mechanical specific energy values give only an indication on what type of the formation is being drilled i.e. lithology, but it is not a precise method for measuring (UCS) of the rock. Laboratory UCS measurements of the penetrated rock formation samples is needed for this validation.

Nevertheless, all the above findings are based on empirical approaches which require field data to predict the wear of the drill bit when drilling various formations. It is essential to come up with a unique methodology to predict wear based on the mechanical properties of the drill bit such as hardness, Young’s modulus and fracture

toughness as well as those of rocks along with the drilling parameters such as weight on bit , rotation speed , bit diameter and rate of penetration.

The previous methods for determining the wear are based on empirical equations based on two body abrasive wear, while it is worthy to present a new approach based on the concept of three body abrasive wear, as introduced by Rabinowicz (1977). The drill bit is typically exposed to three body abrasive wear as the cuttings generated during crushing the rock formation by the drill bit are free to roll and slide against the bit. The obtained specific energy as previously mentioned in section 3.1, was shown to be unreliable technique for monitoring the wear of the bit teeth. In an attempt to overcome the shortcomings of this technique, a modified specific energy formula is presented and evaluated using the concept of three body abrasive wear.

3.2 A New Approach for Predicting the Wear of Roller-Cone Bits using the Concept of Three Body Abrasion

3.2.1 Introduction

In drilling for oil and gas, roller-cone bits with conical- shaped teeth are now widely used due to their favourable durability and cost compared to PDC bits, however generally speaking the prospective rock formation to be drilled plays an important role for bit durability. The state of the bit is assessed according to the status of the tooth and the bearings holding the cones of the bit. Roller-cone bits are classified mainly into two categories, milled tooth bit and insert bits. Milled tooth bits are made of steel, while for insert bits, the body of the insert is manufactured from steel and the tooth from tungsten carbide. As drilling progresses the bits become worn and hence drilling efficiency reduces. The traditional technique for diagnosing the status of the bit wear is by monitoring the Specific Energy (*SE*) simultaneously with rate of penetration (*PR*) against depth. The specific energy approach is considered a reasonable indication of drill bit status throughout its drilling life.

Waughman *et al.* (2002, 2003) studied the real-time specific energy (*SE*) and recommended when to pull out the worn (PDC) bits by producing a plot of (*SE*) versus depth and creating a normal baseline as a reference for monitoring the wear of the drill bits. A significant increase in *SE* in non-balling conditions typically indicates bit wear (Waughman *et al.*, 2002, 2003). When drilling shale formations, additional

interpretation techniques must be used in conjunction with raw *SE* to avoid any potential misinterpretation, e.g. well logs and geophysical information. Specific energy was used by Dupriest and Koederitz (2005) as a trending tool for monitoring the bit status.

In this work a combination of specific energy and bit dullness as an indication for real-time monitoring of drill bit wear for selected wells in the southern Iraq were investigated. In most of the studied wells, the specific energy gave an indication of the bit wear, however there was no correlation between the qualitative bit tooth wear and the calculated values of the specific energy at many depth intervals for various of studied wells. This is attributed to some factors that were not taken into consideration within the specific energy equations of Teale and Rabia: (*i*) the phenomena of the three body abrasive wear of the rock cuttings formed during drilling causing the free motion of these cuttings to roll and slide (*ii*) the type of the material forming the bit and (*iii*) the hardness of the rock formation to be drilled. As stated by Waughman *et al.* (2002) most of the drilling optimization or drilling performance models do not include the effect of rock hardness along drill bit type drilling parameters and the mechanical properties of the minerals that form the drill bit based on the concept of three body abrasive wear. .

This section of the thesis overcomes the deficiency of the previous trending tools for monitoring the real-time bit tooth wear by combining the rock formation hardness, drill bit type, drilling parameters such as a weight on bit, rotary speed etc. and the mechanical properties of the materials that form the drill bit based on the concept of three body abrasive wear.

3.2.2 Objectives

The bit wear obtained from the formula developed in this work is compared to the qualitative *in-situ* bit tooth wear for various drilled formation intervals of a number of wells in the south of Iraq. The new approach for bit wear determination, if successful, could be used as a trending tool to evaluate the status of the drill bits or predicting the wear of roller-cone bits. The study could potentially be extended and applied to other types of drill bits such as Polycrystalline Diamond Compact (PDC) bits.

3.2.3 Classification of the bit tooth wear

Depending on the type of the rock formation to be drilled, the drill bit is classified according to the criteria of The International Association of Drilling Contractors (IADC) that adopted a system for bit classification in 1972, which was later modified in 1987. In 1992 the system was updated to include many factors that reflect the latest technology in drill bit manufacturing. The system defines that rock bit comparison charts should be used for bit selection according to the rock which is being drilled and the availability of the bits. Major bit manufacturers have contributed in producing this chart. Furthermore, each bit type in the chart has its own IADC code classified according to its usage for drilling soft, medium or hard rock formations, and also according to the available features of each bit. For instance, soft rock formation such as limestone has hardness considerably low, therefore this kind of rock is more susceptible to be worn quickly and based on this criterion, the selection of the bit hence is milled-tooth roller-cone bit that has long sharp tooth made form steel as the formation to be drilled has low hardness. On the other hand, hard rock formation has relatively high hardness such as sandstone or marble that high degree of severity and not worn easily. In this case, Tungsten Carbide (TC) or called insert bits are the preferable choice as these bits have short tooth similar to buttons or inserts made from material harder than steel (tungsten carbide embedded in cobalt) . In general, the selection of the bit is based on the severity of the rock. The chart is designed separately for roller cone bits and PDC bits. Within the chart of roller cone bits, the first section represents milled tooth or steel tooth bits, whereas the next following section refers to insert or Tungsten-Carbide (TC) bits. Figure 3.15 shows the IADC classification chart for roller-cone bits provided from Reed Tool Company (McGehee *et al.,* 1992 a).

The IADC classification of drill bits is used in the present study to determine the type of drill bit i.e. milled tooth or Tungsten-carbide (TC) bits. Determination of the exact type of drill bit is crucially important in order to specify the main materials that forms these bits and, thus determines their hardness.

	FORMATION	SERIES	TYPE	BEARING/GAGE (1)	(2)	(3)	(4)	(5)	(6)	(7)	FEATURES AVAILABLE
STEEL TOOTH BITS	SOFT FORMATIONS WITH LOW COMPRESSIVE STRENGTH AND HIGH DRILLABILITY	1	1	R1, OSC3A,, OSC3AJ, DR1, LW3			ATX-1, X3A	ATX-G1, MAX-G1, XG3A, MX3A	ATJ-1, ATJ-1S, ATM-1, ATM-1S, J1	ATM-G1S, ATM-G1, JG1	
			2	R2, OSC3,	S	CSC	X3		ATJ-2, J2, J2T	JG2	
			3	R3, OSC1G, OSC1GJ, DR3, LW1		ODG, C1C	ATX-3, X1G	ATX-G3, MAX-G3, XDG, MX1G, XGG	J3	ATM-G3, JG3, JD3	
			4	OSC, OSCJ, OSC2, OSC2J							
	MEDIUM TO MEDIUM HARD FORMATIONS WITH HIGH COMPRESSIVE STRENGTH	2	1	R4, OWV, OWVJ, OW4, OW4J, DR4, LW	M	ODV, OD4	XY	XDV, XD4, XGV	J4	JG4, JD4	
			2	OW, OWJ, WO, DR5							
			3	OWC, OWCJ, OWS, OWSJ			XC	XCG			
			4								
	HARD SEMI-ABRASIVE AND ABRASIVE FORMATIONS	3	1	R7, W7, W7J, W7C	W7AJ, H	WD7, WD7J	X7	XD7	J7	JG7, JD7	
			2	WFR2, W7R2J, DR7	W7R2AJ		X7R				
			3	W7R, R8	HR						
			4	WR, WRJ		WDR	XWR	XDR	J8	JG8, JD8	
INSERT BITS	SOFT FORMATIONS WITH LOW COMPRESSIVE STRENGTH AND HIGH DRILABILITY	4	1					ATA-05, MAX-05		ATJ-05, ATM-05	
			2							ATJ-05C	
			3					ATX-11, ATX-11H, X11, MAX-		J11, ATJ-11, ATJ-11S, ATJ-11H, ATM-	
			4					ATX-11C		J11C, ATJ-11C, ATM-11C, ATM-	
	SOFT TO MEDIUM FORMATIONS WITH LOW COMPRESSIVE STRENGTH	5	1					X22, ATX-22		J22, ATJ-22, ATK-22S, ATM-22, ATM-22G	
			2							J22C, ATJ-22C, ATM-22C	
			3		HH33			X33		J33, J33H, ATJ-33, ATJ-33S, ATJ-33A, ATM-33	
			4					X33C		J33C, ATJ-33C, ATJ-35C, ATM-33C	
	MEDIUM HARD FORMATIONS WITH HIGH COMPRESSIVE STRENGTH	6	1		G44, A44,	44R		X44, X44R		J44, J44A, ATJ-44, ATJ-44A	
			2		HH75S	55R		X55R		J44C, J55R, ATJ-	
			3		G55, A55, HH55			X55		J55, ATJ-55R, ATJ-55, ATJ-55A	
			4								
	HARD SEMI-ABRASIVE AND ABRASIVE FORMATIONS	7	1		RG7AJ	RG7,RG7J		RG7XJ			
			2								
			3		G77, RG1AJ, HH77	RG1,RG1J		RG1X, X77		J77, ATJ-77	
			4								
	EXTREMELY HARD AND ABRASIVE FORMATIONS	8	1		HH88, A88					J88	
			2								
			3		RG2BAJ, HH99, G99	RG2B, RG2BJ		RG2BX, RG2BXJ		J99, ATJ-99, ATJ-99A	
			4								

Figure 3.15 Classification of roller-cone bits according to IADC
(McGehee *et al.*, 1992 a)

3.2.4 IADC dull bit grading

McGehee *et al.* (1992 b) developed the IADC ideal standard chart for dull bit grading as shown in Figure 3.16. This system of grading has used various codes to distinguish the qualitative wear of each part of the bit. The grading system is highly important for monitoring the bit performance. The chart contains eight different factors related to drill bits bit cutter description, gauge, and other information related to dull characteristics and reason for pulling the bit. The first two columns refer to the condition of inner and

outer rows of tooth, respectively, where the amount of wear is indicated by a value ranging from 0 (indicating intact tooth or no wear) up to 8 (referring to a completely dull tooth). The third column describes the dull characteristics of the bit. IADC uses various codes to indicate the wear condition of the tooth and bearing for roller cone bits, and the cutter conditions for PDC bits.

Rashidi *et al.* (2008) illustrated the dulling degree of the roller-cone tooth and for the inserts of PDC bits according to the IADC classification. The schematic image displays that the wear of the tooth or the insert is represented as a fraction of 8, i.e.1/8, 2/8, etc. For a new tooth or insert, the dulling degree is zero, while a completely damaged cutter or tooth has a classification of 8/8 or 1 as shown in Figure 3.17.

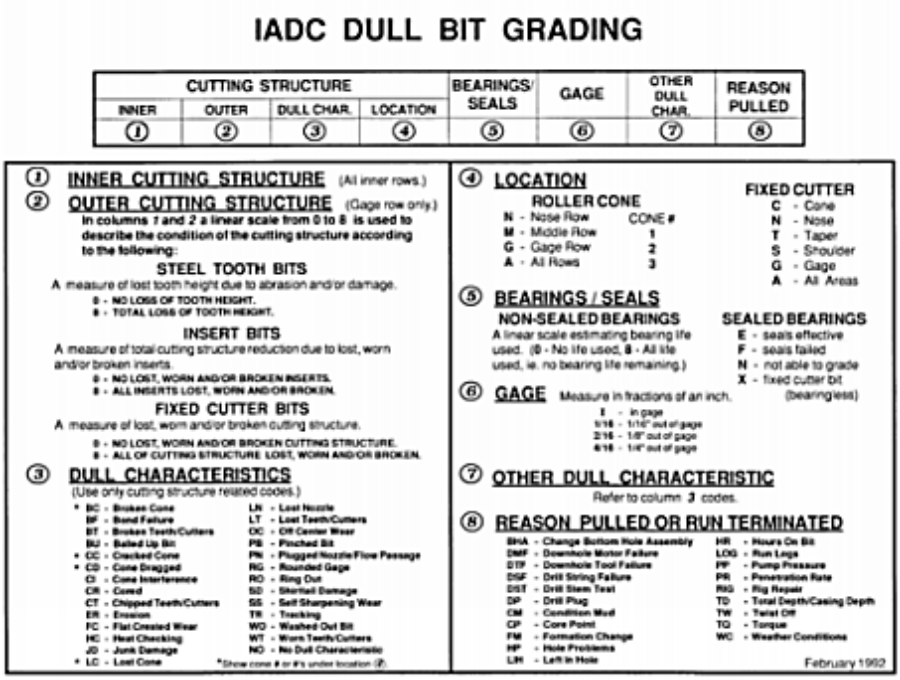

Figure 3.16 IADC grading system for drill bits (McGehee *et al.*, 1992 b)

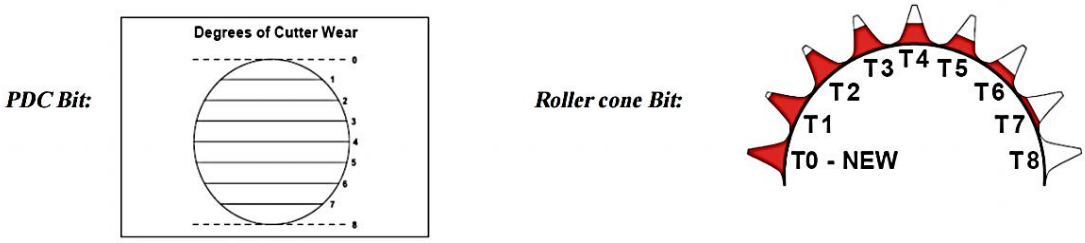

Figure 3.17 IADC grading system for drill bits (Rashidi *et al.*, 2008)

3.2.5 Theory

The mechanism of wear for various materials due to the activity of the solid particles has been discussed by Hutchings (1992), who classified the abrasive wear into two modes: two-body abrasive wear and three body abrasive wear. Two body abrasion is

caused by hard particles that are rigidly fixed to one surface and remove material from the opposing surface, while three-body abrasive wear is attributed to hard protuberances that are trapped between two solid surfaces but are free to roll and slide. Figure 3.18 demonstrates the distinction between the two modes of abrasive wear.

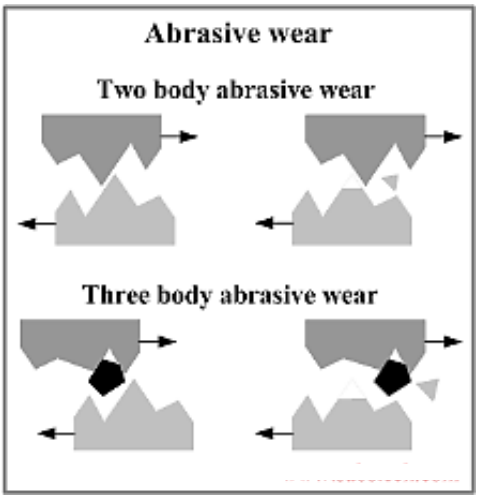

Figure 3.18 Differences between (a) two-body abrasion and (b) three-body abrasion (Kopeliovich, 2015)

During contact between the drill bit and the rock formation, three body abrasive wear is likely to occur due to the free motion of the cuttings produced after crushing the rock by the drill bit. The present study applies the three-body abrasion wear model of Rabinowicz (1977), which is dependent on the hardness of the abrasive and the abraded material. Rabinowicz (1977) proposed Equation (2-13) and Equation (2-14) as mentioned in chapter two of the present study for the determination of the volume of the abraded and the abrasive materials, respectively.

In the present study the hardness of the rock is typically less than 10 GPa ,although in some intervals consolidated sandstone are encountered that have hardness greater than 10 GPa (Al- Ameri *et al.*, 2011). On the other hand, the hardness of the teeth of the roller-cone bit is in the range of 12.95-15 GPa (Mouritz and Hutchings, 1991; Osipov *et al.*, 2010), therefore Equation (2-13) is applicable for approximating the volume of rock removal where roller-cone bits are acting as an abrasive material when drilling into these rock formations.

Since the abrasive material in Equation (2-13) is represented by the drill bit and the abraded material is the rock. Equation (2-13) is modified as follows:

$$V_R = \frac{F.\tan(\theta).X}{\pi H_R} \quad ,when \quad H_R < 0.8H_b \qquad (3-2)$$

where, V_R is the volume of the of rock removed (m^3), H_b is the hardness of the abrasive material or the drill bit (N/m^2) and H_R is the hardness of the rock (N/m^2).

It should be stated that the tooth of an ordinary milled roller-cone bit consist of three materials: uncarburised martensitic steel, high-carbon martensitic steel and hardfacing alloy containing tungsten-carbide-cobalt (Mouritz and Hutchings, 1991). The hardness of the hardfacing alloy as measured by Mouritz and Hutchings (1991) is nearly 1320 HV (12.95GPa) and it is considered to be representative of the milled tooth roller- cone bit. The hardness of the insert or Tungsten Carbide (TC) bits was selected to be 15GPa (Osipov *et al.*, 2010). These values are higher than the hardness of the main types of rocks for the drilled wells as presented in Table 3.8 (Mouritz and Hutchings, 1991 and Gokhale ,2010).

Table 3.8 Hardness of the main rock formations being excavated in the study (Mouritz and Hutchings, 1991 and Gokhale, 2010)

Rock formation type	Micro-hardness (HV)	Hardness (GPa)
Sandstone	1100*	10.79
Limestone	110*	1.079
Shale	250**	2.45
Dolomite	200**	1.961
Anhydrite	160**	1.569
Conglomerate (light calcite)	120**	1.17

* Micro-hardness of rocks was measured by Mouritz and Hutchings (1991).
** Vickers hardness of some rocks was mentioned by Gokhale (2010).

As the hardness of bit is generally more than that of rock formations, for evaluating the wear of bit, Equation (2-14) could be used, where the rock is regarded as an abrasive material, while the bit is the abraded material. However, the ratio of hardness of bit over that of rock could exceed 1.25 when drilling into moderate and soft formation. Rabinowicz (1977) did not suggest a correlation for the case where $H_w > 1.25H_a$, but only stated that the wear is very small. Equation (2-14) can be modified for wear quantification of bit wear volume as follows:

$$V_b = \frac{F.\tan(\theta).X}{5.3\,H_b}\left(\frac{H_R}{H_b}\right)^{2.5} \qquad 0.8 < \frac{H_b}{H_R} < 1.25 \qquad (3-3)$$

where H_b is the hardness of the bit (N/m^2) and V_b is the volume of the material removed from the bit (m^3).

The sliding distance (X) in Equation (3-3) could be determined from the following equation:

$$X = X_r * t \qquad (3-4)$$

where X_r is the linear velocity of the bit given below and t is the time required to drill a specific interval.

$$X_r = \pi N_b d_b \qquad (3-5)$$

where N is the rotational speed , and d_b is the diameter of the bit.

As the inserts are connected with the cones therefore Equation (3-5) could be corrected to the cone instead of the bit as follows:

$$X_r = \pi N_{cone} d_{cone} \qquad (3-5a)$$

Therefore, the sliding distance can be obtained from Equation (3-6) as follows:

$$X = (\pi N_{cone} d_{cone}) * t \qquad (3-6)$$

The time required for drilling a certain depth interval drilling with a constant penetration rate can be calculated in terms of penetration rate from the following equation:

$$t = \frac{L}{PR} \qquad (3-7)$$

where L is the interval of depth being drilled and PR is the penetration rate as obtained from bit records.

The applied load (F) in Equations (3-2) and (3-3) corresponds to the weight on bit (W). Substitution of Equations (3-6) and (3-7) into Equation (3-3) yields:

$$V_b = \frac{\pi . W . d_{cone} . N_{cone} . L . \tan(\theta)}{5.3\ PR . H_b} \left(\frac{H_R}{H_b}\right)^{2.5} \qquad (3-8)$$

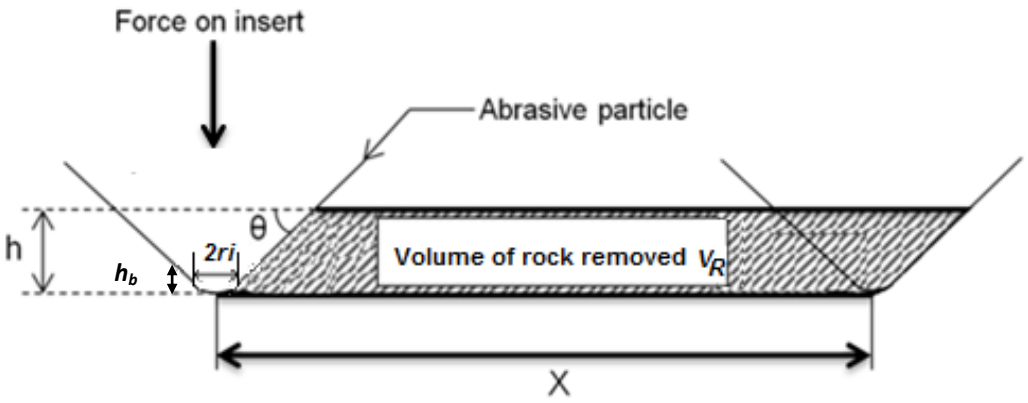

Figure 3.19 Suggested model for abrasive wear (based on Rabinowicz, 1996)

Figure 3.19 shows the schematic sketch of the abrasive wear for the conical inserts based on Rabinowicz model. Assuming a conical shape for the insert, therefore the cross-sectional area of the worn insert is calculated as follows:

$$A_b = \pi . {r_i}^2 \qquad (3-9)$$

where A_b is the cross sectional area of the worn insert , r_i is the radius of the insert cross section (m).

The radius of the insert r_i could be replaced by the worn height (h_b) and the angle of abrasion (θ) ,therefore, h_b can be obtained as follows:

$$A_b = \pi . \left(\frac{h_b}{tan\theta}\right)^2 \rightarrow V_b = \frac{\pi}{3} \frac{h_b^3}{(tan\,\theta)^2} \rightarrow h_b = \sqrt[3]{\frac{3\ V_b * (tan\,\theta)^2}{\pi}} \qquad (3-10)$$

where V_b is the volume of the material removed from the bit (m^3) and h_b is the height of the worn volume of insert (m).

The ratio of height of the worn insert h_b to the initial tooth height of the insert is then calculated (height of the milled-tooth is 1.5 ″, and the height of the insert is 3/4″

according to Eason *et al.*, 2008). The predicted tooth wear as a 0-8 grade is then obtained as follows:

$$Predicted\ wear\ =\ \frac{h_b}{Initial\ \ tooth\ height}\ *8 \qquad (3-11)$$

The real-time predicted rate of bit tooth wear is obtained by dividing the predicted bit tooth wear from Equation (3-11) over the depth interval. This will be compared to the real-time qualitative bit tooth wear rate.

In Equation (3-8), the power index (2.5) is used when the ratio of the hardness of abraded material (H_b) over that of rock (H_R) is less than 1.25. However, when this ratio is higher than 1.25 for softer rocks, it is expected that the power is greater than 2.5 (as less wear is expected for the inserts). Therefore, in this study the power index in Equation (3-8) is replaced by (n) as follows:

$$V_b = \frac{\pi . W . d_{cone} . N_{cone} . L . \tan(\theta)}{5.3\ PR . H_b}\ (\frac{H_R}{H_b})^n \qquad (3-12)$$

The weight on bit is distributed on all inserts (Nguyen, 2011). Figure 3.20 illustrates the weight on bit is equal to the summation of the forces exerted from the teeth.

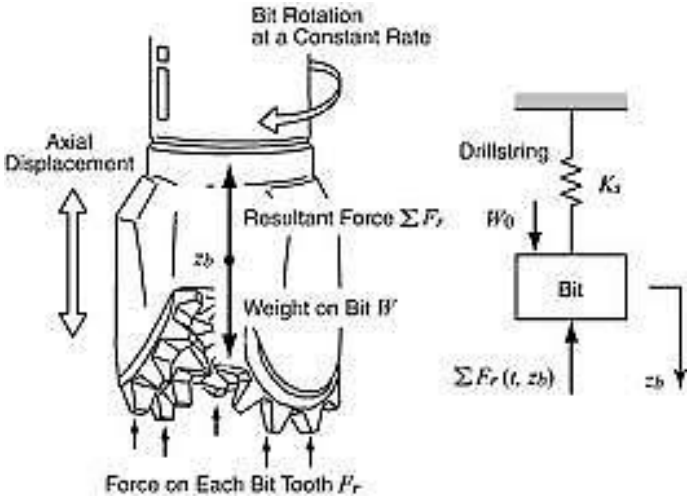

Figure 3.20 Force balance on the bit and the teeth (Nguyen, 2011)

The wear of the worn insert (V_i) has to be adjusted for single insert or tooth by dividing the weight on bit in in Equation (3-12) over the number of the inserts engaged on the bit. It is assumed that the number of the teeth for the milled-tooth bit in contact with the rock is 50 and for Tungsten-Carbide (TC) bit is 65 (in general, this number could vary , but in general, the teeth count for milled-tooth bit is usually lower than the TC bit.

The abrasion angle (θ) in Equation (3-12) has to be expressed in terms of the attack angle (α). The attack angle is defined as to be the angle between the cone axis and the intersection of the insert centre line and the outside surface of the insert (Nguyen and Ouan Van 1995). Figure 3.21a shows the attack angle with the corresponding cone, while Figure 3.21b illustrates a schematic geometry of the insert in contact with rock.

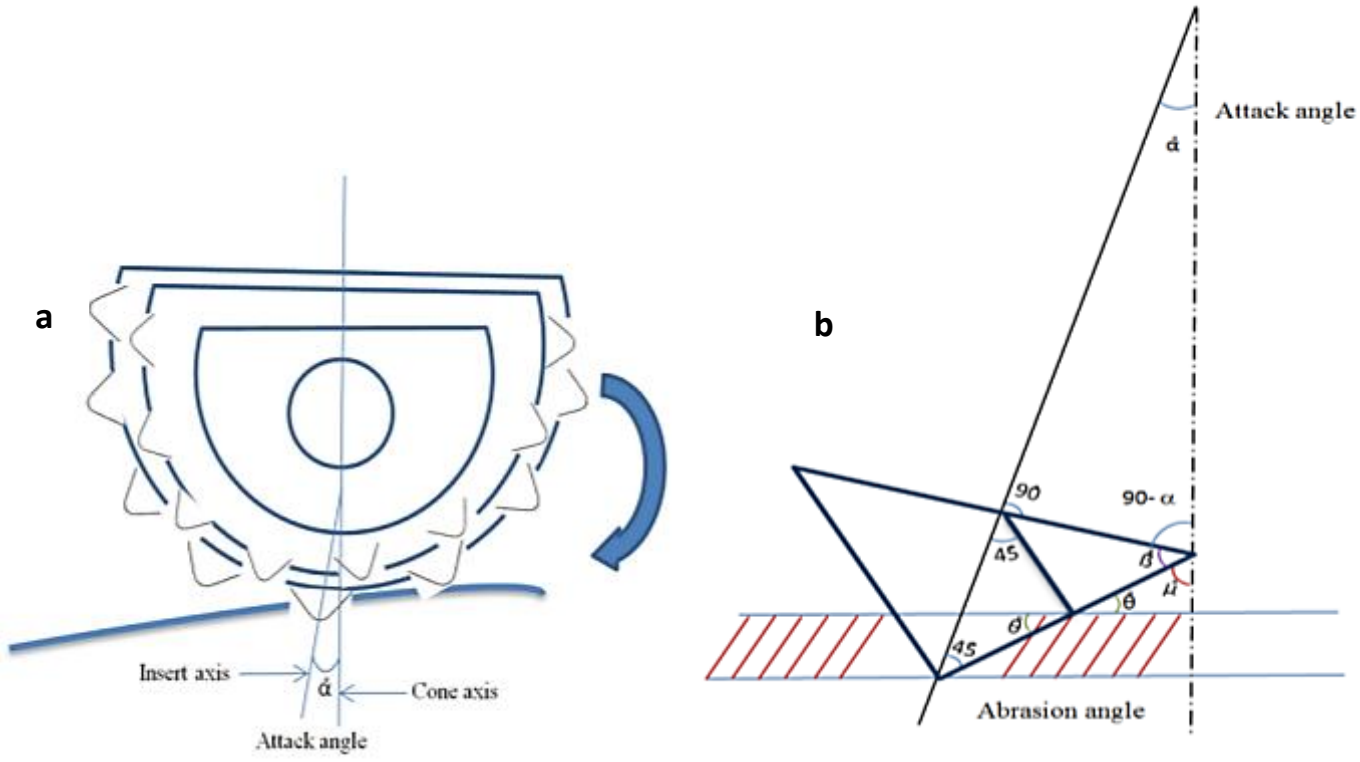

Figure 3.21 Schematic sketch of the cone in contact with the surface of the rock (a) insert in contact with rock (b)

The following mathematical relations are obtained from Figure 3.21b:

$$\theta + \mu + 90° = 180° \rightarrow \mu = 90° - \theta \qquad (3-13)$$

$$90° - \alpha + \beta + \mu = 180° \rightarrow \beta + \mu = 90° + \alpha \qquad (3-14)$$

$$\beta + (90° - \theta) = 90° + \alpha \rightarrow \beta - \theta = \alpha \qquad (3-15)$$

$$90° + 45° + \beta = 180° \rightarrow \beta = 45° \qquad (3-16)$$

$$From\ Eq.\ (3-15):\ 45° - \theta = \alpha \quad \therefore\ \theta = 45° - \alpha \qquad (3-17)$$

The attack angle (α) is ranged between 0˚ and 45˚ (Nguyen and Ouan Van, 1995) and therefore, the abrasion angle (θ) is ranged between 45˚ and 0˚.

The geometry of the bit with its cones is shown in Figure 3.22. The projected view of the bit and its parts is shown in Figure (3.22 b), while the radii of the bit and its cone is shown in Figure (3.22 a), The relationship of the rotary speed of the bit and the cone has to be determined in order to adjust the rotary speed and the diameter of the bit to those of the corresponding cone that the inserts are connected with.

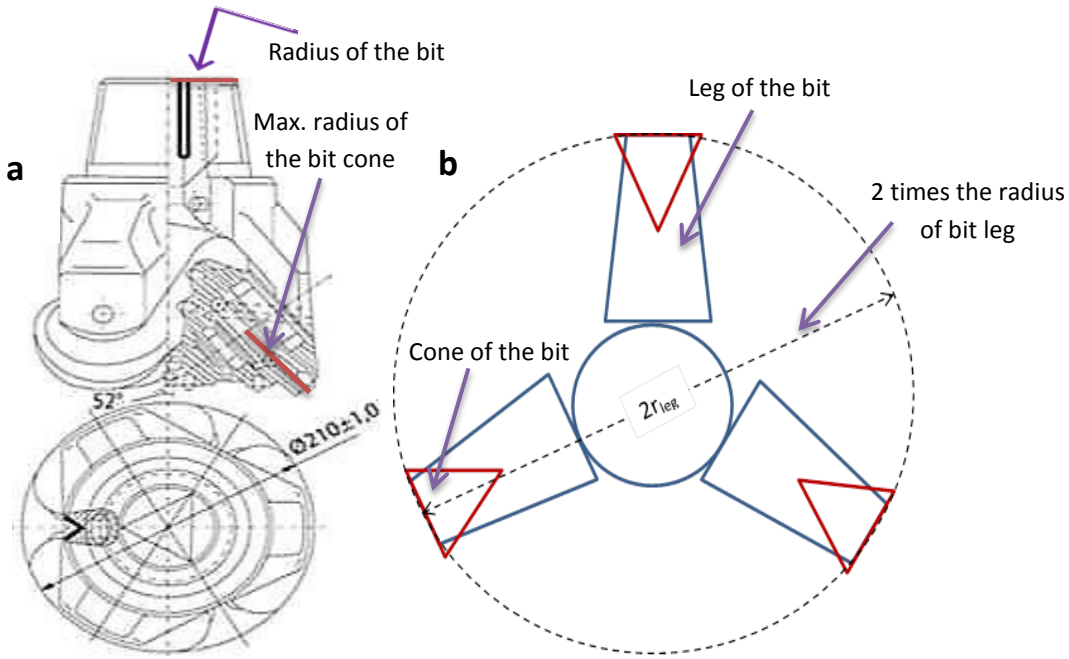

Figure 3.22 Schematic geometry of the bit (a) (Erno, 2014) and schematic sketch of the legs of the cones (b)

From the geometry of Figure 3.22a, it is noted that:

$$N_{bit} = N_{leg} \ as\ the\ leg\ is\ fixed\ with\ the\ bit.$$

$$V_{cone} = V_{leg}\ ,\ but\ N_{cone} \neq N_{leg}\ as\ they\ have\ different\ radii.$$

where, N is the rotary speed (rpm) and V is the linear velocity (m/min). Using engineering drawing scales (Fig.3.22), the following expressions are obtained for geometrically similar bits used during drilling:

$$\frac{r_{cone}}{r_{leg}} = 0.635$$

$$N_{bit} = N_{leg}\ ,\ V_{cone} = V_{leg}$$

$$N_{cone} * r_{cone} = N_{leg} * r_{leg}$$

$$\frac{N_{bit}}{N_{cone}} = \frac{r_{cone}}{r_{leg}} = 0.635$$

$$N_{cone} = N_{bit} * 1.575 \quad (3-18)$$

The new relationship between the rotary speeds of cone and bit is substituted in Equation (3-12) and the final formula of the volume of the material removed from the insert is presented as follows:

$$V_i = \frac{\pi.(W/no.of\ inserts).d_{cone}.N_{cone}.L.\tan(45-\alpha)}{5.3\ PR.H_b}\left(\frac{H_R}{H_b}\right)^n \quad (3-19)$$

where V_i is the volume of the material removed from the insert or tooth of the roller-cone bit (m^3) and α is the attack angle ranged from 0° to 45°. To obtain a full rotation of the teeth, the term tan (45-α) could be integrated with respect to the attack angle α, therefore, Equation (3-19) could be written as follows:

$$V_i = \frac{\pi.(W/no.of\ inserts).d_{cone}.N_{cone}.L.\int_0^{45}\tan(45-\alpha)\,d\alpha}{5.3\ PR.H_b}\left(\frac{H_R}{H_b}\right)^n \quad (3-20)$$

The integral in Equation (3-20) is replaced by $[\ln\cos(45-\alpha)]_0^{45}$. The final value of the integral is equal to 0.3465. The final equation of the volume of tooth wear is as follows:

$$V_i = \frac{0.205.(W/no.of\ inserts).d_{cone}.N_{cone}.L}{PR.H_b}\left(\frac{H_R}{H_b}\right)^n \quad (3-21)$$

3.2.6 Results and discussion

Table 3.8 shows the rock formation and the corresponding hardness in GPa. The commercial name of the drill bit according to IADC classification leads to the determination of the exact type of the drill bit. The material forming the drill bit is determined based on the type of the bit and the further data given by McGehee *et al.* (1992). The roller-cone bit is either a milled-tooth or Tungsten-Carbide (TC) bit. The hardness of the milled-tooth bit was chosen to be 1320 Vickers hardness (HV), or 12. 95 GPa, which represents the hardness of the external layer of the milled-tooth bit according to Mouritz and Hutchings (1991). The hardness of the Tungsten –Carbide bit is taken as 15 GPa (Osipov *et al.*, 2010). Table 3.9 shows the manufacturer of the drill bit, corresponding IADC bit code, and drill bit type along with the hardness for each bit

for well A_1 in the South of Iraq. The data has been obtained for other wells studied in this work using the same procedure.

Table 3.9 Drill bits used to excavate well A_1 south of Iraq

Depth drilled (m)	Drill bit manufacturer	Drill bit commercial name (code)	Drill bit type	Bit hardness (GPa)
0-38	HUGHES	SS5	Milled-tooth	12.95
38-660	HUGHES	R1	Milled-tooth	12.95
660-947	HUGHES	X3A	Milled-tooth	12.95
947-1440	TSK	MSS	Milled-tooth	12.95
1440-1530	SECURITY	M44NF	Milled-tooth	12.95
1530-1721	SECURITY	X3A	Milled-tooth	12.95
1721-1925	HUGHES	JD4	Milled-tooth	12.95
1925-2074	HUGHES	J4	Milled-tooth	12.95
2074-2440	SECURITY	S84F	(TC-bit)	15

Table 3.10 Drilling parameters of well A_1 southern Iraq and the corresponding rock hardness (Data are provided from bit records obtained from the section of Petroleum Engineering of South Oil Company).

Depth Drilled (m)	Rock Formation	Bit Diameter (in)	Weight on Bit (lb)	Rotational Speed (rpm)	Penetration Rate (m/hr)	Interval Drilled (m)	Time (hr)	Rock Hardness (GPa)
0-38	Conglomerate	26	20000	100	6.33	38	6.003	1.17
38-660	Limestone +bit of Anhydrite	17.5	20000	100	5.78	622	107.61	1.25
660-947	Limestone	12 1/4	36000	70	4.94	287	58.097	1.079
947-1440	Dolomite	12 1/4	36000	75	6.36	493	77.515	1.961
1440-1530	Limestone	12 1/4	36000	75	4.5	90	20.00	1.079
1530-1721	Shale +Lime	12 1/4	36000	90	2.19	191	87.21	1.70
1721-1925	Limestone	12 1/4	36000	90	2.45	204	83.26	1.079
1925-2074	Shale +bit of Lime	8.5	30000	100	3.5	147	42.00	2.20
2074-2440	Marl +Shale +Lime	8.5	30000	60	3.5	366	104.57	1.75

From the available data for each well, the volume of the predicted worn insert (V_i) is calculated from Equation (3-21). The height of the worn insert (h_b) is obtained from Equation (3-10). The predicted tooth wear index is determined from Equation (3-11). The obtained values for the worn inserts are used to calculate the real-time predicted bit tooth wear rate by dividing it over the incremental depth being drilled. This predicted bit tooth wear rate is then compared with the real-time qualitative tooth wear rate obtained from field data. The real-time qualitative bit dullness rate is obtained by dividing the qualitative bit tooth wear ranging from 0 to 8 over the incremental depth.

Well A_1

After analysis of the data for well A_1, the real-time predicted tooth wear rate has been obtained at various drilling intervals. It was found that the original proposed power index by Rabinowicz was (2.5) in Equation (3-8) led to match values of the real-time predicted tooth wear rate as shown in Figure 3.23. However, higher values than 2.5 (3 and 3.5) for the power index in Equation (3-21) were also examined, but led to underestimation for the prediction of wear rate. Lower power indices less than 2.5 (2.1-2.4) for the power index in Equation (3-21) were also investigated, but the optimum power index found to be 2.5 according to the calculated Mean Absolute Percentage Error. It is worth mentioning that, when the power index reached 2.3, the predicted bit tooth wear rate was very close to the predicted wear rate when the power index is 2.5. Figure 3.23 illustrates the obtained results of the real-time predicted tooth wear rate from various power indices corresponded to the bit drilled a certain interval.

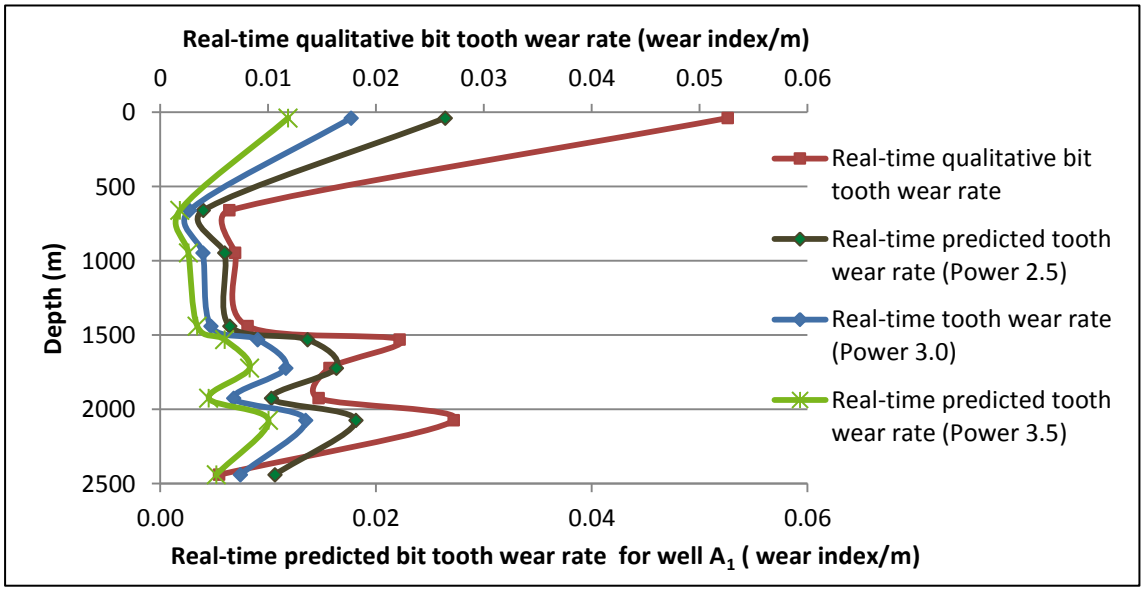

Figure 3.23 Real-time predicted bit tooth wear rate from different power indices of the modified Rabinowicz equation compared to the real-time qualitative bit wear rate for well A_1 in the south of Iraq

In Figure 3.23 it can be seen that the predicted results become much close to the observed ones when power index of 2.5 is used. It is worth mentioning although the wear rate values from power indices of 3.0 and 3.5 are underestimated at all depths, the trend of the plots illustrate good agreement with the real-time measured bit tooth wear rate. Nevertheless, the overall trends obtained from all power indices agree reasonably well with the real-time qualitative tooth wear and exhibit improvement of the predictions as compared to the approach based on the specific energy.

The same analyses were performed for data from all wells and accordingly, the optimum power index form Rabinowicz equation was obtained.

Mean Absolute Percentage Error (MAPE) was used as a statistical indication for selecting the optimum power index in Equation (3-21).The results of MAPE are shown in Table 3.11. The statistical results suggest that the optimum power index applying in Equation (3-21) for all wells is 2.5 as this provided lowest value of MAPE.

Table 3.11 Mean Absolute Percentage Error of the volume of wear using various power indices values for wells A_1, B_1, B_2, A_2 and B_3

Well	(MAPE) Power index (2.5)	(MAPE) Power index (3.0)	(MAPE) Power index (3.5)
A_1	35.83	48.30	58.55
B_1	26.72	42.15	58.99
B_2	48.94	41.54	50.00
A_2	48.82	64.21	74.96
B_3	32.70	44.25	60.87

It can be seen that for well A_2 MAPE values are relatively high and this is further investigated in the next section. The real-time predicted tooth wear rates based on power index of 2.5 for other wells are plotted in Figures 3.24 to 3.27 and are compared to the real-time recorded qualitative wear rate.

The results of the new wear model (power index 2.5) with the previous obtained dimensionless bit tooth flatness (F_D) from section 3.1.4 were compared to the recorded bit tooth wear along depth for well A_1 (Figure 3.24). It is shown from the figure that, the predicted bit tooth wear from the new wear model is relatively better when compared to the field recorded bit tooth wear. The values and trends of the new wear model were

close to the field wear, while for the dimensionless bit tooth flatness, the trend is matching the trend of the recorded wear, but the values are so far.

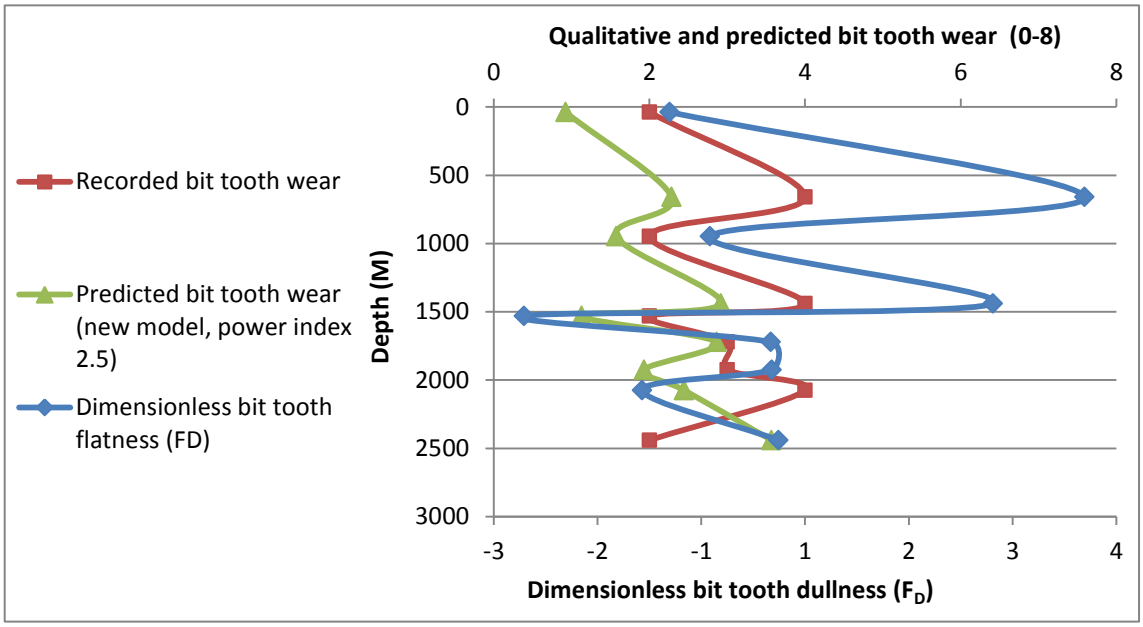

Figure 3.24 Comparison between the predicted wear from the new model (power 2.5) and the dimensionless bit tooth wear along with recorded field bit wear

Well B_1

Figure 3.25 illustrates the plot of the real-time predicted bit tooth wear rate (from power index of 2.5) as compared with the real-time recorded tooth wear rate for well B_1 at various depths. It can be seen that the predicted wear rate reasonably agrees with recorded tooth wear rate at all depths, despite slight divergence of the two curves appearing from depth 1850 m to 2185 m..

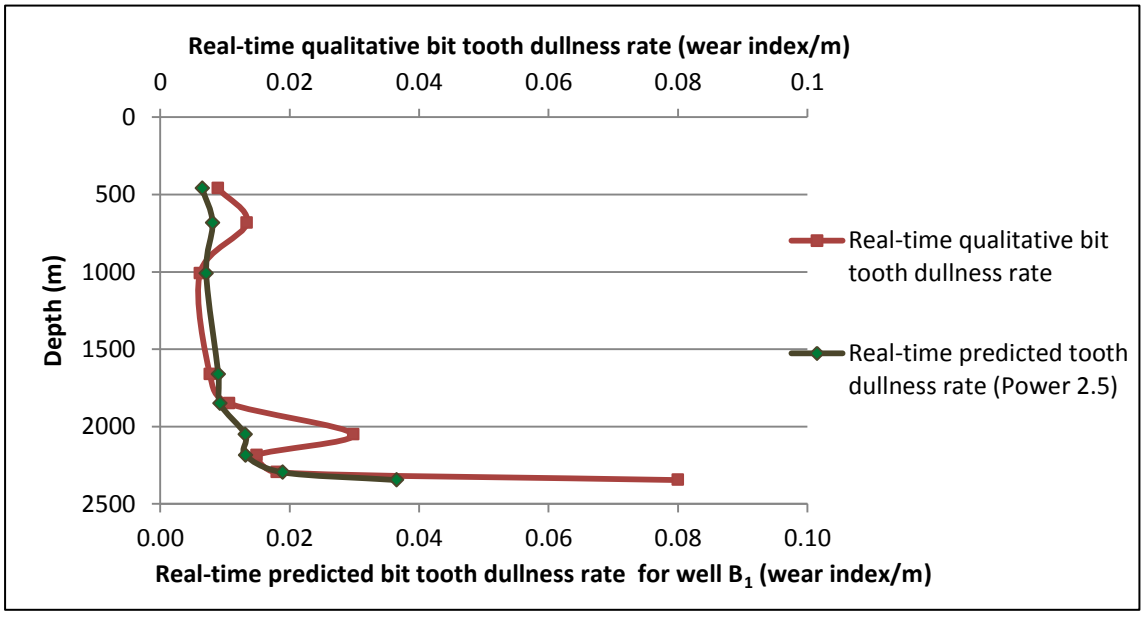

Figure 3.25 Real-time predicted tooth wear rate obtained from power index 2.5 compared with the real-time recorded tooth wear rate for well B_1

Well B_2

Figure 3.26 shows that the predicted wear rate agrees reasonably with the recorded wear rate, however extreme high values of the predicted wear rate were noted from a depth 2561m to 3009 m. This is attributed to the presence of shale formations at this range of depth, as indicated in Figure 3.2, which causes the "bit balling" phenomena. Bit balling causes sticky shale cuttings accumulate at the face of the bit leading to a reduction in penetration rate (*PR*) for given conditions (weight on bit and rotational speed) and therefore an overestimate of wear obtained from Equation (3-21).

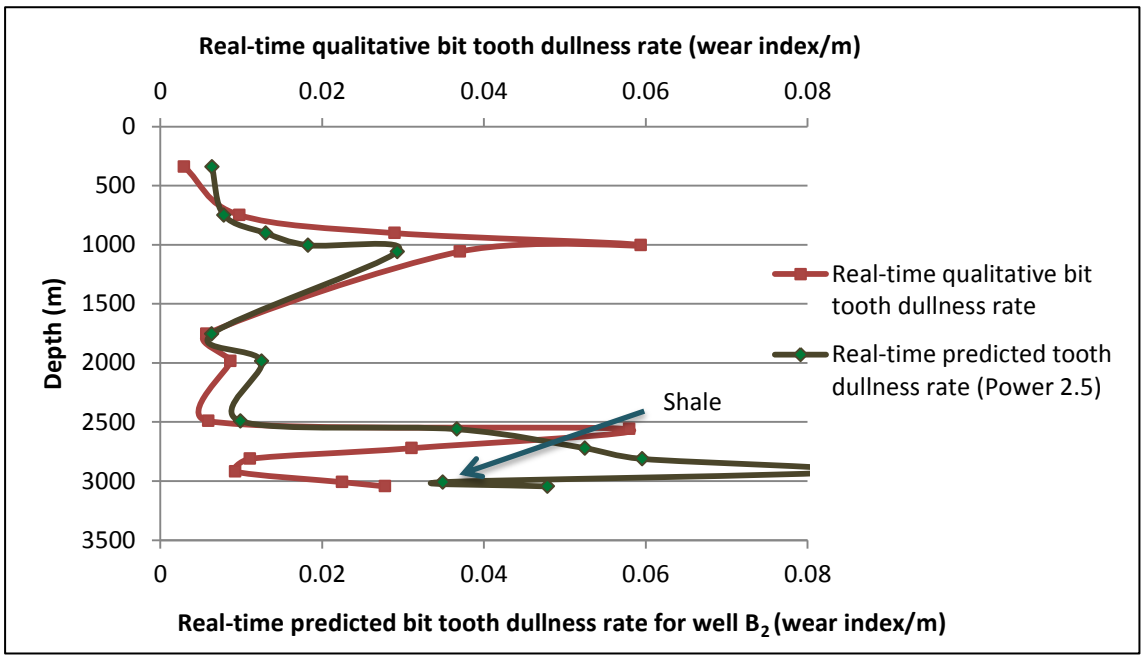

Figure 3.26 Real-time predicted tooth wear rate obtained from power index 2.5 compared with the real-time recorded tooth wear rate for well B_2

The occurrence of shale formations could cause misinterpretation and therefore, the analysis of the obtained data should be carefully carried out with such lithology. For wells where shale formation is encountered, it is preferable to use other tools for wear prediction with the presence of well logs to avoid any misleading results.

Wells A_2 and B_3

For wells A_2 and B_3, as can be seen from Figures 3.27 and 3.28, the predicted tooth wear rate is in agreement with the recorded tooth wear rate. However, for well A_2 at 1920 m, there is a significant difference between the predicted wear rate and the recorded one as shown in Figure 3.27. This significant difference is affecting the high obtained value of MAPE as shown in Table 3.11. This is again presumably due to the occurrence of shale which started at depth below 2000 m. However, the great divergence between the predicted and the recorded bit tooth wear is might be attributed

to the unconformity (surface of erosion) at near depth of 2050 m as shown in Figure 3.2. The presence of such geological structures causes misleading interpretation. Unconformity is represented with a curvy line at near depth 2100 m as shown in Figure 3.2. The specific type of unconformity in this case is disconformity as it separates parallel layers of limestone sedimentary rocks that illustrate erosion was taking part during that period causing a break in the sedimentary geological record. This disconformity affects the results of the predicted wear leading to misleading interpretation. It is recommended to use other reliable techniques such as well logging tools to avoid the misleading results.

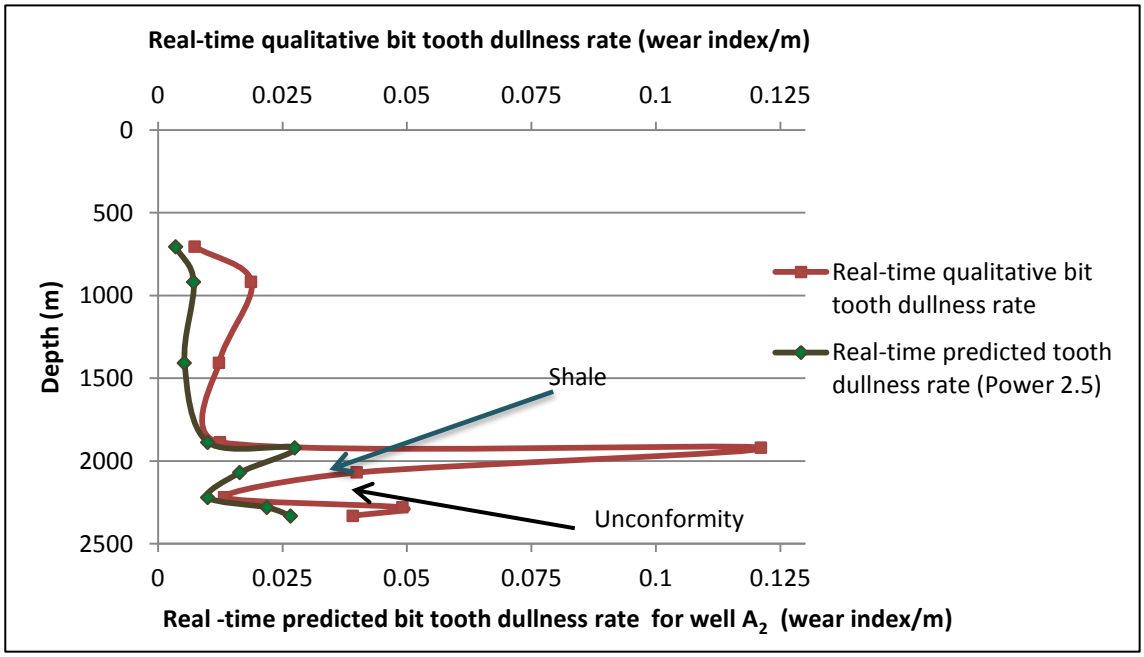

Figure 3.27 Real-time predicted tooth wear rate compared with the real-time recorded wear rate for well A_2

For well B_3, high value of the predicted wear was observed at the depth of 3264 m again due to the existence of shale formation as shown in Figure 3.28.

It is worth mentioning that for well B_3 there was a sharp increase of the ratio (H_R/H_b) in Equation (3-21) from depth 3172 m to 3345 due to the occurrence of sandstone mixed with shale formation that has high hardness. The hardness of the shale rock increased from 2.4 GPa at depth 3172 m up to 6.5 GPa at depth 3264 m corresponding to sandstone mixed with shale formation. In addition, it was noted that the penetration rate for the same well suddenly dropped from 2.64 (m/hr) at depth 3172 m to 0.99 (m/hr) at depth 3264 m which also contributed the sharp increase of the predicted wear rate.

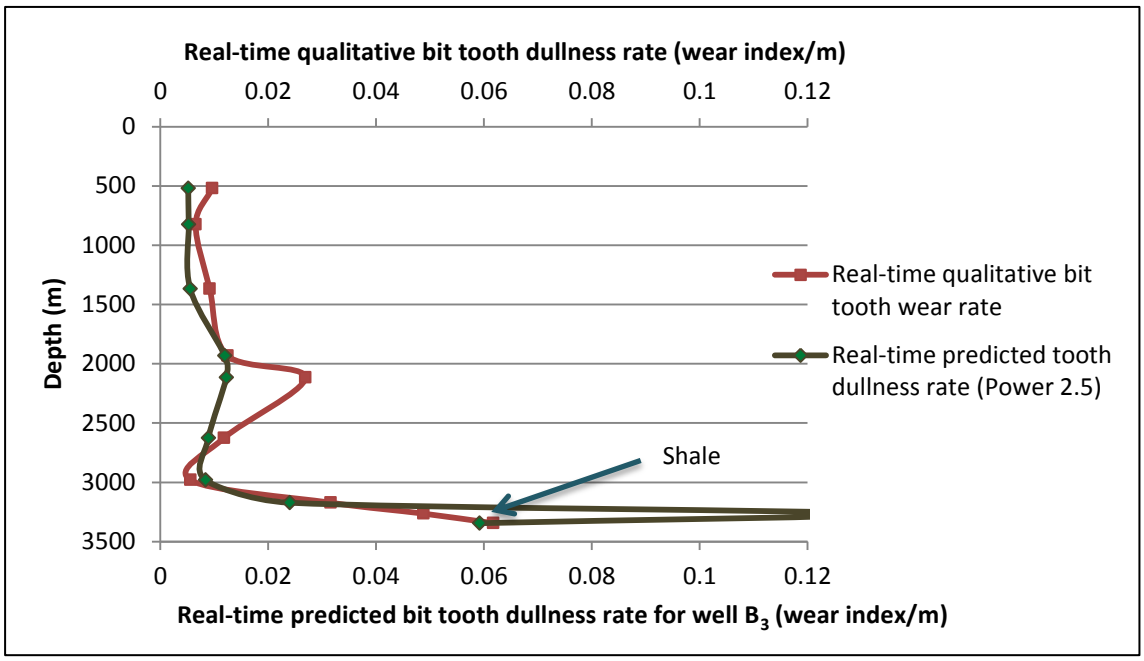

Figure 3.28 Real-time predicted tooth wear rate compared with the real-time recorded wear rate for well B_3

3.2.7 Conclusions

In this chapter, the wear of the roller-cone bits was analysed by using a developed equation based on the principle of three body abrasion, while incorporating, the hardness of the rock formation and the materials forming the drill bit as well as other drilling parameters such as penetration rate, weight on bit and rotational speed .

The new method was applied to five selected oil wells in the south of Iraq from two main big oil fields in the south of Iraq, where only roller-cone bits were used, including both milled-tooth and Tungsten-Carbide (TC) bit types .

The results obtained from the proposed model were compared with the recorded qualitative bit tooth wear rate where a reasonable agreement at different drilling intervals was obtained. Overall, the proposed model agreed well with the recorded bit wear for all oil wells studied in this work, except for some minor anomalies at some depth intervals and this could be related to the existence of shale as when drilling into shale formations bit balling phenomena take part causing misleading interpretation. Well logs should be used while drilling to verify the influence of shale on the obtained results.

Misleading results occurred at certain depths and this could be attributed to a surface of erosion or non-deposition (unconformity) between the parallel layers causing misleading interpretations, therefore more reliable techniques are recommended to be

used when encountering such geological structures to prove the effects of such formations on the obtained results.

This approach could be tested for other wells in other regions for vertical and could also be tested for horizontal drilling to verify its reliability. The developed technique was performed on roller-cone bits only, but could in principle be extended to Polycrystalline Diamond Compact (PDC) bits.

It is worth pointing that based on the proposed model in this chapter, the wear could be predicted based on the material properties of the bit as well as the rock and drilling parameters. Therefore, properties of the bit, notably the hardness could significantly affect the wear and it should be characterised and well understood. Therefore, in the next chapter, attempts have been done to measure and characterise the properties of the material that form the cutting elements of the bit, especially hardness and how it reflects on the amount of wear. More reliable results would be obtained from the aforementioned new developed wear model when precise hardness values are used for both the materials forming the bit as well as the rock formation.

Chapter 4 Experimental Work (Indentation Testing)

This chapter is focused on measuring the mechanical properties of the materials form the PDC cutters by nano and microindentation testing. The mechanical properties include hardness, Young's modulus and fracture toughness. These properties are crucially significant for wear quantification as the available wear models in the literature depend mainly on the mechanical properties, therefore, precise determination of the mechanical properties will reflect on the accuracy of the quantified wear. Sample preparation needs to be done prior to the indentation testing to avoid misleading results due to the high degree of the surface roughness of the samples. The samples investigated throughout the tests are polycrystalline diamond cutters that used in oil field PDC bits. PDC specimens are in form of disks with different dimensions. Figure 4.1 illustrates an image of the two PDC cutters that have been used in the experiments. Table 4.1 demonstrates the dimensions of the PDC cutters supplied from two different manufacturers.

Table 4.1 Dimensions of the PDC specimens

Commercial Order	Cutter Diameter (mm)	Cutter Length (mm)	Diamond Thickness (mm)
M1308	13.44 (± 0.03)	8.0 (± 0.1)	2.2 (± 0.2)
M1313	13.44 (± 0.03)	13.2 (± 0.1)	2.2 (± 0.2)
K1608	16.00 (± 0.05)	8.0 (± 0.1)	2.0-2.5
K1908	19.05 (± 0.05)	8.0 (± 0.1)	2.0-2.5

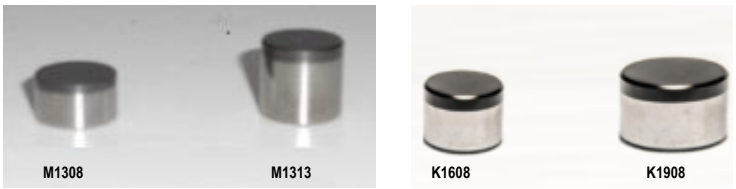

Figure 4.1 Oil PDC cutters manufactured by two different manufacturers

The samples consist of two main parts, the first layer is the diamond table which is clearly shown as black colour and its composition is mainly coarse diamond particles with cobalt as a binder, while the second layer represents the tungsten carbide in cobalt substrate. The first part of the experimental work is focused on the preparation of the specimens using polishing technique to reduce the surface roughness, especially for the

diamond surface. Once the samples are polished well, testing could take place. First testing to be launched are micro and nano-indentation, where the mechanical properties (hardness, Young's modulus and fracture toughness) of the two layers of the PDC inserts are measured within these tests. The indentations tests will be followed by analytical study using Scanning Electron Microscopy (SEM), Energy Dispersive X-ray maps (EDX) along with the Energy Dispersive Spectroscopy (EDS) to examine the element distribution on the surfaces of the substrate and diamond layers of the PDC samples. Microstructural properties (particle size distribution and cobalt content) of the materials forming the substrate and coating of the PDC sample are analysed to study their effect on the mechanical properties which affect later the amount of wear of the PDC samples.

4.1 Samples preparation

4.1.1 Surface roughness test (before polishing)

Surface roughness analysis has been performed on the specimens to evaluate the degree of surface roughness for both layers (diamond and substrate). The most commonly surface roughness parameters are the average surface roughness (R_a) as described in ASME B46.1 and the surface skewness (R_{sk}). Average roughness (R_a) is defined as the arithmetic average deviation of the surface valleys and peaks from profile mean line in micrometres, and it is useful for detecting general variations in overall profile height, while surface skewness (R_{sk}) represents the symmetry of the surface deviations from the mean reference plane. R_q is another surface roughness parameter which is referred to the root mean square of the surface peaks and valleys. R_q is calculated as between 1.11 and 1.25 times the (R_a) value. (R_q) is more sensitive to peaks and valleys, making it more valuable parameter compared to R_a.

A surface with high value of (R_a), or a positive skewness (R_{sk}), will have high wear rate (low wear resistance). The tests were carried out by using Ultra Precision Form Talysurf PGI800 instrument at the Biomedical Engineering School of University of Leeds, with a resolution of up to 3.2 nm. The device uses a motorized column that gives high accuracy and a tiny probe passes the surface of the specimen recording the surface profile precisely within few minutes. The results will be presented as surface profile measurement. Two tests were performed for each layer at various positions to measure the main common surface roughness parameters; average surface roughness (R_a) and skewness (R_{sk}), finally the roughness parameters (R_a) and (R_{sk}) were averaged. Surface

profile measurement test was performed before polishing the samples and after to observe the difference in the surface roughness parameters before and after polishing.

Figure 4.2 illustrates positions 1 and 2 on the surface of the cutter specimen M1313. Figures 4.3 and 4.4 show the surface profile measurements across the surface of the diamond layer of the PDC specimen at position 1 and 2 respectively before polishing sample M1313, while Figures 4.5 and 4.6 illustrate the surface profile measurement for the substrate layer of the PDC insert at position 1 and 2 respectively before polishing. The average roughness for the diamond layer (R_a) was 1.423 µm and the skewness (R_{sk}) was equal to -0.48545 before polishing and according to Table 4.2, the value of the average roughness is corresponded nearly to the roughness grade number N7 as an industrial classification for roughness (Bahushan 2001). A negative value for the surface skewness means, that the surface has deep scratches or pits indicating the sample could have a good wear resistance where just few hills are available that could wear away. The average value of (R_a) for the tungsten carbide layer (substrate) was 0.8626 µm and classified under grade number N6 according to Table 4.2. Surface skewness value at position 1 is -0.7103, while at position 2 is equal to 0.0968 and this indicates that the surface at position 1 has downward spiky bias, and upward spiky peaks in position 2. This could indicate that part of the substrate specifically at position 2 will be worn away due to the spiky upward peaks, while in other parts as in position 1 deep valleys occurred and could be considered as good bearing surfaces. The average value for the surface skewness for sample M1313 was -0.30675.

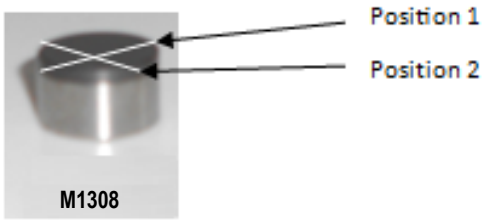

Figure 4.2 Selected positions 1 and 2 on the surface of the PDC sample

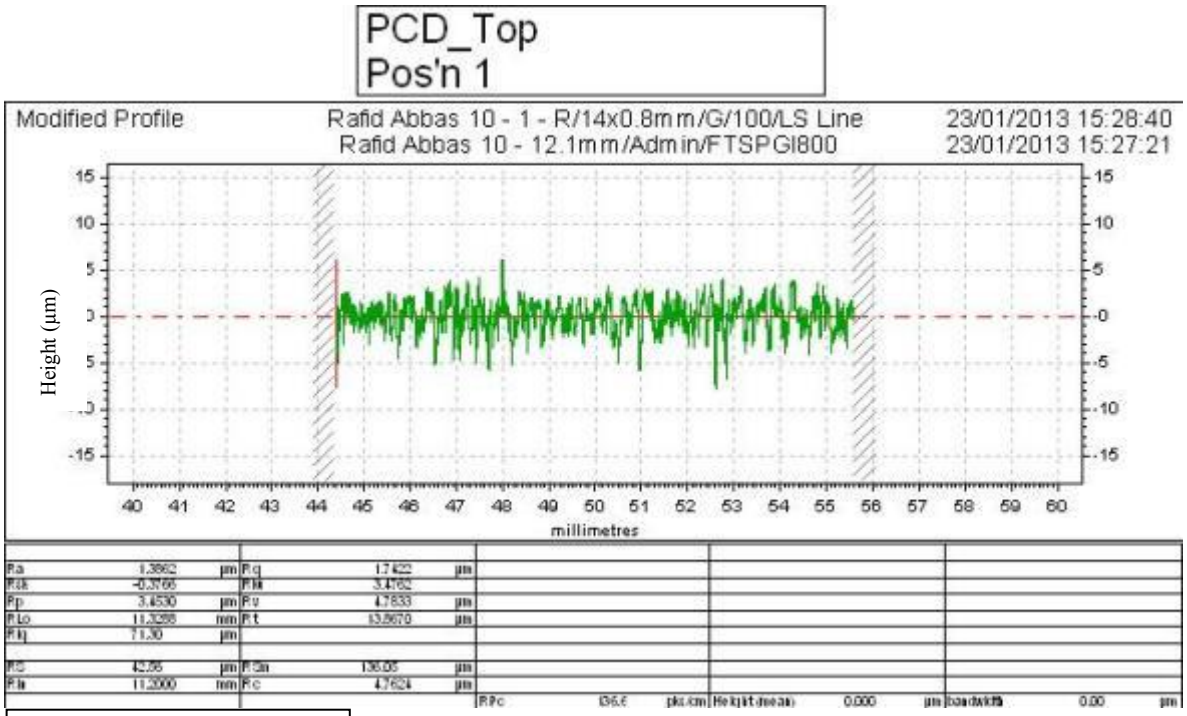

R_a =1.3862 µm , R_{sk} = - 0.3766

R_q = 1.7422 µm , R_{ku} = 3.4762

Figure 4.3 Surface profile measurement of the diamond layer for the PDC insert at position 1 before polishing

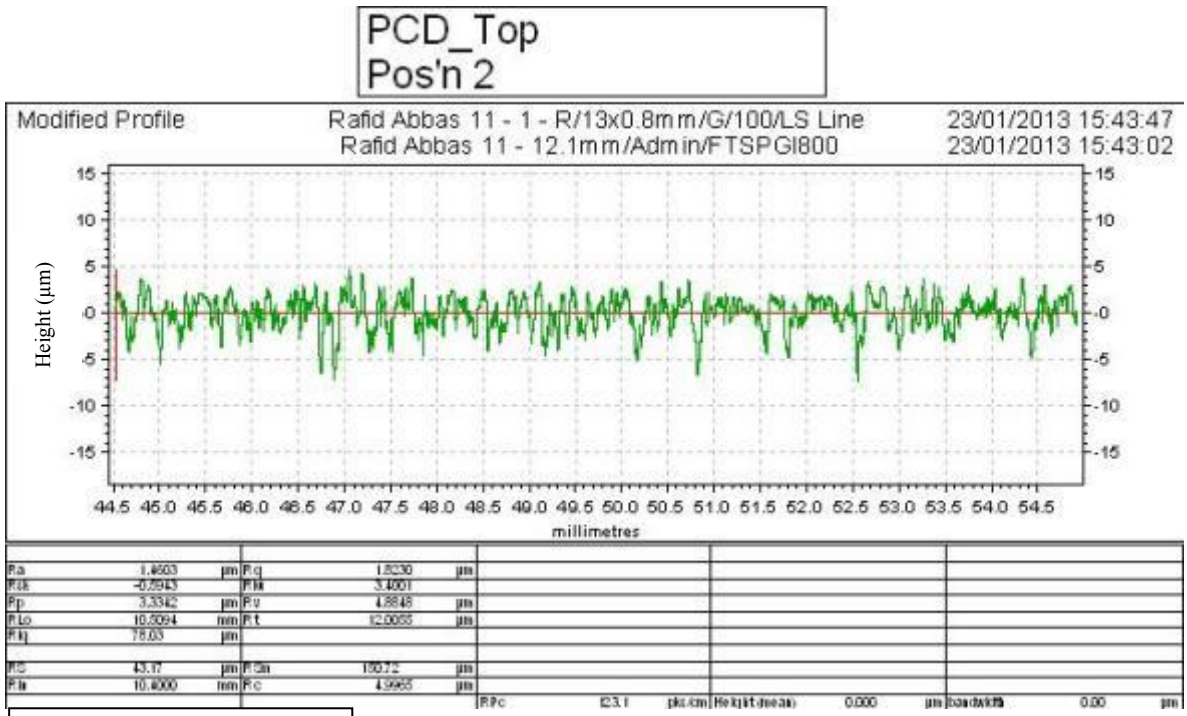

R_a =1.4603 µm , R_{sk} = - 0.5943

R_q = 1.8230 µm , R_{ku} = 3.4.001

Figure 4.4 Surface profile measurement of the diamond surface for the PDC cutter at position 2 before polishing

Table 4.2 Roughness average with the corresponding grade number of roughness as known in industry (Bhushan, 2001)

Roughness Average parameter (R_a), µm	Roughness grade number
0.025	N1
0.05	N2
0.1	N3
0.2	N4
0.4	N5
0.8	N6
1.6	N7
3.2	N8
6.3	N9
12.5	N10
25.0	N11

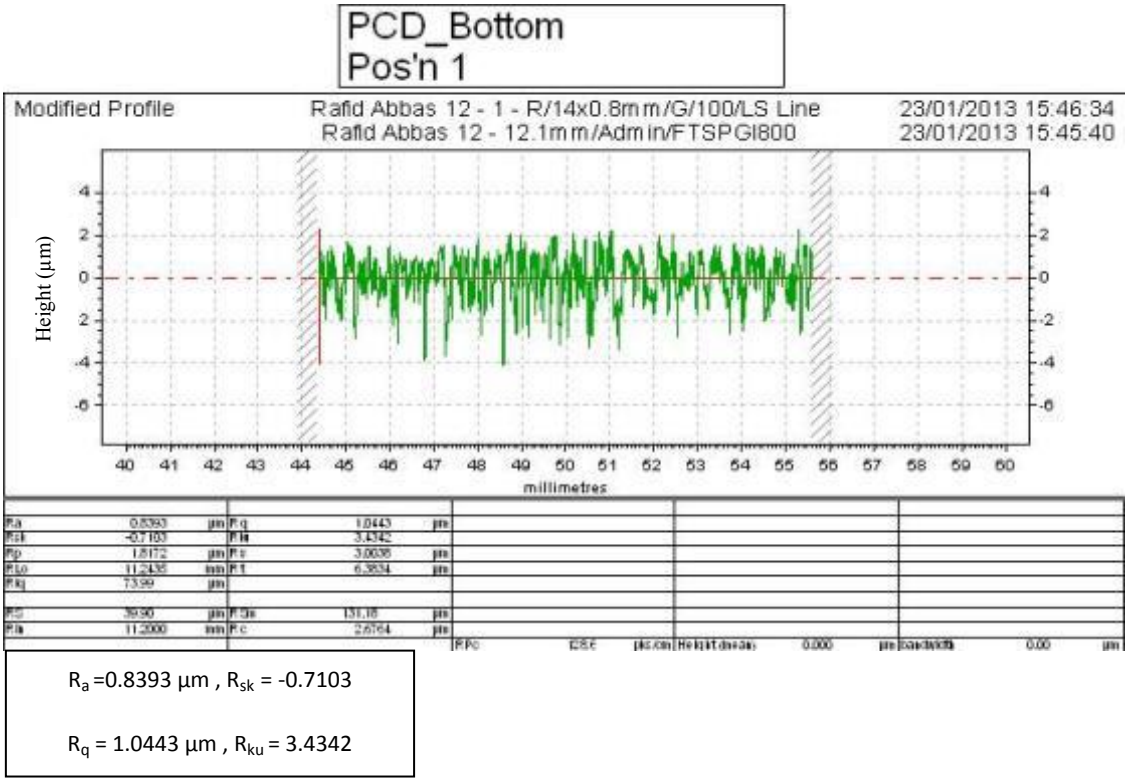

Figure 4.5 Surface profile measurement of the substrate layer for the PDC insert at position 1 before polishing

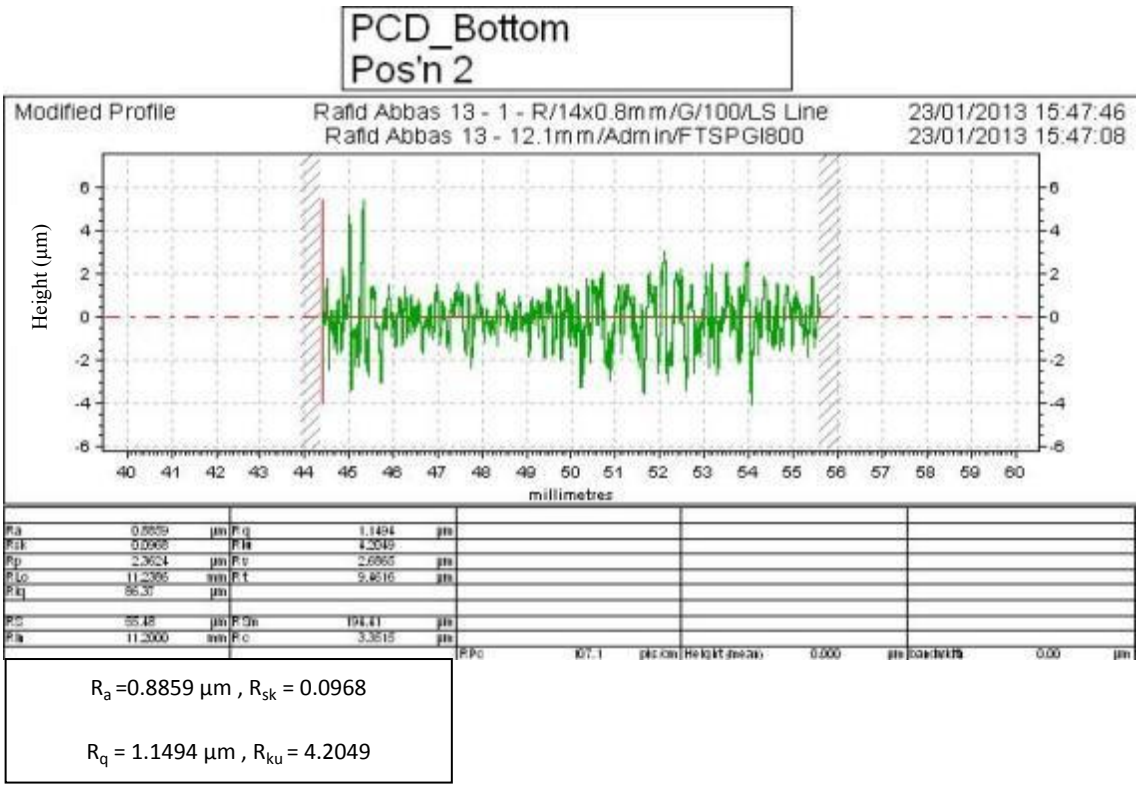

Figure 4.6 Surface profile measurement of the tungsten-carbide layer for the PDC insert at position 2 before polishing

The same test is carried out for all samples for both layers (substrate and diamond) in order to measure the surface roughness of the layers forming the PDC cutters. The results are compared later in Table 4.3. The skewness results showed that the values are so close in different positions of the PDC layer, while it is varied for tungsten carbide layer, where high skewness values available at some points referring to flat surfaces with peaks, while low values found at other parts which it could be a surface having pits. Furthermore, the results showed the need for the polishing operation to reduce the degree of surface asperity especially on the diamond layer.

4.1.2 Polishing process

The aim of the polishing process is to prepare final polished samples to reduce the surface roughness and makes the specimens ready for further tests and analysis. It is important to obtain a flat surface and remove any sectioning deformation to avoid any misleading results might be occurred.

According to the results of the surface roughness parameters for both surfaces of the PDC samples, it is crucially important to polish the surfaces of both layers to reduce the effect of surface asperities and consequently reducing the error with the measurements of hardness, Young's modulus and fracture toughness when using indentation tests.

Furthermore, well-polished surfaces will produce clear imprints that make it easier to measure the diagonals of the obtained indents, especially within micro-indentation testing. The polishing process of the samples in this study was following the ASM international standards (ASM, 2002).

The polishing procedure starts with polishing both sides of the samples with abrasive (silicon-carbide) paper which is widely used for ceramics. The used abrasive papers have various grades from 240 up to 1200. The equipment used for this polishing operation was "Metaserv 250 Grinder-Polisher", manufactured by BUEHLER. Two different grade circular silicon carbide abrasive papers are mounted on the two platens available for the device. Coarse abrasive papers (240) that have grit 52 micron size are used firstly, and then gradually switch to the finest available abrasive paper (1200) that has grit size of 8 microns. The platens are rotated at with moderate speed between 50 to 150 rpm. The sample is mounted manually to the rotated discs for 10 minutes at least. Special care should be taken into consideration when lowering the sample towards the platen. During each polishing process with abrasive papers, water is sprayed underneath the abrasive papers (Figure 4.7). Water taps must be opened while the polishing process is in progress to cool down the friction heat produced (lubrication) as well as to remove any dust might be obtained during the polishing process. Later, each specimen is rubbed with a clean cotton cloth soaked in soapy and warm water to remove the remained dust produced when polishing. Finally, the samples are scrubbed manually with diamond paste provided in a syringe using a clean cloth. The selection of the cloth is significant to get optimum results as it depends mainly on the materials forming the sample. As our samples are made of WC-Co (ceramic) and polycrystalline diamond, therefore, woven cloth is useful for rough polishing of metals with alumina or diamond.

Figure 4.7 shows the Metaserv 250 Grinder-Polisher and Figure 4.8 illustrates the diamond paste used for finishing the polishing process.

Figure 4.7 Metaserv 250 Grinder-Polisher on the left and the circular silicon carbide polishing papers used with the polishing machine on the left.

Figure 4.8 Diamond compound paste for finishing

4.1.3 Surface roughness test (after polishing)

Surface profile measurements were carried out for all samples of the PDC cutters after polishing to observe the degree of the asperities on the samples surfaces. The same surface roughness parameters that were measured previously are measured again after polishing at two positions for the substrate and at one position for the diamond layer ,because the roughness parameters are varied slightly at different positions for the diamond layer. Figure 4.9 illustrates the surface profile measurement for the diamond layer of the M1313 sample at position 1, while Figure 4.10 demonstrates the same measurement for the substrate layer of the same sample at position 1.

The roughness for the diamond layer (R_a) after polishing was 1.138 µm (1.423 µm before polishing) and the skewness (R_{sk}) was -0.1682 after polishing and these values indicate that the surface roughness parameters were reduced after polishing. The roughness (R_a) for the tungsten carbide layer after polishing was 0.3845 µm, while the surface skweness value at position 1 was 0.0796. (R_a) of the substrate layer of sample M1313 was 0.962 µm before polishing, while the same parameter (R_a) was equal to 0.427 µm. For the same sample, (R_a) of the diamond layer before polishing was 1.708 µm, but after polishing (R_a) was reduced to 1.3668 µm. The obtained surface roughness parameters showed clearly the reduction of the degree of the surface roughness parameters for both layers of all PDC samples and accordingly, the measurements of the mechanical properties (section 4.2) of the diamond layer and the substrate could be carried after polishing.

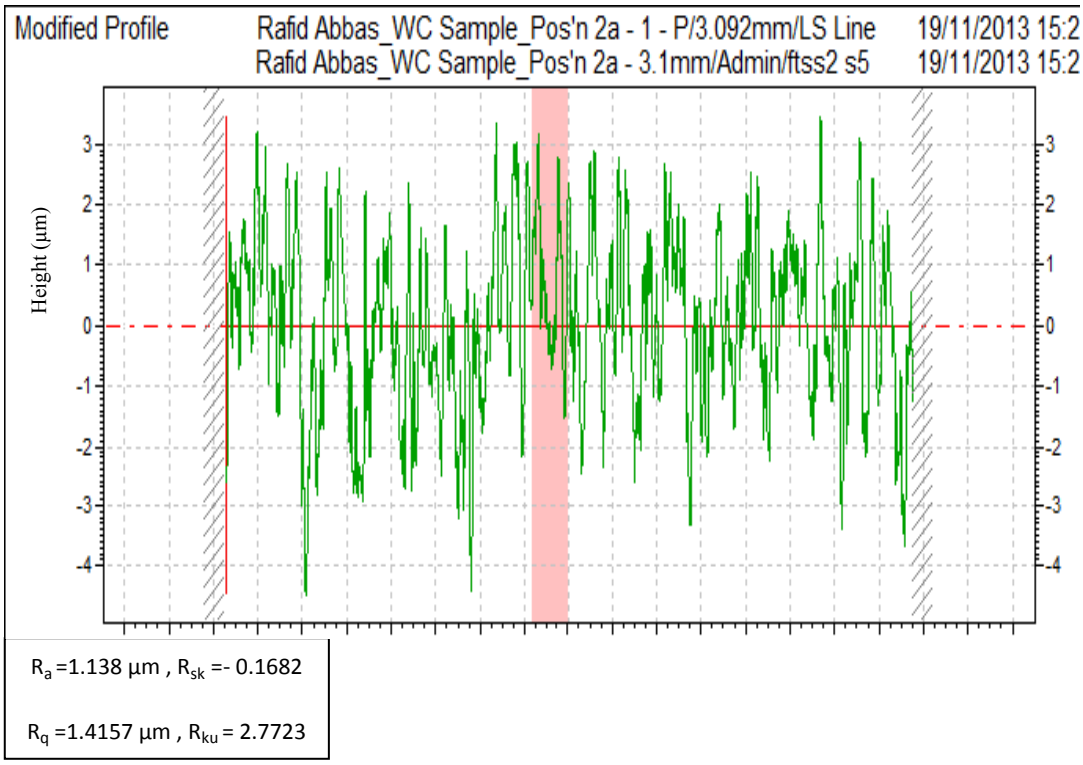

Figure 4.9 Two Dimensional Surface profile measurement of the diamond layer for the PDC cutter after polishing

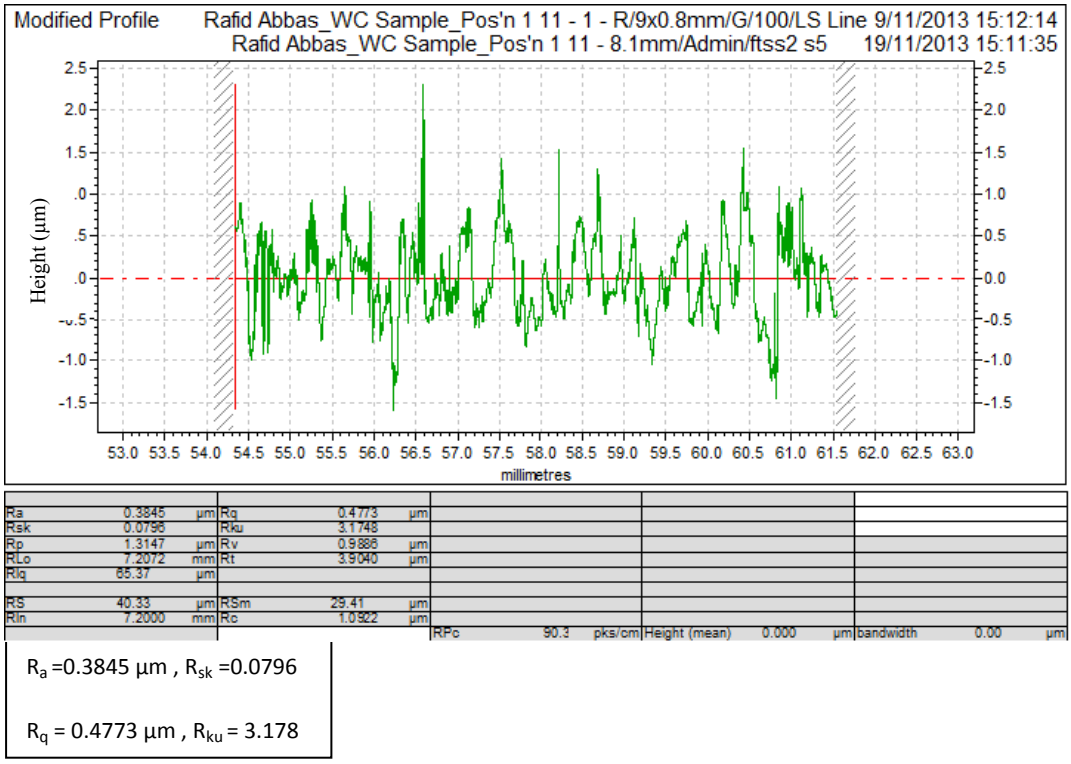

Figure 4.10 Two Dimensional Talysurf graph of the substrate layer at position 1after polishing

Table 4.3 illustrates the surface roughness parameters before and after polishing the two layers of the PDC cutters of different types.

Table 4.3 Surface roughness parameters for various PDC inserts

PDC Cutter	Layer	Average Surface Roughness (R_a), µm (before polishing)	Average Surface Roughness (Ra), µm (after polishing)	Average Root Mean Square Surface Roughness (R_a), µm (before polishing)	Average Root Mean Square Surface Roughness (Rq), µm (after polishing)	Average Surface Skweness (R_{sk}) (before polishing)	Average Surface Skweness (R_{sk}) (after polishing)
M1313	Substrate	0.8626	0.3845	0.962	0.427	-0.30675	0.0796
M1313	Diamond	1.42325	1.138	1.708	1.3668	-0.48545	-0.1682
K1908	Substrate	0.8991	0.4842	1.006	0.542	-0.4671	0.06612
K1908	Diamond	1.6144	1.3031	1.853	1.452	-0.3553	-0.2301

The surface roughness affects the estimated mechanical properties obtained from Nano-indentation tests. Bobji and Biswas (1998) stated that "It has been found that at low indentation depths, the hardness is varied from the bulk hardness and the scattering in the nano-indentation results is high. This difference in the obtained hardness at low penetration depths mainly attributed to the surface roughness of the sample being tested. Bobji and Biswas (1998) added that, the influence of surface roughness on nano-indentation hardness is negligible if the penetration depths are higher than the surface roughness.

Polishing is mainly needed to reduce the influence of surface roughness on the estimated hardness from nano-indentation.

As the indenter is loaded near the surface that has asperities, the contact is first done with a single asperity exists on the rough surface. When the increasing the load, this asperity is deformed plastically and then the adjacent asperities come into contact. During this process, the contact area established on the surface of the sample is varied and accordingly, the hardness would be varied as well.

The surface roughness has crucial effect on the estimated results of nano-indentation hardness as the contact between the indenter and the surface of the sample is not only controlled by the material mechanical properties, but the topography of the sample is significant. When the nano-probe is indenting the surface of the specimen, the deformation (penetration) depth would be greater at low degree of surface roughness

resulting lower hardness. On the contrary, if the indenter comes into contact with a high degree of surface roughness, the contact area is underestimated and accordingly, the estimated hardness would be overestimated (CSM, 2007). Therefore, it is significant to determine the degree of the surface roughness of the samples of a surface before launching with indentation testing. The surface roughness parameter (R_a) value should be lower than 5% of the maximum indentation depth as stipulated in the International Standard ISO 14577-4 (CSM,2007).

4.2 Indentation testing

4.2.1 Nano-indentation test

The apparatus used for this purpose is a NanoTest nano-indenter, provided by Micro Materials Ltd. Wrexham UK available at the University of Leeds. The instrument is highly sensitive towards temperature and sample vibration. The chamber of the instrument has a thermostatically controlled heater, and the chamber is usually kept 2-3 degrees hotter than the room temperature. Figure 4.11 shows an image of the NanoTest equipment.

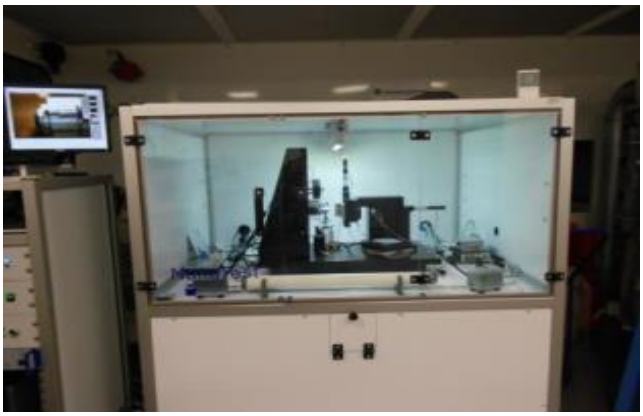

Figure 4.11 NanoTest equipment by Micro Materials Ltd. UK

The experimental work will be focused firstly on measuring the nanoindentation hardness and Young's modulus of the samples as the main reason for that is, within nanoindetation tests, there is no need for machine compliance correction as well as that the hardness and Young's modulus is calculated easily after plotting the force versus penetration, while within microindentation tests, the hardness could not be determined unless a clear image of the imprint is obtained using scanning electron microscopy beside that Young's modulus is affected by machine compliance and it has to corrected for this influence.

The NanoTest measures the movement of a diamond indenter in contact with the surface of the sample. The type of the nano-indenter used in the nano-indentation test is Berkovich that has three sided pyramid with a face angle of 65 °. In order to make a measurement, an increasing load is applied and the probe indents the surface, as shown schematically in Figure 4.12 below:

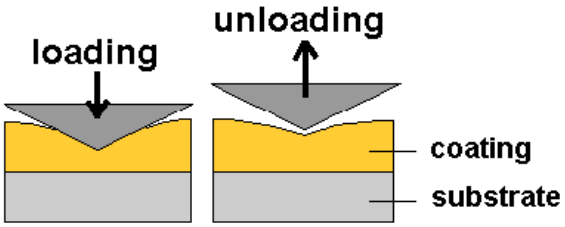

Figure 4.12 Schematic diagram of the indentation action (Beake *et al.*, 2003)

The elastic and plastic properties of the specimen determine the shape of the unloading curve during the indentation process. Before starting the test it is crucially important to calibrate the apparatus precisely otherwise the obtained readings will be imprecise. Cleaning the samples from dust is necessary to avoid any misleading results. Choosing the appropriate indentation conditions like minimum and maximum loads, loading rate, number of indentations cycles, displacement between indentations points, thermal drift effect and many other factors should be taken into account when performing any nanoindentation test. In the present study, fixed and variable loads from 100 mN up to 500 mN for the substrate layer and range of loads from 50 mN up to 350 mN are applied to obtain the load-displacement graphs of the two layers of the PDC samples to monitor the effect of load increment on the obtained indentation depth that affects the hardness and Young's modulus. Numbers of cycles were chosen to be three at each load selection. Load rate was chosen to be 20 mN/sec. The displacement between indentations points was selected to be 20 microns.

The main output results of the nano-indentation testing for this study are hardness and reduced modulus. The software (Platform 3) which was used for running the nano-test is functionalised to determine the applied load and the resulted penetration. The depth resolution provided for the NanoTest is 0.001nm and maximum load up to 500 mN.

The hardness is then calculated from:

$$H = \frac{P_{max.}}{A} \qquad (4-1)$$

where $P_{max.}$ is defined as the maximum applied load (mN) , A is the projected indentation area (nm^2) and H is the hardness (mN/nm^2) and then converted to GPa. The

projected area is determined by the depth of impression (h_p) and the known angle of the indenter as shown in Equation (4-1a):

$$A = 3\sqrt{3}\, h_p^2 \tan^2(65) \qquad (4-1a)$$

Reduced modulus (E_r) is the modulus that incorporate the combined moduli of the specimen (E_s) and the indenter (E_i)) to account for the deformation of the probe.

The reduced modulus is related to the stiffness. The stiffness (S) is defined as the ability of the material to resist elastic or non-permanent deformation. Stiffness is determined from the slope of the unloading curve of the indentation plot. Reduced modulus is determined from the following equation (Oliver and Pharr 1992):

$$E_r = \frac{\sqrt{\pi}}{2}\frac{S}{\sqrt{A}} \qquad (4-2)$$

where S is the stiffness of the material (mN/nm) and A is the indented area (nm^2).

Young's modulus of the sample (E_s) is finally calculated from the following equation (Oliver and Pharr 1992):

$$\frac{1}{E_r} = \left(\frac{1-\nu^2}{E}\right)_s + \left(\frac{1-\nu^2}{E}\right)_i \qquad (4-3)$$

where E_r is the reduced modulus (mn/nm^2) and converted to GPa , E is the Young's modulus (mN/nm^2) and converted to GPa, ν is the Poisson's ratio (dimensionless) , s is referring to the sample and i is referring to the indenter. The Poisson's ratio of the indenter is 0.07, whereas for the sample is 0.07 (diamond layer) and 0.22 (tungsten-carbide) (Chen, *et al*., 2010).Young's modulus for the indenter is 1141 GPa.

Figure 4.13 represents a typical schematic relationship of load-displacement curve in nano-indentation.

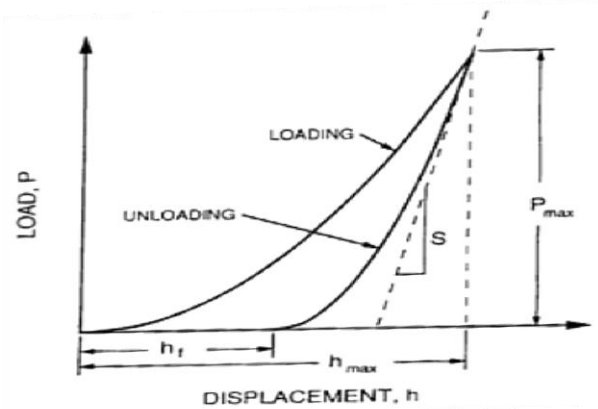

Figure 4.13 Schematic relationship of the relationship between the applied load and the displacement (Oliver and Pharr, 1992)

It is worth mentioning that, the determination of hardness and Young's modulus is crucially important to quantify the wear of the samples being studied as most wear models require these mechanical properties for wear quantification. In addition, fracture toughness cannot be calculated within some models without the determination of hardness and Young's modulus.

4.2.1.1 Nanoindentation of tungsten carbide – cobalt layer (WC-Co)

The nanoindentation test was carried out for M1308 and M1313 PDC specimens. Series of nanoindentation tests were performed on WC-Co alloy with loads in range of 100mN to 500 mN at different cycles were selected to observe the variation of hardness and Young's modulus and when the mechanical properties would be stable as crack (fracture) is initiated. As lower loads were also used, but underestimated values for the mechanical properties were obtained due to the possibility of the effect of the surface roughness. Other settings include fixed indentation loading and unloading speed at 4mN/sec. as the aim was to investigate the effect of the indentation load on the measured mechanical properties. Examples of the nanoindentation graphs for the performed tests are shown in Figures 4.14, 4-.15 and 4.16 where the figures showed regular indentation hardness at 350 mN.

During the nano-indentation test, the elastic-plastic behaviour of the samples and the two main mechanical proprieties of the specimens, i.e. hardness and Young's modulus are analysed. It worth mentioning that the mechanical properties obtained from nano-indentation testing are corrected for the effect of machine compliance, where calibration of the device for machine compliance is performed regularly. Both measured properties will be used later in this chapter to quantify the nano-wear.

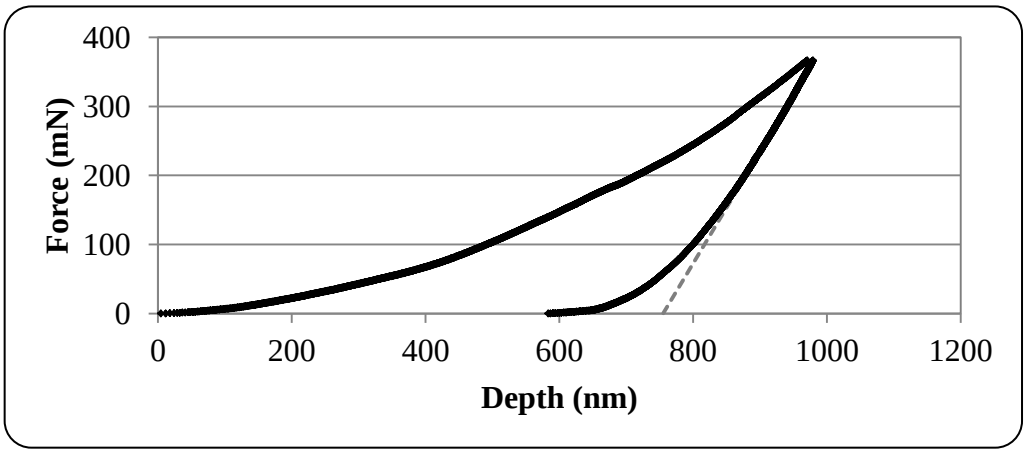

Figure 4.14 Applied force against displacement for tungsten carbide-cobalt (typical graph of test one)

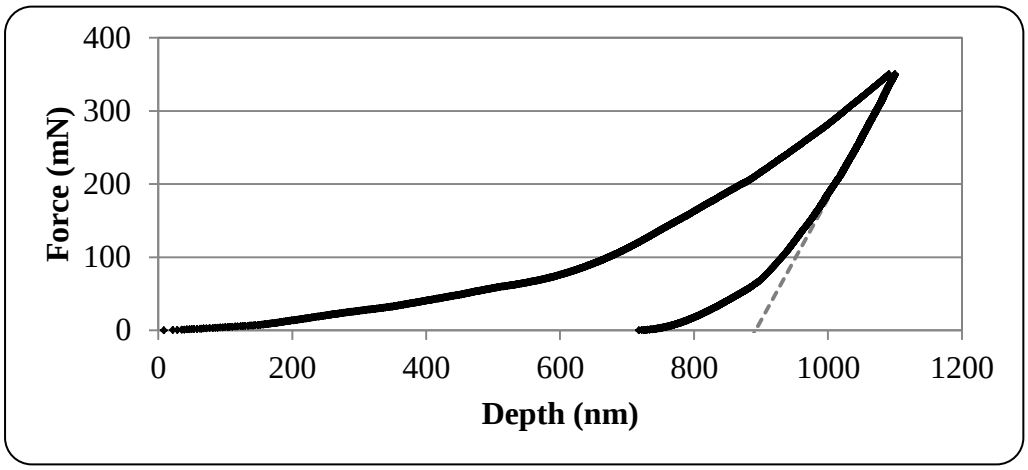

Figure 4.15 Load versus penetration curve for tungsten carbide-cobalt
(typical graph of test two)

The obtained hardness and Young's modulus for three tests are presented in Table 4.4.

It can be seen that the hardness and Young's modulus are fluctuating. The variation of the results might be attributed to the surface roughness.

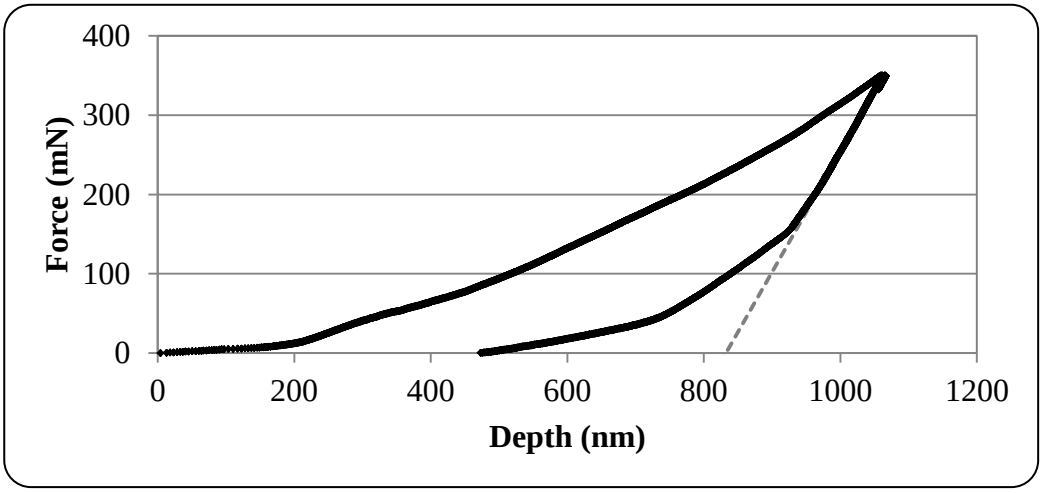

Figure 4.16 Force- displacement curve for tungsten carbide-cobalt
(typical graph of test three)

It is clearly shown from Figures (4.14)- (4.16) that the plastic (indentation) depth of the nano-indentation curves is not exceeding 850 nm and according to the International Standard ISO 14577-4, the surface roughness parameter (R_a) value should be lower than 5% of the maximum indentation depth. Hence, (R_a) should be less than 42.5 nm, but the results obtained from Table (4.3) showed that (R_a) is between (0.385-0.482) µm, therefore, the polishing process did not achieve the International Standard stipulated by ISO 14577-4. This might be the reason why the results of the nano-indentation hardness and Young's modulus are varied.

Table 4.4 Measured nanoindentation hardness and Young's modulus for tungsten carbide-cobalt (substrate layer) of the PDC cutters

Test number	Nanoindentation hardness (GPa)	Young's modulus (GPa)
1 (100-350mN)	20.25	663.40
	19.92	599.87
	3.48	198.49
	17.94	448.66
	20.6	432.35
2 (350mN)	24.72	809.29
	17.84	513.79
	5.18	257.44
	17.13	383.73
	22.33	676.09
3 (100-500mN)	20	484.80
	20.88	478.50
	18.21	553.03
	5.2	332.06
Average	16.69 ± 6.59	487.96 ± 161.18

Figure 4.17 and 4.18 shows the results of hardness and Young's modulus as a function of applied load for the WC-Co layer. WC composite represents the hard phase of the WC-Co and the hardness of the WC itself is much higher than the binder phase of the alloy (cobalt). The reported values of hardness for the binderless WC ranged from 23 to 29 GPa and the reported values of Young's modulus ranged from 705 to 795 GPa (Ndlovu 2009), whereas the reported hardness values of the binder (Cobalt) were between 2.7 and 4.8 GPa and the reported values of Young's modulus were from 117 to 155 GPa (Ndlovu 2009). This could be a reason why hardness values are significantly lower for some applied loads than the others as the indenter may have penetrated to the binder phase (Co) of the composite material of WC-Co. This hypothesis should be further investigated by the Scanning Electron Microscopy (SEM)

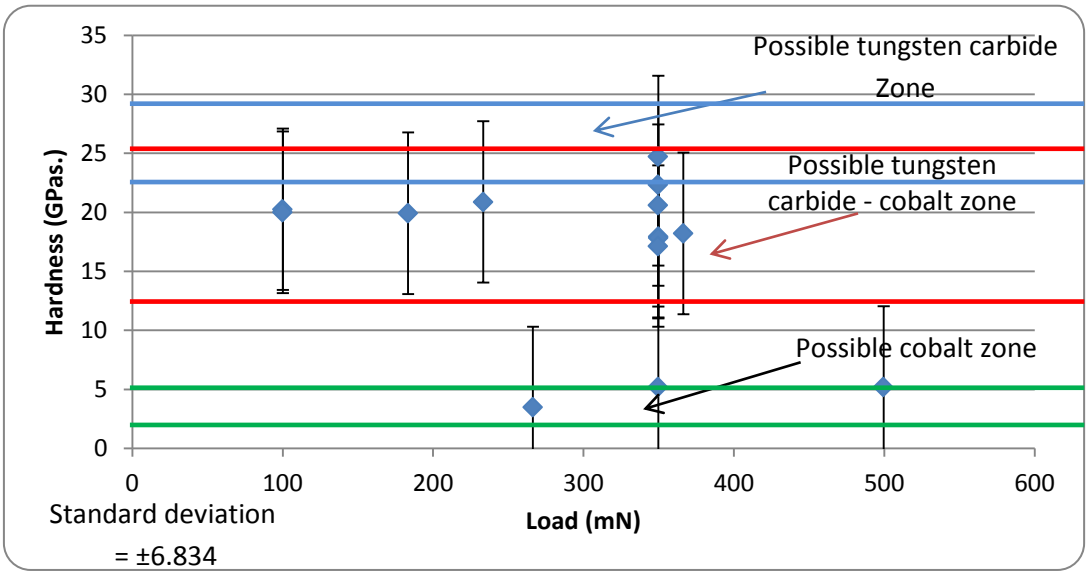

Figure 4.17 Obtained nanoindentation hardness versus applied loads for the tungsten carbide-cobalt layer along with the reported literature values

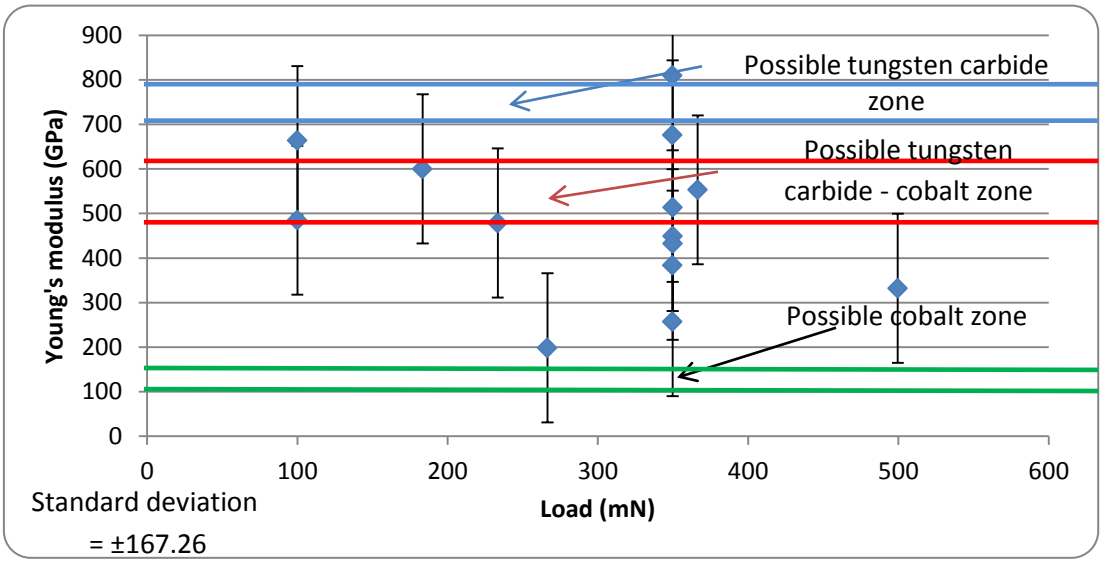

Figure 4.18 Young's modulus results against applied force for the tungsten carbide-cobalt substrate within the reported previous values

In the work of Ndlovu *et al.*(2007), the hardness of tungsten carbide-cobalt reported by values within the range (12.7 – 25.5) GPa and (476-623) GPa for the Young's modulus depending on the WC grain size and the percentage of the cobalt binder which ranged 6% -15%. The obtained experimental results have shown similar results with those of WC with 6% cobalt as a binder. The measured Young's modulus values were plotted versus the obtained nanoindentation hardness in Figure 4.19. The plot illustrates that Young's modulus values are proportional to the hardness and that agrees with the previous study of Vaprek and Argon (2001) where for a large number of diverse super hard nanocomposites a linear increase of the Young's modulus with noindentation hardness was reported.

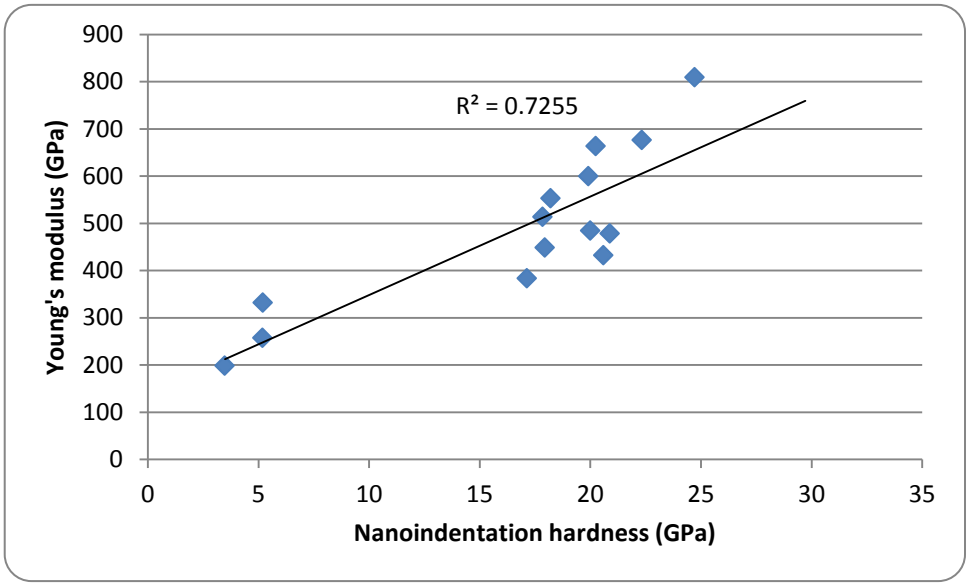

Figure 4.19 Measured Young's modulus vs. hardness for the substrate

4.1.1.2 Nanoindentation of diamond table layer

In general, the top part of the oil PDC cutters represents the diamond layer in form of polycrystalline compact diamond (PDC) with cobalt as a binder, while the lowest layer consists of tungsten carbide - cobalt. Scanning electron micrograph is done for the top layer of the specimens to get a better understanding of the topography of this layer. SEM figures are shown in the next section. As the surface structure of the PDC top layer is dominant by diamond crystals, the main challenge is to indent this layer with a diamond probe without breaking it. Although, the natural diamond which represents the tip of the indenter is harder than the artificial diamond, many researches mentioned their failure to measure the hardness due to the breakage of the indenter and especially the Berkovich type (Sumiya *et al.*, 1997 and Sumiya and Irifune 2004). Berkovich probe was used recently in nanoindetation of nanocrystalline diamond, but with strict limitations of very low load i.e. 3 mN with thermal drift corrections (Couvy *et al.*, 2011). The nano-indentation testing carried out in this study followed The International Organisation for Standardisation ISO-14577 (2015) and ASTM E2546 (2015) which can be applied on nano and micro instrumented indentation testing. The nano-indentation test is controlled by load. A series of nanoindentation tests were performed using fixed loading and unloading rate of 4mN/sec. with indentation loads varied in the range of 50 mN to 350 mN as low loads were also performed, but failed to obtain reliable results. After the tests the indenter was checked for possible damage by carrying out tests against a reference sample. Figures (4.20 – 4.23) represent the typical load-displacement curves for the PDC-Co. layer. The nanoindentation graphs of the diamond layer illustrate a high degree of elastic recovery or elastic relaxation which means that

the ratio of the Young's modulus to the hardness is low due to indenting diamond particles (Sumiya and Irifune 2004).

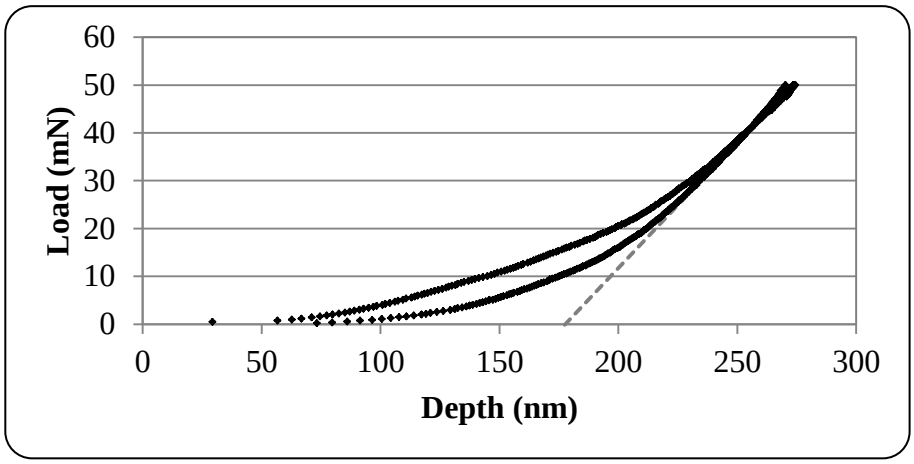

Figure 4.20 Load versus the indentation depth for the PDC-Co layer in test 1 at fixed load of 50 mN

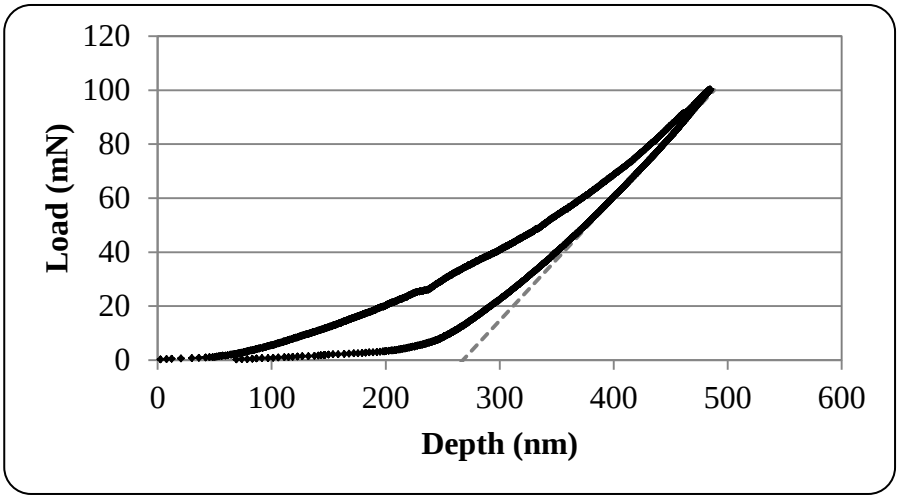

Figure 4.21 Displacement – load graph of the diamond layer in test 2 at fixed load of 100 mN

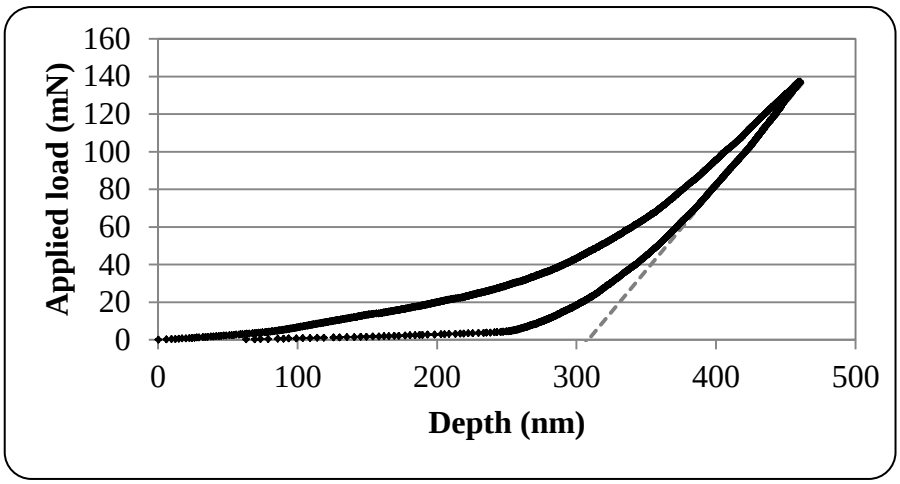

Figure 4.22 Typical graph of test 3 for the diamond table in PDC samples at loads 100-200 mN

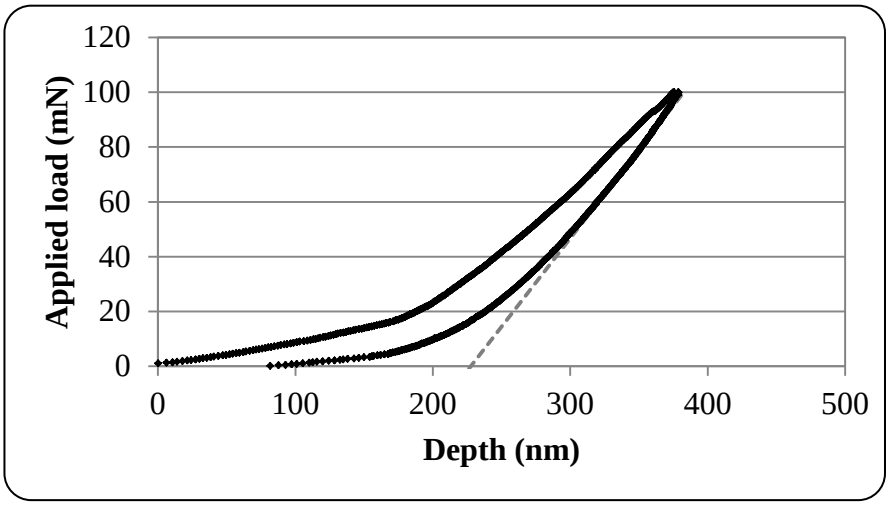

Figure 4.23 Load – penetration curve for the diamond layer
at loads 100-350 mN in test 4

The obtained values of hardness and Young's modulus for four tests were tabulated in Table 4.5.

Table 4.5 Final results of the nanoindentation tests of the PDC-Co layer of the samples

Test number	Nanoindentation hardness (GPa)	Young's modulus (GPa)
1 (50mN)	37.98	718.06
	57.99	889.17
	59.66	969.17
2 (100mN)	56.96	810.98
	13.35	462.7
3 (100-200mN)	78.69	974.05
	56.74	860.4
	58.83	936.08
	97.57	1136.55
	25.31	656.85
4 (100-350mN)	23.23	604.34
	26	671.96
Average	49.36 ± 23.80	807.53 ± 181.98

From Figures (4.20)- (4.23), the penetration depth of the nano-indentation curves is not more than 320 nm, while the value of the surface roughness parameter (R_a) for the diamond layer from Table (4.3) is between 1.423 and 1.6144 µm. According to ISO 14577-4, (R_a) should be less than 16 nm, which means that the required condition of ISO for polishing is not satisfied in the current case. Therefore, the variation of the obtained results from nano-indentation might be attributed to the high degree of surface roughness.

Figures 4.24 and 4.25 show the nanoindentation results as a function of applied load for the PDC layer of the samples.

The previous reported upper limit and lower limit values of the hardness for natural diamond are represented by the two blue lines in Figures 4.24 and 4.25, while the red lines refer to the limiting hardness values of polycrystalline diamond compact with binder (cobalt) and the green lines refer to the reported hardness limit values for the binder (cobalt). It seems from Figures 4.24 and 4.25 that all of the obtained results lie above the reported cobalt limits which might indicate that all of the indented points were not pure binder phase (cobalt).

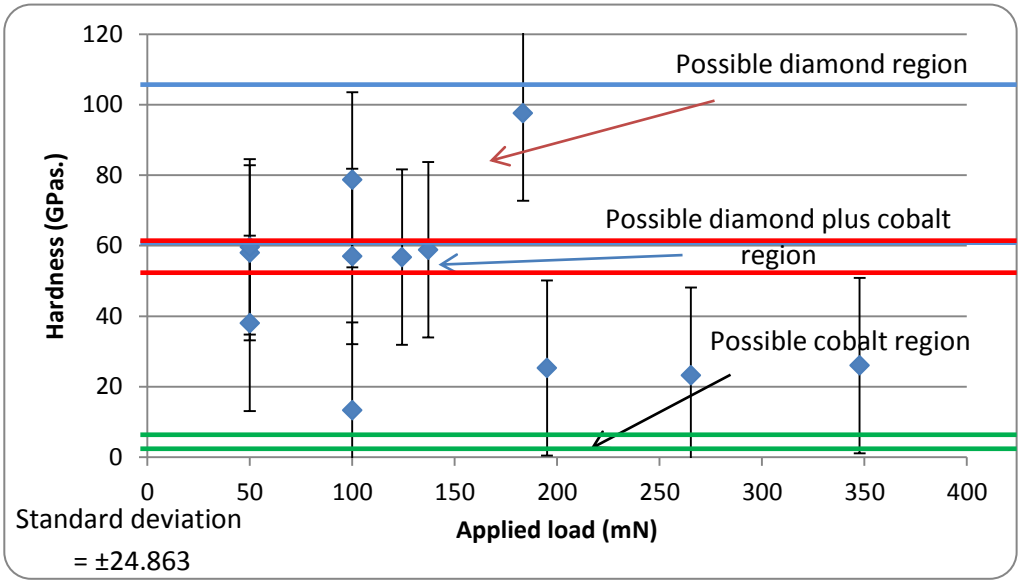

Figure 4.24 Indentation hardness for various zones in PDC layer within the reported previous values obtained from Dubrovinskaia 2006 , Ndlovu 2009 and Osipov 2010

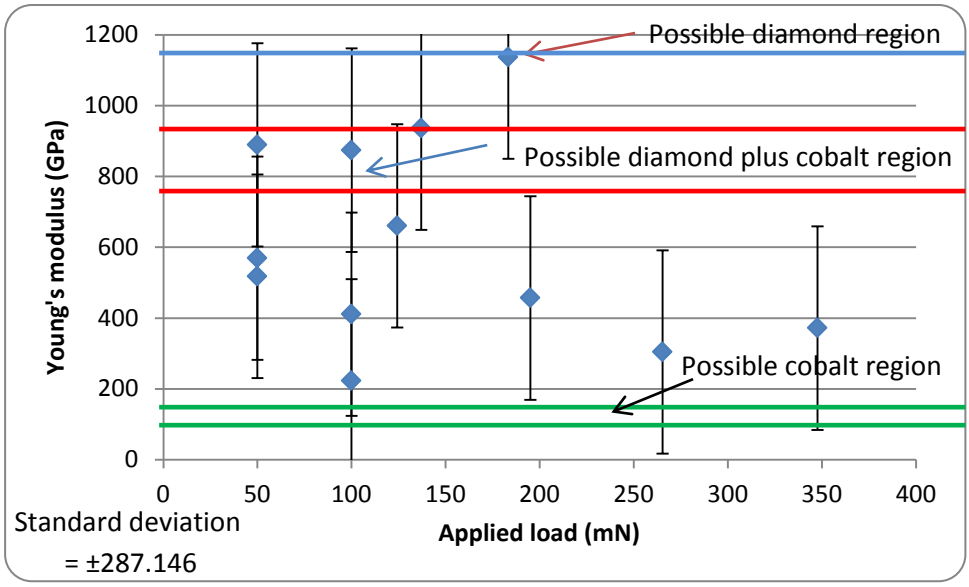

Figure 4.25 Young's modulus for different zones in PDC layer within the reported previous values obtained from Osipov 2010 and Ndlovu 2009

The previous reported value of the hardness and Young's modulus of polycrystalline diamond compact was within the range 50-60 GPa and 776-925 GPa, respectively, depending on the diamond grain size and the percentage of the cobalt binder which varied from 5% to 20% (Dubrovinskaia 2006), (Osipov 2010) and Ndlovu (2009).

Young's modulus values were plotted versus the hardness (Figure 4.26) and their relationship agrees with the previous study of Vaprek and Argon (2001).

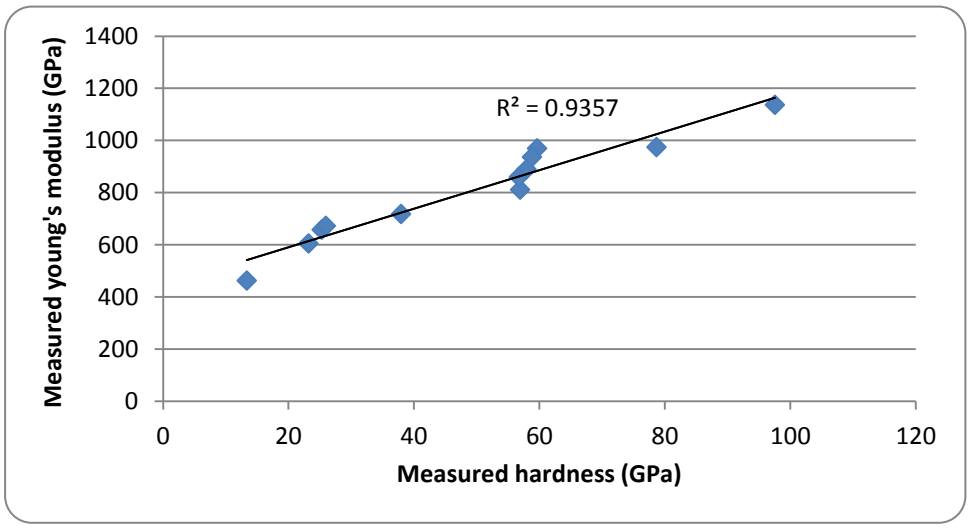

Figure 4.26 Measured Young's modulus vs. hardness for the PDC layer

After achieving the nanoindentation tests of the diamond layer, it is crucially important to verify the status of the Berkovich probe. In order to assess the status of the indenter, nanoindentation checking test was carried out using ceramic sample before and after the indentation process of the diamond layer. Table 4.6 illustrates the results before and

after diamond layer indentation. It was observed that the hardness and Young's modulus of ceramic before and after is nearly the same and this indicates that the tip of the indenter is intact and not deformed.

Table 4.6 Results of the nano-indentation of ceramic before and after testing PDC-Co layer for the purpose of checking the status of the indenter

Test number	Nanoindentation hardness (GPa)	Young's modulus (GPa)
Before nano-indentation of PDC layer	21.83	281.43
After nano-indentation of PDC layer	20.99	296.28
Average	21.41 ± 0.42	288.86 ± 7.42
Coefficient of variation (%)	1.96	2.57

4.2.2 Analytical study of the samples after nano-indentation test

The purpose of performing the microscopic study is to examine the imprints obtained from the nano-indentation test.

It is crucially essential to understand the detected types of signals by the samples and how these signals could be employed to investigate the structure of various materials, topology morphology and the composition. Krumeich (2011) described various types of spectroscopies and imagining techniques which are considered nowadays indispensable methods for sample characterisation. Krumeich (2011) classified the electron microscopy methods depending on the various kinds of electron scattering. Figure 4.27 shows different types of detectable signals:

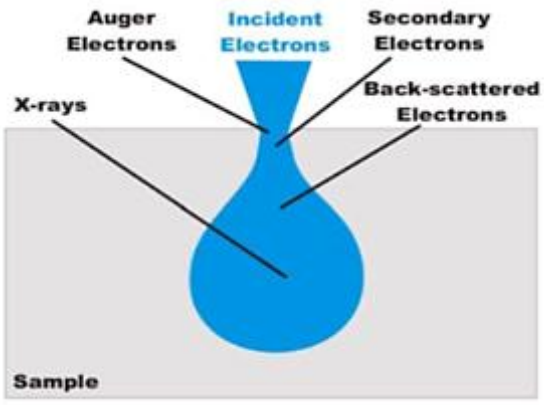

Figure 4.27 Modes of signals interaction in a sample (Krumeich, 2011)

1. **Scanning electron micrograph (SEM):** SEM scans the specimen with a high energy beam of electrons that interact with the surface of the sample generating signals consisting of information about the topography of the specimen's surface and composition. SEM has more than one kind of detectors that are capable for detecting various signals like secondary electrons (SE), backscattered electrons (BSE) and energy dispersive X-ray spectroscopy (EDS or also called EDX).
2. **Back Scattered Electrons (BSE)**: result from elastic interactions between the incident electrons and the target specimen and the electrons interact deeper compared to SEM enables the determination of the microstructure.
3. **Energy Dispersive X-ray (EDX)**: In this technique the electrons interact deeper than the SEM and BSE to the target sample providing maps of the element distribution.

SEM was used to take images for both the diamond layer (top layer) and the tungsten – carbide layer (substrate) to give a better understanding of the mineral distribution of the composite material that forms the PDC cutters. Figure 4.28 illustrates the diamond – substrate interface for the specimen using Secondary Electron Image (SEI).

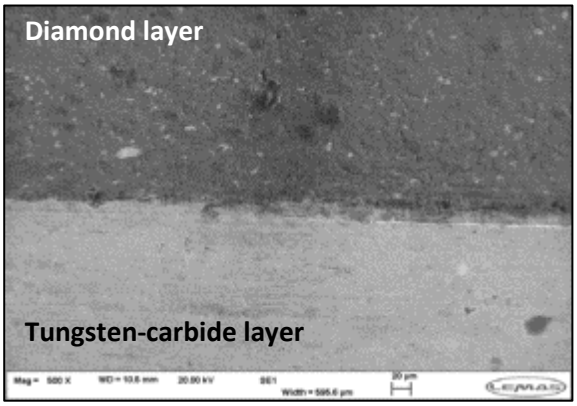

Figure 4.28 Interface section of diamond table and tungsten carbide substrate

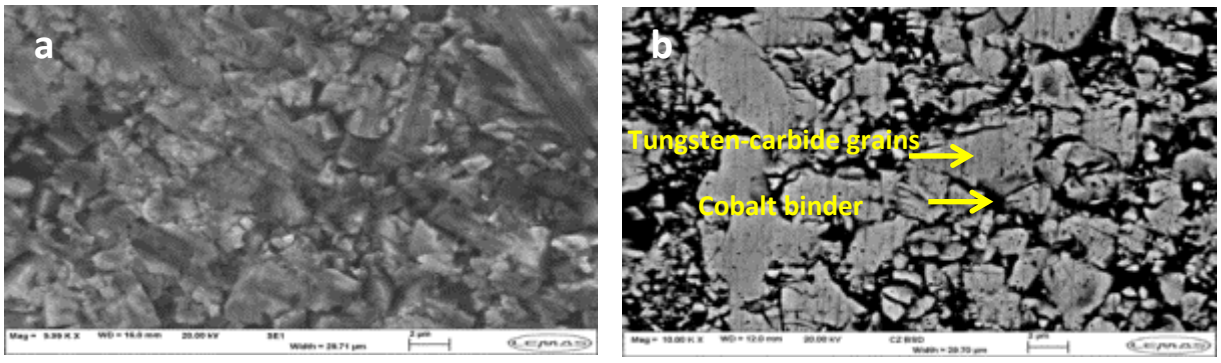

Figure 4.29 SEM micrograph (a) backscattered image (b) for the tungsten carbide-cobalt layer (substrate) of the PDC samples

Figure 4.29 shows a secondary electron image for the tungsten-carbide layer and a backscattered micrograph of the same layer. The BSE image illustrates clearly the tungsten-carbide grains and their size ranged from few nanometres up to 8 µm embedded into the binder (cobalt). Figure 4.30 shows the SEM and BSE images of the diamond table. The arrows point to the diamond grains (black region) and to the cobalt binder (grey region). The BSE image displayed the diamond grains which their size ranged from 4 to 24 microns. Both snapped images of the diamond layer showed high degree of roughness and further SEM technique is needed to display the chemical composition of these layers.

The previous images did not display clearly the main composition of the coating layer (diamond-cobalt) and the substrate (tungsten-carbide-cobalt) of the PDC specimens due to the high surface roughness. BSE was later used to get a better image using the Energy Dispersive X-ray and Spectroscopy (EDX and EDS). Figure 4.31 shows BSE images of the diamond layer where three spectrum points (3, 4 and 7) were selected on the image to examine the composition to identify the hard phase and the binder phase of the PDC layer.

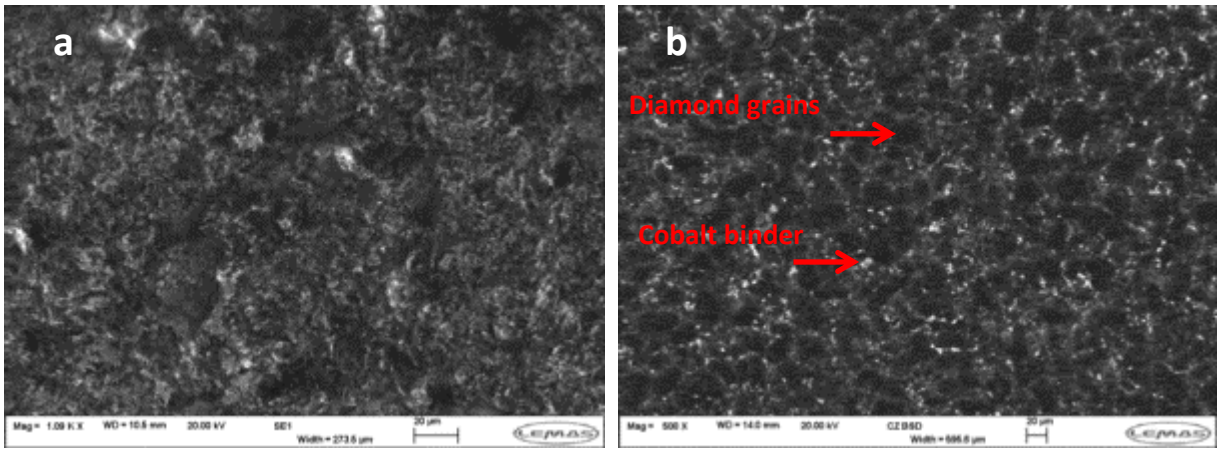

Figure 4.30 SEM image (a) and BSE image (b) for the diamond layer of the PDC cutter

A coloured X-ray map of the same BSE image was produced by EDX as shown in Figure 4.31. The map shows the distribution of diamond grains or carbon (C) and cobalt (Co) with small quantities of other minerals (impurities) such as Iron (Fe) and other minerals. The selected spectrum points were analysed for the composition, Figures 4.32, 4.33 and 4.34 demonstrate the EDS spectra at points 3, 4 and 7 respectively along with the percentage of each element at the selected spots.

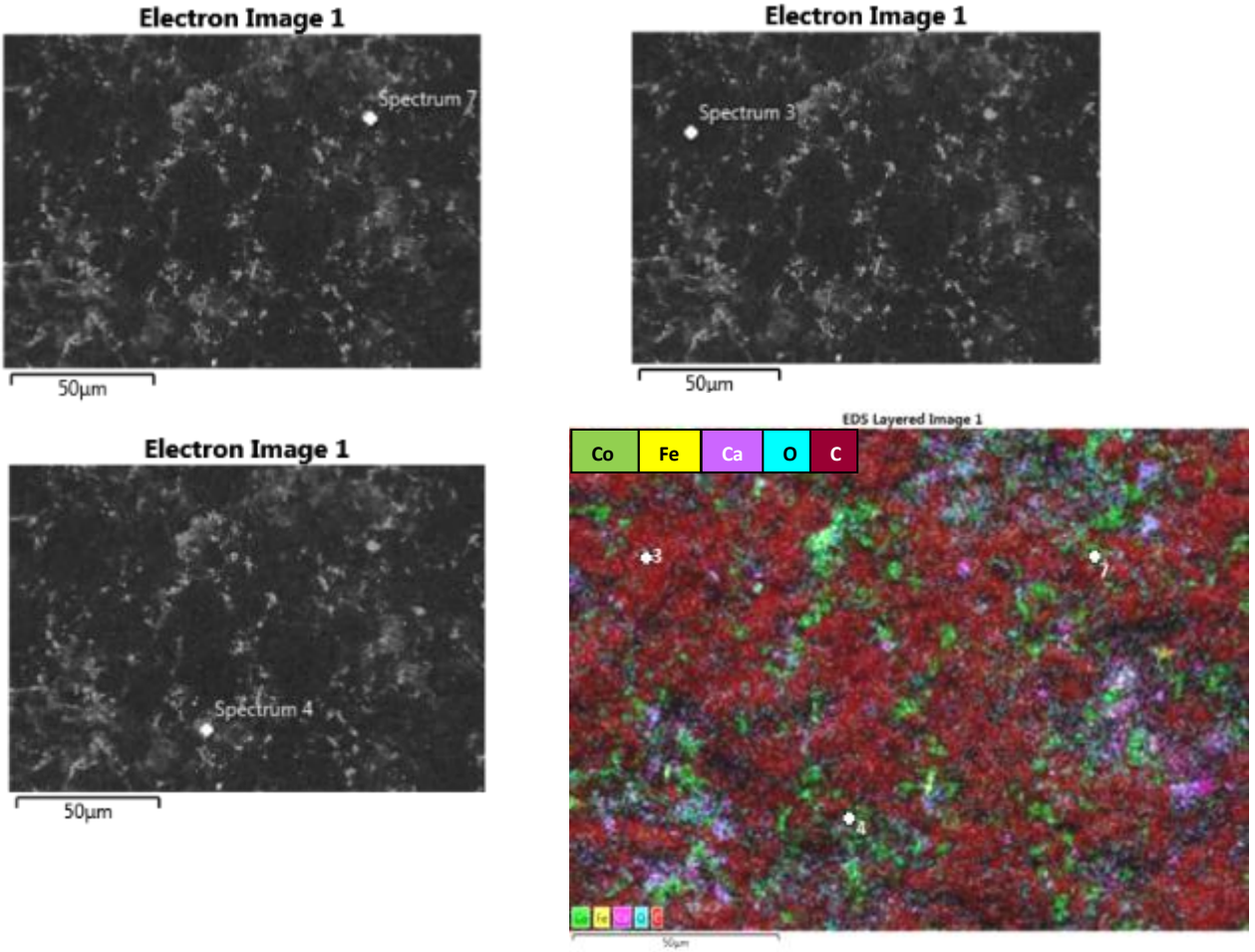

Figure 4.31 Backscaterred micrographs and a coloured X-ray map of the PDC layer displaying three spectrum points

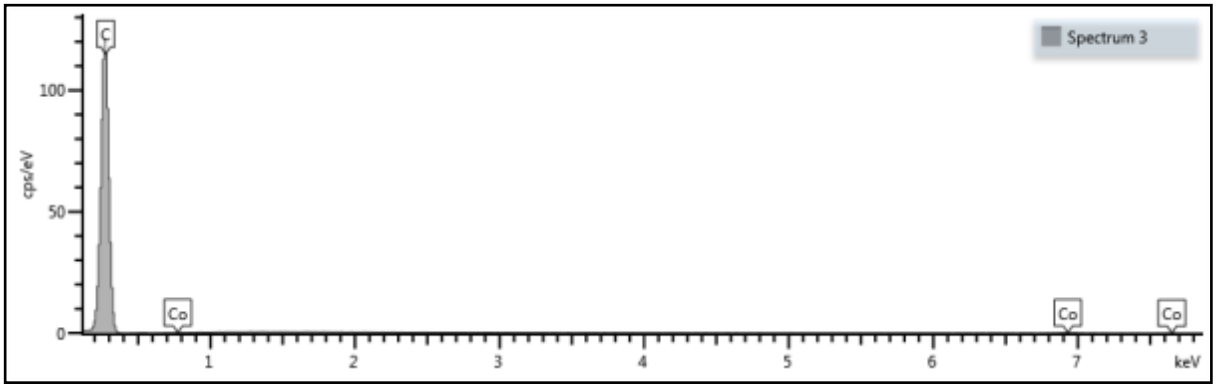

Element	Wt%
C	99.52
Co	0.48
Total:	100.00

Figure 4.32 EDS spectroscopy at point 3 on the diamond layer of the PDC cutter

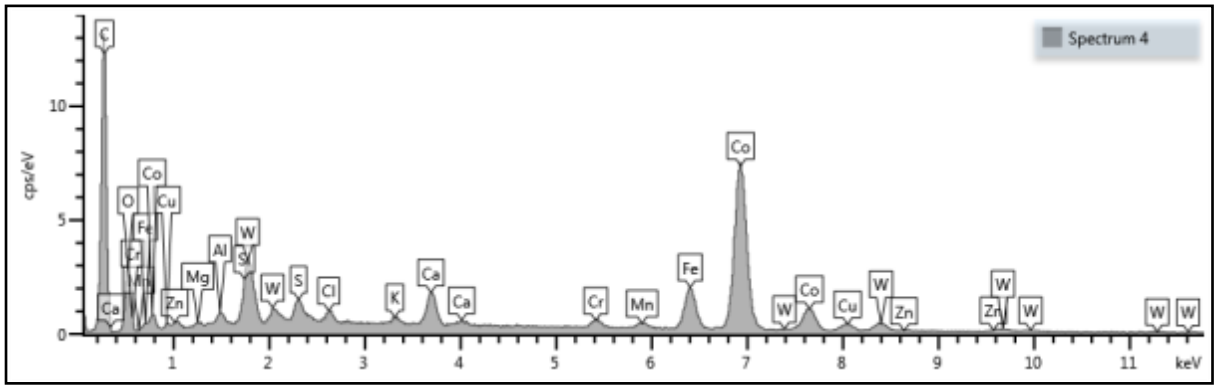

Element	Wt%
C	49.15
O	7.73
Mg	0.19
Al	0.40
Si	0.35
S	0.58
Cl	0.42
K	0.25
Ca	1.49
Cr	0.62
Mn	0.43
Fe	5.25
Co	26.20
Cu	1.61
Zn	0.38
W	4.96
Total:	100.00

Figure 4.33 Spectrum at point 4 on the diamond layer of the PDC insert

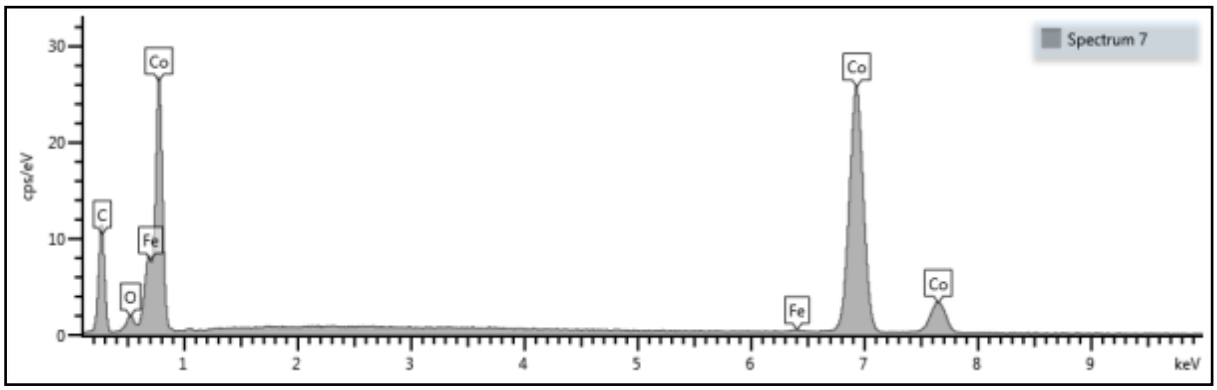

Element	Wt%
C	34.71
O	1.95
Fe	0.35
Co	63.00
Total:	100.00

Figure 4.34 EDS spectroscopy at point 7 on the diamond layer of the PDC specimen

Spectrum 3 illustrates that the main dominant element is carbon (C), with a very small quantity of cobalt (Co). Spectrum 4 demonstrates the diverse composite elements beside the dominant phase (diamond) and the binder phase (cobalt), while spectrum 7 shows the dominant element is cobalt (Co).

From the aforementioned indentation curves it can be inferred that the size of indentation impression is sub-micron, however, as it can be seen from the SEM images, the scale of cobalt rich and diamond rich patches within the sample is larger than indentation impression. Therefore, it is possible that an indentation is completely embedded in the cobalt or diamond patches; hence the obtained properties could indicate the properties of aforementioned materials.

The same scanning work has been done for the tungsten carbide layer to display the composition of that layer. Figure 4.35 represents the backscattered electron images of three chosen points in different positions and the X-ray map of the tungsten- carbide layer (substrate). As expected, the dominant composition is (tungsten carbide) as an alloy, while the cementing material in the substrate is cobalt acting as a binder phase. Other minerals also exists, but with minor amounts. Further X-ray coloured maps and

EDS spectra for the element distribution along the interface of the PDC cutters are shown in Figures B.6 -B.9 in Appendix -B.

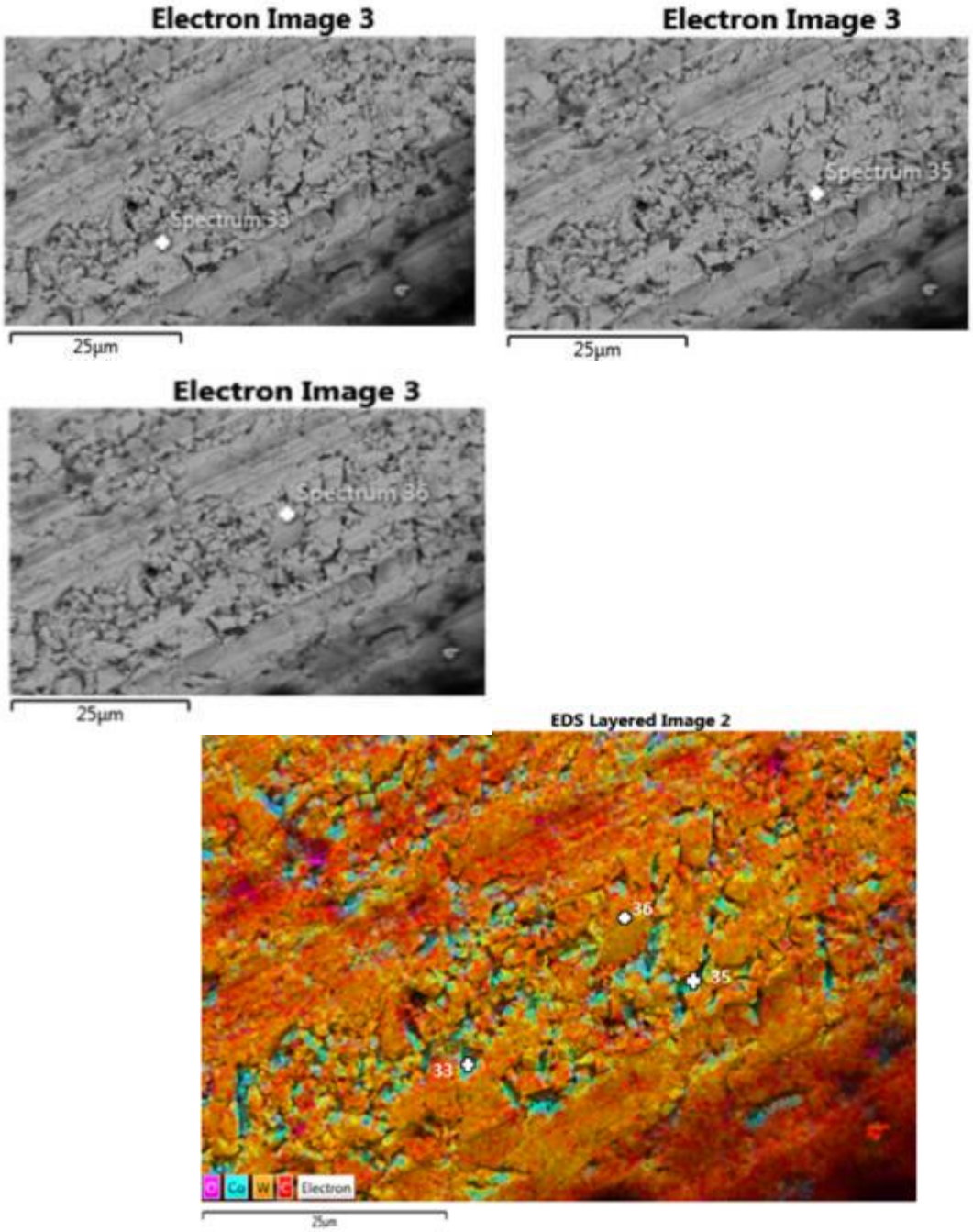

Figure 4.35 Backscattered electron images showing selected spectrum spots with X-ray map of the tungsten carbide layer

EDX spectroscopy reveals the element distribution and their percentage composition of each element that form the substrate of the PDC insert at three selected points 33 , 35 and 36 as shown in Figures 4.36, 4.37 and 4.38 respectively.

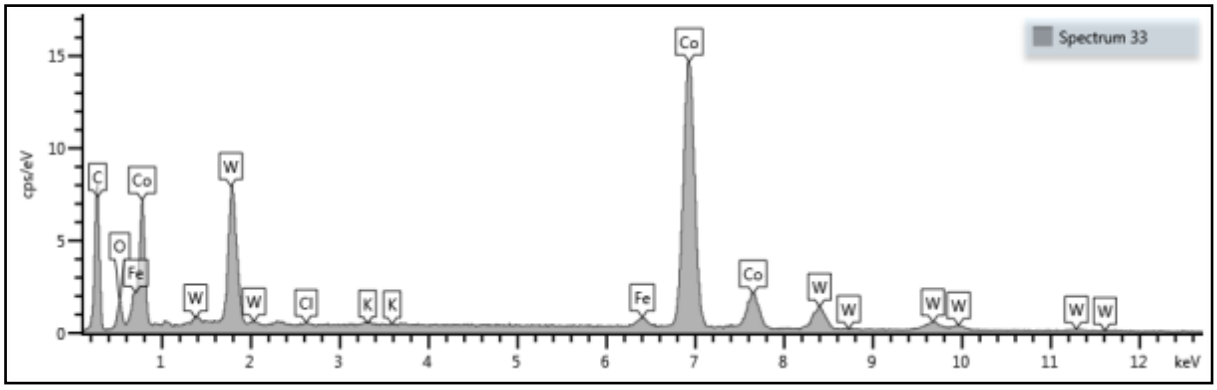

Element	Wt%
C	33.22
O	2.77
Cl	0.09
K	0.10
Fe	1.17
Co	48.17
W	14.47
Total:	100.00

Figure 4.36 EDS spectroscopy at point 33 on the substrate layer of the PDC specimen

The EDX spectroscopy graphs clarify that tungsten- carbide (WC) is the dominant phase material in the substrate layer, shown by the orange colour area, while cobalt as the binder phase represented by the turquoise colour showing the second highest percentage after WC. Other elements are minorities such as iron (Fe), copper (Cu), etc.

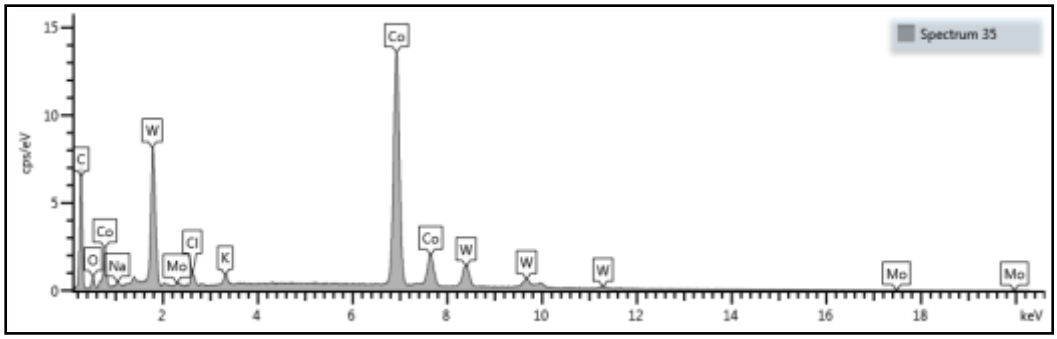

Element	Wt%
C	32.96
O	1.51
Na	0.39
Cl	0.60
K	0.57
Co	47.44
Mo	0.29
W	16.24
Total:	100.00

Figure 4.37 Spectroscopy graph and mineral composition at points 35 of the tungsten carbide layer

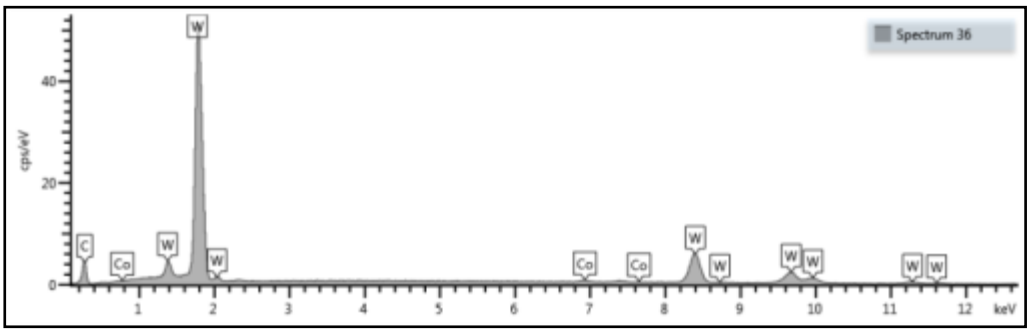

Element	Wt%
C	20.41
Co	1.10
W	78.50
Total:	100.00

Figure 4.38 EDS spectrum at point 36 of the substrate layer of the PDC cutter

Nanoindentation probe could penetrate into the hard phase (WC or diamond) or into the binder phase (Co) and this might cause misleading interpretation of the obtained nanoindentation results. The nanoindentation tests showed a large variance in the results, because the probe could be indenting within a very small area which could be diamond or cobalt areas Microindentation testing will produce much larger indentation impression and could be used to check the nanoindentation results, as microindentation tests produce bulk imprints relatively larger than those in the nanoindentation and presumably reducing the high variance in the results. In addition, no cracks were observed from the nanoindentation tests, therefore, higher loads maybe needed and microindentaion could provide that.

4.2.3 Micro-indentation test

Microindentation was used to address the previous constraints in the nanoindentation tests for quantifying the mechanical properties of the materials forming the layers of the PDC samples. The micro-indentation testing performed in this study using Vickers and Knoop probes followed the standards 14577 (2015) and E2546 (2015) stipulated by ISO and ASTM respectively.

The tests in this study are controlled by force to obtain the mechanical properties which can be calculated from a standard indentation load-depth curve.

4.2.3.1 Vickers micro-indentation

All Vickers indenters for hardness testers use a 136° square base pyramidal diamond indenter. The test is carried out by applying various indentation loads on the sample. The load is kept for a dwell time ranging from 10 to 15 seconds and then the indenter is unloaded. A square shape imprint is left in the sample's surface. The diagonal of the indent is determined using scanning electron microscopy (SEM). The average value for the two diagonal indents is used in the calculation of the hardness according to the following equation (Guder *et al.*, 2011).

$$HV = \frac{F}{A} = \frac{0.1891\,F}{d_a^2} \qquad (4-4)$$

where *HV* is the Vickers hardness number, F is the applied force (N) and d_a is the average length of the indent diagonals (mm). Vickers number needs to be converted to GPa units by multiplying HV by 0.009807.

An Instron 5566 mechanical testing machine is used for the microindentation experiments as shown in Figure 4.39. Vickers hardness values determined from Instron

are continuous over the total range of hardness for metals (HV100 up to HV1000) with the exception of test forces below 200g. Depth resolution for Instron is less than 10 nm and load resolution is 0.1 mN.

.

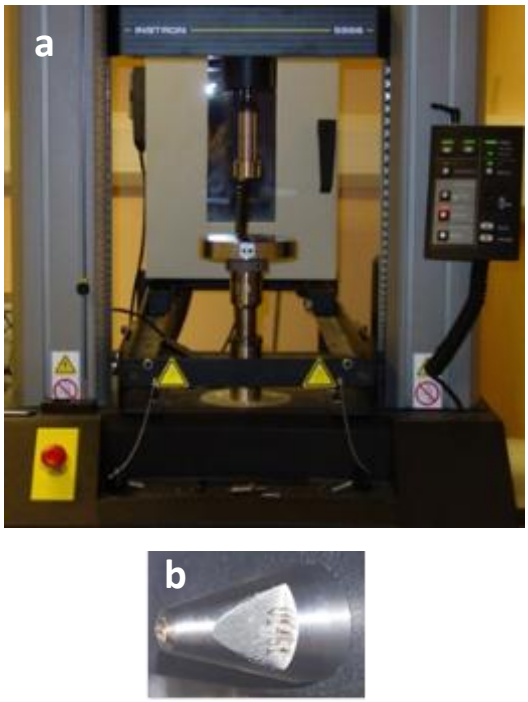

Figure 4.39 Instron 5566 equipment (a) and Vickers indenter (b)

The specimens tested by the Instron were polished using the procedure described in section 4.1.2 in order to obtain clear imprints that are examined later using scanning electron microscopy. Figure 4.40 illustrates the PDC samples mounted on a threaded stainless steel base, where the cutters are marked to determine the area of the surface to be indented. A series of microindentation tests were carried out to determine the mechanical properties of the materials forming the PDC samples.

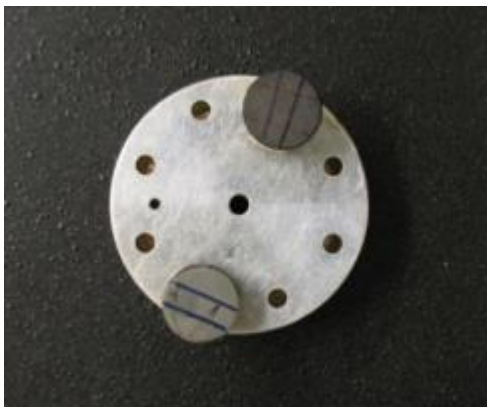

Figure 4.40 PDC samples mounted on a threaded base and marked microindentation test

4.2.3.1.1 Vickers microindentation of the substrate layer

Microindentation tests were performed on the substrate layer of the PDC inserts to determine the hardness, the Young's modulus and the fracture toughness of the material forming the substrate layer. Loads applied were ranged from 10 to 300 N, where lower loads were also applied, but unclear imprints were obtained. Loads higher than 300 N were not used as loads between 100 and 200 N produced cracks at the edges of the imprint.Figure 4.41 shows the imprints left after carrying out micro-indentation tests on the substrate layer of the K1908 PDC sample at 50 N indentation load.

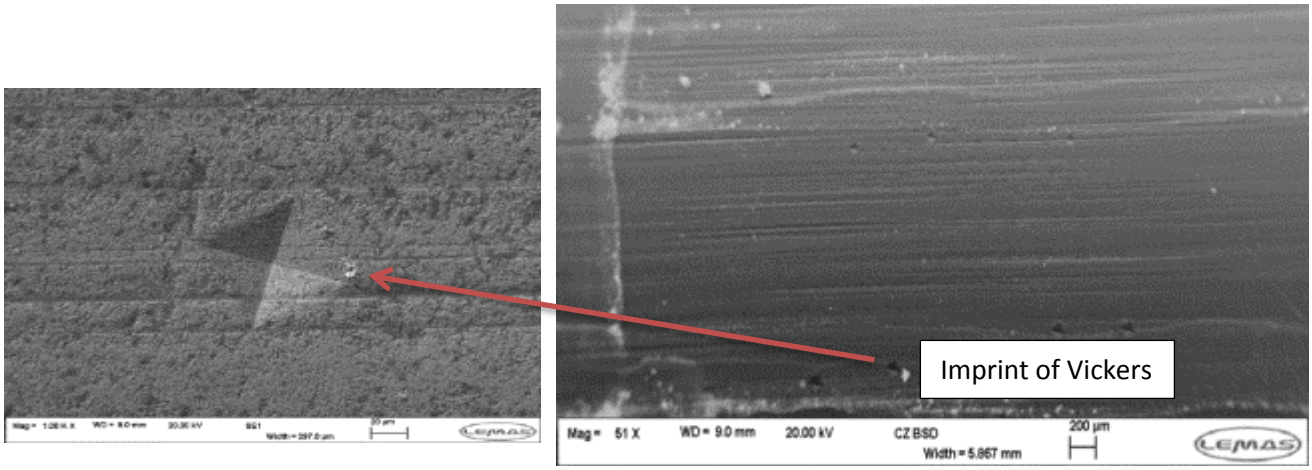

Figure 4.41 BSE image shows Vickers imprints on the substrate layer of the K1908 sample when applying 50 N

Figure 4.42 demonstrates the indent left after applying 100 N on the substrate layer of the M1313 sample. Digital Micrograph software 3.7 is used for analysing the SEM and BSE images for determining the length of the diagonals of the imprints obtained after the micro-indentation test.

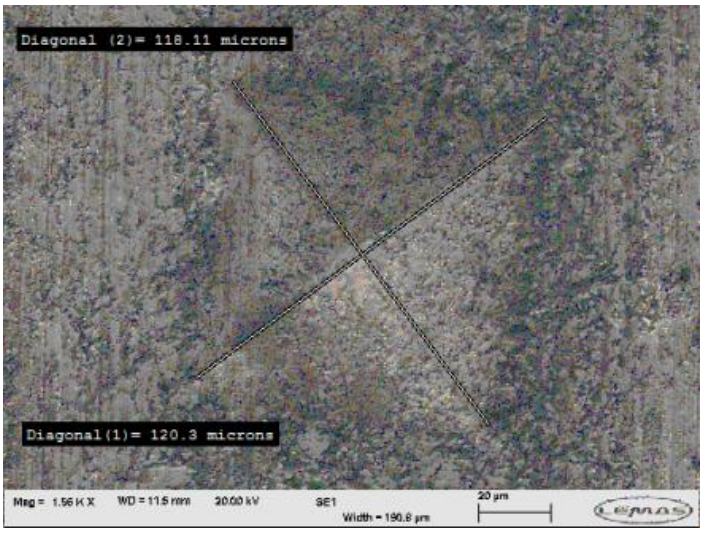

Figure 4.42 Indents left after applying 100 N on the substrate surface for the sample M1313

The micro-indentation test was performed for all samples at various loads. The length of the obtained diagonals for each sample after the test is averaged. The hardness of the specimens is obtained from applying Equation (4-1). Table 4.7 and 4.8 display the micro-indentation results for the substrate layer of the sample M1313 and K1908, respectively. Low applied loads on sample M1313 were carried out, but the imprints were not clear.

Table 4.7 Mechanical properties along with the diagonal indents length for tungsten-carbide layer resulted from Vickers indentation for the sample M1313

Load (N)	Length of first diagonal indent (µm)	Length of Second diagonal indent (µm)	Average diagonal length (µm)	Vickers hardness (HV)	Vickers hardness (GPa)	Young's modulus (GPa)
100	120.3	118.11	119.205	1335.318	13.095	517.286
200	170.1	166.21	168.155	1339.768	13.139	519.411
300	207.53	206.82	207.175	1323.852	12.983	514.131

Table 4.8 Mechanical properties for the substrate layer of the sample K1908 using Vickers probe

Load (N)	Length of first diagonal indent (µm)	Length of Second diagonal indent (µm)	Average diagonal length (µm)	Vickers hardness (HV)	Vickers hardness (GPa)	Young's modulus (GPa)
10	39.71	37.49	38.6	1269.161	12.446	512.831
15	49.29	46.34	47.815	1240.664	12.167	515.044
20	52.46	55.62	54.04	1277.979	12.533	514.912
50	85.28	84.26	84.77	1315.761	12.903	513.870
100	121.46	119.55	120.505	1302.211	12.771	515.062

The Young's modulus of the PDC samples is not determined directly from the plot of the applied load with the extension of the specimen as carried out for nano-indentation testing , where the effect of the machine compliance took place and therefore, this effect should be removed from the calculation of the Young's modulus for microindentation testing . This could be performed by a series of microindentation testing for the sample with Vickers indenter and other testing of applying load by a bar (i.e. not with an

indenter) on the anvil and plotting the graphs of the applied load vs. the extension of the two tests .The total stiffness of the sample and the machine is obtained from the first plot, while the stiffness of the machine is obtained from the second graph. The stiffness represents the slope of the unloading curve of the plot (Oliver and Pharr 1992).

In order to obtain the net stiffness of the sample, Hook's law is applied for this purpose. The net stiffness of the specimen is calculated from the following equation:

$$S_{net} = \frac{S_{Total} \cdot S_m}{S_m - S_{Total}} \qquad (4-5)$$

where S_{net} is the net stiffness of the sample, S_{total} is the stiffness of the sample plus the stiffness of the machine and S_m is the stiffness of the machine without the sample. The derivation of Equation (4-5) is shown in Appendix A.B.

Figure 4.43 shows the plot of the loading and unloading of the applied load versus the extension for the substrate layer of the sample M1313.

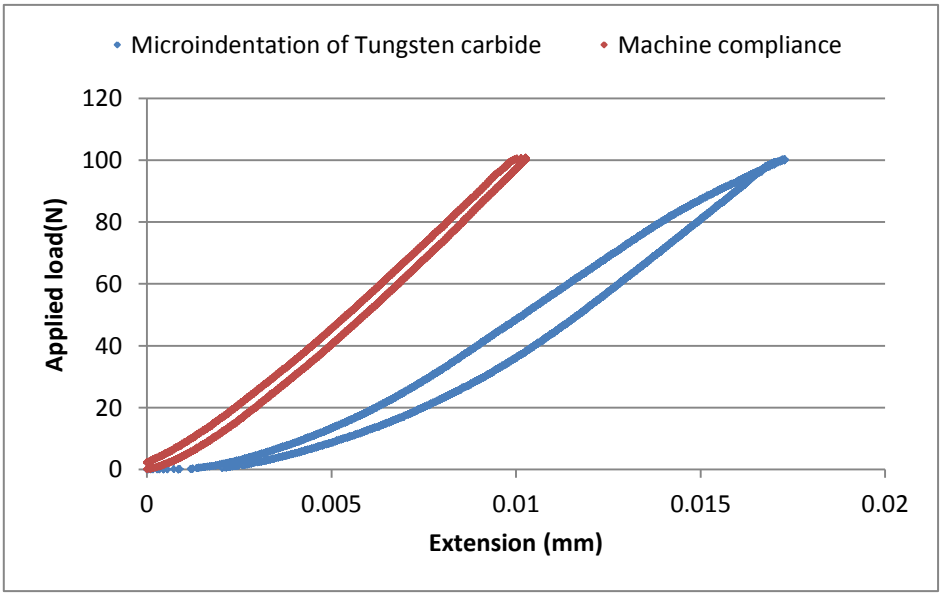

Figure 4.43 Micro-indentation of tungsten-carbide and machine compliance for 100 N applied load for sample M1313

Once the stiffness of the sample is determined, the reduced modulus of the sample is obtained from Equation (4-2) and finally the Young's modulus is determined from Equation (4-3). Young's modulus of the tungsten-carbide-cobalt layer for the sample M1313 is tabulated in Table 4.7.

4.2.3.1.2 Vickers microindentation of the diamond layer

A series of microindentations with various applied loads (30-300) N were carried out on the diamond layer of the PDC samples to determine its mechanical properties. As

mentioned previously, the diamond coating layer has to be finely polished to obtain clear imprints. Few clear indents were produced as a result of the microindentation testing due to the high degree of surface roughness of the diamond layer even after the polishing process. Figure 4.44 displays a Vickers imprint on the diamond layer for the sample M1313 obtained after applying a load of 300 N.

Young's modulus is determined by applying the same approach of that of the substrate layer. Figure 4.45 shows the plot of the relationship between the applied load and the extension when maximum load is 300 N. The figure illustrates the high degree of the elastic recovery of the diamond layer as the loading and the unloading curves are nearly coincided.

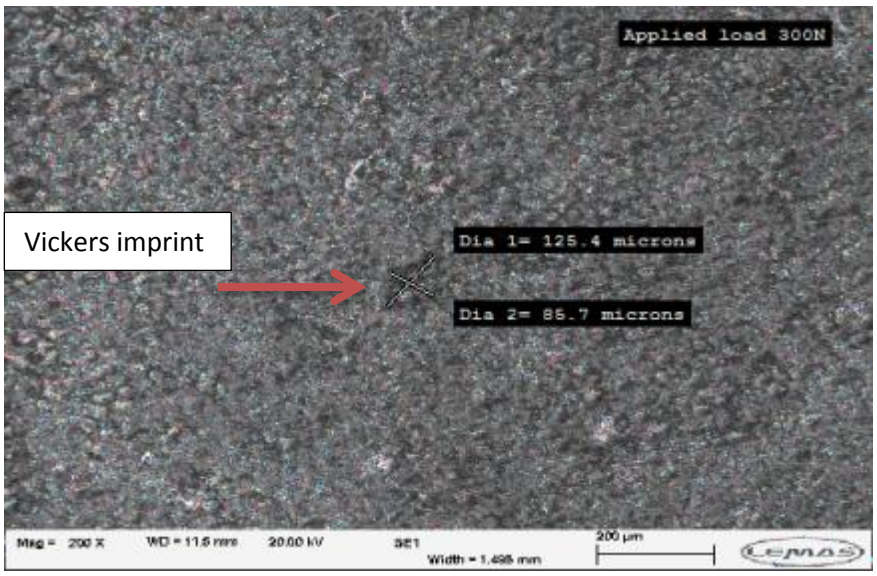

Figure 4.44 Imprint of a Vickers indenter on diamond layer at 300N applied load for the sample M1313

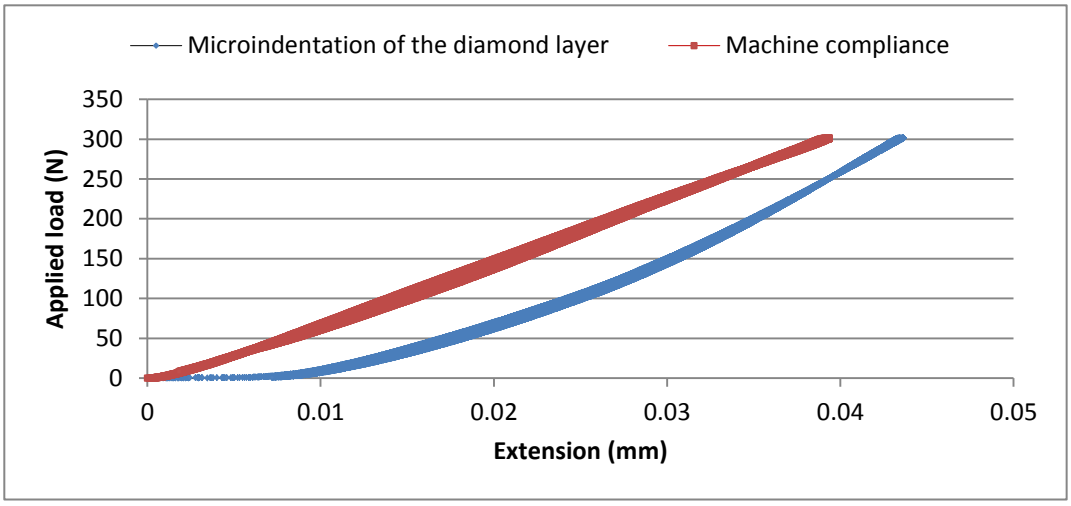

Figure 4.45 Microindentation of diamond layer at 300N applied load using Vickers indenter for sample M1313

The results of the microindentation using Vickers indenter for the diamond layer are displayed in Tables 4.9 and 4.10 for the samples M1313 and K1908, respectively. The

applied loads were different for the two samples as few clear indents were obtained at certain loads.

Table 4.9 Mechanical properties and diagonal indents length of the diamond-cobalt layer resulted from Vickers microindentation for the sample M1313

Load (N)	Length of first diagonal indent (µm)	Length of Second diagonal indent (µm)	Average diagonal length, (µm)	Vickers hardness (HV)	Vickers hardness (GPa)	Young's modulus (GPa)
50	45.18	39.47	42.325	5277.978	51.7611	865.52
300	125.4	85.7	105.55	5092.092	49.938	863.548

Table 4.10 Mechanical properties of the diamond layer for the sample K1908 after Vickers microindentation

Load (N)	Length of first diagonal indent (µm)	Length of Second diagonal indent (µm)	Average diagonal length, (µm)	Vickers hardness (HV)	Vickers hardness (GPa)	Young's modulus (GPa)
30	37.21	32.27	34.74	4700.598	46.0987	850.35
60	52.35	44.95	48.65	4793.768	547.012	855.25
120	74.52	65.87	70.195	4605.326	45.1644	861.29

After each microindentation testing of the diamond layer, the tip of the indenter has to be checked using SEM to observe any damage that may have occurred.

4.2.3.2 Knoop microindentation

Knoop microindentation testing was carried out to determine the hardness and the Young's modulus of the diamond layer as low loads are required for the Knoop microindentation compared to the Vickers one. Knoop hardness testing is also used to create cracks on the diamond layer for fracture toughness determination. The tip of the indenter was made from natural diamond that has geometry of rhombic-based pyramidal shape. The Instron 5566 mechanical testing machine is used to conduct the Knoop microindentations on the diamond layer of the PDC sample. Before achieving the Knoop indentations, the surfaces of the samples were polished to reduce the asperities that might distort the obtained results.

The Knoop indenter is pressed into the cutters surface under a certain load for a period of 15 seconds and then the load is released. The selected applied loads for Knoop

testing were chosen from 5 -50 N. The indents are examined by SEM to determine the longest diagonal of the rhombus imprint. The hardness of the material is calculated from Equation (4-6) as follows (Sumiya and Irifune 2004):

$$HK = \frac{14229 * F}{d_l^2} \qquad (4-6)$$

where *HK* is the knoop hardness (GPa), *F* is the applied force (N) and d_l is the length of the longest indent diagonal (μm). Figure 4.46 shows the indents left after Knoop microindentation on the diamond layer of the sample M1313.

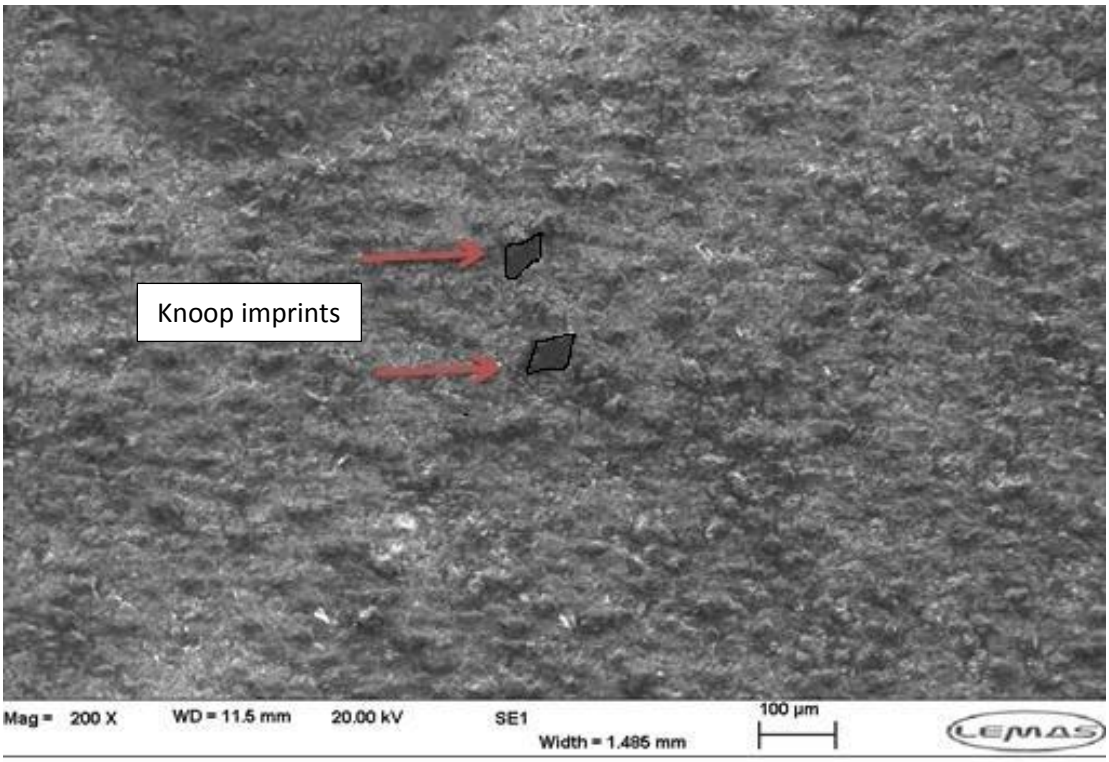

Figure 4.46 Knoop indents on diamond-cobalt layer at 20 N load for the sample M1313

Due to the rough surface of the diamond, just a few imprints left after the Knoop microindentation for sample M1313, while it was not possible to obtain any clear undistorted imprint on sample K1908 when using loads rather than 20 N even after careful examination by SEM. The Young's modulus of the diamond layer related to the Knoop microindentation testing is determined similarly to the Vickers, microindentation testing. Unfortunately, no cracks were produced after Knoop microinendtation. Table 4.11 shows the mechanical properties of the diamond layer of the sample M1313 obtained from the Knoop microindentation.

Table 4.11 Mechanical properties and diagonal indents length for diamond layer resulted from Knoop microindentation of the sample M1313

Load (N)	Length of the long diagonal indent (μ)	Knoop Hardness (GPa)	Young's modulus (GPa)
20	73.4	52.821	860.008
20	72.3	54.441	883.230

4.2.3.3 Fracture toughness measurements

Fracture toughness indicates the resistance of a material to a fracture in the presence of a sharp crack. Fracture toughness in this study is determined from Vickers microindentation testing, where various loads are applied to the sample using a Vickers probe to initiate a crack or fracture. The fracture toughness values of the materials investigated in this study were determined from the lengths of the radial cracks. Figure 4.47 shows a schematic sketch of a palmqvist and radial cracks formed after performing Vickers microindentation testing. Many researchers have developed a number of formulas for fracture toughness determination. Some equations require the mechanical properties of the material being tested, i.e. hardness and Young's modulus.

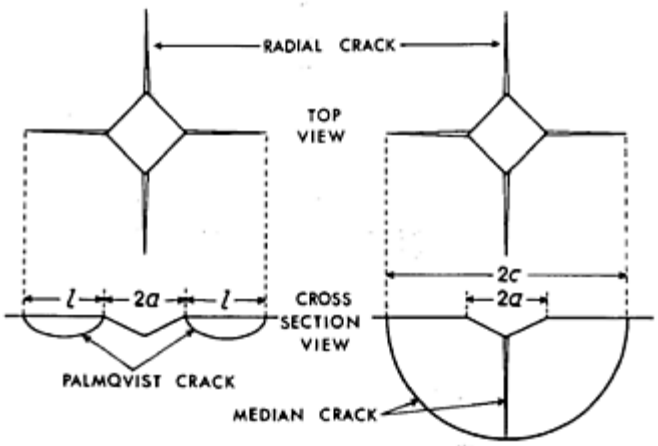

Figure 4.47 Geometries of cracks generated by Vickers indentation. (a) Pamlqvist crack and (b) radial/median (half penny) (Niihara, 1983)

Shetty *et al.* (1985) postulated the following equation for fracture toughness determination:

$$K_{IC} = 0.0889 \sqrt{\frac{H * F}{\sum C_i}} \qquad (4-7)$$

where K_{IC} is the fracture toughness (MPa .$m^{0.5}$) ,H is the hardness of the material being tested (MPa), F is the applied load (N) and C is the crack length (m) measured from end

to end distance between opposite cracks subtracting the length of the diagonal of the indent.

Evans and Charles (1976) suggested a semi-empirical equation for fracture toughness calculation. Crack and indent length as well as the hardness of the indented material were the most dependant parameters for fracture toughness determination as follows.

$$K_{IC} = 0.16\, H\, .\, a^{\frac{1}{2}}\, .\, \left(\frac{C}{a}\right)^{-\frac{3}{2}} \qquad (4-8)$$

where, K_{IC} is the fracture toughness (MPa .m$^{0.5}$), H is the hardness (MPa) , a is the half length of the diagonal indent (m) and C is the crack length (m). The crack length represents the distance from the centre of the indent to the crack tip.

Lawn *et al*. (1980) suggested an experimental technique for fracture toughness which depends primarily on the previous work of Evans and Charles (1976). However, this technique shows that the fracture toughness depends on the elastic-plastic properties of the material along with the total crack length. The proposed equation is found to be more applicable to ceramics. The suggested equation is as follows:

$$K_{IC} = 0.028\, H\, .\, a^{\frac{1}{2}}\, .\, \left(\frac{E}{H}\right)^{\frac{1}{2}}\, .\, \left(\frac{C}{a}\right)^{-\frac{3}{2}} \qquad (4-9)$$

where K_{IC} is the fracture toughness (MPa .m$^{0.5}$), H is the hardness (MPa) , a is the half length of the diagonal indent (m) , C is the crack length (m) and E is the Young's modulus of the material (MPa).

Other formulas for fracture toughness determination depend mainly on the mechanical properties of the material being tested. Anstis *et al*. (1981) investigated the radial-median cracks left after Vickers indentations. The suggested equation, derived by testing on ceramics, is as follows:

$$K_{IC} = 0.016\, \sqrt{\frac{E}{H}}\, .\, \frac{F}{C^{3/2}} \qquad (4-10)$$

where K_{IC} is the fracture toughness (MPa .m$^{0.5}$), H is the hardness (MPa) , E is the Young's modulus of the material (MPa) , C is the crack length (m) and F is the applied load (N). The crack length represents the distance from the centre of the indent to the crack tip.

Laugier (1985) postulated an equation which could be applied on various materials soft to hard and the obtained results were close to the literature.

$$K_{IC} = 0.010 \left(\frac{E}{H}\right)^{\frac{2}{3}} . \left(\frac{F}{C^{\frac{3}{2}}}\right) \qquad (4-11)$$

where K_{IC} is the fracture toughness (MPa .m$^{0.5}$), H is the hardness (MPa) , E is the Young's modulus of the material (MPa) , C is the crack length (m) and F is the applied load (N).

The measurements of the fracture toughness presented in this study were carried out using the software DigitalMicrograph 3.7 to analyze the SEM and BSE images for determining the cracks length obtained from microindentation testing.

4.2.3.3.1 Fracture toughness measurements of WC-Co

Vickers microindentation tests were conducted on the substrate layer of the PDC samples by applying various loads for a dwelling time of 5 seconds and then releasing the load. It was observed that when applying 100 N load cracks developed around the edges of the imprints, whereas no clear cracks initiated at loads lower than 100 N. Figure 4.48 illustrates the cracks caused from Vickers microindentation on the substrate layer of the sample K1908, where 170 N was applied. The orange arrows demonstrate the extension of the cracks from the edge of the diagonals of the imprint.

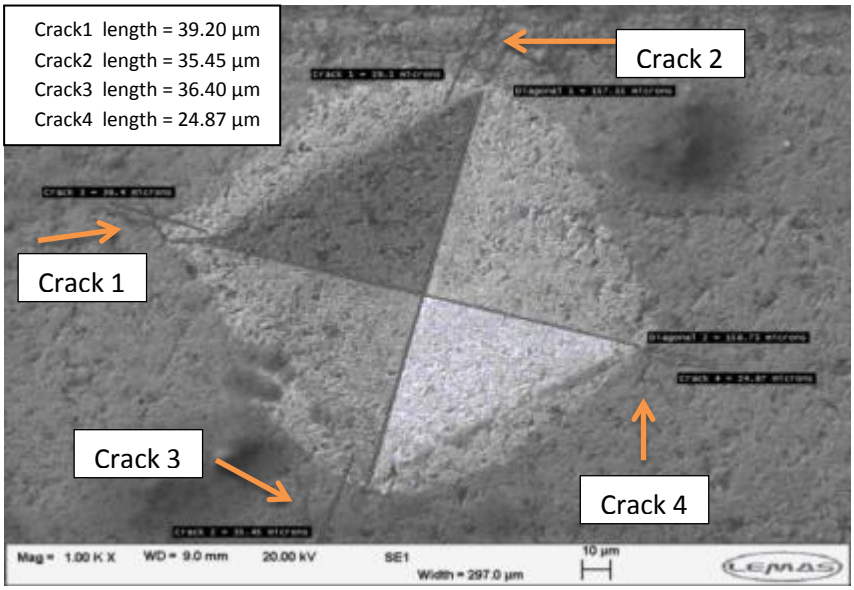

Figure 4.48 Cracks occurring when applying 170 N load on WC substrate for the sample K1908

Table 4.12 shows the results of fracture toughness obtained from Vickers microindentation testing for the substrate layer for samples K1908 and M1313. Various equations are used for this purpose, where it is clear from the results that Lawn *et al*.

(1980) and Shetty *et al.* (1985) approaches exhibited good agreement with the reported values in the literature for the same material. Figure 4.49 illustrates the comparison between the literature and the obtained values of fracture toughness for the substrate layer of sample

Table 4.12 Results of fracture toughness calculated from different methods for WC substrate for samples K1908 and M1313.

Load (N)	K_{IC} (MPa.m$^{1/2}$) Literature (Osipov *et al.*, 2010)	K_{IC} (MPa.m$^{1/2}$) (Anstis *et al.*, 1981)	K_{IC} (MPa.m$^{1/2}$) (Lawn *et al.*, 1980)	K_{IC} (MPa.m$^{1/2}$) (Laugier, 1985)	K_{IC} (MPa.m$^{1/2}$) (Evans and Charles, 1976)	K_{IC} (MPa.m$^{1/2}$) (Shetty *et al.*, 1985)	K_{IC} (MPa.m$^{1/2}$) Average
100 (K1908)	11-12	13.371	10.808	15.478	9.725	11.1194	12.1 ± 2.064
170 (K1908)	11-12	13.872	11.138	16.069	10.002	11.1873	12.454 ± 2.21
100 (M1313)	11-12	12.367	10.068	14.266	9.154	10.384	11.338 ± 1.804
200 (M1313)	11-12	13.747	11.172	15.860	10.154	N/A	12.733 ± 2.23

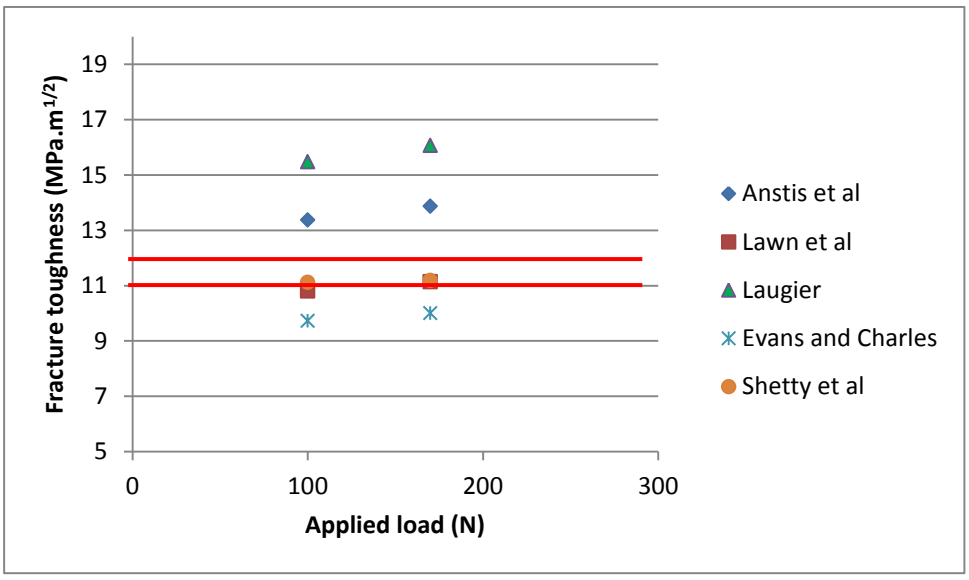

Figure 4.49 Fracture toughness for the substrate layer from different models for the substrate layer of sample K1908

K1908. Figure 4.50 shows the fracture toughness for sample M1313 obtained from various equations along with the range literature value represented with the red lines.

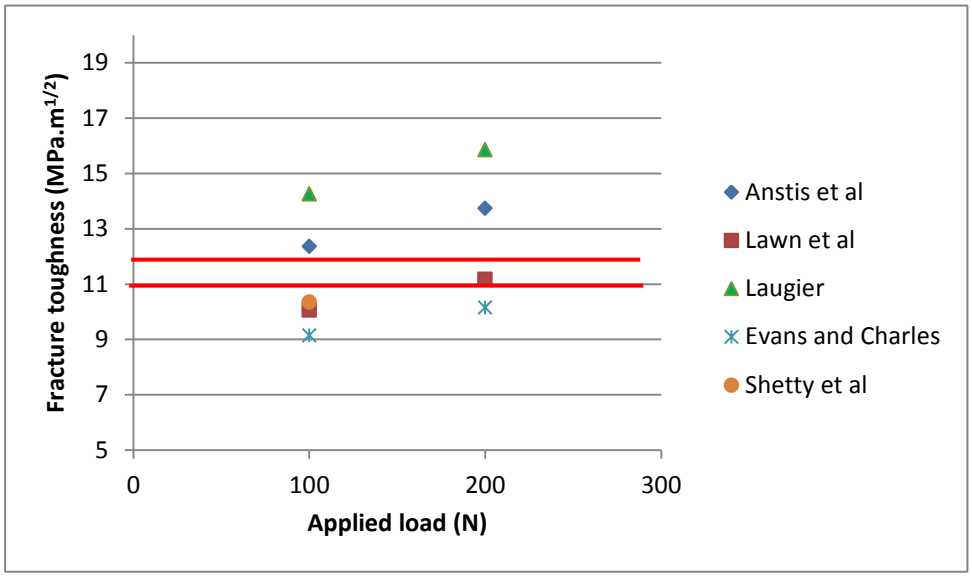

Figure 4.50 Fracture toughness versus applied loads for the substrate layer for sample M1313

4.2.3.3.2 Fracture toughness measurements of diamond layer

As mentioned previously that, no fractures were created from Knoop microindentation, therefore Vickers microindentation was the choice for creating fractures, especially on the diamond surface. Many attempts were performed to obtain fractures around the diamond layer of the PDC samples using various loads from 10 N up to 100 N, using Vickers indenter, but clear cracks were obtained with just a few imprints, due to the high surface roughness of the diamond layer even after fine polishing. However, indents with cracks were obtained using a Vickers indenter at 30N and 50N on very well polished diamond surfaces of the PDC sample (K1908).

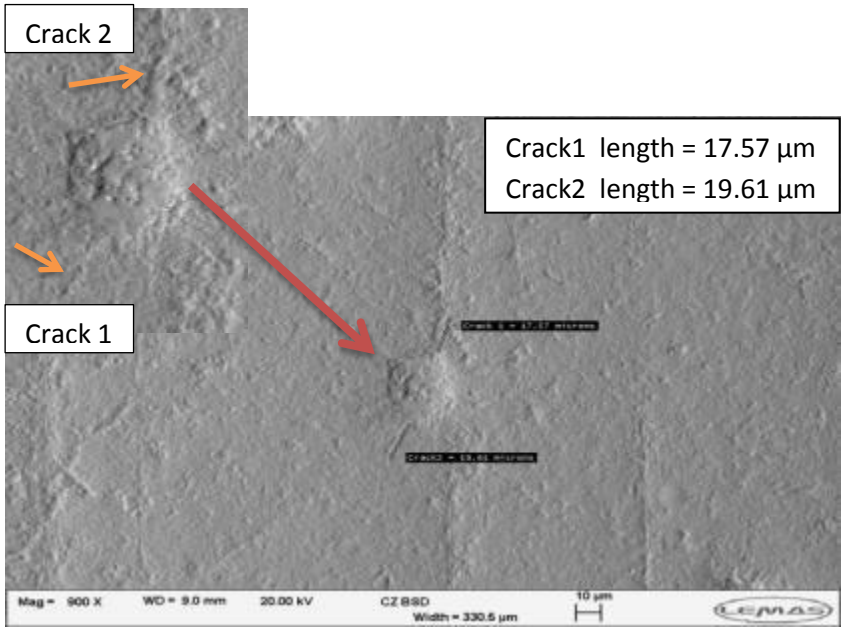

Figure 4.51 Crack lengths when applying 30 N load on the diamond layer for the sample K1908

Figure 4.51 demonstrates a BSE image of a very fine polished diamond surface of the PDC sample K1908. The orange arrows show opposite cracks occurred when applying 30 N. Figure 4.52 shows a Vickers imprint with four cracks occurring; one at each diagonal edge when applying a load of 50 N for sample M1313.

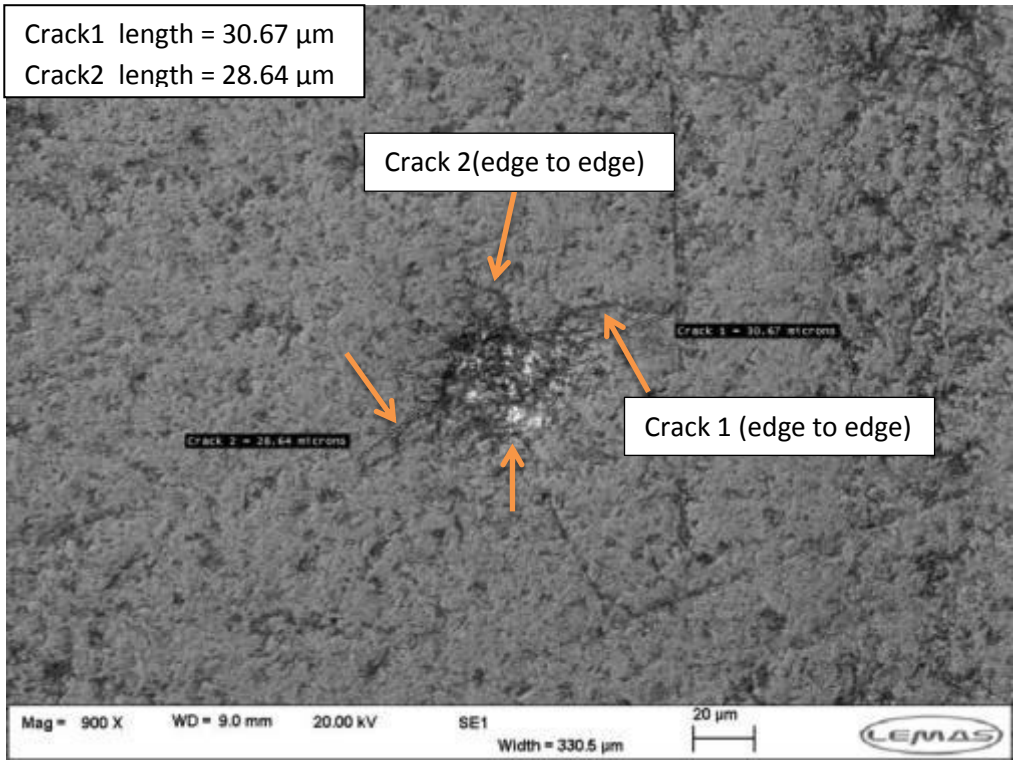

Figure 4.52 Crack lengths when applying 50 N load on the diamond layer for sample M1313

Table 4.13 Fracture toughness calculated by various methods for the diamond layers of samples M1313 and K1908

Load (N)	K_{IC} (MPa.m$^{1/2}$) Literature (Osipov *et al., 2010*)	K_{IC} (MPa.m$^{1/2}$) (Anstis *et al.*, 1981)	K_{IC} (MPa.m$^{1/2}$) (Lawn *et al.*, 1980)	K_{IC} (MPa.m$^{1/2}$) (Laugier, 1985)	K_{IC} (MPa.m$^{1/2}$) (Evans and Charles, 1976)	K_{IC} (MPa.m$^{1/2}$) Average
30 N K1908 sample	9-10	9.214	8.576	9.361	11.411	9.641 ± 1.064
50 N M1313 sample	9-10	8.662	8.008	8.658	11.191	9.13 ± 1.219

Table 4.13 exhibits the obtained values of fracture toughness of the diamond layer of the PDC samples. Figure 4-53 illustrates the fracture toughness of the diamond layer for two PDC samples at loads 30 N and 50 N. The obtained results were close for both samples. Fracture toughness calculated from Laugier (1985) and Anstis *et al*. (1981) show good agreement with the literature value of the diamond layer of the PDC cutters. The method of Shetty *et al*. (1985) is not applicable due to lack of clear cracks at each end of the diagonals of the indent for the samples.

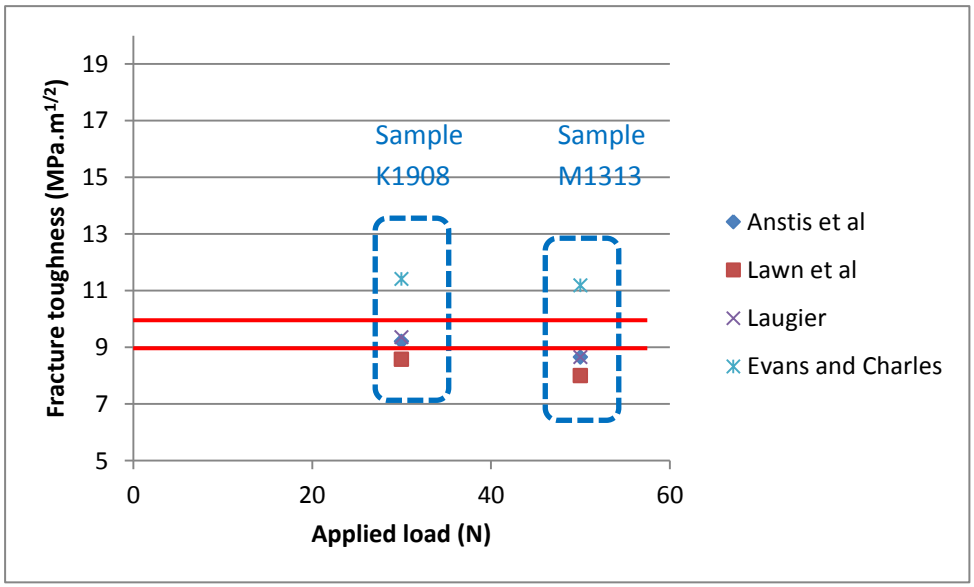

Figure 4.53 Fracture toughness for the diamond coating of the PDC inserts obtained from various approaches

The overall average results of the mechanical properties of the PDC samples obtained from the microindentation testing can be summarised in Table 4.14 as follows:

Table 4.14 Overall results of the microindentation testing for the substrate and the diamond layers of the PDC samples

PDC sample	Vickers hardness (GPa)	Yong's modulus (GPa)	Fracture toughness ($MPa.m^{1/2}$)	Layer
M1313	13.072 ± 0.066	516.943 ± 2.169	11.908 ± 2.152	Substrate
K1908	12.564 ± 0.257	514.344 ± 0.877	12.277 ± 2.146	Substrate
M1313	50.85 ± 0.912	864.534 ± 0.986	9.13 ± 1.219	Diamond
K1908	46.092 ± 0.754	855.63 ± 4.474	9.641 ± 1.064	Diamond

4.3 Micro-structural properties and cobalt content of PDC cutters

This part of the work is carried out to study the effect of the micro-structural properties of the PDC inserts and cobalt content on the mechanical properties of the materials forming the PDC cutters. The study aimed to determine the particles size of the coating (diamond) and the substrate (tungsten-carbide) and the weight percentage of the binder (cobalt) in the PDC samples.

Combined BSD and coloured EDX images are used to analyse the micro-structural properties of the PDC cutters. BSD images are used for displaying the best resolution of the particle distribution compared to normal SEM images. EDX maps are used for determining the cobalt content in the diamond and the substrate layers of the PDC cutters.

The particle size diameter of the diamond and substrate is determined by using image J software after analysing the BSD images and obtaining the area of the particles and then converting the area into Circular Equivalent Diameter (CED) which is defined as the diameter of a circle with the same area as the particle (Olson, 2011). CED is determined from the following equation:

$$CED = \sqrt{\frac{4\,A_p}{\pi}} \qquad (4-12)$$

where, A_p is the area of the particle determined from Image J software (μm^2). *CED* is measured in μm.

Figure 4.54 shows the processing steps of the software (Image J) for an imported SEM image used in the study.

Figure 4.55 shows the diamond particles embedded in the binder (cobalt) for the diamond layer of samples M1313 (a) and K1908 (b). The particle size distribution of the diamond grains of samples M1313 and K1908 is shown in Figure 4.56.

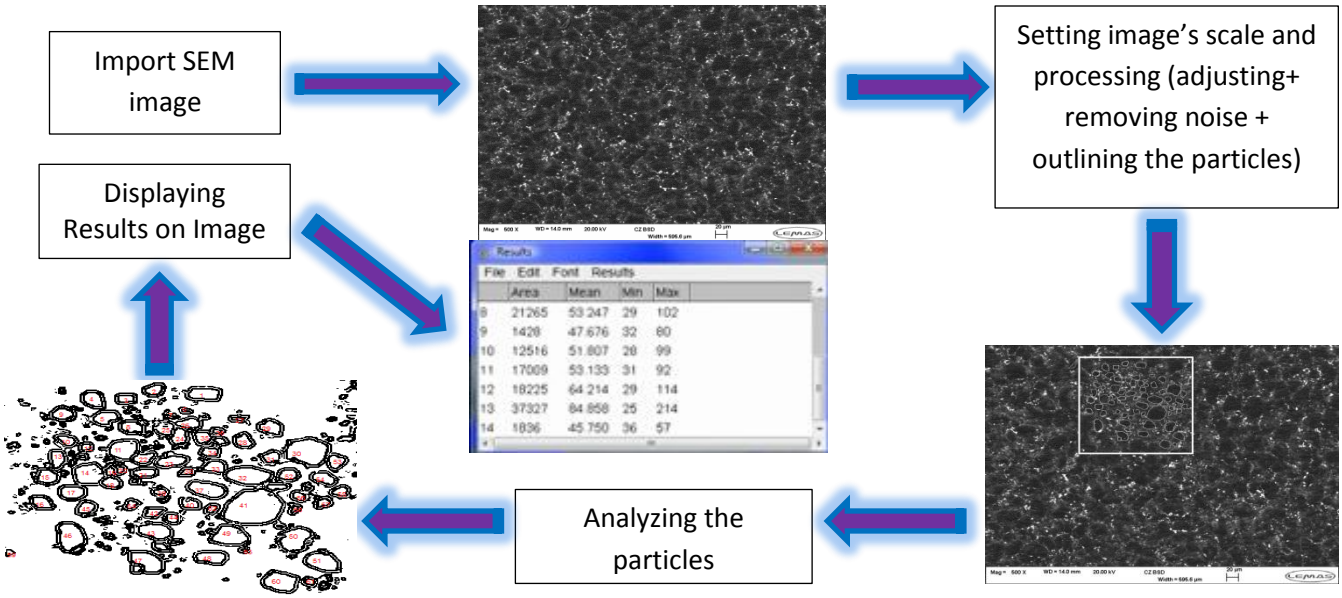

Figure 4.54 Processing cycle of Image J software used for analysing SEM images in the study for particles size determination

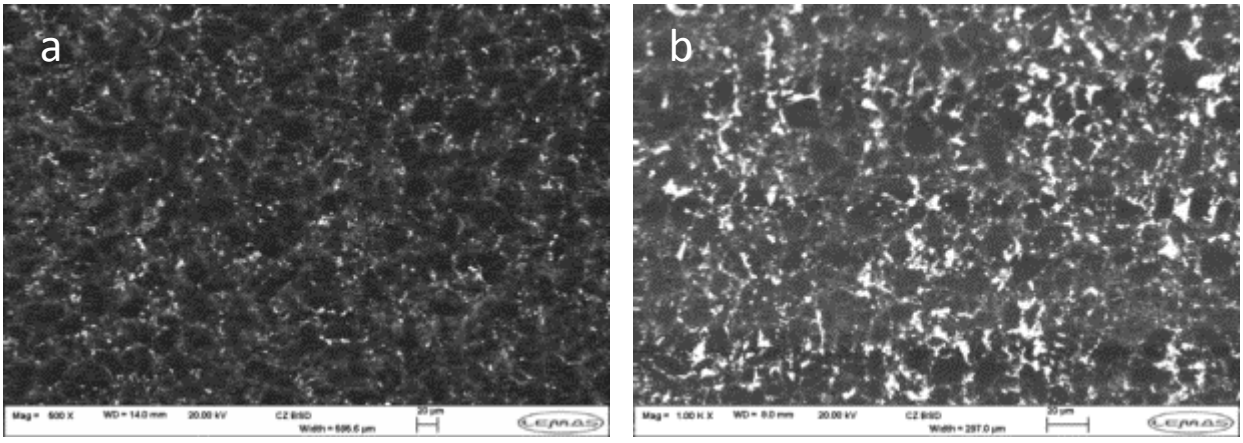

Figure 4.55 BSD images (a) sample M1313 (b) sample K1908 of the diamond layer displaying the diamond grains (black) and the cobalt (white)

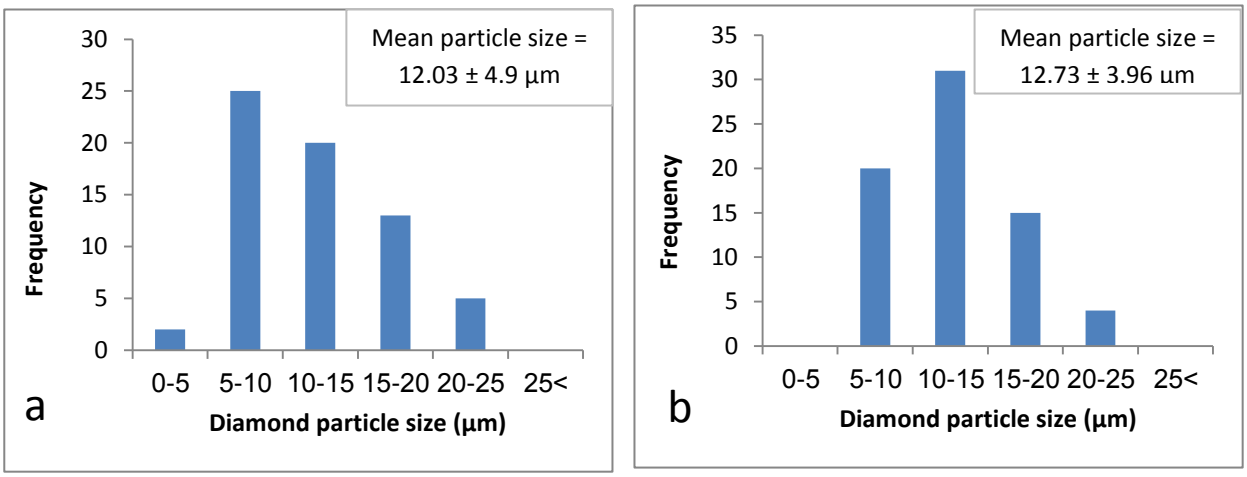

Figure 4.56 Diamond particle size distribution of sample M1313 (a) and sample K1908 (b)

The major constraint was the shape of tungsten-carbide particles that were not spherical and therefore, the determination of the diameter of the particle directly from the area

obtained from J image software would be wrong. Therefore, the areas of the irregular shapes obtained from the software were used to determine the Circular Equivalent Diameter (CED).

Figure 4.57 illustrates the irregular shape of tungsten-carbide (substrate) particles embedded in cobalt for (a) sample M1313 and (b) sample K1908, while Figure 4.58 demonstrates the tungsten-carbide grain size distribution of specimen M1313 and sample K1908.

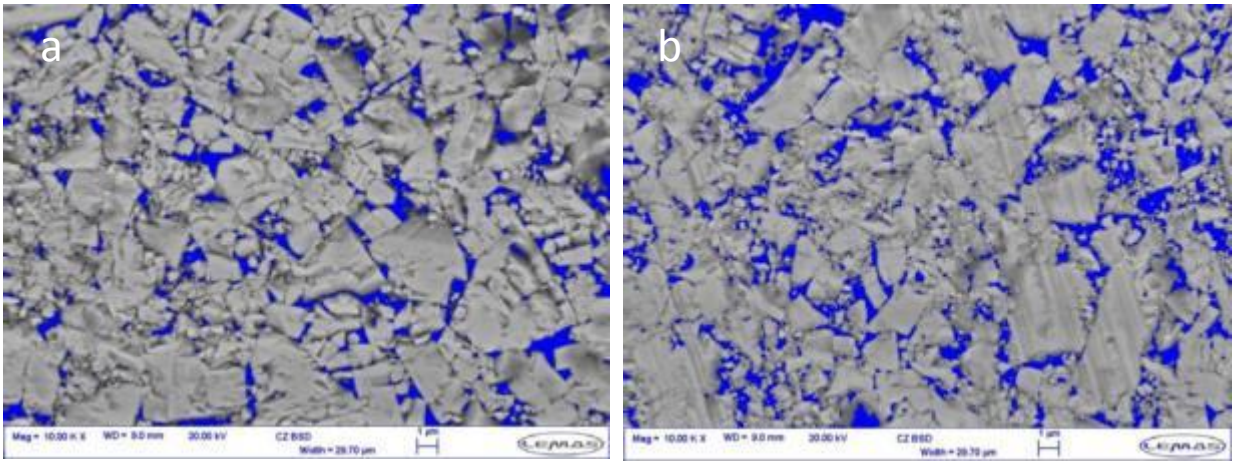

Figure 4.57 BSD images (a) sample M1313 (b) sample K1908 of the substrate layer displaying the tungsten-carbide particles (grey) and the cobalt (blue)

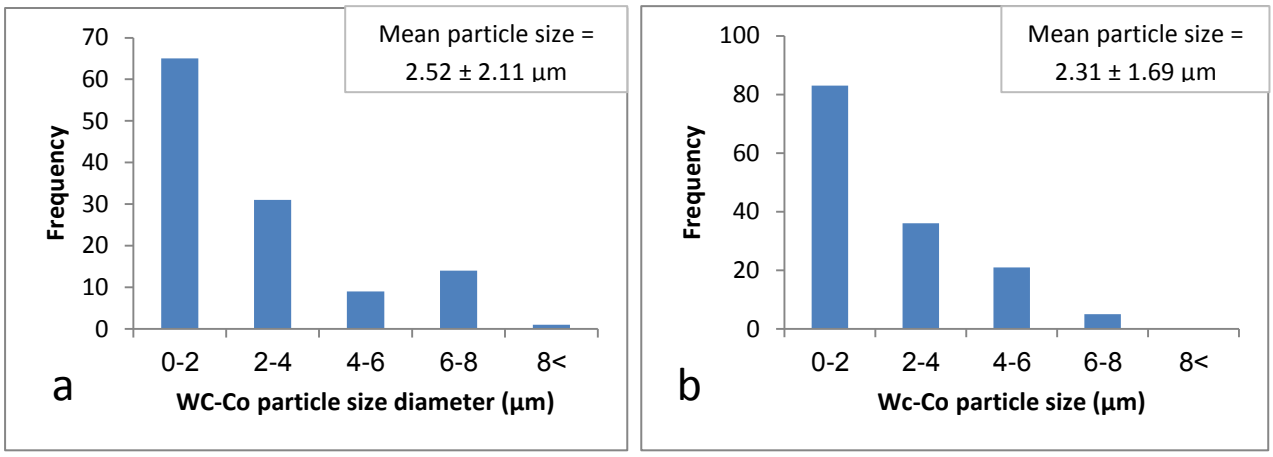

Figure 4.58 Substrate grain size distribution (a) specimen M1313 (b) specimen K1908

The cobalt content represented as weight percentage is determined from EDX maps at selected various spectrum areas of the material surface (diamond and substrate layers) and then averaging the results. Figure 4.59 shows the EDX maps with the corresponding

element content for five different selected parts (a-e) of the diamond layer of sample M1313.

Element	Wt%
C	94.37
Co	3.21
W	2.42
Total:	100.00

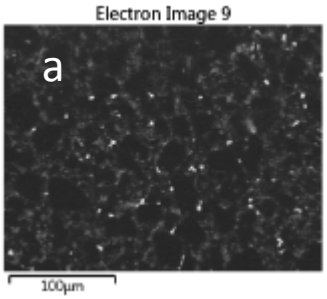

Element	Wt%
C	95.38
Co	3.39
W	1.23
Total:	100.00

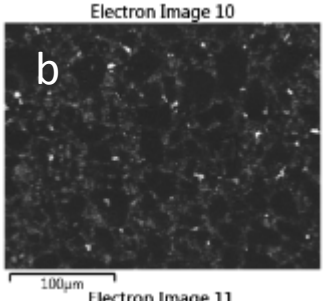

Element	Wt%
C	93.74
Co	2.85
W	3.41
Total:	100.00

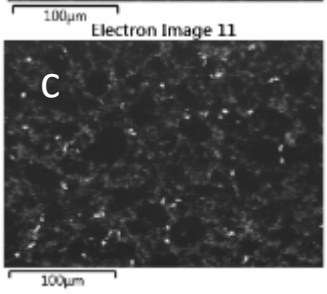

Element	Wt%
C	96.17
Co	2.82
W	1.01
Total:	100.00

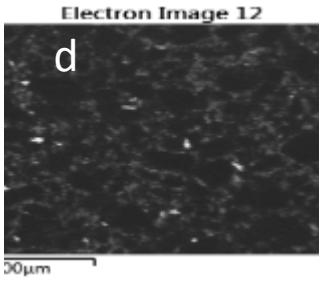

Element	Wt%
C	95.12
Co	4.04
W	0.84
Total:	100.00

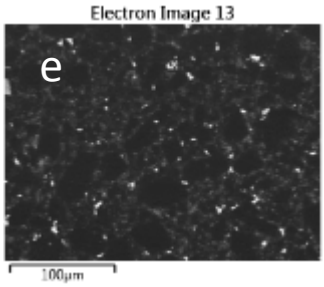

Figure 4.59 EDX maps (a-e) and the corresponding mineral content for the diamond layer of sample M1313

Similarly, Figure 4.60 shows the binder content (cobalt) in the diamond layer of sample K1908 for various areas (a-e).

Element	Wt%
C	93. 45
Co	4.11
W	2.44
Total:	100.00

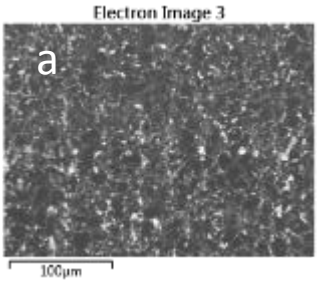

Element	Wt%
C	92.01
Co	4.48
W	3.51
Total:	100.00

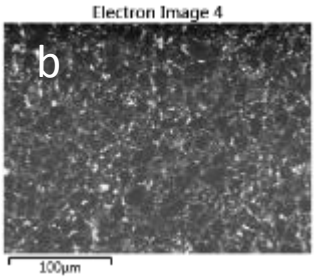

Element	Wt%
C	91.11
Co	5.04
W	3.85
Total:	100.00

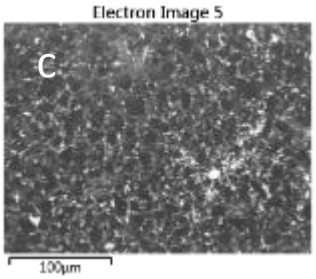

Element	Wt%
C	92.55
Co	4.67
W	2.78
Total:	100.00

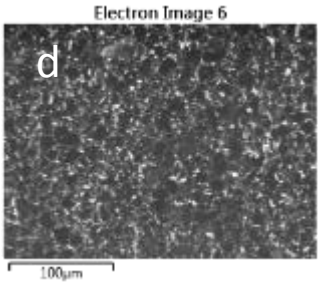

Element	Wt%
C	94. 61
Co	3.70
W	1.69
Total:	100.00

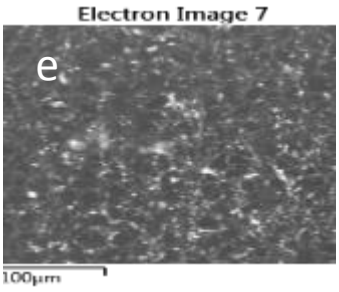

Figure 4.60 EDX maps (a-e) and the corresponding element content for the diamond layer of specimen K1908

Cobalt weight percentage is also measured for five different spectrums of the substrate layer for samples M1313 and K1908 as shown in Figures 4.61 and 4.62 respectively.

Element	Wt%
C	10.70
O	3.68
Co	7.06
W	78.56
Total:	100.00

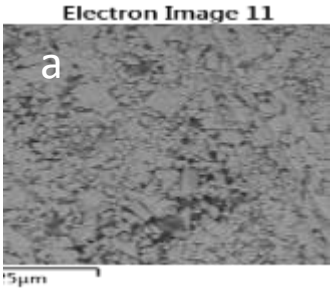

Element	Wt%
C	10.60
O	4.30
Co	7.93
W	77.17
Total:	100.00

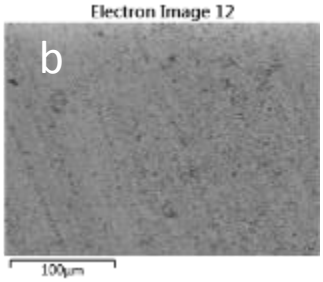

Element	Wt%
C	10.70
O	4.81
Co	7.00
W	77.50
Total:	100.00

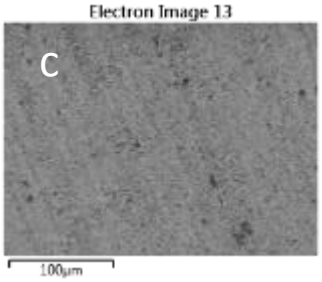

Element	Wt%
C	10.94
O	5.20
Co	7.25
W	76.61
Total:	100.00

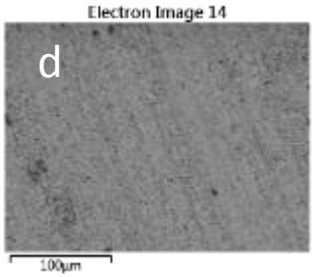

Element	Wt%
C	11.22
O	4.93
Co	7.63
W	76.22
Total:	100.00

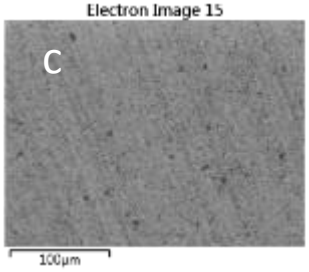

Figure 4.61 Electron images and the corresponding element weight percentage for the substrate layer of sample M1313

Element	Wt%
C	12.05
O	3.37
Co	9.06
W	75.51
Total:	100.00

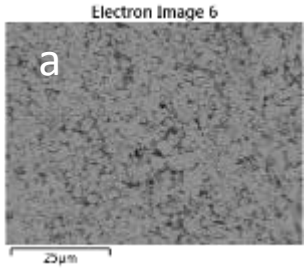

Element	Wt%
C	13.01
O	4.77
Co	8.54
W	73.68
Total:	100.00

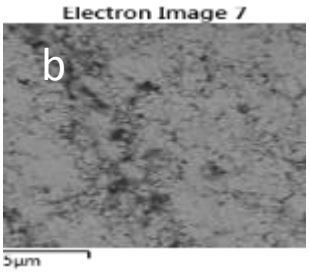

Element	Wt%
C	12.55
O	4.64
Co	8.70
W	74.11
Total:	100.00

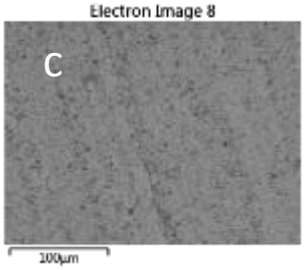

Element	Wt%
C	11.98
O	4.91
Co	8.56
W	74.55
Total:	100.00

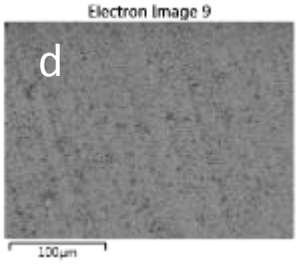

Element	Wt%
C	12.17
O	4.04
Co	9.26
W	74.53
Total:	100.00

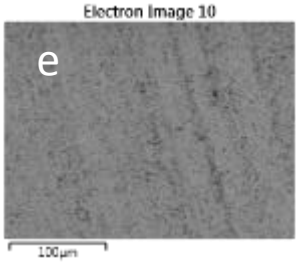

Figure 4.62 EDX images and the corresponding element content for the tungsten-carbide-cobalt layer of sample K1908

Table 4.15 shows the micro-structural properties of two PDC inserts from different manufacturers.

Table 4.15 Structural properties of PDC inserts from different manufacturers

PDC samples	M1313	K1908
Diamond particle size (µm)	12.03 ± 4.9 min < 4.52 max > 23.25	12.73 ± 3.96 min < 6. 9 max > 23.9
WC particle size (µm)	2.52 ± 2. 11 min < 0.38 max > 8.23	2.31 ± 1.69 min < 0.3 max > 7.73
Co wt.% (in diamond)	3.26 ± 0.5	4.4 ± 0.51
Co wt.% (in WC-Co)	7.37 ± 0. 39	8.82 ± 0. 32

Increasing cobalt content for a given substrate particle size causes the fracture toughness to increase but reduces the hardness (Bellin *et al.*, 2010 c). It is found that, fine substrate (WC) grain size and low level of cobalt content leads to higher hardness and good wear resistance , whereas coarse WC particles and high mass content of cobalt produce low hardness and high wear rate (Mori *et al*., 2003 and Ndlovu ,2009). Hong *et al*. (1988) stated that cobalt infiltrates through the voids between diamond particles by capillarity during the sintering process. Larger spaces are directly associated with larger particle size which prefers dislodgment of cobalt, so when the cobalt content is high, therefore it is corresponding to large particle grain size. Yahiaoui *et al.*, (2013) mentioned that the grain size and the content of cobalt are the most significant parameters relevant with the material loss of PDC cutters as high wear rate is associated with large particle size. High wear rate is also associated with high cobalt content of the diamond layer. Bellin *et al.* (2010 b) explained the role of cobalt content towards fracture toughness. Increasing the cobalt content in the diamond layer and the substrate will increase the fracture toughness, whereas the wear resistance increases with lower cobalt content.

The particle size of the substrate layer of samples M1313 and K1908 is close around 2.3-2.5 µm, whereas the cobalt content in the substrate of sample M1313 is 7.37% compared to 8.82% in sample K1908. Accordingly, it is expected from these results that the abrasion (wear) resistance of sample M1313 is slightly greater than sample K1908, while sample K1908 is more durable against impact wear or fracturing (chipping) than sample M1313.

Longitudinal measurement of the binder (cobalt) across the interface between the diamond and the substrate layers is achieved by performing (EDX-Quantline) measurement of the cobalt as weight percentage for the two PDC samples to monitor the binder behaviour of the two samples at the interface of two layers. Figures C.1-C.4 in Appendix-C illustrate the EDX maps along with spectra of the element distribution on the diamond and the substrate layers of the PDC cutter as well as at the interface between these two layers. Figures 4.63 show the cobalt content measurement across the interface of the diamond and the substrate layers of samples M1313 and K1908. Figures 4.63 demonstrate that the binder content of both PDC cutters in the substrate layer is lower than the standard traditional PDC cutters of (6-18%) (Yahiaoui *et al.*, 2013) suggesting the two PDC samples are having low fracture toughness.

In general, from Figures 4.63, it is shown that sample K1908 has greater cobalt content in both layers (substrate and diamond) confirming the previous results obtained from EDX maps of Figures 4.59 and 4.60 for the diamond layer and Figures 4.61 and 4.62 for the substrate layer of the PDC samples.

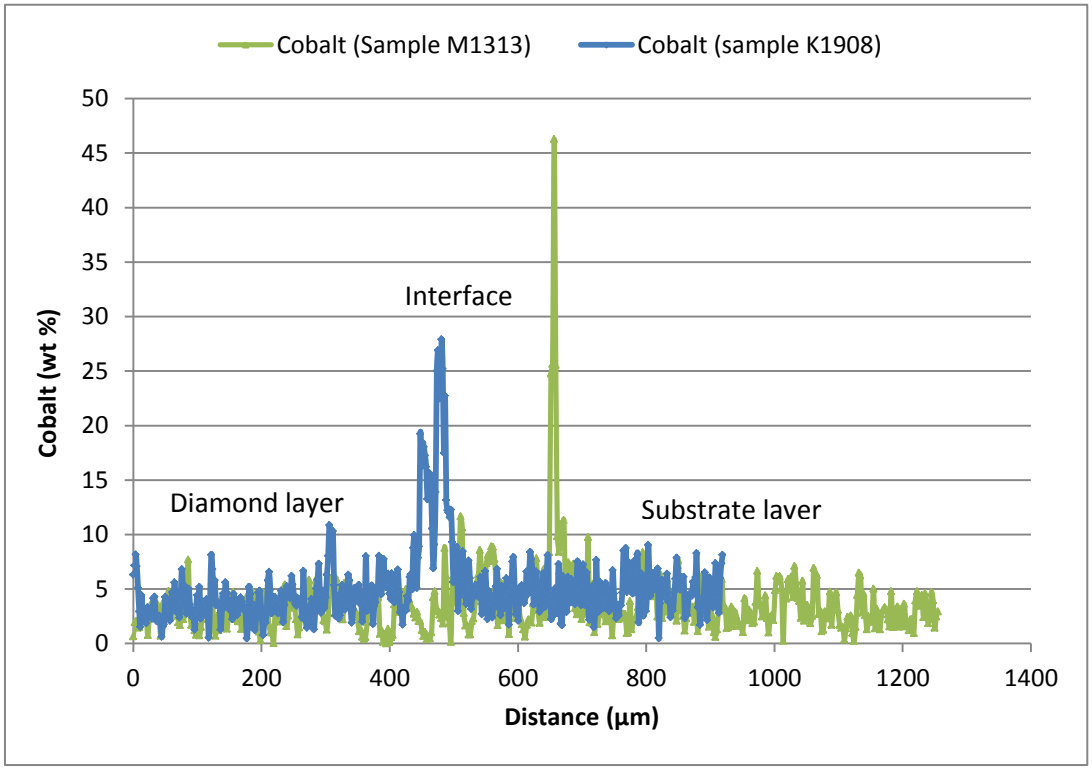

Figure 4.63 Longitudinal cobalt content across the interface of samples M1313 and K1908

Figure 4.63 shows that cobalt weight percentage exceeds 45% at the interface for sample M1313, whereas sample K1908 shows fluctuating spectra near the interface and a maximum cobalt content of about 29%. These results show that the sintering process

in sample M1313 could be more efficient compared to sample K1908, therefore the degradation of sample K1908 is expecting to be quicker than sample M1313.

4.4 Conclusions

Nano-indentation testing was carried out to measure the hardness and the Young's modulus of the materials forming the PDC samples using a Berkovich indenter. EDX images revealed that PDC cutters have three proposed zones attributed to the different components (WC, diamond and cobalt as a binder). Since the imprints from nano-indentation were of similar size to the grain/areas of a given material, a wide scatter in the hardness and Young's modulus data was unavoidable. In addition, the second reason for the variation of the obtained results from nano-indentation might be attributed to the high degree of surface roughness as the polishing process failed to satisfy the International Standard stipulated by ISO 14577-4 for polishing the specimens, therefore, in order to prevent the large fluctuation in the measurement of material properties, micro-indentation experiments were carried out as micro-indentation testing would give a bulk imprint of the tested surface of the material.

The hardness of the diamond layer of sample M1313 found to be greater than the hardness of the sample K1908 as shown in Table 4.14. This is mainly due to: (1) lower level of binder content (3.26%) in sample M1313 compared to sample K1908 that has higher cobalt content (4.4%); (2) smaller grain size of sample M1313 (12.03 μm) compared to sample K1908 (12.73 μm).

For the substrate layer, the hardness of the tungsten-carbide layer of sample M1313 is found to be higher than sample K1908 as shown in Table 4.14 and this is attributed to the difference in the cobalt content of the substrate for the two PDC cutters. The cobalt mass weight percentage in sample M1313 is near 7%, whereas sample K1908 has cobalt content of about 9%. The mean grain size of samples M1313 and K1908 is very similar.

Fracture toughness was calculated from various models based on the mechanical properties of the materials forming the PDC specimens as well as the cracks developed at the end of the indents obtained from Vickers microindentation. It was found that Lawn *et al*. (1980) and Shetty *et al*. (1985) methods provide the closest agreement to the literature values of the fracture toughness for the substrate layer of the PDC cutter, whereas the approaches of Anstis *et al*. (1981) and Laugier (1985) found to be the closest to the literature for the diamond layer of the PDC sample.

The determined mechanical properties of the materials forming the PDC specimens are strongly affected by the microstructure properties, especially the particle size distribution and cobalt content. From the obtained results, samples with high particle size distribution and high cobalt content are having low hardness and high values of fracture toughness and consequently having low abrasion wear resistance and better impact wear resistance, whereas samples having high hardness and low fracture toughness are expected to have good abrasion wear resistance and less impact wear resistance, therefore, it is expected that the amount of wear is consequently influenced by the microstructure properties of the material.

It is worth mentioning that, the balancing of the cobalt content with the particle size distribution should be achieved to gain high hardness and high fracture toughness. It is recommended for manufacturing the PDC cutters that, the grains of the tungsten-carbide alloy in the substrate layer as well as the particles of diamond in the coating layer of the PDC samples should be a mixture of coarse and fine grain size. This mixture will maintain high hardness and high fracture toughness without compromising of each one and consequently increasing the wear rate resistance for impact and abrasion. In addition, cobalt content within the substrate and the coatings should be also balanced. Leaching process (depleting the binder) of the diamond layer is needed to minimise the cobalt content after sintering to avoid the thermal expansion of cobalt when the PDC cutters are subjected to elevated temperatures causing the chipping of these cutters. Therefore, the balancing of cobalt content and the particle size distribution will enhance the PDC inserts against impact and abrasive wear.

The next chapter will discuss the quantification of the abrasive wear for the substrate and the coating layers of the PDC cutters that mainly depend on the properties of the materials forming these layers.

Chapter 5 Experimental Scratch Testing

Any macroscopic or microscopic removal or fracture of material, especially at the cutter surface, or any degradation that reduces bit life, is considered to be wear (Mouritz and Hutchings 1991). Richardson (1968) as well as Mouritz and Hutchings (1991) showed that the abrasive wear of the material depends on the term of abrasive hardness over material hardness (H_a/H_m). It is found that when (H_a/H_m) less than 1, a very low abrasive wear rate will occur. However, when (H_a/H_m) is greater than 1.2, the abrasive could scratch the material causing a high abrasive wear rate. The wear of the roller-cone bits, as well as PDC bits, is a major issue during drilling that leads to severe time losses which affect the overall drilling operation cost. Therefore, it is essential to evaluate the wear tendency of the material forming the drill bits.

In the literature, different tests have been performed, especially on PDC bits, and particularly for the cutters, to evaluate their effectiveness and reliability in harsh environments. The majority of the previous tests are destructive (Bellin *et al.*, 2010). The abrasion test is the most commonly used one, where the abrasive wear of the material is evaluated against the rocks with different hardnesses. In these tests, the mass loss measurements represent the volume of bit wear. Although, previous tests for evaluating the wear of the PDC inserts are beneficial, precise measurement of the material loss remains an issue.

The current chapter is focused on studying the wear mechanisms of PDC cutters and the effect of their mechanical properties on the extent of wear. The volume of wear for the PDC cutters was determined experimentally using micro and nano-scratch tests on different layers of PDC cutters, i.e. the diamond layer and tungsten-carbide (substrate layer) by implementing an approach based on the geometry of the removed material after such tests. In addition, this chapter illustrates how the experimental wear is compared to the predicted wear based on current approaches in the literature. Various wear models are evaluated for micro and nano- scratch tests on both layers of the PDC samples: WC-Co and diamond.

5.1 Micro-scratch testing

The scratch caused by a sharp indenter produces abrasion wear. The wear mechanism caused by scratch testing is mainly dominant by ploughing and cutting. A series of micro-scratch tests are carried out by applying various loads to a probe acting on the surface of the PDC specimens (substrate and coating); moving the probe a sufficient

sliding distance to produce a scratch. The resulting scratch length and width are focused to evaluate the wear of the material. Budinski (2007) proposed an approach to determine the hardness of the material from scratch tests based on the width of the obtained groove and the applied load to cause that scratch. Figure 5.1 demonstrates the scratching using a hard particle or indenter and the grooves generated. In this study, micro-scratch tests are also applied for determining the hardness of the material being scratched, for which Equation (5-1) is applied.

$$SHN = \frac{8\ F}{\pi\ w_s^2} \qquad (5-1)$$

where *SHN* is the scratch hardness number (GPa), *F* is the applied force (mN) and w_s is the scratch width (μm).

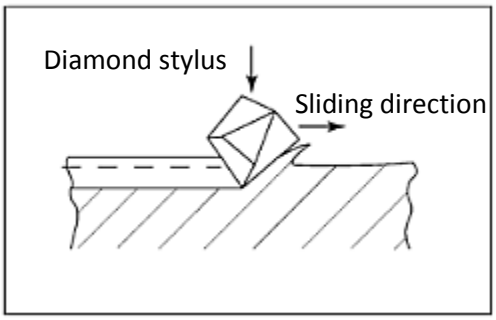

Figure 5.1 Scratch test using a sharp indenter (Budinski, 2007)

Experimentally, the micro-scratch test is performed using Instron 5566 mechanical tester with a diamond probe. Vickers and conical-spherical diamond indenters have been used during the micro-scratch tests on both layers of the PDC samples.

It is quite challengeable to standardise the scratch testing (micro and nano) as there are many variable parameters affect this testing. However, ISO-14577 and ASTM E2546 standards could be applied for micro and nano-scratch testing as mainly these tests are controlled by load or depth selection (CSM, 2002). In this study, the micro and nano-scratch testing are controlled by load selection.

The obtained micro-scratches were examined by SEM, EDX and surface profilemeter.

5.1.1 Micro-scratch test of the substrate layer of the PDC samples using Vickers indenter

A series of micro-scratch tests using a Vickers indenter were conducted on both layers of the PDC specimens under various loads. The samples were mounted on an anvil that has a manual controller to alter the sliding distance. The substrate of the PDC sample

was scratched using loads of 100 - 300 N as at this load range the corresponding mechanical properties are available from section 4.2.3.1.1. Measured wear from micro scratch tests was compared to the predicted wear based on approaches in the literature by Rabinowicz (1996), Hutchings (1992) and Ning and Ghadiri (2006). Figure 5.2 shows a SEM image of a groove obtained from a micro-scratch test when applying a load of 200 N on the tungsten-carbide layer using a Vickers indenter for the sample M1313. SEM images for the same scratch testing using Vickers indenter on the substrate of sample M1313 at applying loads 100 and 300 N are shown in Figures D.1 and D.2 respectively in Appendix- D. Table 5.1 illustrates the results obtained from the scratch tests using a Vickers probe on the substrate layer of the sample M1313. Once the grooves were obtained from micro-scratch test, the scratches are examined by SEM to determine their width and finally, the scratch hardness number is calculated from Equation (5-1).

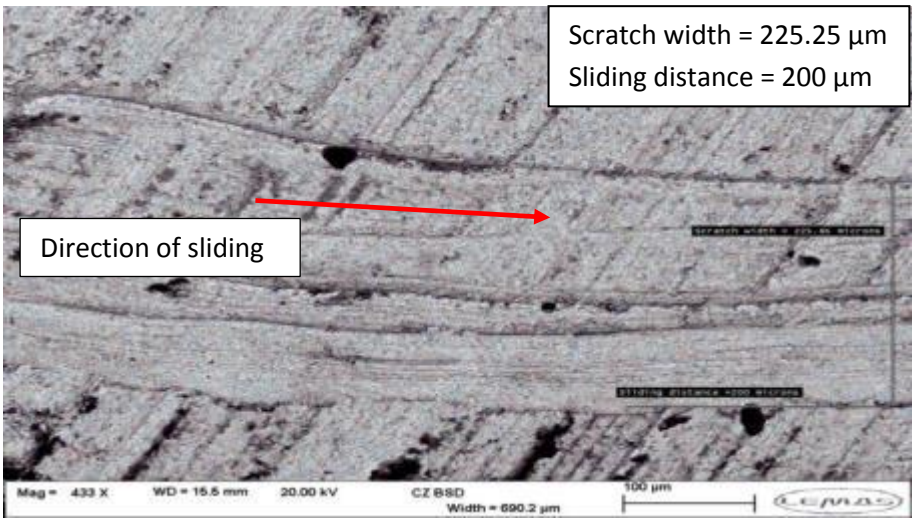

Figure 5.2 Tungsten-carbide layer after a scratch test with a Vickers indenter under 200 N load

Table 5.1 Results of the scratch test of the tungsten-carbide layer of the sample M1313

Load (N)	Vickers hardness (GPa)	Sliding distance (µm)	Scratch width, (b), (µm)	Scratch height (h), (µm)	Scratch hardness number (GPa)
100	13.095	200	177.8	35.918	8.055
200	13.139	200	225.25	45.503	10.038
300	12.983	200	251.03	50.711	12.123

The scratch height of the obtained groove from the micro-scratch test is measured by a 2D Talysurf profilemeter. Groove depths measurements were carried out using Ultra

Precision Talysurf PGI800 with a resolution up to 3.2 nm. Figure 5.3 shows a profilemeter image of a scratch obtained after applying a 100N load on the substrate layer of sample M1313 using Vickers indenter.

The volume of wear is calculated experimentally from the geometry of the removed material using the following equation:

$$V_W = \frac{b\,.\,h}{2}\ X \qquad (5-2)$$

where b is the width of the scratch (measured here by scanning electron microscopy), h is the height of the scratch (obtained using the 2D profilemeter and X is the sliding distance.

Figure 5.3 Two dimensional Talysurf profilemeter showng the depth of scratch occurred on the substrate layer after applying 100 N for sample M1313

In the literature, abrasion wear models are used to quantify the wear between the abrasive and the abraded bodies for different kinds of materials. The experimental wear obtained from the micro-scratch tests is compared with three different wear models Rabinowicz (1996); Hutchings (1992) and Ning and Ghadiri (2006) using Equations (2-14), (2-15) and (2-19) respectively as these wear models depends mainly on the mechanical properties of the material being tested and they are used to quantify the wear of ceramics and alloy metals using various loads and sliding distances. Therefore, the experimental results of wear obtained from micro and nano-scratch testing are validated with the three wear models mentioned above. Archard wear model is used for the determination of the coefficient of abrasive wear, while other models such as the model of Element six Ltd. is turned out due to inadequate explanation for this empirical model.

When applying Vickers indenter during the micro-scratch test, the volume of wear of the material is determined based on the geometry of the removed material as shown in Figure 5.4.

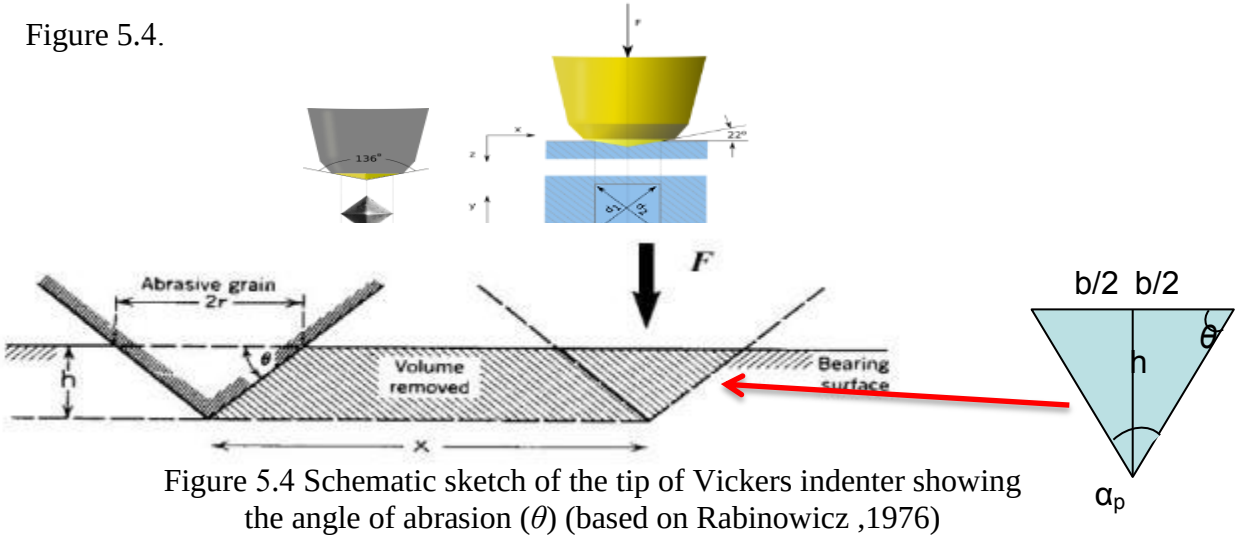

Figure 5.4 Schematic sketch of the tip of Vickers indenter showing the angle of abrasion (θ) (based on Rabinowicz ,1976)

Figure 5.4 shows a schematic sketch of the abrasive probe and the angle of abrasion. The angle of abrasion (θ) is 22˚ and the angle (α_p) or the half angle of the abrasive indenter is (136˚ /2) or 68˚, when using a Vickers indenter. The hardness and the fracture toughness of the material used in Equations (2-14), (2-15) and (2-19) are obtained from previous microindentation results shown in chapter four.

Figure 5.5 demonstrates the results of experimental wear along with the calculated abrasive wear obtained from three models for the substrate layer of the sample M1313.

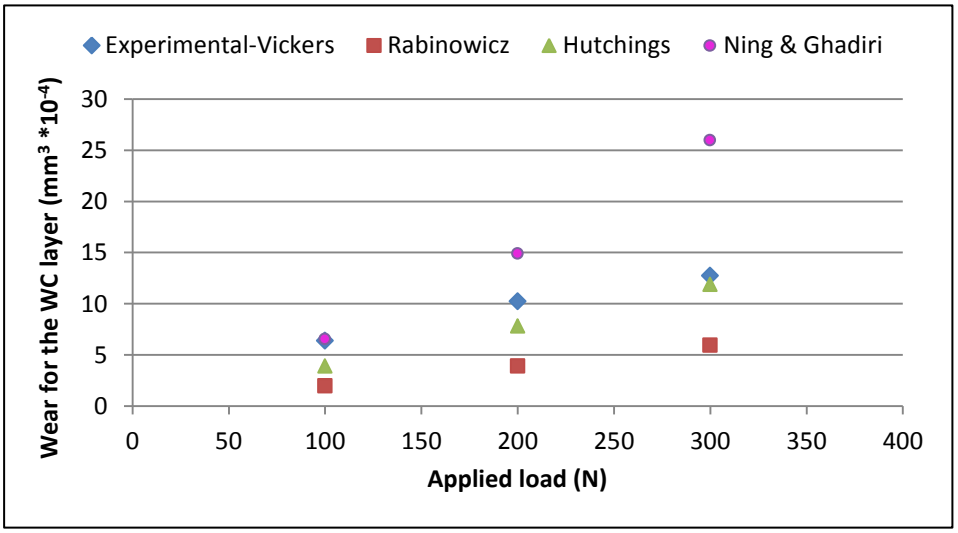

Figure 5.5 Wear calculated from different techniques for the substrate of sample M1313

The wear increases with load, as predicted by all models. The model of Rabinowicz (1996) gave lower wear values than the experimental wear, while Ning and Ghadiri's (2006) model displays a higher trend than the experimental one. Hutchings' (1992) wear model displays the closest agreement to the experimental data. As mentioned in section

2.3.2.3 that the expected obtained wear values from Hutchings' (1992) would be double of those obtained from Rabinowicz and this is due to the different assumption made upon deriving their models. Rabinowicz developed his model basing on the projected area of the cone indenter which assumed to be a whole circle, while Hutchings assumed that the projected is half circle. Ning and Ghadir model is following a polynomial fitting, where at low loads, the wear predicted by this model shows a close agreement to the experimental wear. However, when the load is increased, the wear predicted by this model has higher trend. Ning and Ghadiris' model depends mainly on the fracture toughness and not affected by the angle of abrasion or the half angle of the abrasive particle as in Rabinowiczs' and Hutchings' models.

5.1.2 Micro-scratch test of the diamond layer of the PDC samples using Vickers indenter

A series of micro-scratch tests using a Vickers probe were carried out on the diamond layer of the PDC specimen. Special care should be taken in scratching the surface of the diamond layer, and low loads, varied from 10 N to 20 N were applied to avoid damaging the tip of the indenter due to the high resistance of the material surface and a high degree of asperities. Figure 5.6 illustrates the groove as a result of applying a 20 N load on the diamond layer of the PDC insert of the sample M1313 using a Vickers indenter. More images showing the micro-scratches resulting from using Vickers indenter are presented in Figures D.3 and D.4 in Appendix –D, where the applied loads used were 10 and 15 N respectively. Table 5.2 illustrates the results obtained from scratching the diamond layer of the sample M1313. The Vickers hardness is taken to be the average value from the previous microindentation tests for the sample M1313.

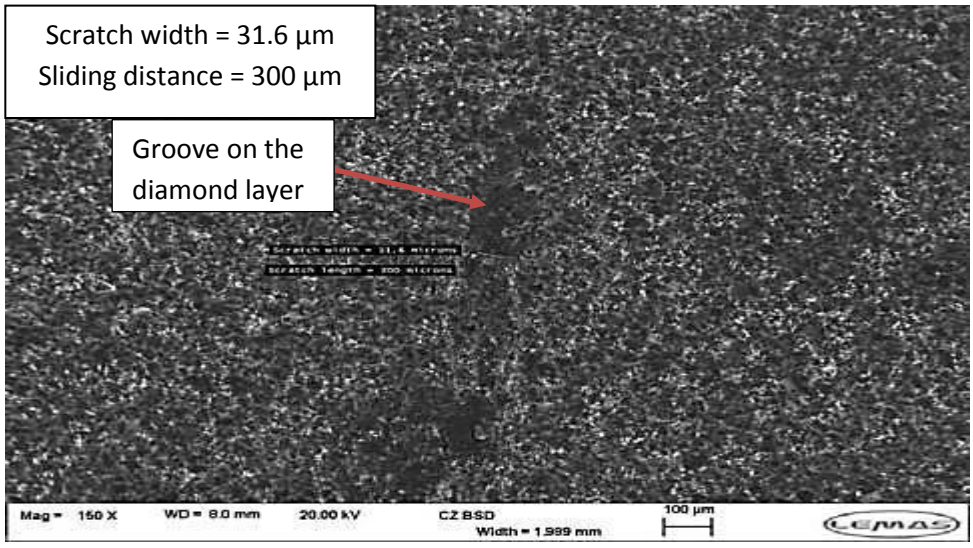

Figure 5.6 Scratch obtained with Vickers probe at 20 N for the diamond layer of the sample M1313

Table 5.2 Micro- scratch test results of the diamond layer of the sample M1313

Load (N)	Vickers hardness (GPa)	Sliding distance (µm)	Scratch width, (b) µm)(	Scratch depth (h), (µm)	Scratch hardness number (GPa)
10	50.85	300	23.7	4.787	45.336
15	50.85	300	28.4	5.737	47.358
20	50.85	300	31.6	6.383	51.003

The experimental wear of the diamond layer as a result of micro-scratch test using Vickers indenter is calculated from Equation (5-2) and then compared to the predicted wear based on approaches in the literature.

Average values for hardness and fracture toughness from previous chapter were used for the calculation of wear from the models of Rabinowicz (1996); Hutchings (1992) and Ning and Ghadiri (2006). Figure 5.7 illustrates the wear obtained from the experiments and predicted from the models.

From Figure 5.7, the trend of wear versus load for the diamond layer of the sample M1313 is similar to that of the substrate, where Hatchings' wear model seems to be the nearest to the experimental wear, whereas Ning and Ghadiri's (2006) model shows the greatest disagreement to the experimental one. This might be due to the great influence of fracture toughness on the Equation of Ning and Ghadiri as shown in section 2.3.2.3.

Despite the special care which was taken into account during the tests, the tip of the indenter was found to get damaged after applying 20N. Figure 5.8 shows an SEM image for the tip of the Vickers probe after preceding micro-scratch tests at load 20 N on the diamond coating of the PDC sample M1313. The image shows that the tip of the probe was damaged by the above tests and could not be used for further-scratch tests. As such, further scratch tests were completed using a spheroconical indenter.

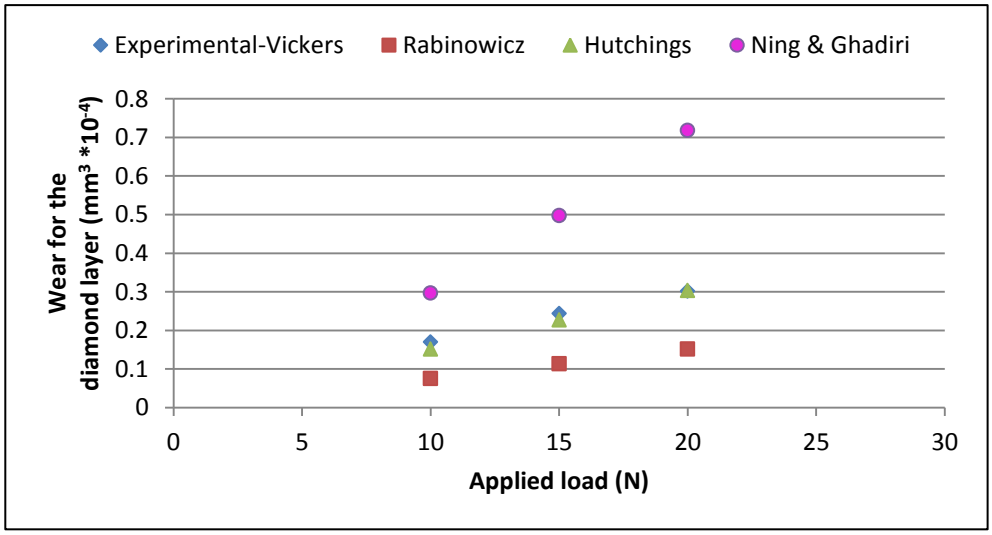

Figure 5.7 Experimental and predicted wear calculated for the diamond-cobalt layer for the sample M1313

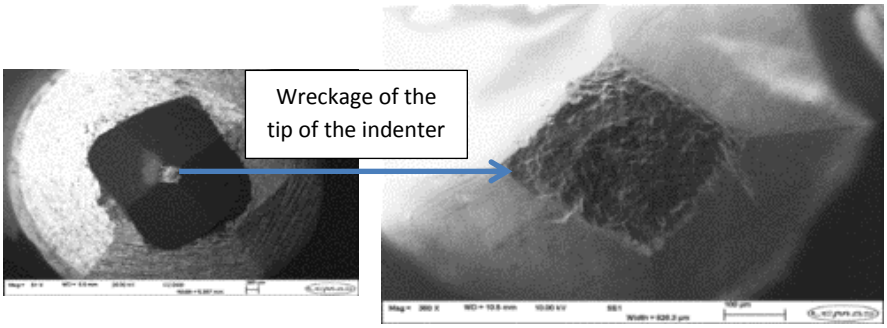

Figure 5.8 Damaged tip of the Vickers indenter after scratching the diamond layer of sample M1313 at 20 N applied load

5.1.3 Micro-scratch test of the substrate layer of the PDC samples using a spheroconical indenter

Due to the high risk of damaging the diamond indenter , especially when conducting the micro- scratch testing on the diamond layer of the PDC samples as shown above, further scratch tests were performed using spheroconical indenter. The use of a spherical tip of the probe is an effective option that reduces the risk of breakage compared to the use of sharp indenters, particularly when scratching hard coatings (Beake *et al.*, 2011). The spheroconical indenter has a 100 micron radius and conical angle of 91.579˚ and is shown in Figure 5.9.

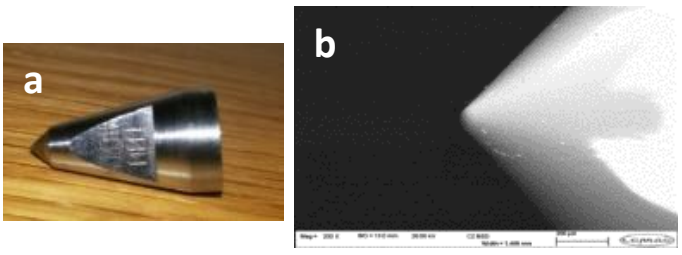

Figure 5.9 Spheroconical probe used in the micro-scratch testing (a), SEM image of the tip of the spheroconical indenter (b)

The spheroconical indenter is used to carry out a series of micro-scratch tests for the substrate layer of different PDC samples at various loads.

Figure 5.10 shows an SEM image of a groove obtained from micro-scratch testing of the substrate layer of M1313 sample using a spheroconical indenter at 75 N, while Figure 5.11 shows the groove produced after applying 50 N on the substrate layer of sample K1908 using diamond spheroconical tip indenter. Figures D.5-D.8 in Appendix-D show the grooves obtained from micro-scratching with a spheroconical indenter after applying loads 100, 200, 25 and 75 N respectively on the substrate layer of sample K1908, while Figures D.9 and D.10 in Appendix-D illustrate the scratches obtained when applying loads 50 and 65 N respectively on the substrate layer of sample M1313. The SEM images in Figures 5.10 and 5.11 show that the debris resulting from the ploughing action due to the micro-scratching of the samples M1313 and K1908 is dispersed outside the groove as well as accumulating on both sides of the scratch. Tables 5.3 and 5.4 illustrate the micro-scratch testing results (scratch width and height) performed on the substrate layers of the samples M1313 and K1908 respectively with a spheroconical probe. Scratch hardness number was calculated for comparison with Vickers hardness.

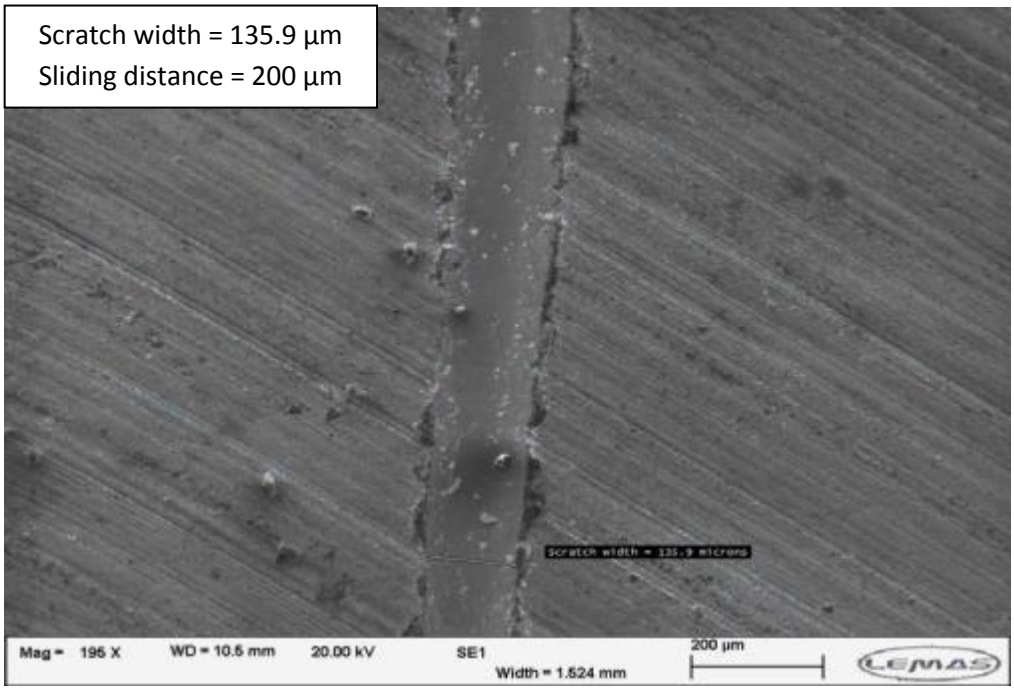

Figure 5.10 Scratch obtained at load 75 N on the substrate layer of the sample M1313 due to micro-scratching with spheroconical probe

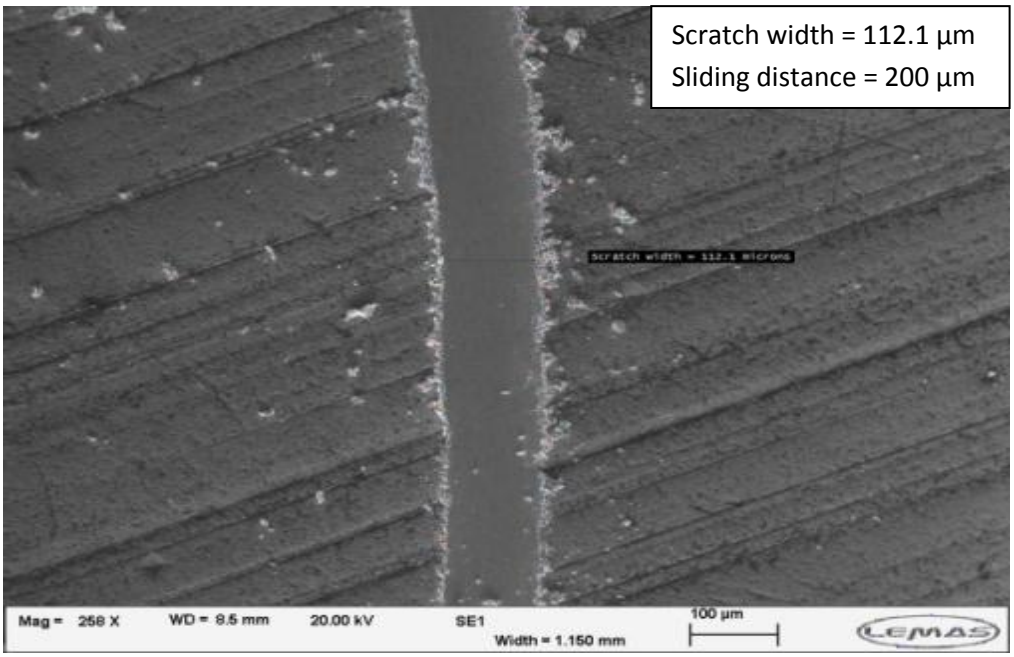

Figure 5.11 Groove obtained using spheroconical indenter at 50 N load for the WC-Co layer of the sample K1908

Table 5.3 Results of micro-scratch testing of the substrate layer using spheroconical indenter for the sample M1313

Load (N)	Vickers hardness (GPa)	Sliding distance (µm)	Scratch width, (b) µm)(	Scratch depth (h), (µm)	Scratch hardness number (GPa)
50	13.072	200	108.2	21	10.875
65	13.072	200	126.74	25.75	10.304
75	13.072	200	135.9	27.3	10.341

Table 5.4 Results of micro-scratch testing of the substrate layer using spheroconical probe for the sample K1908

Load (N)	Vickers hardness (GPa)	Sliding distance (µm)	Scratch width, (b) µm)(	Scratch depth (h), (µm)	Scratch hardness number (GPa)
25	12.533	200	72.64	15	12.065
50	12.903	200	112.1	22.02	10.132
75	12.752	200	125.8	30.11	12.068
100	12.771	200	145.2	37	12.078
200	12.770	200	203.9	44.03	12.25

The height of the groove is determined from the 2D profilemeter. Figure 5.12 shows the topography of a scratch using spheroconical indenter for the substrate layer of the sample K1908 when applying load of 50N.

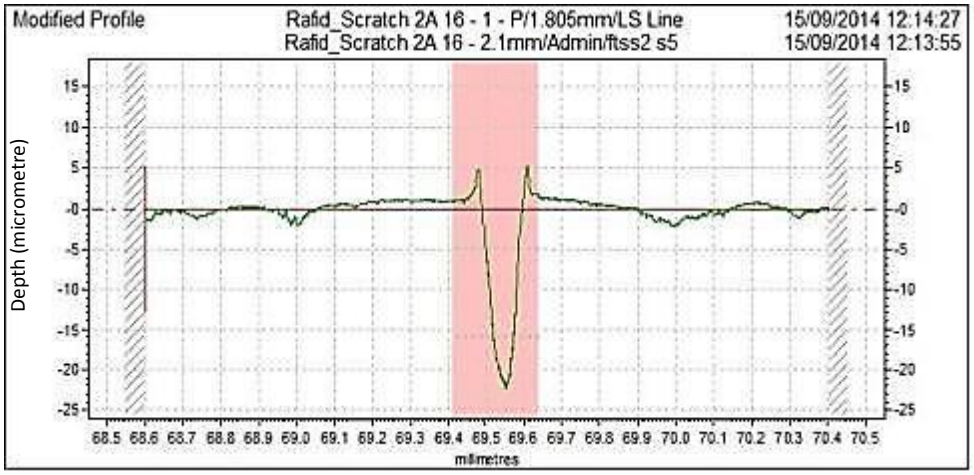

Figure 5.12 Two-dimensional Talysurf profilemeter of a scratch occurred on the substrate layer after applying 50 N for the sample K1908 using spheroconical probe

The schematic geometry of the micro-scratch process with a spheroconical indenter is illustrated in Figure 5.13, where the depth or height of the material removed (h) is shown along the scratch distance (X).

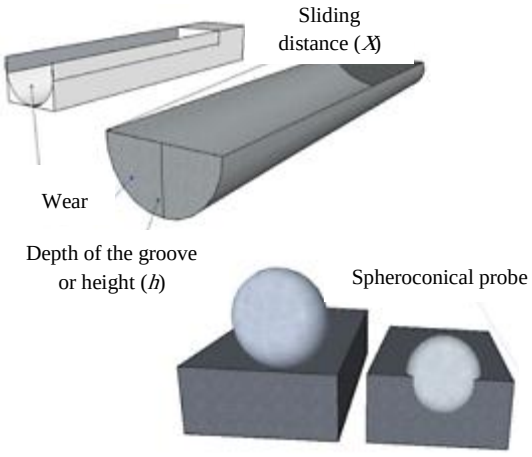

Figure 5.13 Schematic geometry of the worn material using spheroconical indenter during micro-scratch testing

The resulting wear from micro-scratch test is determined from the following equation which is found to quantify the wear volume along the scratch path as follows (CSM Instruments., 2002):

$$V_w = A_{segment} * L \qquad (5-3)$$

where $A_{segment}$ is the area of the circular segment as seen from Figure 5.14 and L is the sliding distance .The final equation of the circular segment is determined from Equation (5-4): (The full derivation is shown in Appendix –A.C.

$$A_{segment} = \frac{1}{2} * {R_C}^2 * \ [\theta - sin\theta] \qquad (5-4)$$

where θ is the angle opposing the segment of the circle (Figure 5.14) and it can be obtained from Equation (5-5):

$$\theta = 2\,cos^{-1}\left(1 - \frac{h}{R_C}\right) \qquad (5-5)$$

where R_C is the radius of the circle and h is the residual depth of the micro- scratch as shown in Figure 5.14:

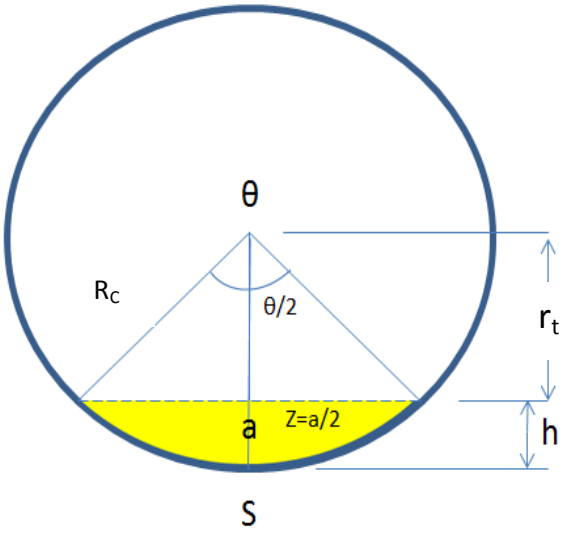

Figure 5.14 Sketch of the circular segment of the spheroconical indenter tip that indents the layer of the sample

The experimental wear at various load points obtained from the micro-scratching with a spheroconical indenter of the substrate layer of the sample M1313 is compared to the literature wear models (Figure 5.15). Figure 5.16 displays the experimental wear compared to the predicted one obtained from various wear models for the substrate layer of the sample K1908. The mechanical properties of the substrate layer and the diamond needed for the wear models are taken from chapter four.

Figures 5.15 and 5.16 display that Hutchings' (1992) wear model is the nearest to the experimental wear for the substrate layer when a spheroconical indenter is used, while other models show lower values than the experimental one. This is attributed to the

assumption of the projected tip of the cone indenter is a half circle when scratching is achieved with a conical indenter as mentioned by Hutchings'. This assumption is so close to the geometry of the removed material within scratch testing illustrated in Figure 5.13. It is worth mentioning that, the abrasion angle as well as the half angle of the abrasive particle when scratching with a conical indenter are 44.2 ° and 45.78 ° respectively, while the same angles are 22 ° and 68 ° when Vickers indenter is used. This clearly shows that the values of wear volume obtained from Rabinowicz and Hutchings are higher when conical indenters are used compared to the previous values of wear volume when Vickers are used. Ning and Ghadiris' model exhibits low wear at low loads and then showing higher trend due to the polynomial behaviour]r of this model

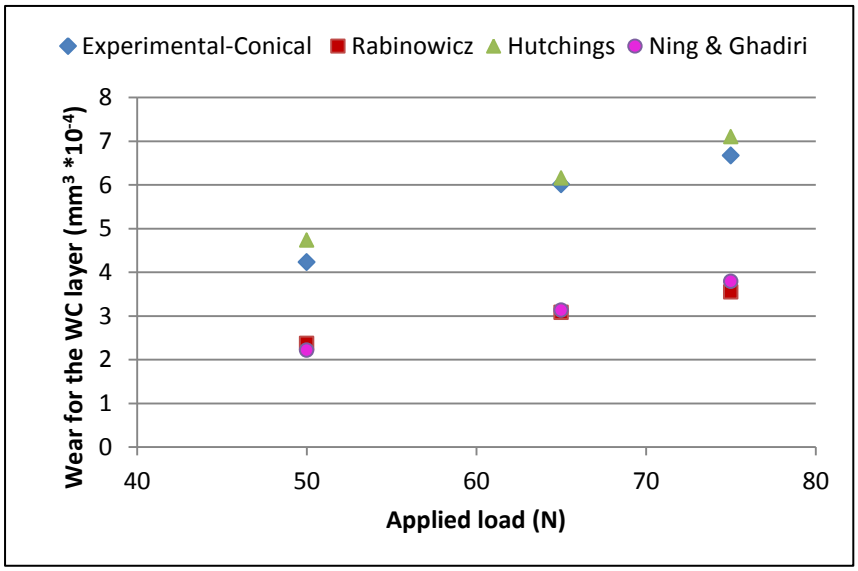

Figure 5.15 Experimental wear compared to the literature wear models for the WC-Co layer of sample M1313

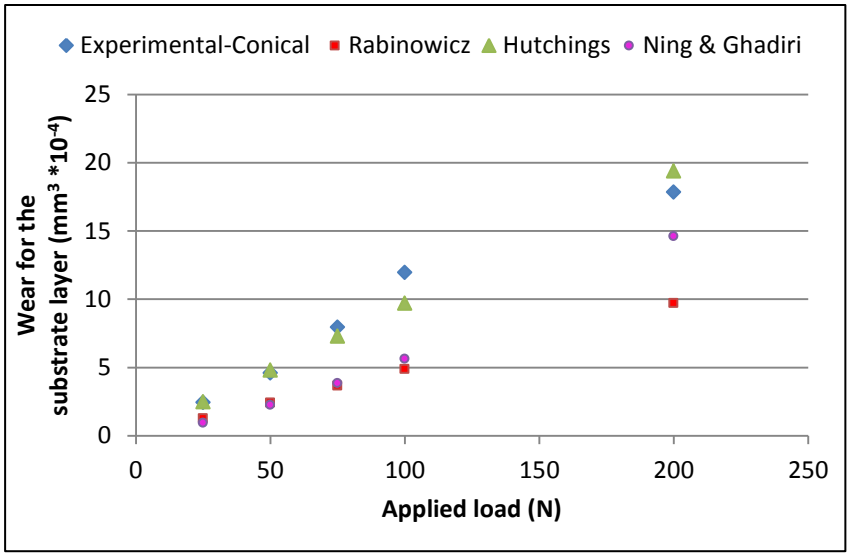

Figure 5.16 Wear comparison for the substrate layer of sample K1908 using spheroconical indenter

The wear in Figures 5.15 and 5.16 illustrate an increasing trend with load. Ning and Ghadiri's (2006) wear model show values lower than the experimental one, while the same model exhibits values higher than the experimental wear in the case of micro-scratching with Vickers indenter and this due to the fact of Ning and Ghadiri's model depends on the fracture toughness of the sample and there is no effect of the abrasion angle (θ) and the half angle of the abrasive indenter (α_p).

5.1.4 Micro-scratch test of the diamond layer of the PDC samples using spheroconical indenter

Series of micro-scratch tests with spheroconical probe were performed on the diamond layer of different PDC samples at various loads. Figure 5.17 shows a BSE image displaying the groove obtained from the micro-scratch test of the diamond layer with a spheroconical indenter for the sample M1313 at 5 N. There is no evidence of debris inside or around the groove. Figure 5.18 shows the scratch produced after scratching the diamond layer of the sample K1908 at 2.5 N. Also, no debris is found to be produced after carrying-out the micro-scratch test for the diamond layer of this sample. Figures D.11 and D.12 in Appendix-D show the SEM images of the grooves produced from micro-scratching with a spheroconical indenter for the diamond layer of sample K1908 when applying 20 and 10 N respectively. Figures D.13 and D.14 in Appendix-D illustrate the scratches obtained from the micro-scratch testing of the diamond layer at applied loads of 7.5 N for samples M1313 and K1908 respectively.

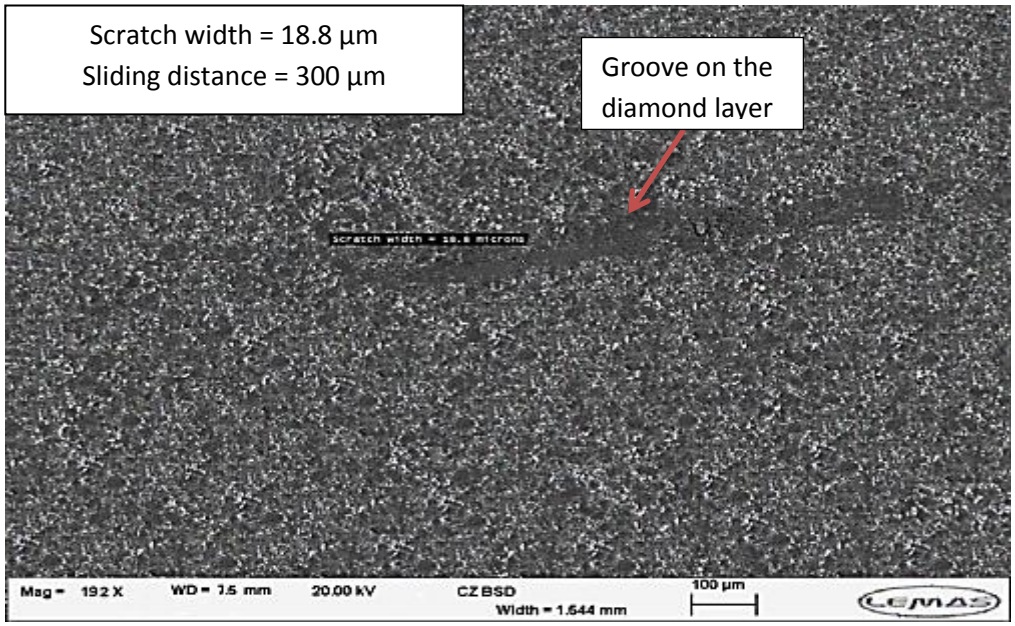

Figure 5.17 BSE image illustrates a groove obtained when applying 5 N load on the diamond layer of sample M1313

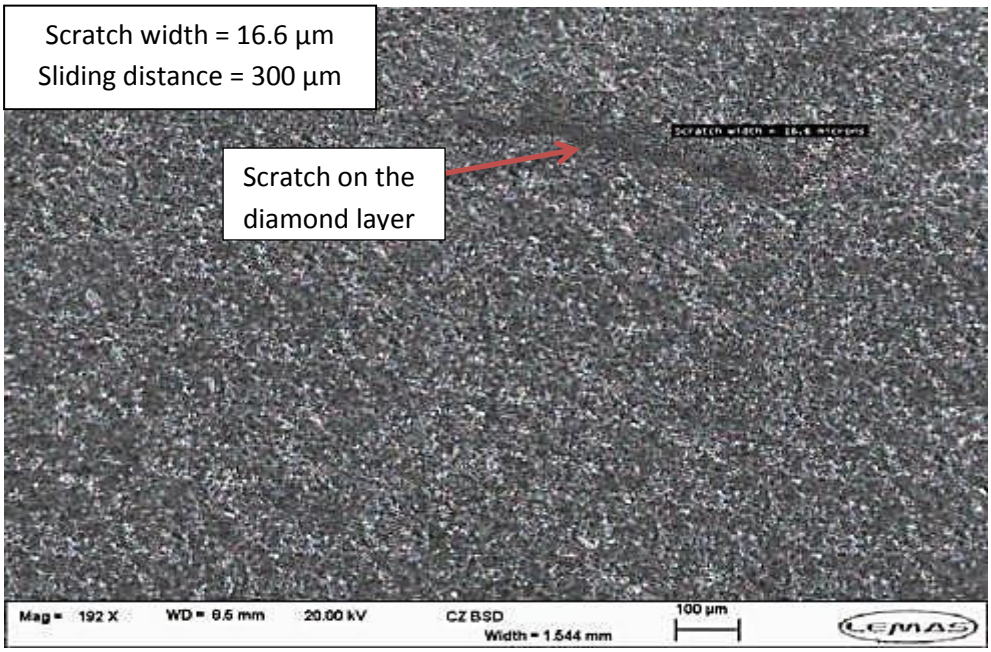

Figure 5.18 BSE image shows a scratch obtained when applying 2.5 N load on the diamond layer of sample K1908

Tables 5.5 and 5.6 illustrate the micro-scratch testing results (scratch depth and width) performed on the diamond layers of the samples M1313 and K1908 respectively, with a spheroconical probe. The scratch hardness number was calculated from the results of the scratch tests. At low loads, the results of the scratch hardness number show low hardness and increased with load until the value will be fixed.

Table 5.5 Results of micro-scratch testing of the diamond layer using spheroconical indenter for the sample M1313

Load (N)	Vickers hardness (GPa)	Sliding distance (µm)	Scratch width, (b) µm)(	Scratch depth (h), (µm)	Scratch hardness number (GPa)
3	50.85	300	17.8	1.73	24.111
5	50.85	300	18.8	2.4	36.024
7.5	50.85	300	20	3	47.746

Table 5.6 Results of micro-scratch testing of the diamond layer using spheroconical indenter for the sample K1908

Load (N)	Vickers hardness (GPa)	Sliding distance (µm)	Scratch width, (b) µm)(	Scratch depth (h), (µm)	Scratch hardness number (GPa)
2.5	46.1	300	16.6	1.6	23.102
7.5	46.1	300	21.4	3	41.703
10	46.1	300	24	4.1	44.209
20	46.1	300	34.3	5.8	43.289
30	46.1	300	41.48	7.3	44.4

Figure 5.19 illustrates the topography of a scratch obtained from the micro-scratching of the diamond layer of the PDC sample K1908 at load 2.5 N where the indentation depth is obtained. Figure 5.19 shows two positive peaks at the edges of the groove. These two peaks refer to the ridges of the scratch causing as called (pile-up). It might be that cobalt is showing this kind of pile-up as it is shown later in the analytical study that cobalt is dislodged from the groove after scratching the area and accumulated at the edges of the scratch.

Figure 5.20 and 5.21 show the comparison between the experimental wear obtained from the micro-scratch test with a spheroconical probe for the diamond layer and the wear predicted by various wear models for the samples M1313 and K1908, respectively.

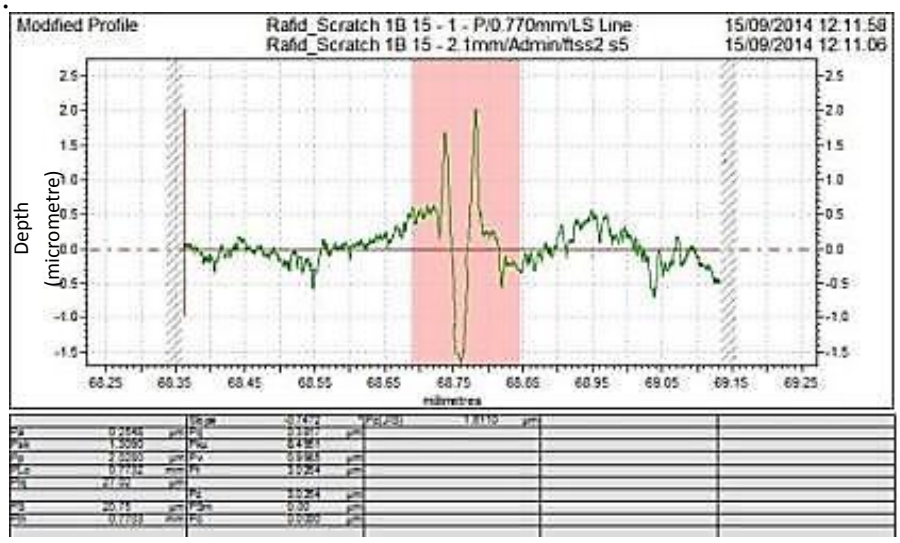

Figure 5.19 Two-dimensional Talysurf profilemeter of a groove obtained after applying load of 2.5 N using spheroconical indenter on the diamond layer of the sample K1908

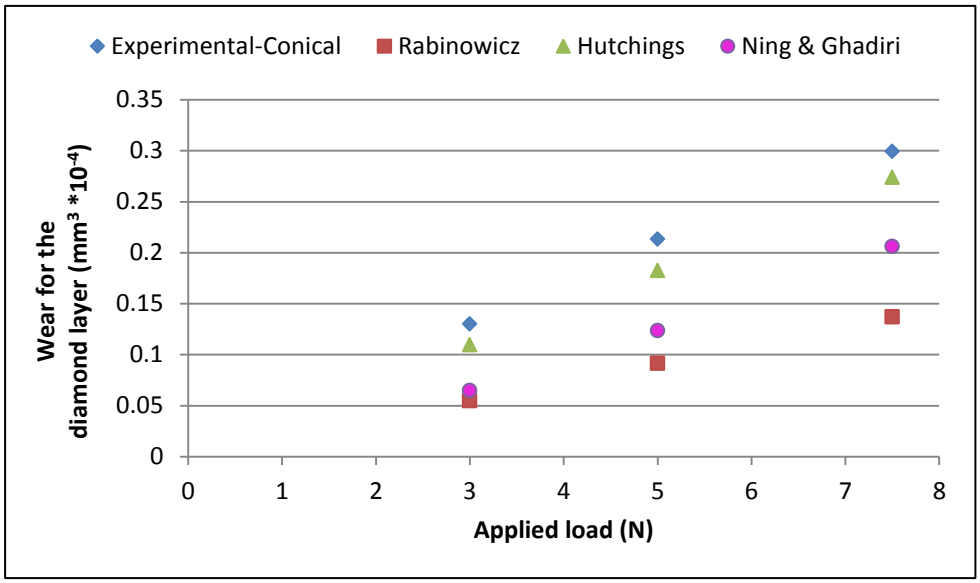

Figure 5.20 Experimental and predicted wear of the diamond layer of the sample M1313

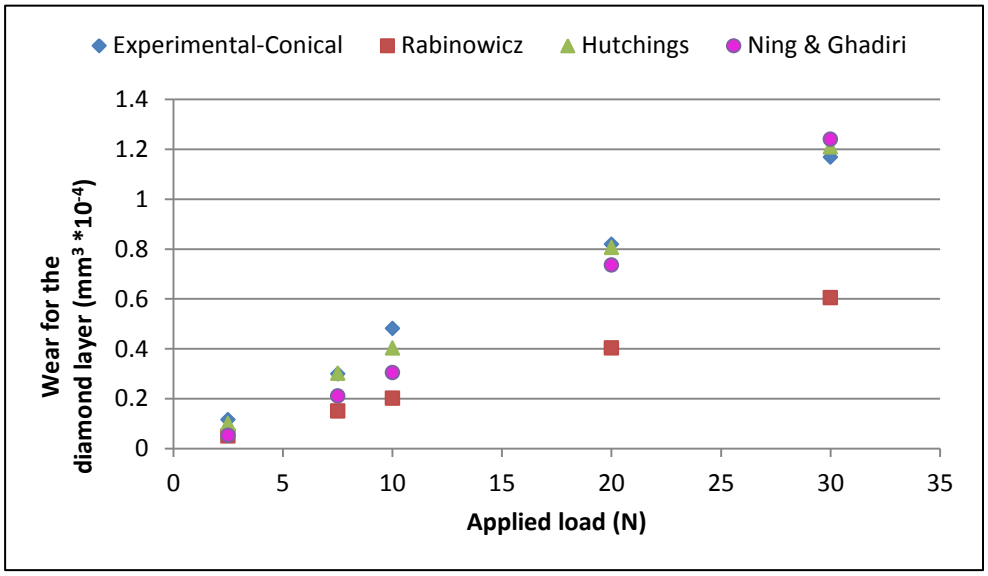

Figure 5.21 Predicted wear compared to the experimental one of the diamond layer of the sample K1908

Figure 5.20 shows that Hutching's (1992) model is the closest to the experimental wear within the micro-scratch test when using spheroconical indenter, whereas Ning and Ghadiri's (2006) model gave lower values as compared to the micro-scratch test when using Vickers indenter. This may be due to the fact that the abrasion angle (which has no effect in this model) of the conical probe is greater than the abrasion angle of the Vickers probe.

It is worth noting that the obtained graphs for sample K1908 show that all measured wear models have lower values than the experimental wear except Hutchings'(1992) model which displays close results to the experimental from micro scratching.

The tip of the spheroconical indenter is examined for any damage might occur after performing the micro-scratch testing. Figure 5.22 shows the tip of the spheroconical probe and it seems that the indenter is intact after carrying out micro-scratching on the diamond layer of the PDC samples.

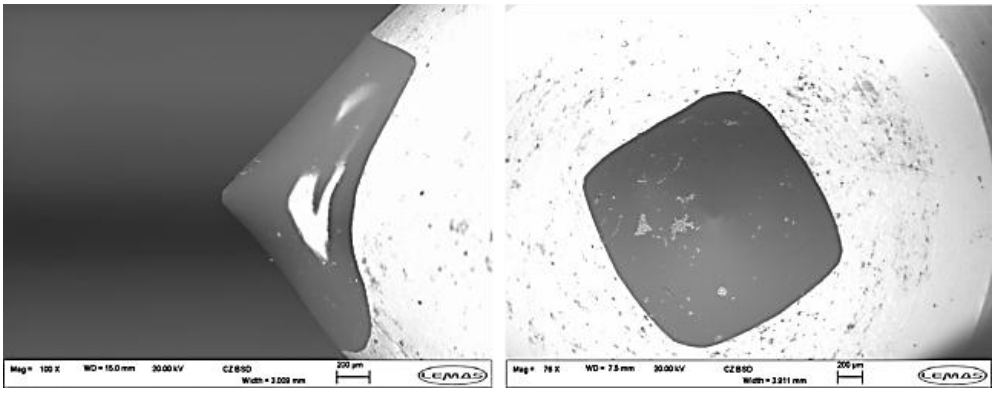

Figure 5.22 SEM image of the tip of the spheroconical indenter shows undamaged tip

5.1.5 Analytical study

5.1.5.1 Substrate layer

The objective of the analytical study is to study the wear mechanisms of the PDC samples and the composition distribution along the scratched areas on both surfaces of the PDC sample (coating and substrate). Analytical part is carried out on both scratched layers of the PDC inserts obtained from the micro-scratch test with two indenters Vickers and spheroconical. Energy dispersive X-ray maps and spectroscopy analyses were applied on scratches to investigate the mechanisms of wear. Figure 5.23a demonstrates a coloured X-ray map of the main minerals forming the substrate layer: Tungsten (W), Carbon (C) and Cobalt (Co) as a binder for sample M1313, while Figure 5.23b shows the mineral spectroscopy along a micro-scratch obtained from Vickers probe on the WC-Co layer of the same sample of the PDC cutter at 100 N.

It can be seen that amount of tungsten (W) decreased sharply at the edges of the scratch with an overall decrease within the scratch distance. Carbon (C) seems to increase on the scratch edges with reduction trend in between, while the binder (Co) rises along the scratch. X-ray maps displays clearly that composite alloy of W-C is almost dislodged

from the scratch and the cobalt grains are occupying the scratch instead of the displaced WC particles.

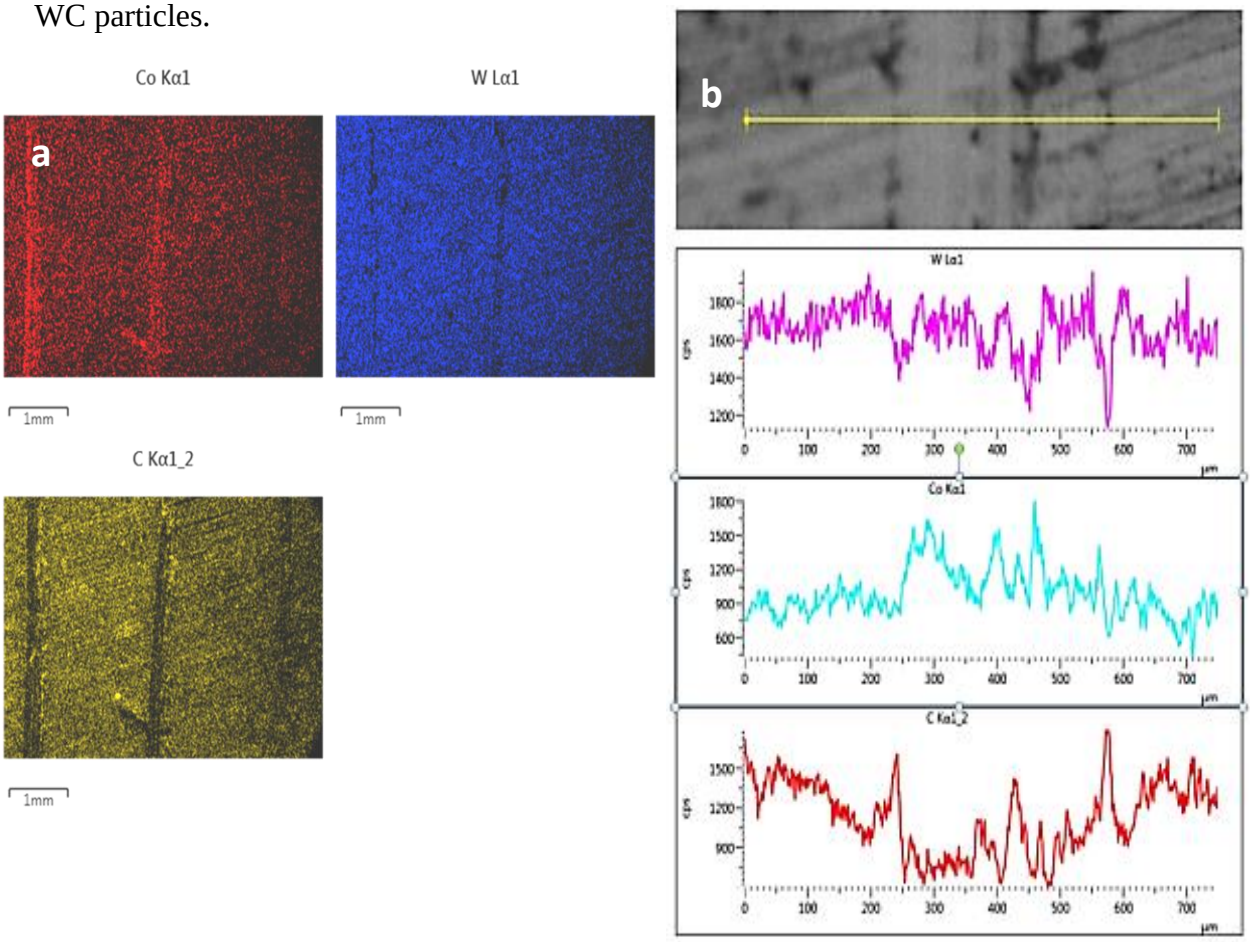

Figure 5.23 (a) X-ray maps of microscrtaches on the substrate layer using Vickers indenter of the sample M1313, (b) Spectroscopy of main minerals along the scratch on the substrate for the sample M1313

Analysis of the scratches obtained from using spheroconical indenter is also carried out on the substrate layer of both samples. Figure 5.24 illustrates the X-ray maps of a groove obtained from micro-scratching the substrate layer of the sample K1908 with a spheroconical indenter, while Figure 5.25 shows the EDS analysis along the scratch on the substrate layer of the sample K1908 at load 25 N.

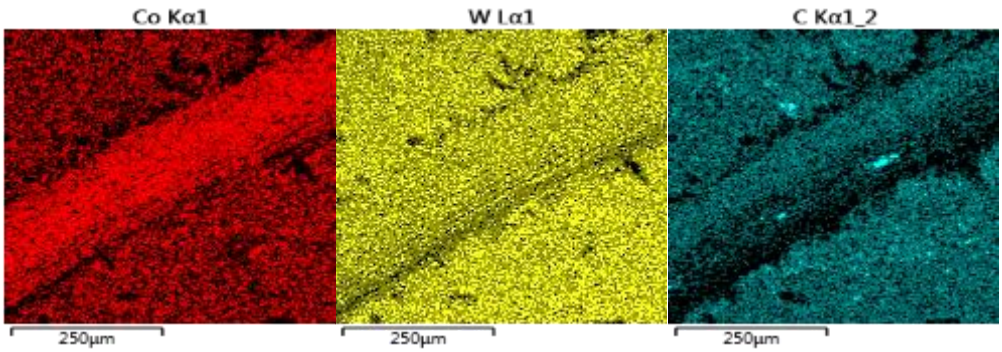

Figure 5.24 X-ray maps of a scratch on the WC-Co layer after applying 100 N for sample K1908

The X-ray analysis of micro-scratch tests on the substrate layer of the PDC samples (Figures 5.23a and 5.24) reveals the fact that the bonds between the tungsten-carbide alloy and the binder (cobalt) are broken showing that cobalt occupies the scratched area and possibly produces piling up of carbon on the scratch edges.

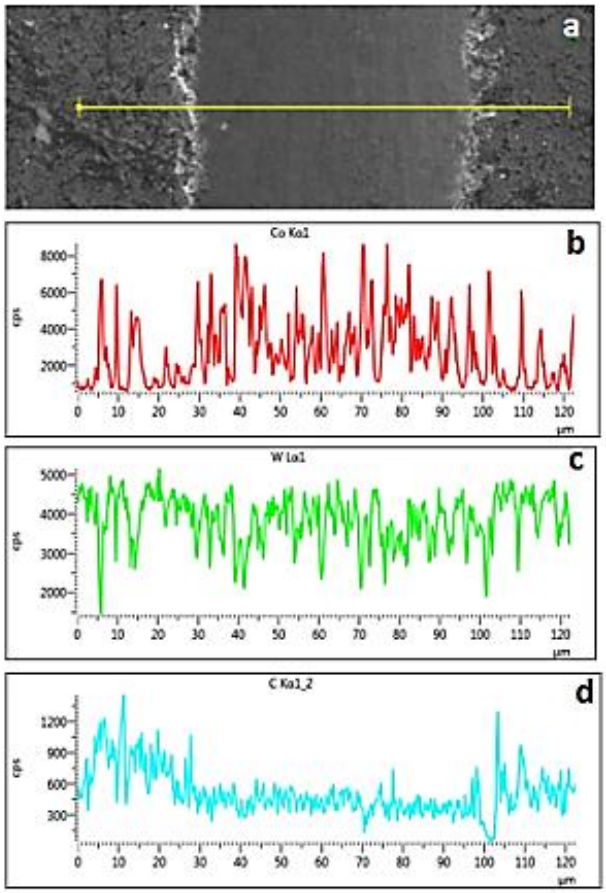

Figure 5.25 EDS spectra of the groove produced after applying 25 N on the substrate layer of sample K1908

Figure 5.26 demonstrates a 3D profilemeter image of the scratch after applying high load of 300 N. The image shows the pile up of the materials on the groove's sides in agreement with EDX spectroscopy.

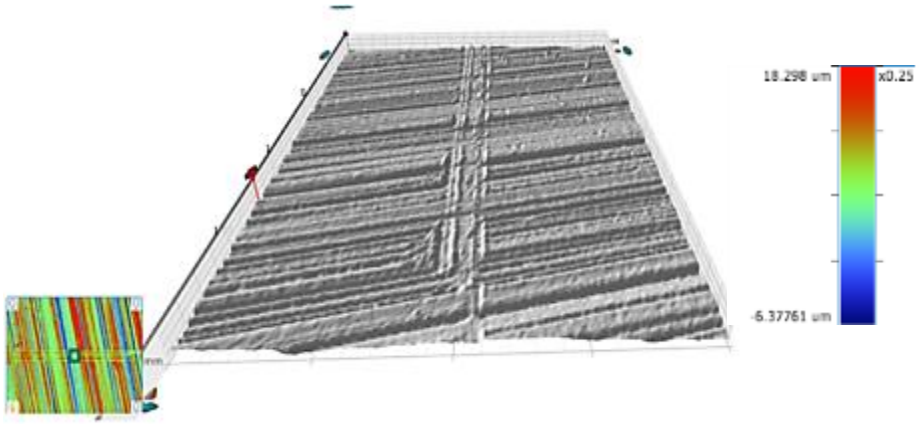

Figure 5.26 Three- dimensional image shows the scratch test after applying 300 N load on the tungsten-carbide layer for sample M1313 with Vickers indenter

5.1.5.2 Diamond layer

The main cause of diamond wear or failure of the PDC cutters is due to the back transformation of diamond to graphite and high difference in the thermal expansion coefficient between diamond and cobalt causing the breakage of the diamond-diamond bonds producing diamond failure. Reducing the binder content in the diamond layer produces better thermal stability and wear resistance than the diamond layer that has high cobalt content (Bellin *et al*., 2010 a and Bellin *et al*., 2010 b).

X-ray maps of the obtained scratches as a result of micro-scratching on diamond layer of the PDC cutters were also examined. Figure 5.27 illustrates the composition distribution in and outside the groove after micro-scratch test for the diamond layer of the sample M1313 using Vickers probe. Unlike the substrate, the cobalt grains (as shown in Figure 5.27b) were expelled from the groove and the main remnant mineral left inside the scratch is diamond, whereas Figure 5.27a illustrates the amount of carbon increases inside the scratch area.

Micro-scratching of the diamond layer will cause the dislodgment of the binder grains out of the groove leaving the diamond grain to occupy the scratch area. This is caused due to the breakage of the diamond –cobalt bonds. Figure 5.28 shows the EDX coloured maps of the scratch and the adjacent area of the diamond layer of the PDC specimen M1313 using Vickers indenter at varying loads.

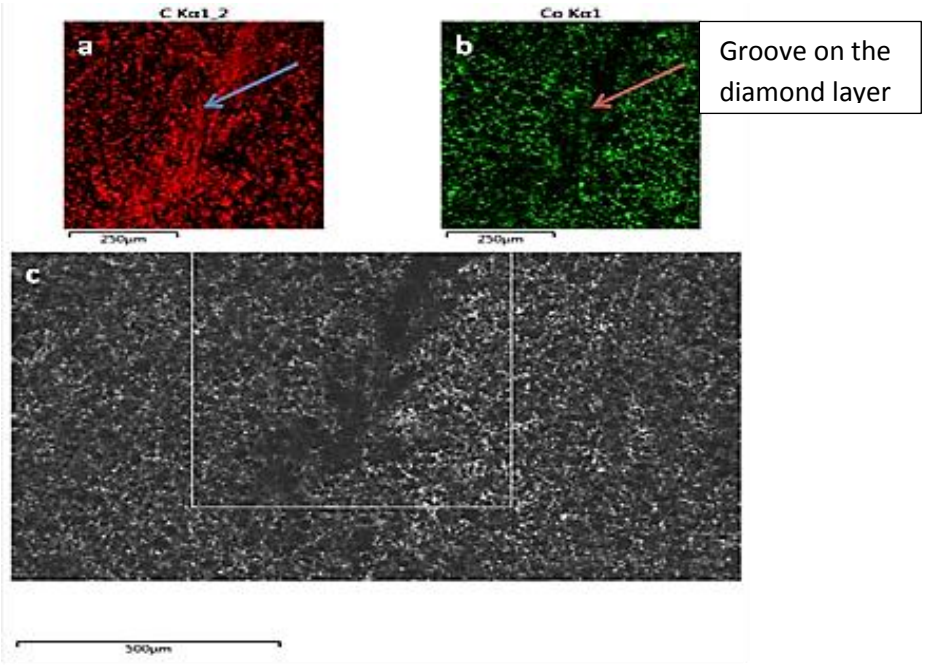

Figure 5.27 Coloured X-ray map of a groove on the diamond layer as a result of micro-scratching using Vickers indenter of sample M1313 at 15 N load

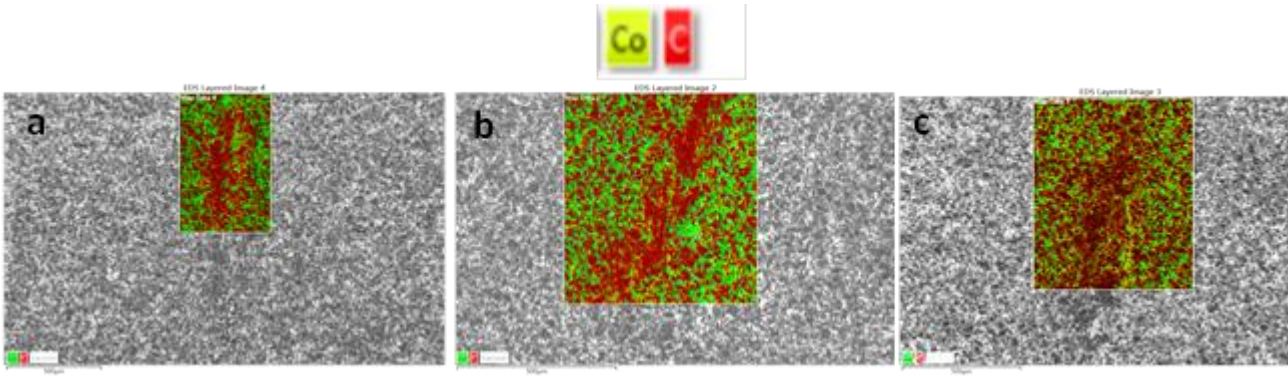

Figure 5.28 Coloured X-ray maps of three scratches obtained after applying various loads (a) 10N, (b) 15N and (c) 20N on the diamond layer of sample M1313

It is worth mentioning that the main wear mechanism of the diamond wear is ploughing where, no debris was found after the micro-scratch test when applying various loads. When the diamond layer was scratched the cobalt grains (green) were removed from the groove and the main mineral remaining in the scratch was diamond (red-brown).

A possible explanation for this mechanism could be attributed to the micro wear of the tip of the diamond indenter leaving some material on the scratched surface. Another reason could be due to the fact that the adhesion between the diamond grains and cobalt is presumably strong and extreme contact pressure can squeeze out the excessive cobalt while further compacting of the diamonds grains. Displacement of cobalt could also be further occurred due to a significant difference in the thermal expansion coefficient between diamond and cobalt ($2.7*10^{-06}\ ^{\circ}C^{-1}$ for diamond compared to $1.2*10^{-05}\ ^{\circ}C^{-1}$ for cobalt) causing cobalt to expand quicker than diamond and consequently breaking the bonds between the diamond particles causing failure (Sneddon and Hall 1988). Investigating these hypotheses requires further work which could be a topic of future studies. The findings of the analytical work for the diamond layer shows dissimilar behaviour for the substrate as mentioned previously in section 5.1.5.1, where it was shown that the binder (cobalt) is concentrated within the scratched area and the carbon of (WC) was found to be increased at the edges of the groove. This might be attributed as the load applied to the probe during the scratch test, WC grains are deformed and therefore, the bonds between the WC grains are broken as well as the bonds between the WC grains and the cobalt are no longer bonded causing the emergence of cobalt. Furthermore, there was a pile-up of WC observed at the edges of the groove (Ndlovu, 2009).

Similar analytical study is performed on the scratches obtained on the diamond layer when using spheroconical indenter. The same findings of the EDX analysis after the

micro-scratching using Vickers were obtained for conical tip indenter. Figure 5.29 displays EDX coloured maps of a groove obtained from micro-scratching the diamond layer with a spheroconical tip for the sample K1908 at load 10 N.

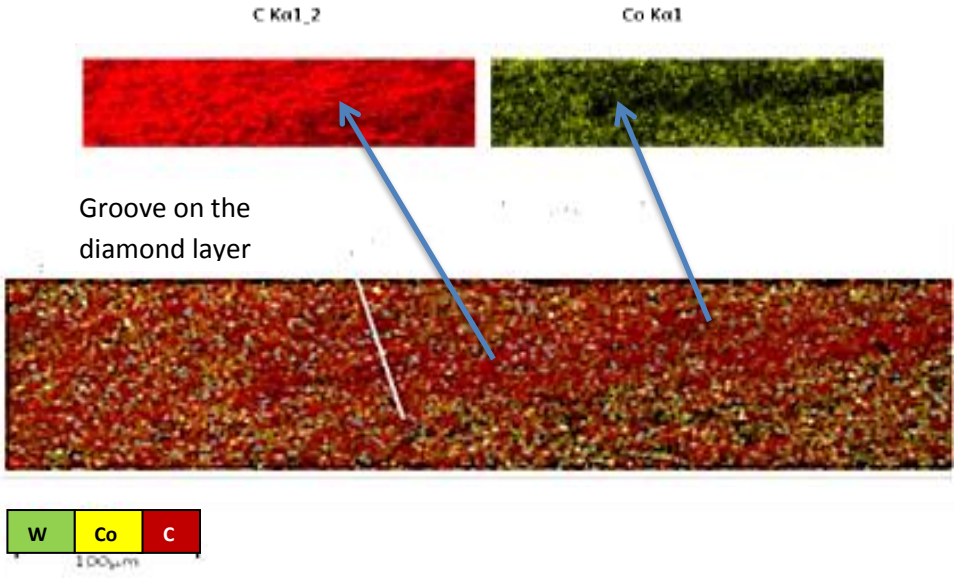

Figure 5.29 EDX maps of the main minerals in and around the scratch on the diamond layer after applying 10 N for the sample K1908

It seems that carbon occupies the scratched area as shown in the bottom X-ray map of Figure 5.29, while the binder grains are dislodged outside the groove as shown in the top right map of Figure 5.29. This is presumably attributed for the same reasons mentioned above for the micro-scratching of the diamond layer with Vickers indenter.

Figure 5.30 shows the EDS spectra of the two main minerals across a groove scratched by a spheroconical probe at load 30 N of the sample K1908 as the width of the groove was around 41.5 microns. The binder (cobalt) is likely to be decreased within the scratched area and increased at the edges of the groove, whereas carbon (diamond) increased along the groove compared to the non-scratched area. This is confirmed with the mineral distribution of the EDX maps of Figures 5.27, 5.28 and 5.29.

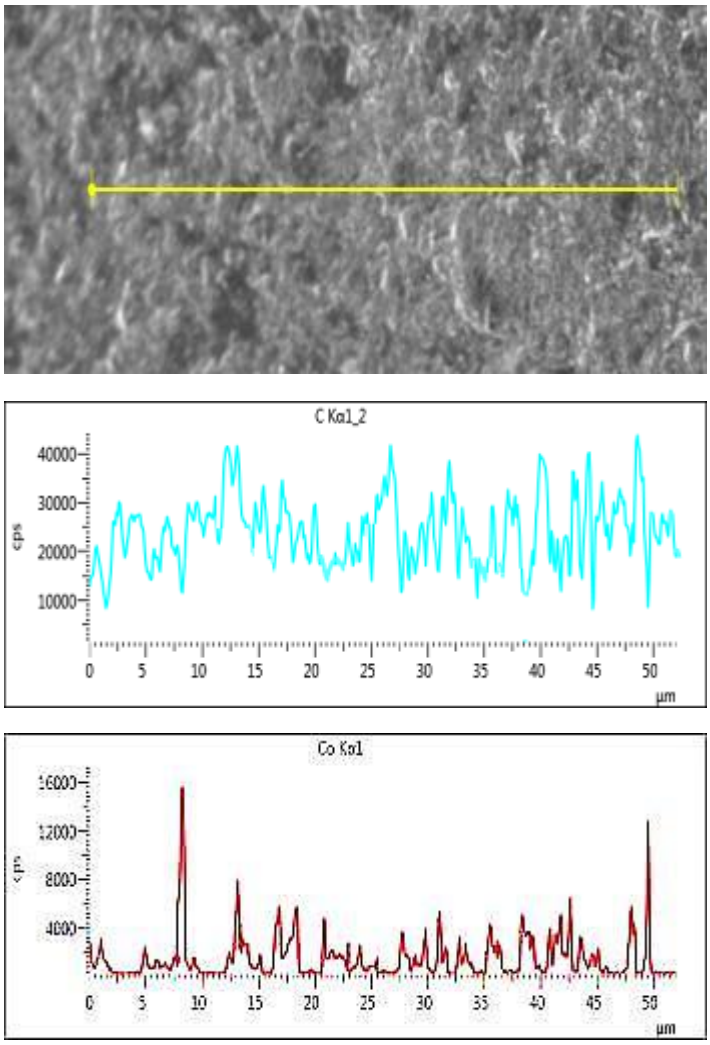

Figure 5.30 EDS spectra of the groove produced after applying 30 N on the diamond layer of sample K1908

5.2 Nano-mechanical testing (Scratch test)

Nano-mechanical testing is a technique that has been used recently for the evaluation of mechanical failure of ceramics and notably the nano-tribolgical measurements. Nano-scratch testing approach has preference as it can overcome problems regarding the breakage of the indenters and the contribution of the machine compliance (Beake *et al*., 2006/2013).

Beake *et al*. (2013) applied the nano-scratch technique for the assessment of different kinds of ceramics. Beake and his co-workers used topography multipass scratch test or three-scan procedure which includes pre-scratch topography scan, progressive scratch and post topography scan in order to discard the effect of the machine compliance on wear quantification or deformation. In addition, this method enables obtaining precise

scratch depths after correction of the raw data for the influence of sample topography or surface roughness. The recommended indenters used in nano-scratch tests are spheroconical probes.

The selection of the probe's radius is crucially important in the nanoscratch test. If the tip of the indenter is blunt, then it is not possible to scratch the samples surface to initiate failure. The probe used in this study was a spheroconical indenter with a 25 μm tip radius. This represents an effective choice ensuring that deformation is monitored carefully within the force range of the instrument (500 mN) but without risking the damage of the probe due to repetitive scanning which could occur when sharper indenters are used (like Berkovich indenters), especially when applying scratch tests on hard and rough coatings. Within the progressive load scratch test, a probe is moved over a sample surface with a linearly increasing load until failure happens at critical loads. The failure is examined by an optical microscope or can be detected by load deformation data.

The nano-scratch test produces three curves representing the relationship between the depth and the distance or the scratch length. The first scan is the pre-scan scratch, while the rest are the on-load scratch and post-scratch scans. Scan one or (pre-scan) is a method for measuring the background profile of the surface of the specimen, while scan two provides the true depth of the scratch, taking into account any curvature. After the scratch is complete, a post-scratch scan or scan three carried out at the same location of the scratch. This scan represents the residual depth of the scratch. The residual scratch depth reveals the plastic deformation or the destruction occurred.

Before analysing the obtained data, correction for instrument compliance and surface topography is performed within the equipment software according to the study of Beake *et al*. (2009). The obtained nano-scratch after applying the progressive load is examined using optical microscope available with the NanoTest equipment and/or by SEM. It is worth mentioning, that the specimen's surface should be polished finely before launching the nano-experiments to increase the reliability of the results.

5.2.1 Nano-scratch of the substrate layer

Nano-scratch test was performed on the substrate layer of the PDC samples. Multi-pass nano-scratch test at constant load was selected to perform the test. The settings were as follows: 1200 μm scratch distance, maximum load of 500 mN, 200 μm distance to start

increasing the load, load rate of 20 mN/sec and scratch speed of 10 µm/sec. Figure 5.31 shows the image of the nano- spheroconical indenter used in the nano-scratch tests. The tip of the indenter has a radius of 25 µm.

Figure 5.31 nano- spheroconical probe with a tip of 25 µm radius

Figure 5.32 shows a SEM image of a groove obtained after nano-scratch testing on the substrate layer of sample K1908 using spheroconical indenter of 25 µm radius.

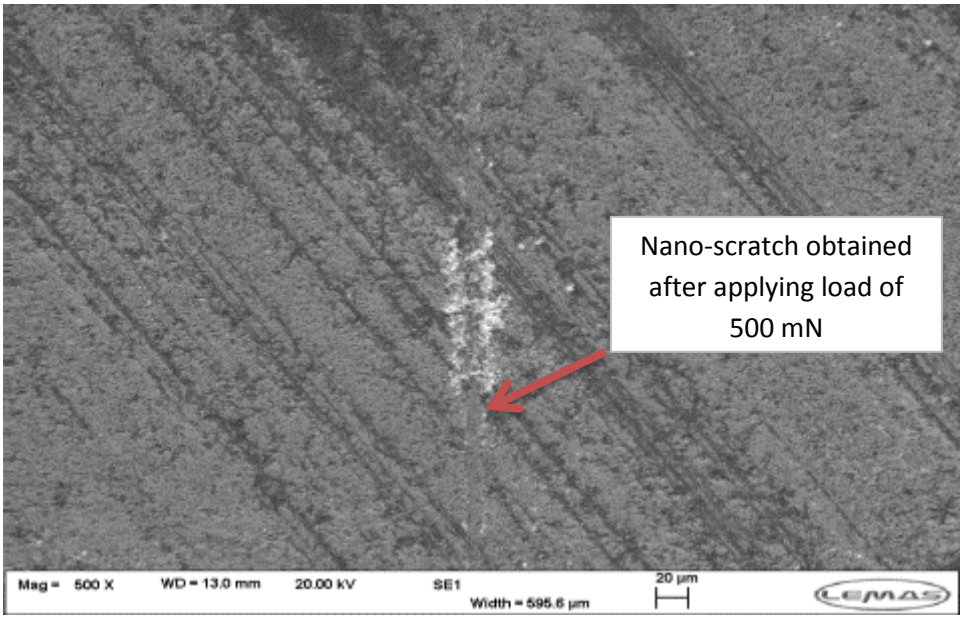

Figure 5.32 Groove obtained from nano-scratch testing on the WC-Co layer of sample K1908

The penetration depth of the post-scratch test residual depth (h) used in Equation (5-5) represents the residual depth. Equation (5-3) could be re-written to calculate the wear volume (V_w) at different points as follows:

$$V_w = \frac{(A_n + A_{n-1})}{2} * \quad (L_n - L_{n-1}) \qquad (5-6)$$

where n is the index of incremental area and sliding distance.

The total volume of nanowear for the selected PDC sample for 1200 µm distance under 500 mN load was calculated from Equation (5-7) and plotted as cumulative wear:

$$V_{wt} = \sum_{i=1}^{i=N} V_w \qquad (5-7)$$

Plot of the multi-pass nanoscratch test is shown in Figure 5.33, where the three consecutive scratch tests can be observed. It is crucially important to mention that the results obtained from the software provided with the nano-scratch equipment are corrected for the surface roughness and machine compliance.

Results of the measured nano-wear of the substrate layer for sample K1908 after applying nano-scratch test were plotted vs. sliding distance at different points as shown in Figure 5.34. It is shown that, the volume of wear is increasing in areas that exhibit high values of residual depth. Figure 5.33 shows that high peaks of residual depth existed around 200, 322, 750, 886 and 1033 µm distance. Negative peaks also appeared in the graph and this might be due two reasons (1) a result of a small residual sample slope not being corrected out (2) at parts in the post-scan, the probe cannot reach the bottom of the track and instead moves over the wear debris (3) the occurrence of fracture rather than plasticity. Similarly, Figure 5.34 illustrates high wear rates at same displacement values corresponded with high values of residual depths.

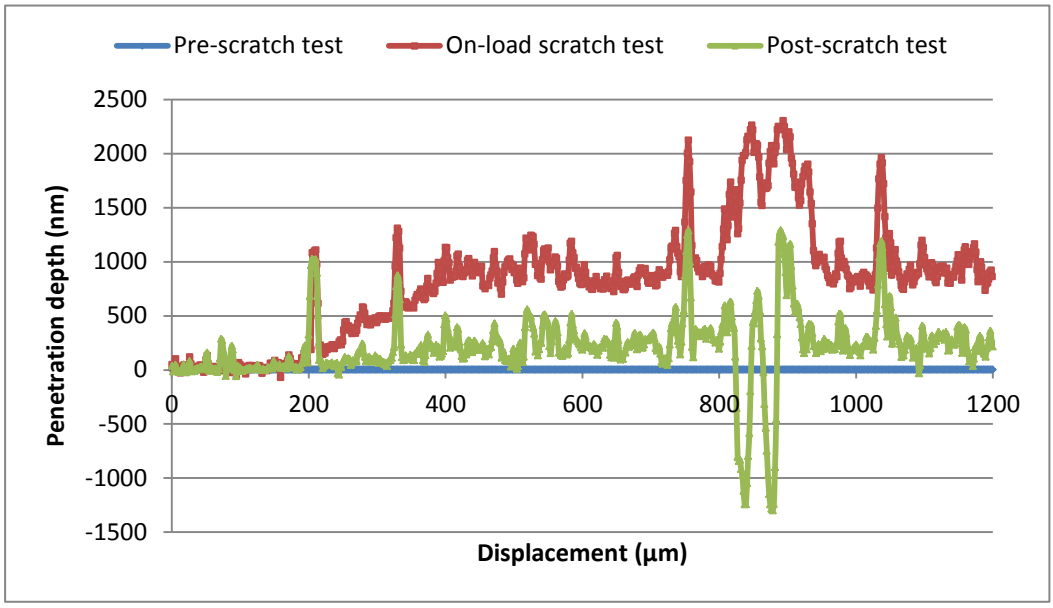

Figure 5.33 Multi-pass nano-scratch test on substrate layer of sample K1908

The total loss of the substrate material (wear) of sample K1908 obtained from the nano-scratch test using spheroconical probe as shown in Figure 5.34 was 172.113 $*10^{-08}$ mm^3.

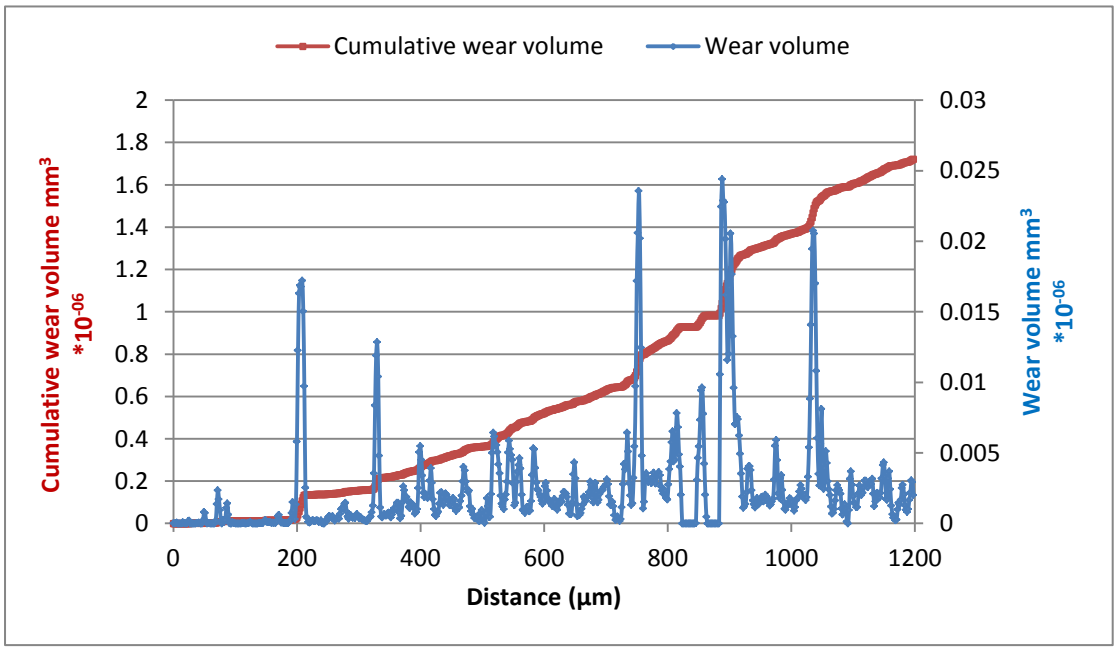

Figure 5.34 Wear and cumulative wear of the substrate layer of the sample K1908

Similarly, for sample M1313 the multi-pass nano-scratch test is shown in Figure 5.35.

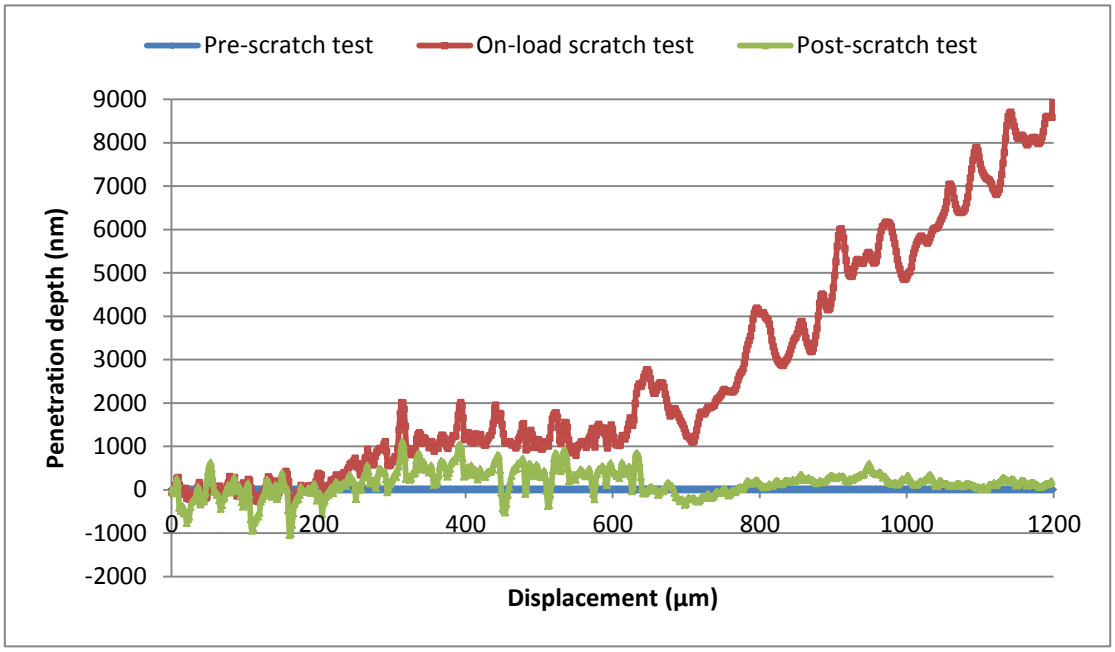

Figure 5.35 Multi-pass nano-scratch test on substrate layer of sample M1313

For the sample M1313, the residual depth showed sharp positive peaks near distances of 50 and 947 µm, while the majority of the positive sharp peaks existed between distances 300 and 624 µm. Negative peaks (negative residual depths) also exists due to the same reasons mentioned in Figure 5.34 above. The high values of residual depth affects the

total nano-wear calculated from Equation 5-7. Figure 5.36 shows the plot of nano-wear and cumulative nano-wear for the substrate layer of sample M1313.

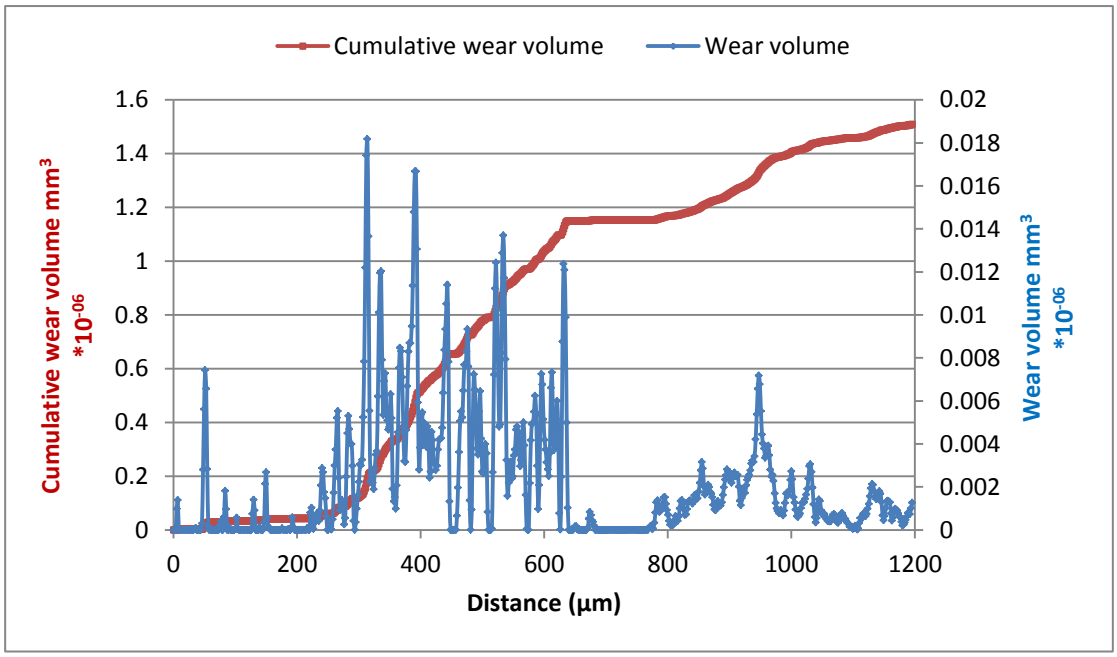

Figure 5.36 Nano-wear of the substrate layer of sample M1313

It is clearly seen, that the sharp peaks of nano-wear is corresponding to the high peaks of residual depth as shown in Figure 5.35. The total material loss of the substrate layer due to the nano-scratch test for sample M1313 was 150.948 $*10^{-08}$ mm^3.

Obtained wear from nano-experimental scratch test together with those of micro scratch test of the substrate layer for samples K1908 and M1313 were compared with the wear prediction base on the three models (Rabinowicz, 1996, Hutchings, 1992 and Ning and Ghadiri, 2006), as shown in Figures 5.37 and 5.38 respectively. The nearest wear model to the experimental one was Hutchings' (1992), while Rabinowicz (1996) model was the furthest from the experimental wear as illustrated in blue dashed line. Figures 5.37 and 5.38 illustrate the correlation between the measured micro and nano-wear with those from wear models using the spheroconical indenter.

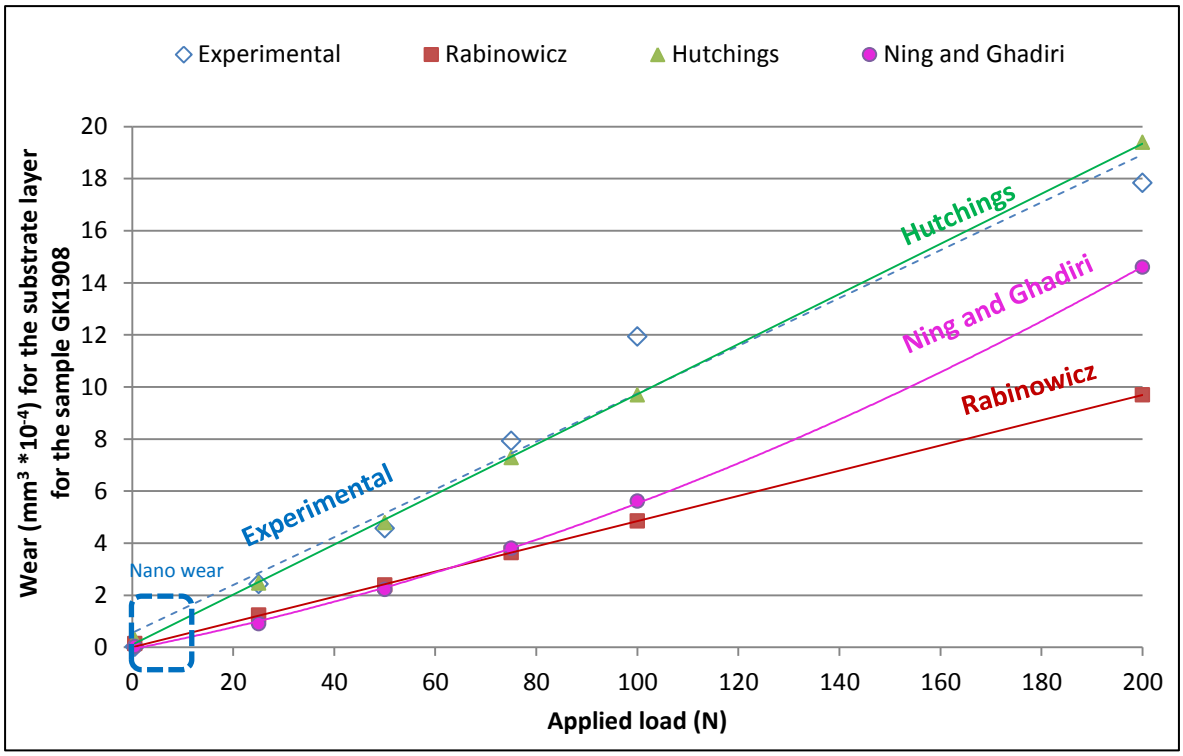

Figure 5.37 Trendlines of wear for the substrate layer of sample K1908 using spheroconical probe

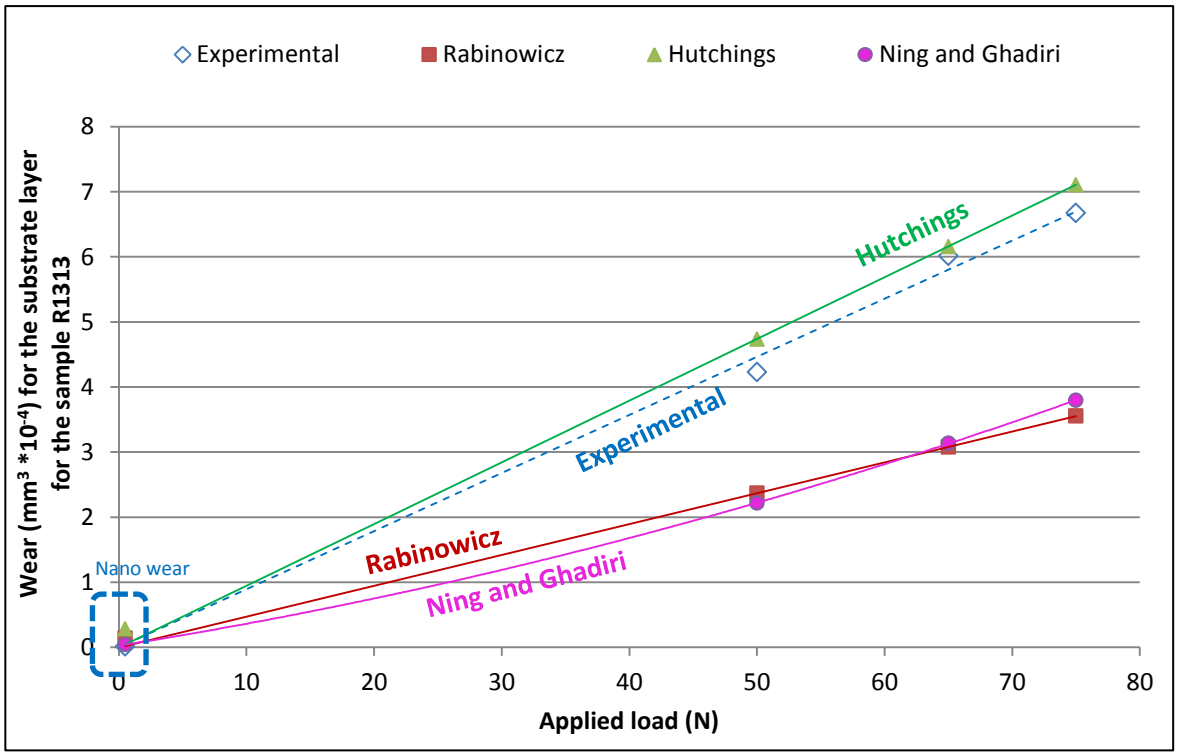

Figure 5.38 Wear trendlines for the substrate layer of sample M1313 using spheroconical indenter

5.2.2 Nano-scratch of the diamond layer

Similar nano-scratch tests are performed on the diamond layer of the two PDC samples K1908 and M1313. The multi-scratch test was performed under similar experimental settings used for the substrate layer. Figure 5.39 illustrates an optical image of the groove obtained from a nano-scratch test of the diamond layer of sample K1908.

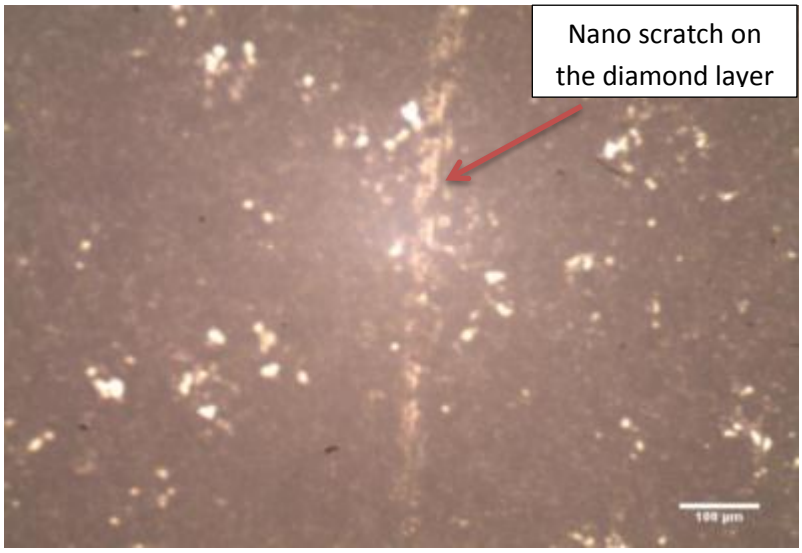

Figure 5.39 Optical microscope image shows the nano-scratch obtained after applying 500 mN on the diamond layer of sample K1908

Plot of multi-pass nano-scratch test on the diamond layer of sample K1908 is shown in Figure 5.40, where the three scans of the nano-scratch test are displayed.

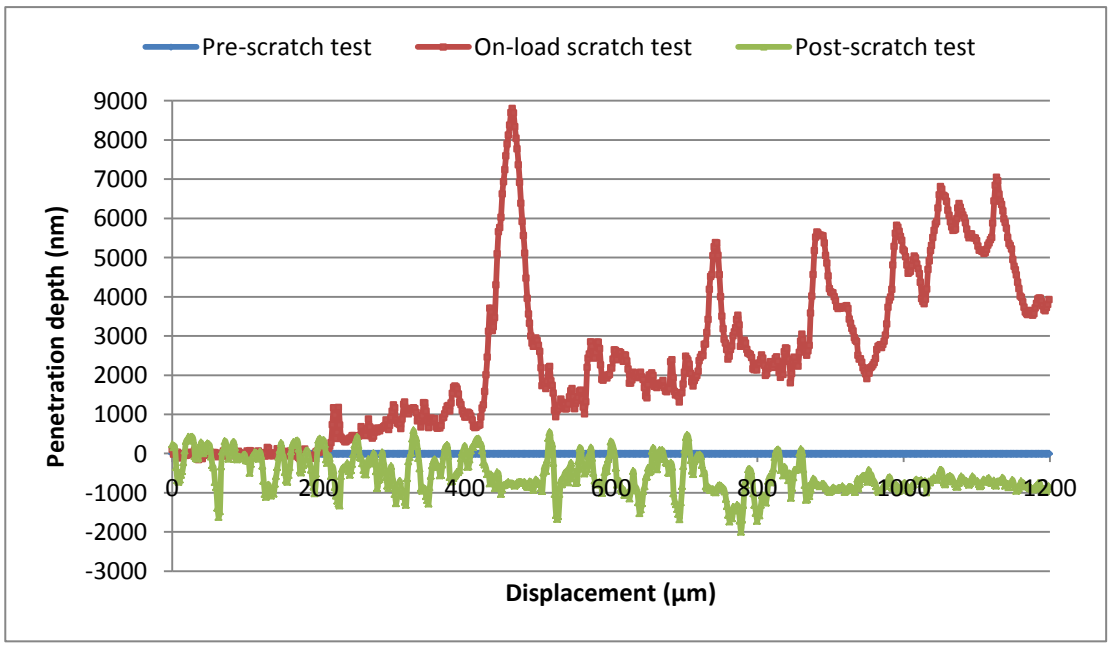

Figure 5.40 Scans of multi-pass scratch test of the diamond layer of sample K1908

Corrected residual penetration depths from Figure 5.40 were shown to be shallower than the residual depths of the substrate layer for the same sample (Figure 5.33) indicating that the wear of the diamond layer for this sample is lower than that of its substrate. Figure 5.41 illustrates the results of wear obtained from nano-scratch testing for the diamond layer of sample K1908.

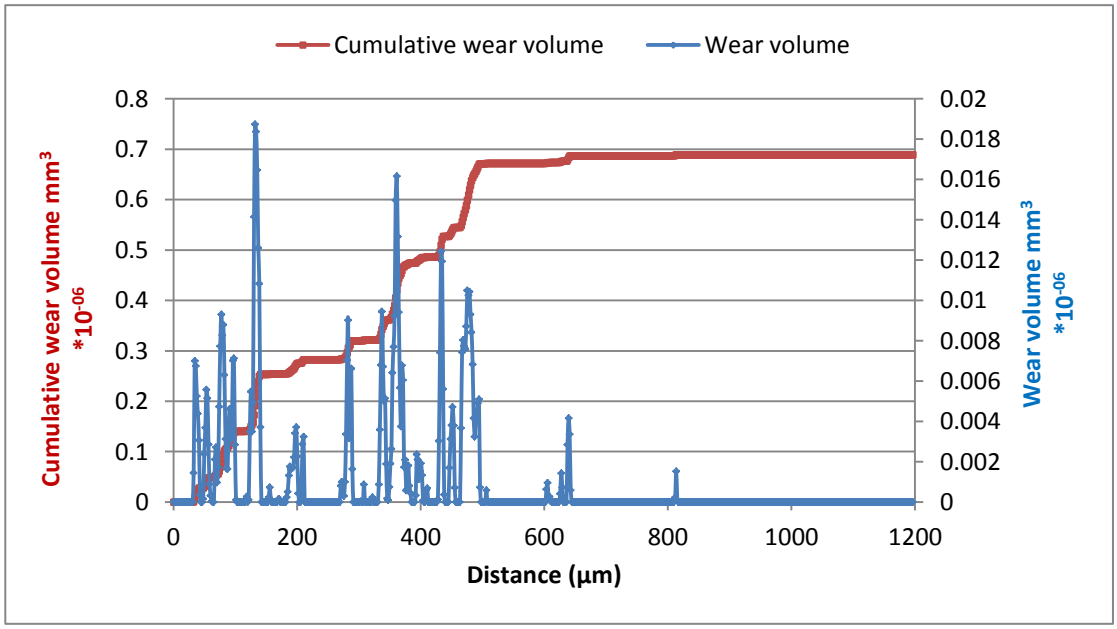

Figure 5.41 Wear results after nano-scratch testing on the diamond layer of sample K1908

Sharp peaks of wear were existed at distances between 35 and 490 µm. The wear of the diamond material within the nano-scratch test using spheroconical probe was $68.942*10^{-08}$ mm^3. The cumulative wear was nearly constant beyond scratch length of 500 µm after a gradual increase from the starting point of the test and this is due to low values of residual depths from scratch length 500-1200 µm as shown in Figure 5.40. The low values of residual depths will produce low nano-wear as displayed in Figure 5.41.

Similarly, the plot of multi-pass nanoscratch test for sample M1313 is displayed in Figure 5.42.

The residual scratch depth displayed lower values than those of the substrate layer of the same sample. Figure 5.43 illustrates the wear behaviour of the diamond layer of sample M1313.

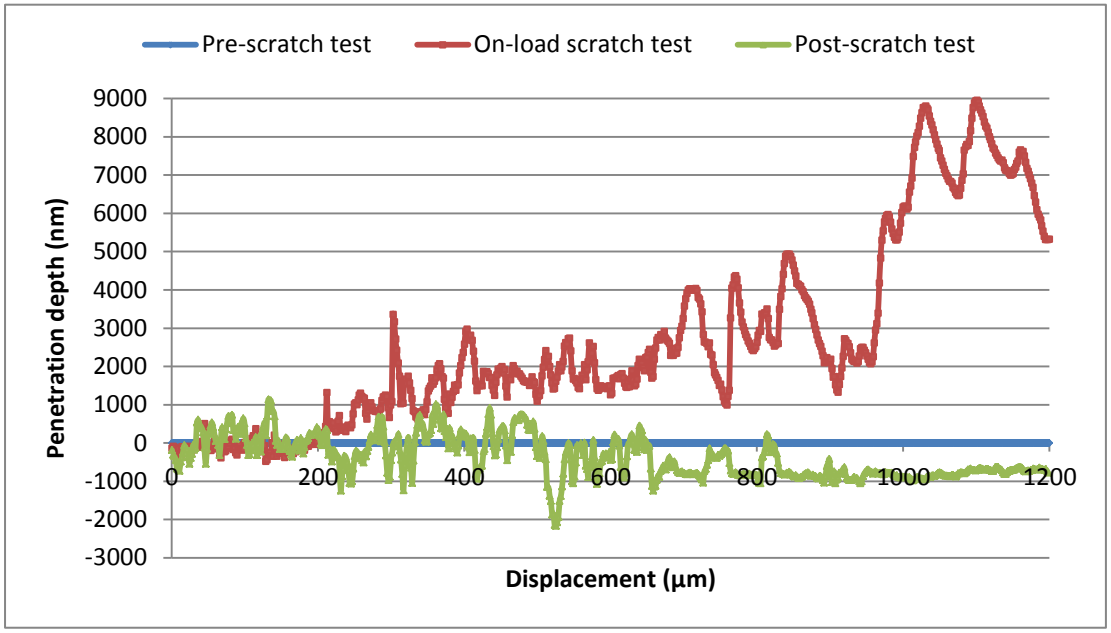

Figure 5.42 Scan of scratch tests of the diamond layer of sample M1313

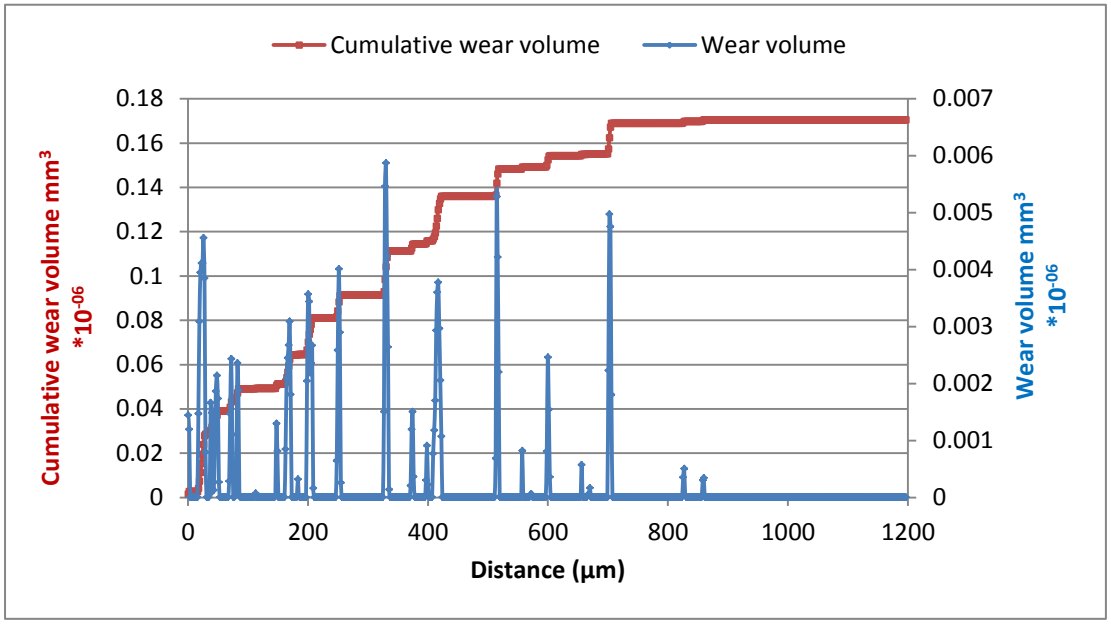

Figure 5.43 Results of wear obtained from nano-scratch test of the diamond layer of sample M1313

Peaks shown to be existed from the starting point of the test until 700 µm , but these peaks has lower values than those of sample K1908 giving an indication that the diamond layer of sample K1908 exhibited higher wear rates than the same layer of sample M1313. The total loss of the diamond material for sample M1313 was $17.037*10^{-08}$ mm^3. The cumulative wear volume is increased gradually until distance of 700 µm, beyond which

was shown to be almost constant as also attributed to low values of residual depth beyond distance of 700 µm.

The wear obtained from micro and nano-experimental scratch test of the diamond layer for samples K1908 and M1313 were plotted and compared with the wear obtained from three models of (Rabinowicz 1996, Hutchings 1992 and Ning and Ghadiri 2006), as displayed in Figures 5.44 and 5.45, respectively. Figures 5.44 and 5.45 illustrate the correlation between the measured micro and nanowear with those from wear models using the spheroconical indenter. Again, the obtained results of the nano-scratch test follow the wear trend obtained from micro-scratch testing. Hutchings' (1992) wear model was found to be the closest to the experimental wear, while Rabinowicz (1996) model displayed furthest trend from the experimental wear.

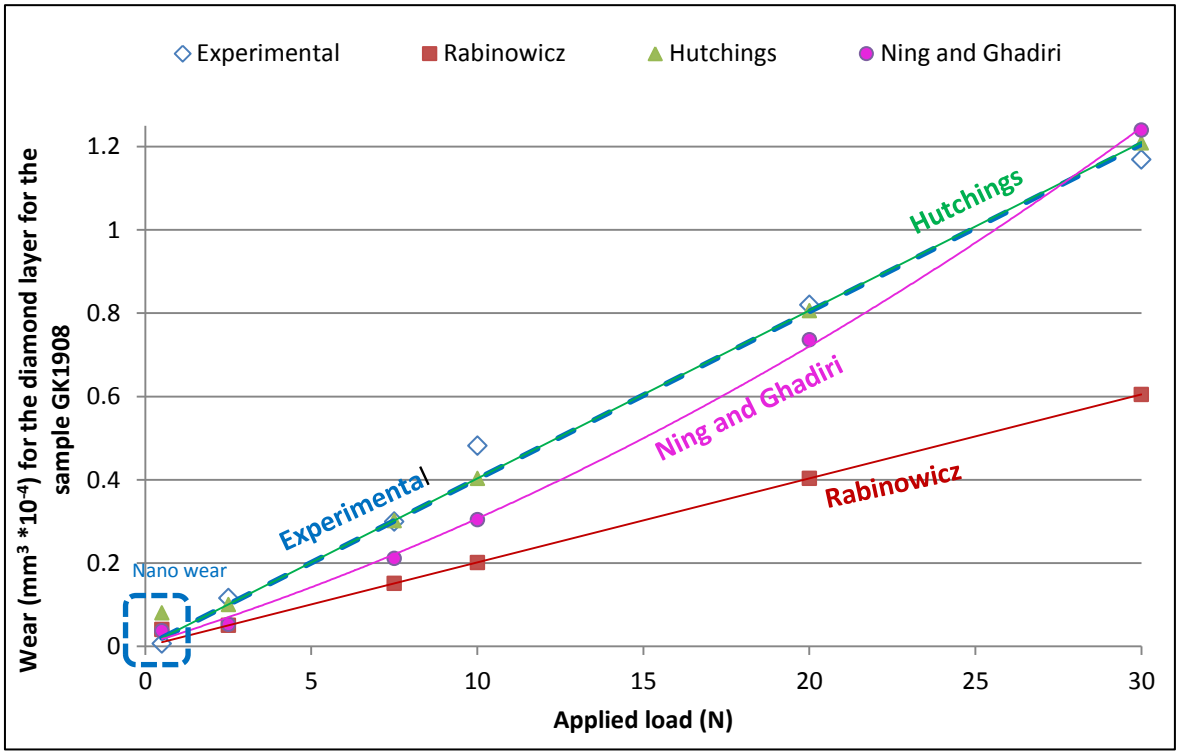

Figure 5.44 Experimental nano-wear compared to various wear models for the diamond layer of sample K1908 using spheroconical probe

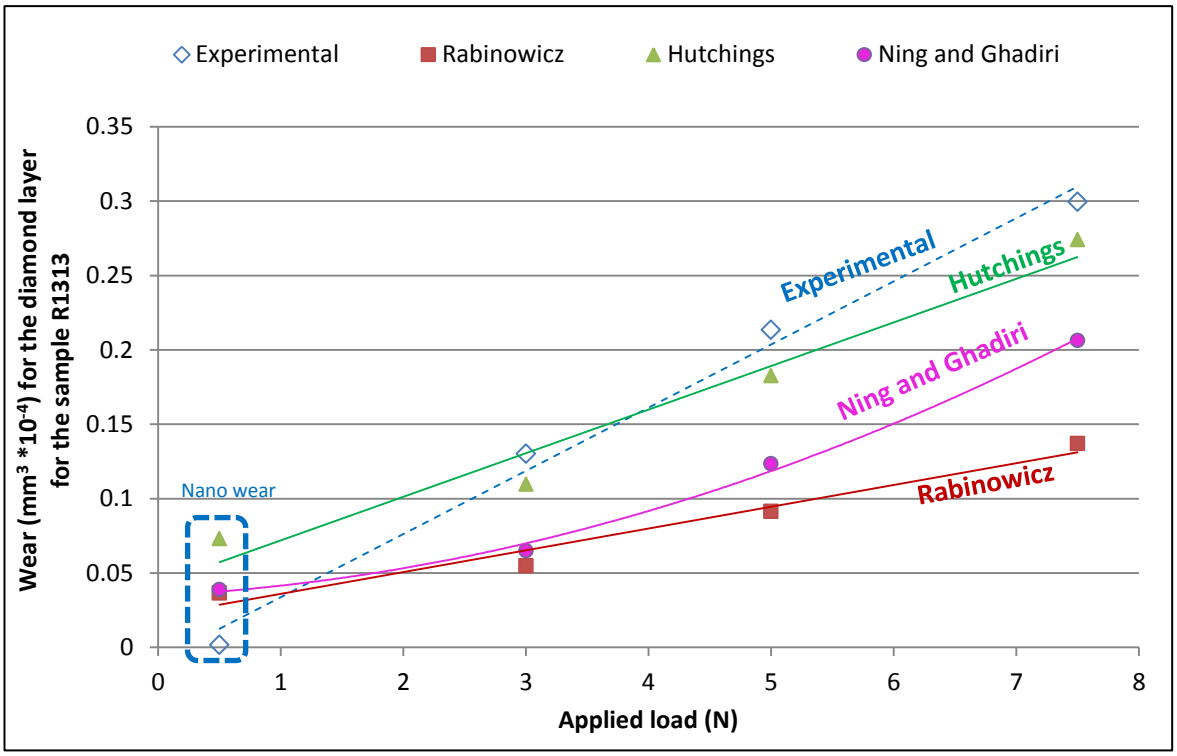

Figure 5.45 Trendlines of wear for the diamond layer of sample M1313 using spheroconical indenter

5.3 Normalisation of the wear

Normalisation of the experimental wear for both layers of the samples by sliding distance and hardness exhibited a linear increasing trend when increasing the load.

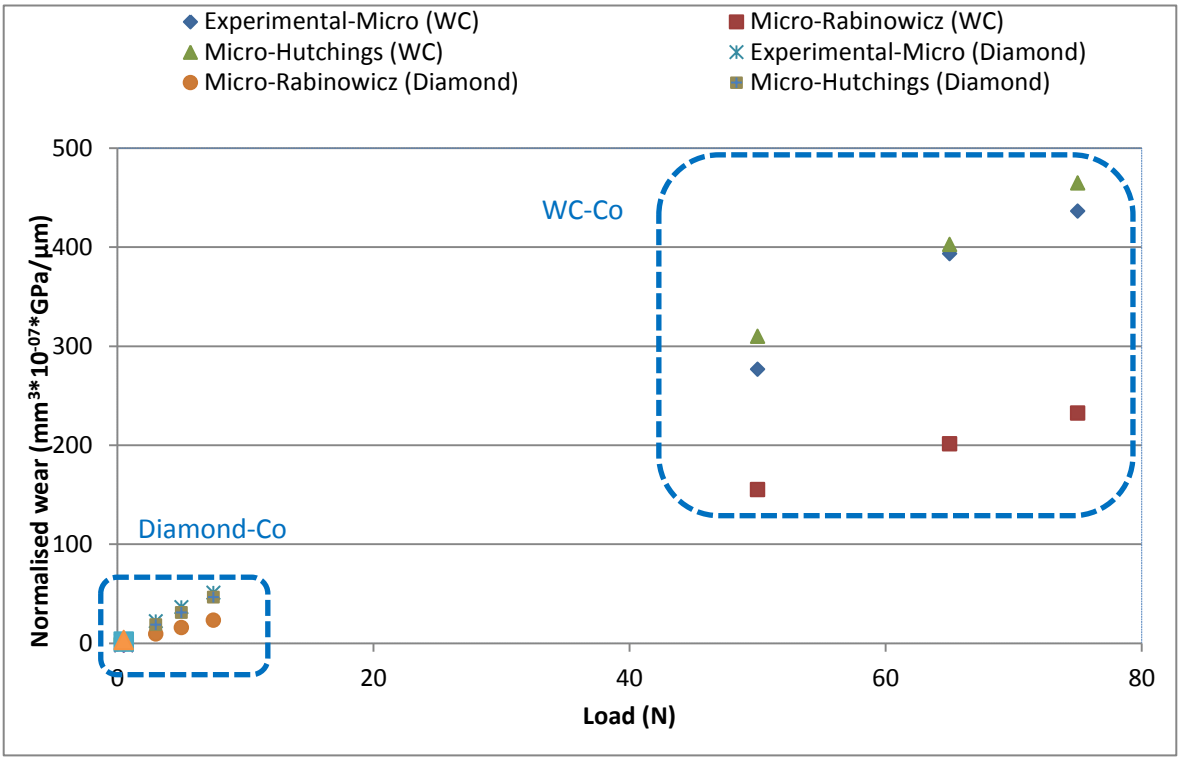

Figure 5.46 Wear normalised for sliding distance and hardness for sample M1313

This normalisation showed clearly that the wear is linearly proportional with sliding distance and inversely proportional with hardness. Figures 5.46 and 5.47 illustrate the normalised nano and micro wear for sliding distance and hardness for samples M1313 and K1908 respectively. All wear models along with the experimental wear showed a linear increasing trend with load.

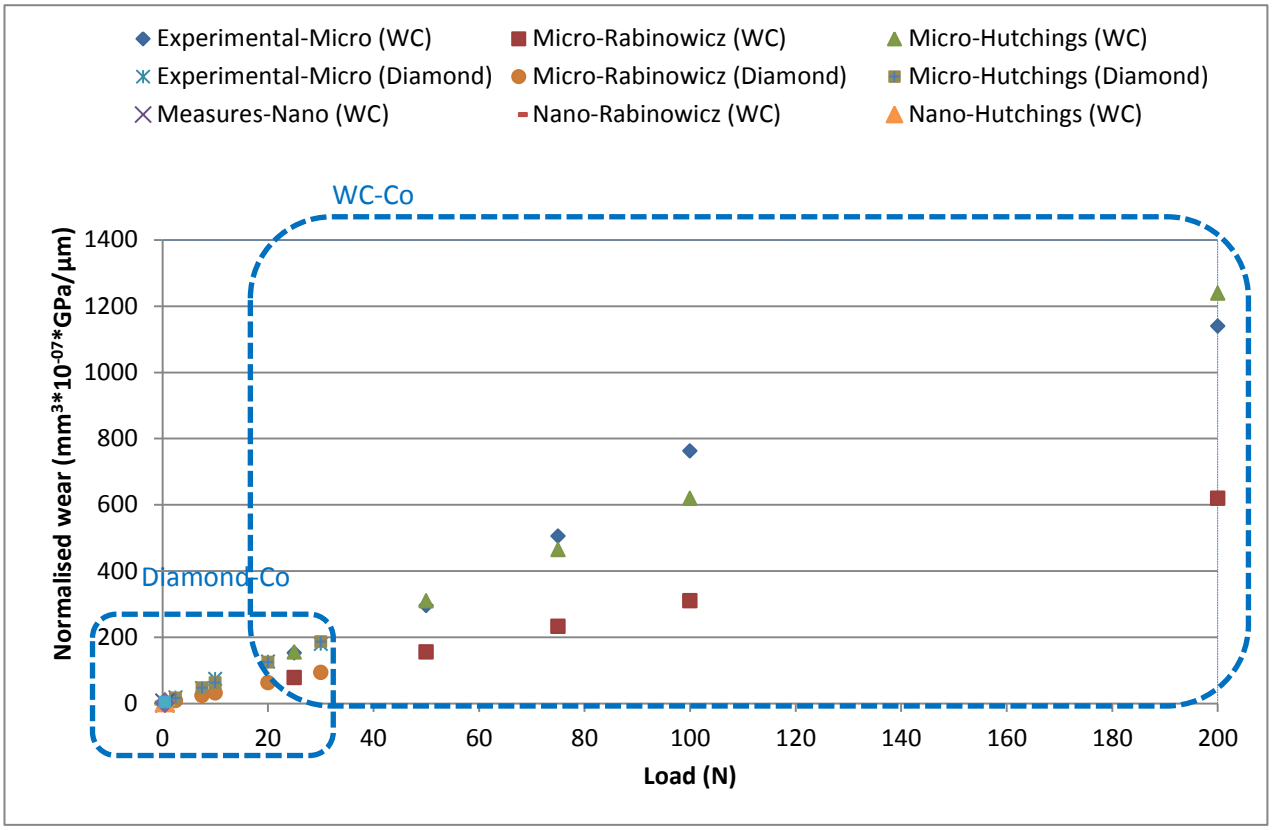

Figure 5.47 Wear normalised for sliding distance and hardness for sample K1908

Ravikiran (1999) mentioned various definitions of wear quantification. Specific wear rate is defined as the wear volume normalised for the applied force and the sliding distance as shown in Equation 5-8:

$$Specific\ wear\ rate = \frac{V_w}{F\ .L} \qquad (5-8)$$

where V_w is the volume of material loss (mm^3*10^{-05}), F is the applied load (N) and L is the sliding distance (µm). The specific wear rate obtained from scratch testing is calculated for two PDC samples from two different manufacturers (M1313 and K1908). Figures 5.48 and 5.49 illustrate the average specific wear rate comparison obtained from micro and nano scratch tests over a long load range for the substrate and the diamond layers of the two PDC cutters, respectively. It is clearly shown, that sample M1313

displayed less specific wear rate than sample K1908 for layers of the substrate and diamond and consequently sample M1313 has higher wear resistance than sample K1908.

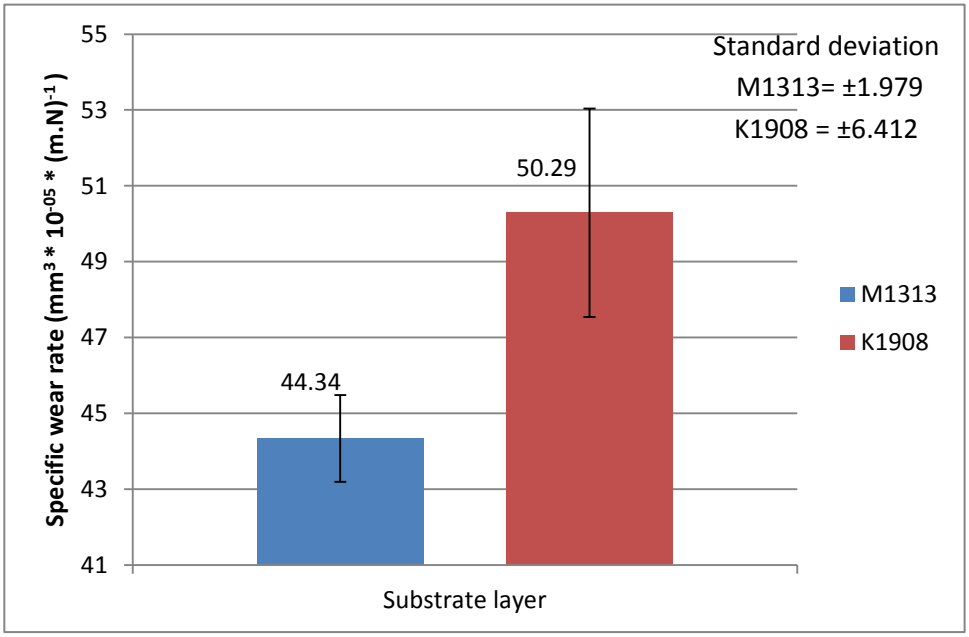

Figure 5.48 Specific wear rate comparison for the WC-Co layer for samples K1908 and M1313

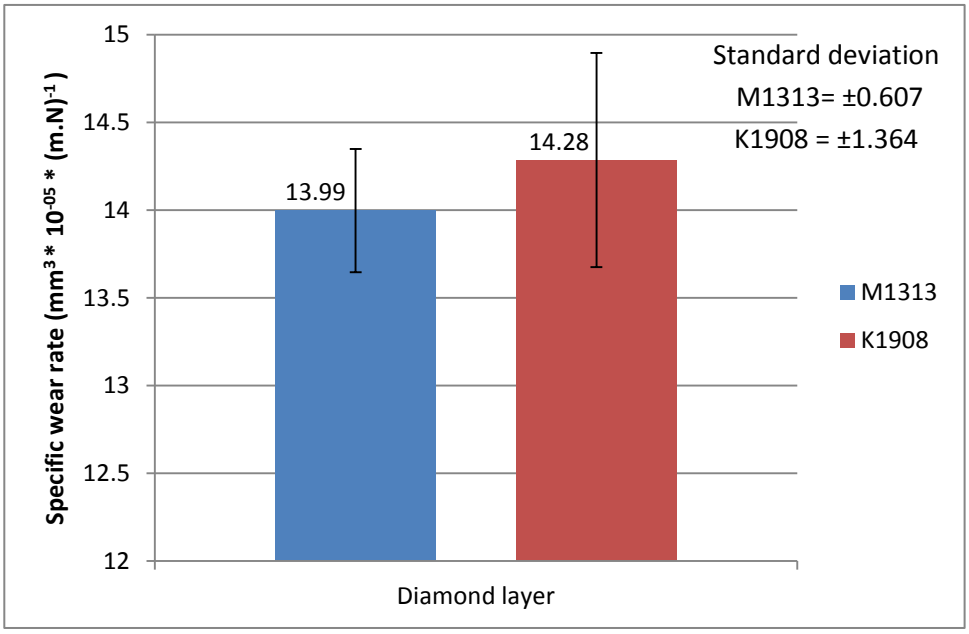

Figure 5.49 Specific wear rate comparison for the diamond layer for samples K1908 and M1313

Yahiaoui *et al.* (2013) concluded that diamond particle size and cobalt content are significant parameters towards the wear of PDC inserts. High wear rate is associated with large particle size. High material loss is also associated with high cobalt content of the diamond layer.

By comparing Tables 5.3 and 5.4 for the substrate as well as Tables 5.5 and 5.6 for the diamond layer, it can be seen that the difference in wear rate for the two samples is attributed to the difference in their hardness, where the hardness amount of the diamond and the substrate is attributed mainly to the microstructural properties such as particle size and binder content (cobalt) as shown section 4.3.

Archard (1953) wear model (Equation 2-17) describes wear in terms of sliding distance, load and hardness, where a linear relationship is suggested as follows:

$$Wear \propto \frac{F\,.\,L}{H} \quad \rightarrow \quad Wear \propto F(A) \qquad (5-9)$$

where F is the applied load, L is the sliding distances and H is the hardness.

Figure 5.50 shows the plot of the experimental wear results obtained from micro and nano-scratch tests with spheroconical indenter for both layers of the two different PDC samples against *F(A)*.

It can be seen that, a linear correlation of the wear with the *F(A)* for both diamond and substrate layers of the PDC cutters could be obtained as follows:

$$V_w = 0.6061 * \frac{F\,.L}{H} \qquad (5-10)$$

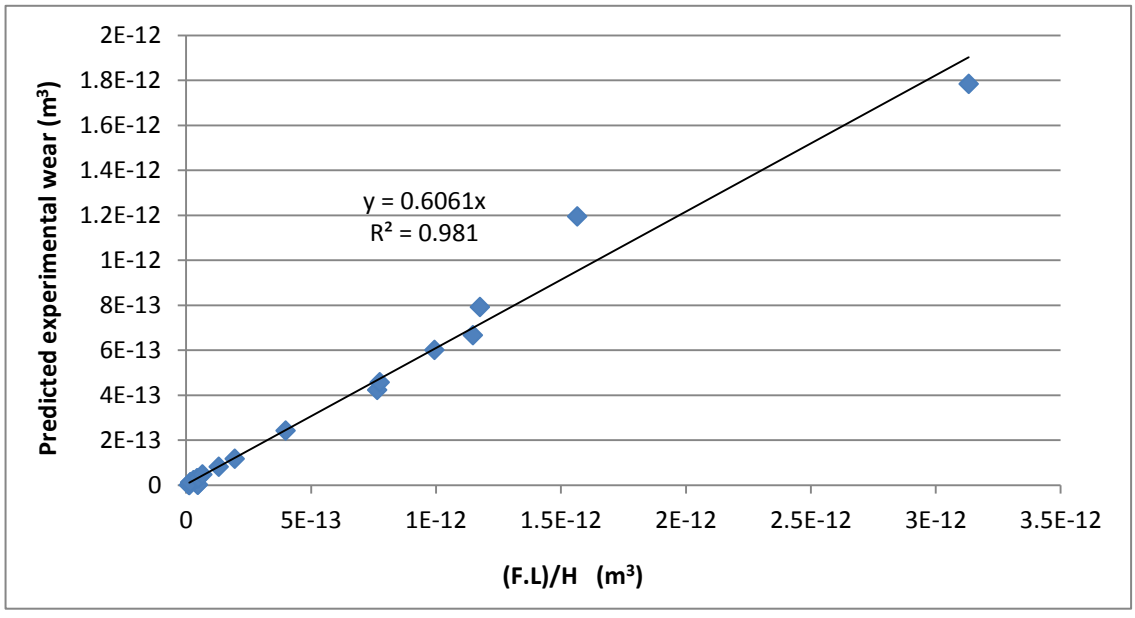

Figure 5.50 Predicted wear versus the function *F(A)*

It can be seen that, the data obtained from nano and micro scratch tests can be fitted into a single curve based on this model with a reasonable error, suggesting that wear of various samples in this study could be predicted by knowing the three parameters in Equation (2-17), i.e. hardness of the sample, applied force and sliding distance. However, it is worth noting that in real drilling conditions, the existence of lubricant and high temperature of the environment could affect the wear trends and this should be further investigated in future studies.

5.4 Conclusions

In this chapter, the wear of PDC samples was assessed using micro and nano-scratch facilities. The tests were carried out on both layers of PDC samples from two different manufacturers.

Micro and nano scratch testing depends mainly on the geometry of the removed material and consequently gives better representation of the volume of wear being quantified. Furthermore, nano-scratch test provides valuable information of the groove along the sliding distance showing the stages of failure after testing.

As the scratching the substrate and the diamond layers of the PDC samples, the material of the two layers is removed by the tip of the diamond indenter (Vickers and spheroconical) and hence, the type of the abrasive wear is in considered two body abrasion. The experimental wear volume obtained from micro and nano-scratch testing was compared with the predicted abrasive wear calculated from two body abrasive wear models available in the literature. It was concluded that Hutchings' wear model showed the best agreement with the experimental data compared with other abrasive wear models.

The EDX analysis of PDC samples in and outside the grooves obtained from the micro-scratch tests showed that for the substrate layer, the carbon grains accumulate at the edges of the groove forming pile-up which is called ploughing, however debris of the substrate was simultaneously found inside and outside the grooves being scratched causing cutting action instead of ploughing. Therefore ploughing and cutting wear mechanism were believed as the main mechanisms to occur in the tungsten-carbide layer of the PDC cutter. EDX shows that tungsten decreased along the scratch, while the binder (Cobalt) was observed to increase along the scratch and specifically on the ridges. On the other hand, the mechanism of wear for the diamond layer is different,

where the diamond grains occupied the scratch dislodging the cobalt outside the groove. Due to the pile-up occurring during the scratching of the diamond layer of the PDC samples and no wear debris were found, this confirms that the main dominant wear mechanism for the coating layer (diamond) is ploughing. Two dimensional profilemeter graphs of the obtained scratches of the diamond layer show that ridges occurred around the grooves, suggesting again that ploughing is the main dominant wear mechanism for the diamond layer of the PDC inserts.

It was shown that all the data for both PDC samples can be unified on a master curve considering the three parameters mentioned above (load, sliding distance and hardness) suggesting wear tendency of samples could be predicted based on the mechanical properties, notably hardness.

The findings of this study could be extended to various types of PDC cutters from different manufacturers to evaluate the amount of wear as a quality index rather than using the previous traditional abrasion tests.

Chapter 6 Conclusions and Recommended Future Work

6.1 Conclusions

1- The overall aim of this thesis was to study and analyse the wear of oil drill bits. The main wear mechanisms of the PDC samples were investigated. It is concluded from the obtained analytical images that ploughing is the dominant mechanism of abrasive wear occurring in the diamond layer of the PDC samples of the PDC bits, whereas cutting and ploughing are the main wear mechanisms occurred in the substrate layer of the PDC specimens that represent insert or (TC) roller-cone bits.

2- Approaches of the specific energy and the dimensionless drilling parameters available in the literature for predicting the real-time wear of drill bits while drilling were evaluated for selected wells in Southern Iraq. It was shown that these methods were unreliable for monitoring the bit tooth wear when compared to the field qualitative bit tooth wear of the studied wells due to the presumed effects of bit balling phenomena when drilling shale formations as well as the unconformity surface.

3- A new original approach for predicting the wear of the roller-cone bit is presented based on the concept of three body abrasion. The new approach incorporates the hardness of the rock formation and the materials forming the drill bit as well as other drilling parameters such as penetration rate, weight on bit and rotational speed. The new method was applied to roller-cone bits as all the bits penetrated the wells in this study were of this type.

4- The results obtained from the new theoretical wear method were compared with the qualitative bit tooth wear rate of the selected oil wells in Southern Iraq, where a good reasonable agreement was obtained compared to the previous approaches mentioned in point 3 above. The only exceptions occurred when reaching shale rocks; causing bit balling phenomena, and also when reaching unconformity structures, where misleading results could be obtained. This misinterpretation might be attributed to the reason that, when approaching such structures, channels in the rock occurred as a result of unconformity. Unconformity is occurring when there is a missing in the geological interval of the deposited rocks and accordingly, the obtained results might be unreliable.

5- The proposed method suggests that in order to predict the wear, characterisation of the material properties of the bit is needed. The mechanical properties of the materials forming the two layers of the PDC cutters were determined by micro and nano-indentation techniques.

6- Indentation results showed that both layers of sample M1313 have higher hardness than sample K1908. Furthermore the fracture toughness of both layers of sample K1908 is found to be higher than that of sample M1313.

7- The microstructural properties of the materials forming the PDC cutters found to have a great influence on the mechanical properties, especially hardness and fracture toughness and consequently on the amount of wear.

8- Hutchings' (1992) wear model was found to be the closest to the experimental wear compared to the models of Rabinowicz (1996) and Ning and Ghadiri (2006).

9- An analytical study showed that, when the diamond layer was scratched, the cobalt grains were removed from the scratch and the dominant mineral left in the groove was diamond. The hypothesis of this mechanism is due to the micro-wear of the tip of the diamond probe leaving some material on the scratched surface, although it might also be attributed to the adhesion between the probe and the diamond layer. In contrast, for the substrate layer, cobalt occupies the scratched area.

10- In conclusion, micro and nano-scratch testing could replace the traditional techniques for testing the PDC against abrasive wear for two reasons: 1. Micro and nano-scratch are semi-destructive tests as the samples could be tested many times compared to the traditional vertical turret lathe technique which is relatively destructive as the samples could not be tested again. 2. For wear quantification, old traditional techniques are depending on the measurements of the mass of the removed material after testing which is not precise, whereas micro and nano-scratch testing depend on the geometry of the removed material. In addition, nano scratch testing provides a method to quantify the volume of wear along the scratch that enables the full analysis of the failure behaviour of the material being tested.

6.2 Contribution to the Knowledge

1. Due to the shortage of references related to the prediction of the wear of roller-cone bits, a developed new model for wear prediction of these bits was obtained

2. by incorporating the drilling parameters as well the mechanical properties of the materials forming the drill bit led to a more enhanced model.
3. In the literature, PDC samples have been tested with destructive methods and cannot be used for further tests, therefore carrying tests for wear resistance on the PDC samples which are non-destructive were useful. Using state of the art testing techniques based on micro and scratch mechanical testing provides information of the amount of the volume of wear at different distances.
4. Indenting and scratching the diamond is challengeable and it was overcome by using spheroconical indenters rather than sharp indenters that performed the tests without significant problems.
5. Modulating the microstructure properties of the diamond and the tungsten-carbide grains as well as the cobalt content is crucially important to manufacture more durable PDC cutters against abrasion and impact wear.

6.3 Recommended Future Work

The suggested approach for predicting the bit wear based on three body abrasive wear could be tested for other wells in other regions for vertical drilling and could also be tested for horizontal drilling to verify its reliability. The developed technique was performed on roller-cone bits only, but could in principle be extended to Polycrystalline Diamond Compact (PDC) bits.

The specific energy technique is still considered an unreliable approach for monitoring the wear of the drill bit while drilling, unless other techniques are used simultaneously with the specific energy, such as well logs and geological information to understand sudden changes in the specific energy when the bit drills shale rock formations and other geological structures such as unconformity.

It is recommended to modulate the particle size distribution along with the cobalt content when manufacturing the PDC cutters to find at what optimum binder content and particle size can give maximum hardness and fracture toughness and consequently decreasing the wear rate caused due abrasion and impact.

The findings of the experimental scratch test could be applied to various types of PDC cutters from different manufacturers to evaluate the amount of wear as a quality index rather than using the traditional abrasion tests.

DEM models could be used to simulate the rock drilling where torque and wear could be quantified. The models of Archard (1953), Rabinowicz (1996), Ning and Ghadiri (2006) and Hutchings (1992), could be incorporated into DEM models for wear prediction of the bit. Drilling parameters, particularly bit size, weight on bit, penetration rate, revolution speed, and other bit design parameters, as well as the mechanical properties of the materials forming the drill bit should be considered to obtain a reliable model for wear quantification for PDC and roller-cone bits.

Further work is needed to investigate the displacement of cobalt from the scratched area as shown from the EDX maps, where the hypothesis mentioned within the study needs to be proven by further analytical study such as Atomic Force Microscopy (AFM) which is considered a very high resolution scanning probe microscopy which can be used to analyse the scratched areas with high resolution.

References

Abbas, R. K., Hassanpour, A., Hare, C., and Ghadiri, M. (2014). "Real-time Monitoring of Drill Bit Wear and Specific Energy as a Criteria for the Appropriate Time for Pulling Out Worn Bits". Paper SPE 172269 presented at the Annual Caspian Technical Conference and Exhibition. Astana, Kazakhstan, 12-14 November, 2014.

Abeed, Q., Frank, S., Detlev, L., and Ralf, L. (2012). "Petroleum system analysis of the Upper Jurassic-Middle Cretaceous sedimentary sequences of the Southern Mesopotamian Basin, Southern Iraq". Paper presented at the Geofluids VII 2012.

Akbari, B., Butt, S. D., Munaswamy, K., and Arvani, F.(2011) "Dynamic Single PDC Cutter Rock Drilling Modeling and Simulations Focusing on Rate of Penetration Using Distinct Element Method " Paper ARMA 11379 at the 45th US Rock Mechanics / Geomechanics Symposium . San Francisco, CA, 26–29 June, 2011.

Al-Ameri, T. K., Jafar, M.S. and Pitman, J. (2011). "Modelling Hydrocarbon Generations of the Basrah Oil Fields, Southern Iraq, Based on Petromod with Palynofacies Evidences". Paper presented at the AAPG Annual Convention and Exhibition. Houston, Texas, 10-13 April, 2011.

Anstis, G.R., Chantikul, P., Lawn, B.R. and Marshall, D.B. (1981). "A Critical Evaluation of Indentation Techniques for Measuring Fracture Toughness: I, Direct Crack Measurements." Journal of the American Ceramic Society **64**(9): 533-538.

Archard, J. F. (1953). "Contact and Rubbing of Flat Surfaces." Journal of Applied Physics **24**(8): 981-988.

ASM International. 2002. *Grinding and Polishing*. [Online]. [Accessed 29 January 2016]. Available from: http://www.asminternational.org/documents/10192/3447544/06958G_Chapter_4.pdf/a6cda448-291f-491b-bf6f-456322c4e386

ASTM E2546. 2015. *Standard Practice for Instrumented Indentation Testing*. [Online]. [Accessed 2 February 2016]. Available from: http://www.astm.org/Standards/E2546.htm

Beake, B. D., S. R. Goodes, S. Jones, Parkinson, R., Pickford, N. and Smith, J. 2003. *NanoTest User Manual*. Wrexham, Micro Materials Ltd.

Beake, B. D., S. R. Goodes and B. Shi (2009). "Nanomechanical and nanotribological testing of ultra-thin carbon-based and MoST films for increased MEMS durability." Journal of Physics D: Applied Physics **42**(6): 065301.

Beake, B. D., A. J. Harris and T. W. Liskiewicz (2013). "Review of recent progress in nano-scratch testing." Tribology - Materials, Surfaces & Interfaces **7**(2): 87-96.

Beake, B. D., V. M. Vishnyakov, R. Valizadeh and J. S. Colligon (2006). "Influence of mechanical properties on the nano-scratch behaviour of hard nanocomposite TiN/Si 3 N 4 coatings on Si." Journal of Physics D: Applied Physics **39**(7): 1392.

Beake, B. D., B. Shi and J. L., Sullivan (2011). "Nanoscratch and nanowear testing of TiN coatings on M42 steel." Tribology - Materials, Surfaces & Interfaces **5**(4):141-147.

Beaton, T., Miko, C. W., Denouden, B. P., & Herman, J. (2008). "New Steel PDC Drill-Bit Technology Redefines Performance Standards in Key Natural-Gas Applications". Paper SPE 115008 presented at the CIPC/SPE Gas Technology Symposium. Calgary, Canada, 16-19 June, 2008.

Bellin, F., Dourfaye ,A. , King, W. and Thigpen ,M. (2010 a). "The current state of PDC bit technology". World oil , **September** :41-46.

Bellin, F., Dourfaye ,A. , King, W. and Thigpen ,M. (2010 b). "The current state of PDC bit technology". World oil , **October** :53-58.

Bellin, F., Dourfaye ,A. , King, W. and Thigpen ,M. (2010 c). "The current state of PDC bit technology". World oil, **November** :67-71.

Bhushan, B. 2001. *Modern tribology handbook*, Boca Raton, FL, CRC Press.

Boland, J. N. and X. S. Lee (2010) ."Microstructural Characterisation and Wear Behaviour of Diamond Composite Materials". Materials **3**(2):1390-1419.

Bobji, M. S. and S. K. Biswas (1998). "Formation of hardness by nanoindnetation of rough surfaces". Materials Research **13**(11):3227:3233.

Budinski, K.G. (2007). Guide to friction, wear, and erosion testing .West Conshohocken, PA: ASTM International. Section 2, (Alternatives to testing: Modeling and simulation):16-23.

Burgess, T. M. (1985). "Measuring the Wear of Milled Tooth Bits Using MWD Torque and Weight-on-Bit". Paper SPE/IADC 13475 presented at the SPE/IADC Drilling Conference. New Orleans, Louisiana, 6-8 March 1985.

Chen, F., *et al*. (2010). "Thermal residual stress of polycrystalline diamond compacts." Transactions of Nonferrous Metals Society of China **20**(2): 227-232.

Cobb, R. T., D. E. Scott and D. Nelms (2011). "Superior Quality Diamond Heel Inserts Improve Cutting Structure and Seal Life in Abrasive and Directional Applications". Paper CSUG/SPE 146058 presented at the Canadian Unconventional Resources Conference. Alberta, Canada, 15-17 November 2011.

Couvy, H., D. Lahiri, J. Chen, A. Agarwal and G. Sen (2011). "Nanohardness and Young's modulus of nanopolycrystalline diamond". Scripta Materialia **64**(11): 1019-1022.

CSM Instruments. 2002. *Overview of Mechanical Testing Standards*. [Online]. [Accessed 29 June 2015]. Available from:

http://www.csm-instruments.com/en/webfm_send/42

CSM Instruments. 2007. *The Influence of Surface Roughness on Instrumented Indentation Testing (IIT)*. [Online]. [Accessed 31 January 2016]. Available from:

http://www.csm-instruments.com/fr/the-influence-of-surface-roughness-on-instrumented-indentation-testing-iit-nht-mht

Donald, H. (2010). "New Approach to Drilling Hard Chert Contaminated Carbonate Formations in Kazakhstan". Paper SPE 139412 presented at the SPE Caspian Carbonates Technology Conference. Atyrau, Kazakhstan, 8-10 November 2010.

Dubrovinskaia, N. , S. Dub, and L. Dubrovinsky (2006). "Super wear resistance of aggregated diamond nanorods". Nano Lett. **6**(4): 824-826.

Dunn, K..J. and M. Lee (1979). "The fracture and fatigue of sintered diamond compact". Journal of Material Science **14**(4): 882–90.

Dupriest, F. E. and W. L. Koederitz (2005). "Maximizing Drill Rates with Real-Time Surveillance of Mechanical Specific Energy". Paper SPE/IADC 92194 presented at the SPE/IADC Drilling Conference. Amsterdam, The Netherlands, 23-25 February 2005.

Eason, J., J. Westhoff and J. Stevens (2008). Sintered bodies for earth-boring rotary drill bits and methods of forming the same, Google Patents. [Online], [Accessed 5 June 2015]. Available from:

https://www.google.co.uk/patents/US20080101977?dq=Eason+,+Westhoff+and+Stevens+2008&hl=en&sa=X&ei=IWpxVZzjCoGzUI_qgbgH&ved=0CCoQ6AEwAQ

Erno, L. 2014. *Drilling and Well design.* [Online]. Hungary: Miskkolci Egyetem Foldtudomanyi Kar. [Accessed 1 November 2015]. Available from:

http://www.tankonyvtar.hu/en/tartalom/tamop412A/2011_0059_SCORM_MFKOT5052-EN/sco_03_03.htm

Evans, A. G. and E. A. Charles (1976). "Fracture Toughness Determinations by Indentation." Journal of the American Ceramic Society **59**(7-8): 371-372.

Evans, T., and P. F. James (1964). "A Study of the Transformation of Diamond to Graphite". Proceedings of the Royal Society of London. Series A, Mathematical and Physical Sciences **277**(1369): 260-269.

Falconer, I. G. and D. Normore (1987). "Well Site Applications of an MWD Bit Efficiency Model", Paper SPE 16644, Society of Petroleum Engineers.

Fang, Z., A. Griffo, B. White, D. Belnap, R. Hamilton, G. Portwood, P. Cox, G. Hilmas and J. Bitler "Chipping Resistant Polycrystalline Diamond and Carbide Composite Materials for Roller Cone Bits". Paper SPE 71394 presented at the SPE Annual Technical Conference and Exhibition, 30 September-3 October, New Orleans, Louisiana.

Farrelly, M. and H. Rabia (1987). "Bit Performance and Selection: A Novel Approach". Paper SPE/IADC 16163 presented at the IADC/ SPE Drilling Conference. New Orleans, Louisiana, 15-18 March 1987.

Favier, J. (2007)"Industrial application of DEM: Opportunities and Challenges" Available from: http://www.efluid.com.cn/topic/detail.aspx?id=4232.

Fujiwara, J. (2012). "Cutting Mechanism of Sulfurized Free-Machining Steel, Scanning Electron Microscopy", Dr. Viacheslav Kazmiruk (Ed.), ISBN: 978-953-51-0092-8, InTech, Available from: http://www.intechopen.com/books/scanning-electron-microscopy/cutting-mechanism-of-sulfurized-free-machining-steel.

Geoffroy, H., D. N. Minh, J. Bergues and C. Putot (1999). "Interaction Between Rock And Worn PDC Bit: Theory And Experiments". Paper ISRM 244 presented at the 9th ISRM Congress. Paris, France , 25-28 August.

Gokhale, B. V. (2010). *Rotary drilling and blasting in large surface mines*. Kent: CRC Press.

Guder, H.S., E. Sahin, O. Sahin, H. Gocmez, C. Duran and H. Ali Cetinkara (2011). "Vickers and Knoop Indentation microhardness Study of β-SiAION Ceramic". ACTA PHYSICA POLONICA A **120**(6): 1026-1033.

Hong, S.-M., M. Akaishi, H. Kanda, T. Osawa, S. Yamaoka and O. Fukunaga (1988). "Behaviour of cobalt infiltration and abnormal grain growth during sintering of diamond on cobalt substrate." Journal of Materials Science **23**(11): 3821-3826.

Hutchings, I.,M. (1992) *Tribology: Friction and Wear of Engineering Materials*. London: Edward Arnold**.**

ISO 14577-1.2015. *Metallic materials -Instrumented indentation test for hardness and materials parameters*. [Online]. [Accessed 2 February 2016]. Available from:

http://www.iso.org/iso/iso_catalogue/catalogue_tc/catalogue_detail.htm?csnumber=56626

Katiyar, P. K., P. K. Singh, R. Singh and A. l. Kumar (2016). "Modes of failure of cemented tungsten carbide tool bits (WC/Co): A study of wear parts." International Journal of Refractory Metals and Hard Materials **54**: 27-38.

Kopeliovich, D., *SubsTech website.* [Online]. 2015. [Accessed 3 June 2015]. Available from: http://www.substech.com/dokuwiki/doku.php?id=main_page

Kromka, A., J. Breza, M. Kadleciková, J. Janik and F. Balon (2005). "Identification of carbon phases and analysis of diamond/substrate interfaces by Raman spectroscopy." Carbon **43**(2): 425-429.

Krumeich, F., (2011). "Properties of Electrons, their Interactions with Matter and Applications in Electron Microscopy". Available from:

http://www.microscopy.ethz.ch/downloads/Interactions.pdf.

Kuru, E. and A. K. Wojtanowicz (1992). "A Theoretical Method For Detecting In Situ PDC Bit Dull And Lithology Change." Journal of Canadian Petroleum Technology **31**(7): 35-40.

Larsen-Basse J. (1973). "Wear of hard-metals in rock drilling: a survey of the literature". Powder Metallurgy **16**(31):1–31.

Laugier, M. T. (1985). "The elastic/plastic indentation of ceramics." Journal of Materials Science Letters **4**(12): 1539-1541.

Lawn, B. R., Evans, A. G. and Marshall, D. B. (1980). "Elastic/Plastic Indentation Damage in Ceramics: The Median/Radial Crack System." Journal of the American Ceramic Society **63**(9-10): 574-581.

Lin, T.-P., G. A. Cooper and M. Hood (1994). "Measurement of the fracture toughness of polycrystalline diamond using the double-torsion test." Journal of Materials Science **29**(18): 4750-4756.

Lu P., X.C. Xiao, M. Lukitsch, Y. K. Chou (2012). "Micro-Scratch Testing and Simulations for Adhesion Characterizations of Diamond-coated Tools". In: Annual SME North American Manufacturing Research Conference (NAMRC39), 13/17 June 2011, Oregon State University, Corvallis, Oregon, US.

McGehee, D. Y., J. S. Dahlem, J. C. Gieck, B. Kost, D. Lafuze, C. H. Reinsvold and S. C. Steinke (1992 a). "The IADC Roller Bit Classification System." Paper SPE/IADC 23937 presented at the SPE/IADC Drilling Conference. New Orleans, Louisiana, 18-21 February 1992.

McGehee, D. Y., J. S. Dahlem, J. C. Gieck, B. Kost, D. Lafuze, C. H. Reinsvold and S. C. Steinke (1992 b). "The IADC Roller Bit Dull Grading System." Paper SPE/IADC 23938 presented at the SPE/IADC Drilling Conference. New Orleans, Louisiana, 18-21 February 1992.

Mendoza, J. A., I. K. Gamwo, W. Zhang and J. S. Lin (2010). "Discrete Element Modeling of Rock Cutting Using Crushable Particles". ARMA conference paper 10-232 presented at the 44th U.S. Rock Mechanics Symposium and 5th U.S.-Canada Rock Mechanics Symposium, Salt Lake City, Utah. June 27 – 30.

Mori, N., H. Moriguchi, A. Ikegaya, Y. Shioya and K. Ohbi (2003). "Development of Highly Durable Materials for Drilling Hard and Abrasive Rocks". Paper SPE 80457 presented at the SPE Asia Pacific Oil and Gas Conference and Exhibition. Jakarta, Indonesia, 15-17 April 2003.

Mouritz, A. P. and I. M. Hutchings (1991). "The Abrasive Wear of Rock Drill Bit Materials", Society of Petroleum Engineers, Paper SPE 24222.

Ndlovu,S., K. Durst and M. Goken (2007). "Investigation of the sliding contact properties of WC-Co hard metals using nanoscratch testing. " Wear **263**, (7–12): 1602-1609.

Ndlovu Siphilisiwe (2009). "The wear properties of Tungsten Carbide-Cobalt Hardmetals from the Nanoscale up to the Macroscopic Scale". A PhD dissertation submitted to the materials Science and Engineering, University of Erlangen-Nuremberg, Germany.

Nguyen, T . 2011. Drilling Engineering –An Introduction to Drilling Drill Bits PE 311. [Online]. [Accessed 1 November 2015]. Available from:

http://www.google.co.uk/url?sa=t&rct=j&q=&esrc=s&frm=1&source=web&cd=1&ved=0CCEQFjAAahUKEwiC_pqwrOXIAhVEQBoKHZ8UBeE&url=http%3A%2F%2Finf

ohost.nmt.edu%2F~petro%2Ffaculty%2FNguyen%2FPE311%2FPresentations%2FC3%2F1_Classification.ppt&usg=AFQjCNGxVyeO5AwBm5bH4x74FXYg0QUe5A&sig2=3D8Ow4sBO3AX8SwhE22Eeg

Nguyen, T. and Q. Van. 1995. Insert attack angle for roller cone rock bits. EP0452058 B1. 1995-25-10.

Niihara, K. (1983). "A fracture mechanics analysis of indentation-induced Palmqvist crack in ceramics." Journal of Materials Science Letters **2**(5): 221-223.

Ning, Z. and M. Ghadiri (2006). "Distinct element analysis of attrition of granular solids under shear deformation." Chemical Engineering Science **61**(18): 5991-6001.

Oliver, W.C., G.M. Pharr (1992). "An improved technique for determining hardness and elastic modulus using load and displacement sensing indentation experiments" J. Material Research **7** (6): 1564-1583.

Olson, E. (2011). "Particle Shape Factors and Their Use in Image Analysis–Part 1: Theory | IVT". Journal of GXP Compliance **15** (3): 85-96.

Ortega, A. and D. A. Glowka (1984) "Frictional Heating and Convective Cooling of Polycrystalline Diamond Drag Tools During Rock Cutting." SPE Journal **April** 1984:121-128.

Osburn, H. J. (1969). "Wear Of rock drilling tools". Powder Metallurgy **12**(24):471–502.

Osipov, A. S., N.A. Bondarenko, I. A. Petrusha, and V.A. Mechnik (2010). "Drill bits with thermostable PDC inserts" Diamond tooling journal online **70**(625): 31-34. Available from: http://www.dtj-online.com/userfiles/file/Vol70Num625_31-34.pdf

Perrott, C. M. (1979). "Tool materials for drilling and mining". Annual Reviews Material Science 9:23–50.

Pessier, R. C. and M. J. Fear (1992). "Quantifying Common Drilling Problems With Mechanical Specific Energy and a Bit-Specific Coefficient of Sliding Friction". Paper SPE 24584 presented at the SPE Annual Technical Conference and Exhibition. Washington, D.C., 4-7 October 1992.

Rabia, H. (1982). "Specific Energy as a Criterion for Drill Performance Prediction." International Journal of Rock Mechanics and Mining Sciences & Geomechanics Abstracts **19**(1): 39-42.

Rabia, H. (1985). "Specific Energy as a Criterion for Bit Selection." SPE Journal of Petroleum Technology **37**(7): 1225-1229.

Rabia, H., Farrelly, M., & Barr, M. V. (1986). "A New Approach to Drill Bit Selection." Paper SPE 15894 presented at the SPE European Petroleum Conference. London 20-22 October 1986.

Rabinowicz, E. (1977) "Abrasive Wear Resistance as a Material Test", Lubrication Engineering **33**(7): 378-381.

Rabinowicz, E. (1996) *Friction and wear of materials*. Second edition. Toronto, ON: John Wiley & Sons**.**

Rashidi, B., G. Hareland and R. Nygaard (2008) "Real-Time Drill Bit Wear Prediction by Combining Rock Energy and Drilling Strength Concepts" Paper SPE 117109 presented at the SPE International Petroleum Exhibition and Conference. Abu Dhabi, UAE, 3-6 November 2008.

Ravikiran, A. (1999). "Wear Quantification." Journal of Tribology **122**(3): 650-656.

Reshetnyak, H. and J. Kuybarsepp (1994). "Mechanical properties of hard metals and their erosive wear resistance." Wear **177**(2): 185-193.

Richardson, R. C. D. (1968). "The wear of metals by relatively soft abrasives." Wear **11**(4): 245-275.

Sandvik hard material Company (2009). "Cemented carbide, Sandvik new developments and applications". The brochure is available from: http://www2.sandvik.com/sandvik/0130/HI/SE03411.nsf/88c2e87d81e31fe5c1256ae80035acba/651f6e334db04c46c125707600562c88/$FILE/Cemented%20Carbide.pdf

Sawa, T. and K. Tanaka (2002). "Nanoindentation of natural diamond." Philosophical Magazine A **82**(10): 1851-1856.

Shetty, D. K., I. G. Wright, P. N. Mincer and A. H. Clauer (1985). "Indentation fracture of WC-Co cermets." Journal of Materials Science **20**(5): 1873-1882.

Sinha, K.S. (2006) *Scratching of Materials and Applications*. Amsterdam, Elsevier.

Sneddon, M. V. and D. R. Hall (1988). "Polycrystalline Diamond - Manufacture, Wear Mechanisms, and Implications for Bit Design." Journal of Petroleum Technology **40**(12): 1593-1601.

Sumiya, H. and T. Irifune (2004). "Indentation hardness of nano-polycrystalline diamond prepared from graphite by direct conversion." Diamond and Related Materials **13**(10): 1771-1776.

Sumiya, H., N. Toda and S. Satoh (1997). "Mechanical properties of synthetic type IIa diamond crystal." Diamond and Related Materials **6**(12): 1841-1846.

Teale, R. (1965). "The concept of specific energy in rock drilling." International Journal of Rock Mechanics and Mining Sciences & Geomechanics Abstracts **2**(1): 57-73.

Tze-Pin, L., M. Hood, G. A. Cooper and L. Xiaohong (1992). "Wear and failure mechanisms of polycrystalline diamond compact bits." Wear **156**(1): 133-150.

Vaprek, S and A. S., Argon (2001). "Mechanical properties of superhard nanocomposites." Surface and coatings Techmology (**146-147**): 175-182.

Varel International. 2010. *Advanced PDC Bit Cutter Technology*. [Leaflet]. Dallas: Varel International.

Warren, T. M. (1984). "Factors Affecting Torque for a Roller Cone Bit." SPE Journal of Petroleum Technology **36**(9): 1500-1508.

Waughman, R. J., J. V. Kenner and R. A. Moore (2002) "Real-Time Specific Energy Monitoring Reveals Drilling Inefficiency and Enhances the Understanding of When to Pull Worn PDC Bits." Paper IADC/SPE 74520 presented at the IADC/SPE Drilling Conference. Dallas, Texas, 26-28 February 2002.

Waughman, R. J., J. V. Kenner and R. A. Moore (2003) "Real-Time Specific Energy Monitoring Enhances the Understanding of When To Pull Worn PDC Bits." SPE Drilling & Completion **18**(1): 59-68.

Wirojanupatump, S. and P. H. Shipway (1999). "A direct comparison of wet and dry abrasion behaviour of mild steel." Wear **233–235**: 655-665.

Xie, Y and H. M. Hawthrone. 2006. The cohesive strength of a surface material by controlled scratching. In Sinha, S. K. K. Scratching of materials and applications. Amsterdam: Elsevier, pp.186-209.

Xu Wang (2008). "Grain growth, Densification and mechanical properties of nanocrytalline WC-Co." A PhD dissertation submitted to the department of Metallurgical Engineering, University of Utah ,US.

Yahiaoui, M., L. Gerbaud, J. Y. Paris, J. Denape and A. Dourfaye (2013). "A study on PDC drill bits quality." Wear **298–299**(0): 32-41.

Yahiaoui, M., J. Y. Paris, J. Denape and A. Dourfaye (2015 a). "Wear mechanisms of WC–Co drill bit inserts against alumina counterface under dry friction: Part 1 — WC–Co inserts with homogenous binder phase content." International Journal of Refractory Metals and Hard Materials **48**: 245-256.

Yahiaoui, M., J. Y. Paris, J. Denape, C. Colin, O. Ther and A. Dourfaye (2015 b). "Wear mechanisms of WC-Co drill bit inserts against alumina counterface under dry friction: Part 2 — Graded WC-Co inserts." International Journal of Refractory Metals and Hard Materials **48**: 65-73.

Zacny, K. (2012). "Fracture and Fatigue of Polycrystalline Diamond Compacts." SPE Drilling & Completion **27**(1): 145-157.

Zhao, J., V. Labiouse , J. Dudt and J. Mathier (2010). "Rock Mechanics in Civil and Environmental Engineering". Florida: CRC Press.

Ziaja, M. B., and S. Miska, (1982) "Mathematical Model of the Diamond-Bit Drilling Process and Its Practical Application". SPE Journal **22**(6): 911-922.

Ziaja, M. B. (1985) "Mathematical Model of the Polycrystalline Diamond Bit Drilling Process and Its Practical Application". Paper SPE 14217 presented at the 60th SPE Annual Technical Conference and Exhibition . Las Vegas, NV, 22-25 September 1985.

Appendix-A (Derivations of Equations)

A-Derivation of the Mechanical Specific Energy (MSE) equation of Teale (1965) and the Specific Energy (SE) equation of Rabia (1985)

$$MSE = \frac{Work\ done}{Volume\ of\ rock\ removed} \qquad (A-1)$$

$$Work\ done\ = (W * PR) + (T * \omega) \qquad (A-2)$$

where W is the weight on bit , PR is the penetration rate T is the torque and ω is the angular velocity.

$$\omega = 2\pi.N \qquad (A-3)$$

$$Volume\ of\ rock\ excavated\ = Area\ of\ the\ bit * PR \qquad (A-4)$$

$$MSE = \frac{W.PR + 2\pi N.T}{A_{bit} * PR} \qquad (A-5)$$

And the final equation in imperial units will be as follows:

$$MSE = \frac{W}{A_{bit}} + 120\pi \frac{N.T}{A_{bit} * PR} \qquad (A-6)$$

Derivation of the Specific Energy (*SE*) Equation for rotary drilling (Rabia 1985):

$$SE = \frac{En}{V} \qquad (A-7)$$

where E_n is the energy in Joules in 1 min. and V is a unit volume of rock in m^3, removed in 1 min. Energy can be calculated from the following Equation (A-8):

$$E_n = T * \omega \qquad (A-8)$$

where T is the torque and ω is the angular velocity.

Equation (A-8) can be written as follows:

$$E_n = W.r.2\pi.N \qquad (A-9)$$

where W is the weight on bit (Kg) , r is the bit radius (mm) and N is the rotary speed (rev/min.).

Volume of rock removed can be calculated from the following Equation:

$$V = \pi r^2 . PR \qquad (A-10)$$

where PR = rate of penetration (m/hr).

Substituting Equation (A-9) and (A-10) into Equation (A-7) leads to Equation (A-11).

$$SE = \frac{2\pi . r . N . W}{\pi r^2 . PR} \qquad \frac{9.81 * 10^{-03} \left(\frac{J}{min.}\right)}{\frac{10^{-06}}{60}\left(\frac{m^3}{min.}\right)} \qquad (A-11)$$

Simplifying Equation (A-11) by replacing 2r with d (bit diameter) and using conversion factors to make all parameters homogeneous in units will make Equation (A-12) as follows:

$$SE = 2.35 \frac{W . N}{d . PR} \qquad (A-12)$$

where SE (MJ/m^3)

In Imperial or field units SE will be in units of (lb.in/in^3) or (lb/in^2) or psi, Equation (A-12) becomes:

$$SE = 20 \frac{W . N}{d . PR} \qquad (A-13)$$

where N (RPM), W (lb), d (in) and PR (ft/hr).

B- Hook's law derivation of the net stiffness of the sample

$$\Delta x = \frac{F}{S} \qquad (A-14\ )$$

where F is the applied load and S is the stiffness.

$$(\Delta x)_{total} = \Delta x_1 + \Delta x_2 = \frac{F}{S_1} + \frac{F}{S_2} \qquad (A-15\ )$$

$$\therefore \frac{1}{S} = \frac{1}{S_1} + \frac{1}{S_2} \qquad (A-16\ )$$

or it could be written as follows:

$$\frac{1}{S_{Total}} = \frac{1}{S_m} + \frac{1}{S_{net}} \qquad (A-17)$$

where, S_{net} is the net stiffness of the sample, S_{total} is the stiffness of the sample plus the stiffness of the machine without the sample and S_m is the stiffness of the machine without the sample.

Then finally, the net stiffness of the sample could be determined by simplifying Equation (A-17):

$$S_{net} = \frac{S_{Total} \,.\, S_m}{S_m - S_{Total}} \qquad (A-18)$$

C-Derivation of the area of the worn material after micro-scratch test with conical indenter

The area of the segment or the area of the yellow part of the sketch as illustrated in Figure 5.14 represents the area of the circular sector minus the area of the triangle above the segment.

$$A_{Segment} = A_{circular\ sector} - A_{triangle} \qquad (A-19)$$

The area of the circular sector is:

$$A_{circular\ sector} = \frac{1}{2} R_C * Sa \qquad (A-20)$$

where R_C is the radius of the circle, Sa is the arc length of the sector.

The area of the triangle is:

$$A_{triangle} = \frac{1}{2} ac * r_t \qquad (A-21)$$

where ac is the chord length, r_t is the height of the triangle.

Hence, Equation (A-19) could be re-written as follows:

$$A_{segment} = \frac{1}{2} * R_C * Sa - \frac{1}{2} ac * r_t \qquad (A-22)$$

Equation (A-21) can be written as follows:

$$A_{triangle} = \frac{1}{2}\left(2\, R_C * sin\frac{\theta}{2}\right) * \left(R_C * \cos\frac{\theta}{2}\right) = {R_C}^2 * \sin\frac{\theta}{2} * \cos\frac{\theta}{2} \qquad (A-23)$$

From the following trigonometric relation:

$$Sin\ 2\theta = 2\ sin\ \theta * \cos\theta \qquad (A-24)$$

Equation (A-24) can be written as follows:

$$Sin\,\theta = 2\sin\frac{\theta}{2} * \cos\frac{\theta}{2} \qquad (A-25)$$

Substituting Equation (A-25) into Equation (A-23):

$$A_{triangle} = \frac{1}{2} * {R_C}^2 * \sin\theta \qquad (A-26)$$

The arc length Equation is follows:

$$Sa = R_C * \theta \qquad (A-27)$$

Substituting Equation (A-27) into Equation (A-20):

$$A_{circular\ sector} = \frac{1}{2}\,{R_C}^2 * \theta \qquad (A-28)$$

Now substituting Equations (A-26) and (A-28) into Equation (A-18), the final Equation of the cross- sectional area of the sphere or the segment is as follows:

$$A_{Segment} = \frac{1}{2}\quad {R_C}^2\,[\,\theta - \sin\theta] \qquad (A-29)$$

The angle θ can be determined from the following functions:

$$\cos\frac{\theta}{2} = \frac{r_t}{R_C} = \frac{R_C - h}{R_C} = 1 - \frac{h}{R_C} \qquad (A-30)$$

where r_t is the height of the triangle and h is the residual depth of the nano-wear scratch.

$$\frac{\theta}{2} = \cos^{-1}\left(1 - \frac{h}{R_C}\right) \rightarrow \quad \theta = 2\cos^{-1}\left(1 - \frac{h}{R_C}\right) \qquad (A-31)$$

CSM Instruments (2002) used the following relation to quantify the wear volume of the x-track or linear track could be calculated from the following Equation:

$$V_w = A_{segment} * L \qquad (A-32)$$

where $A_{segment}$ is the cross sectional area of the track and L represents the length of the scratch or distance.

By benefitting from Equation (A-32), volume of the predicted nano-wear could be calculated from Equation (A-33) as follows:

$$V_w = \frac{(A_n + A_{n-1})}{2} * \quad (L_n - L_{n-1}) \qquad (A-33)$$

Appendix-B (Further Figures of Chapter Three)

Figure B.1 illustrates a sample of bit record for a well-being drilled in the South of Iraq. The record shows information of the commercial bits used while drilling as well as drilling parameters such as weight on bit, rotary speed, interval depth, etc. The status of the drill bit is shown on the columns of dullness condition which include three sub-columns (T for Tooth, B for Bearings and G for gauge).

COUNTRY: IRAQ	FIELD:	STATE:	SCTION:	TOWNSHIB:	RANGE	LOCATION:	WELL NO.
CONRACTOR: I.D.CO.		RIG. :	OPERATOR:		TOOLPUSHER:	SALESMAN:	
SPUD	UNDER SURF :	UNDER INTER:	SET SAND ST	PUMP NO.1 LINER :6½"	PUMP NO.2 LINER :6½"	PUMP POWER F-1000	TYPE MUD: FWB+FCL

	SIZE		TYPE	OD		NUMBER	O.D	I.D	LENGTH	
DRILL PIPE	5"	TOOL JOINT	4½IF	6⅝"	DRILL COLLARS	18	8"	3"	158.43m	DRAWWORKS POWER1
	3½"		3½IF	4¾"		18	8"	3"	158.43m	
						24	6¾"	2 13/16"	220.02m	
						24	4¾"	2¼"	223.6m	

NO.	SIZE	MAKE	TYPE	JET	SERIAL	DEPTH OUT	M	HRS	M/HR	ACCUL. DRILL.HRS	WT. TON	RPM	PUMP PRESS. Kg/cm²	L/M	SPM		MUD			DULL COND.				REMARK
															1	2	W T	V	W L	T	B	G	Other	
1.	17½"	Hughes	R1	3*20	861KK	656	620	57.25	10.8	57.25	15	100	40	2402	80	80	1.06	50	14	3	4	-	-	-
2.	12¼"	Hughes	X1G	-	941NL	896	242	37	6.5	94.25	8	60	30	1200	80	-	1.06	50	10	5	4	-	-	-
3.	12¼"	T.S.K	JM33	3*16+1*16	20884TK	1311	413	72	5.7	166.25	10	70	40	1220	40	40	1.10	45	8	5	6	-	-	-
4.	12¼"	T.S.K	JM33-a	3*16+1*16	21053TK	1627	317	70	4.5	236.25	15	80	78	1800	60	60	1.14	50	8	4	6	-	-	-
5.	12¼"	SEC	S86F	3*14	523577	1929	301	130	2.3	366.25	15	60	95	1800	60	60	1.14	55	9	2	3	-	-	-
6.	8½"	Hughes	J4	12,13,14	AM509	2077	148	35	4.22	401.25	15	85	105	1621	50	58	1.17	45	6	5	4	-	-	-
7.	8½"	Hughes	J4	3*12+2*14	CD753	2232	155	48	3.8	448.25	15	85	100	1621	50	58	1.16	47	4.5	3	4	-	-	-
8.	8½"	Hughes	J3	3*12+2*14	963NS	2364	52	17.5	2.97	466.75	15	85	100	1621	50	58	1.16	47	3	4	4	-	-	-
9.	5⅞"	SEC.	M88F	2*16+1*20	673546	2287	23	9	2.55	475.75	6	50	110	750	50	-	1.18	49	6	4	4	-	-	-
10	5⅞"	SEC.	M88F	2*16+1*20	673491	2375	88	34	2.58	509.75	6	50	110	750	50	-	1.18	45	4	5	5	-	-	-

Figure B. 1 Bit record of an oil well in the south of Iraq

Figure B.2 shows the plot of the dimensionless square root of the rate of penetration against the dimensionless torque for well B_1. Intercept a_1 and slope a_2 is determined from the plot that are used in further calculations of the dimensionless drilling parameters.

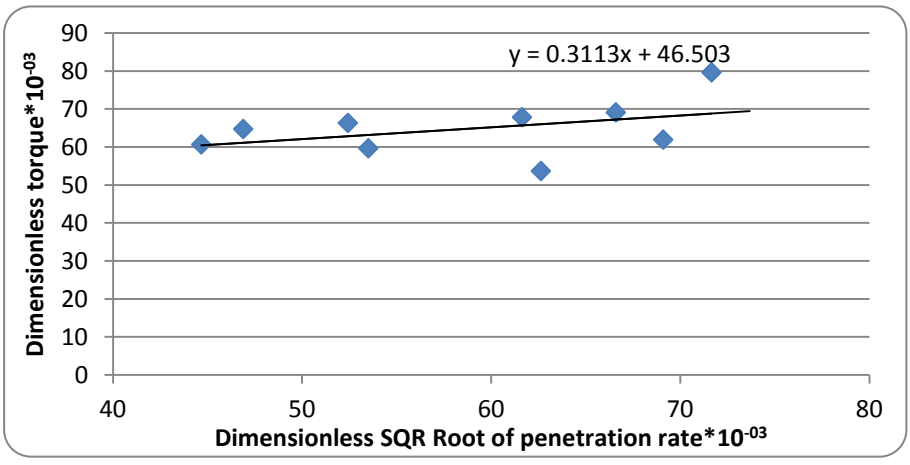

Figure B. 2 Cross plot of dimensionless torque (T_D) with dimensionless square root of penetration rate (R_D) for well B_1

Figure B.3 illustrates the plot between the dimensionless square root of the penetration rate versus the dimensionless torque for well B_2. Constants a_1 and slope a_2 is obtained for the calculations of the bit tooth flatness (F_D).

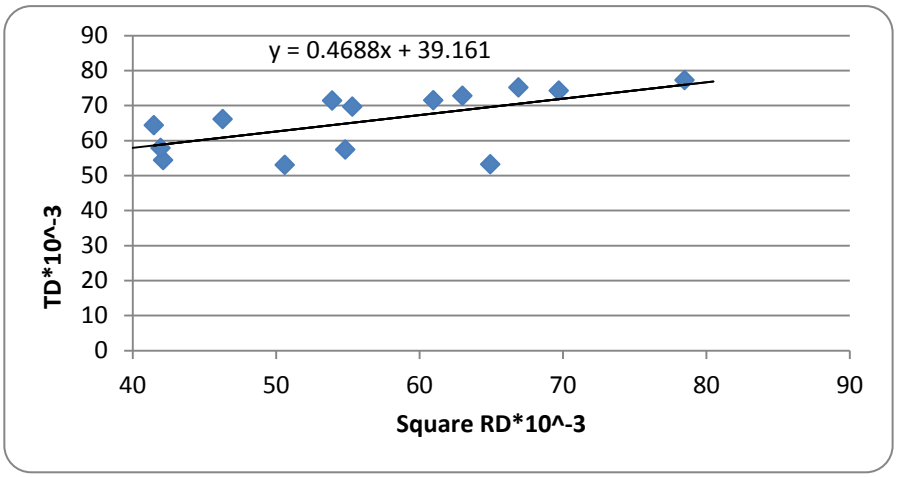

Figure B. 3 Cross plot of dimensionless torque (T_D) with dimensionless square root of penetration rate (R_D) for well B_2

For wells A_2 and B_3 the plot of the square root of the dimensionless penetration rate versus dimensionless torque are illustrated in Figures B.4 and B.5.

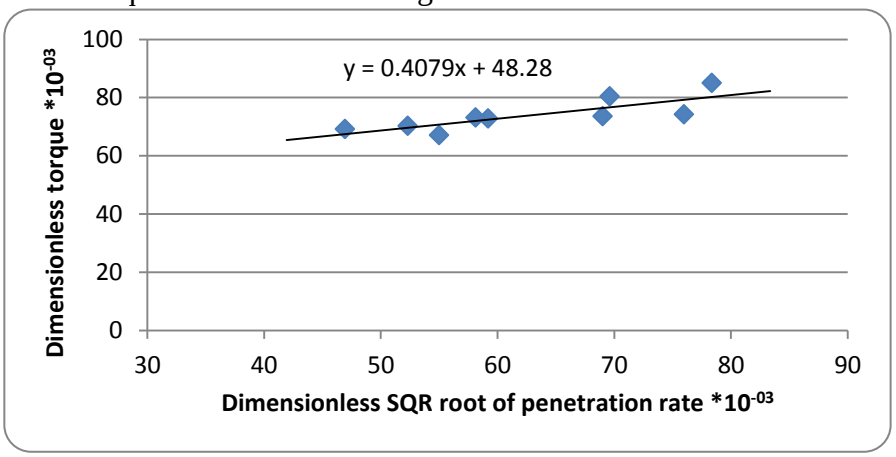

Figure B. 4 Cross plot of dimensionless torque (T_D) with dimensionless square root of penetration rate (R_D) for well A_2

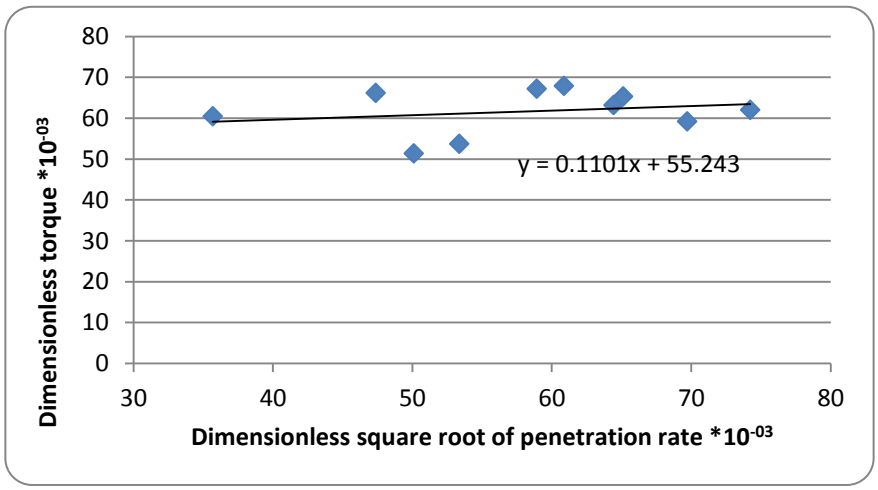

Figure B. 5 Cross plot of dimensionless torque (T_D) with dimensionless square root of penetration rate (R_D) for well B_3

Appendix-C (Further Figures of Chapter Four)

Figure C.1 shows the coloured EDX maps of the interface between the coating and the substrate layers of the PDC sample. Tungsten, cobalt, calcium and carbon in the diamond phase are shown within the maps. Cobalt is shown to have greater content in the substrate layer compared to the coating.

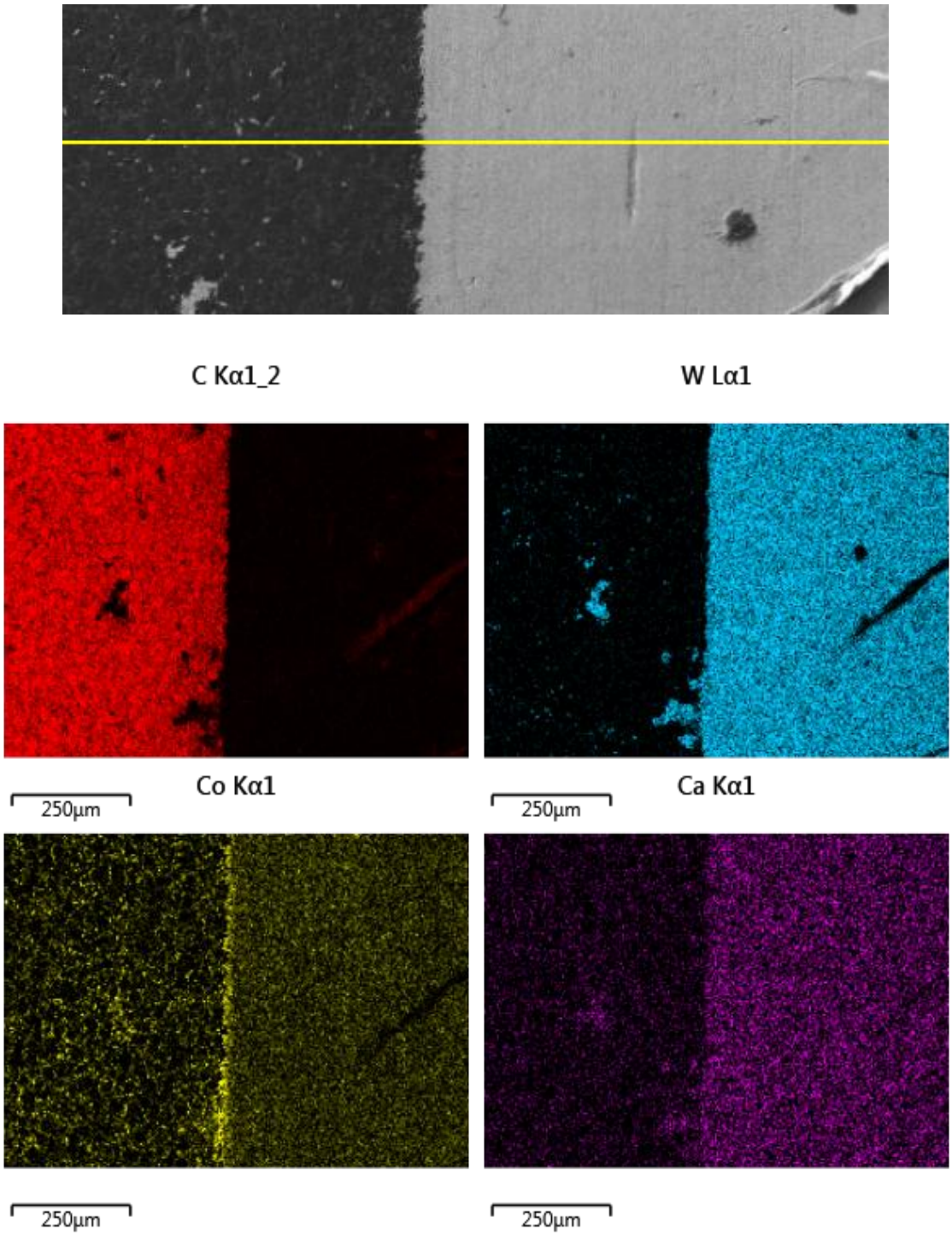

Figure C. 1 EDX maps of the interface of the PDC insert shows the mineral distribution through diamond and substrate layers

Figure C.2 illustrates the coloured EDX map of the interface between the coating and the substrate layers along with Energy Dispersive Spectroscopy EDS for a PDC specimen (Figure C.3). The spectra for tungsten, cobalt and carbon (diamond) are shown along the interface.

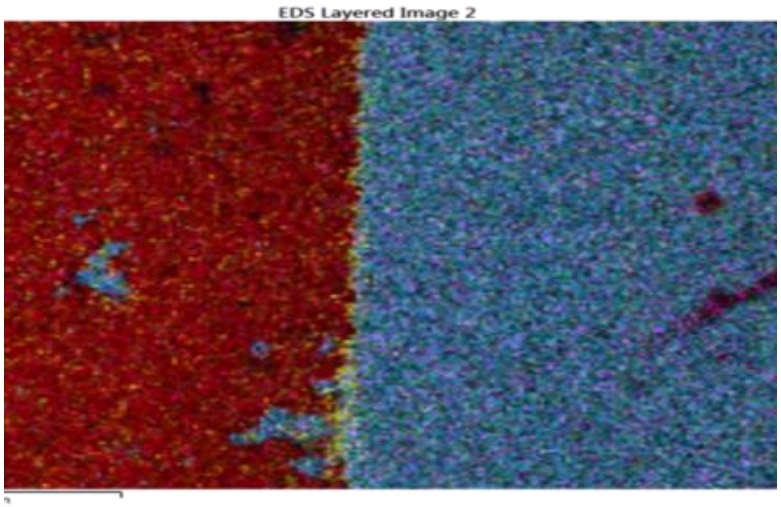

Figure C. 2 X-ray map of the interface between diamond layer and tungsten carbide

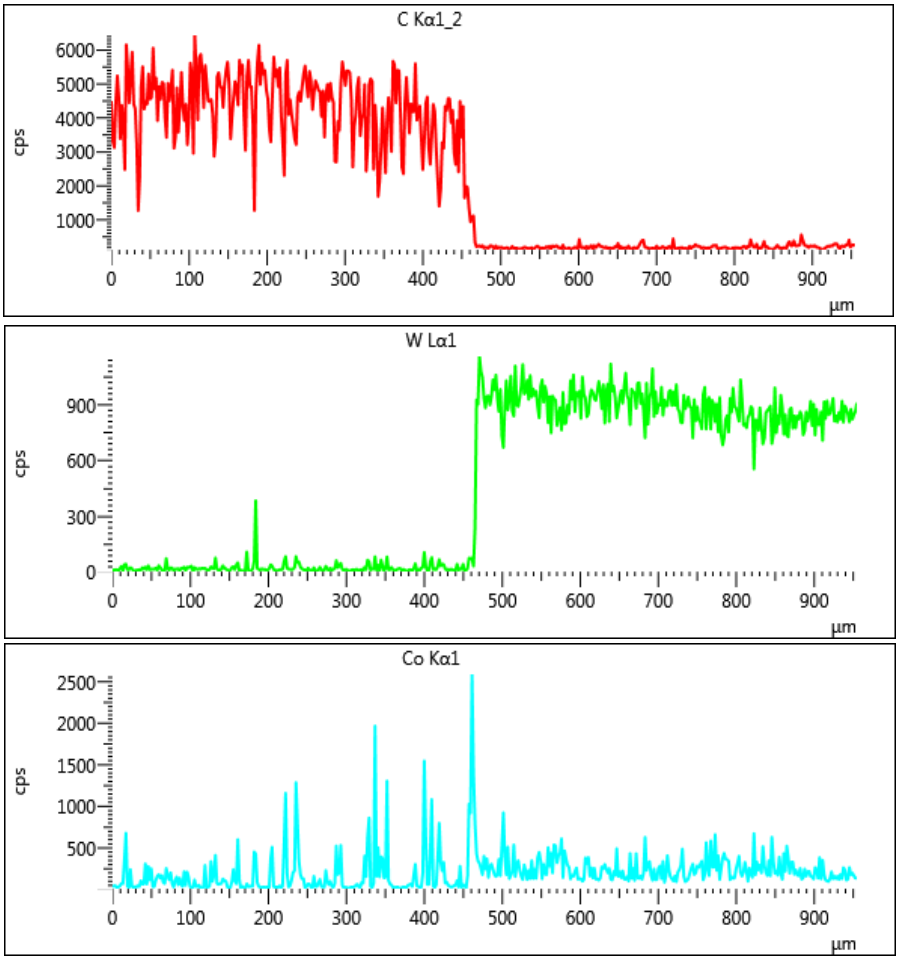

Figure C. 3 Energy dispersive spectroscopy maps for the major minerals form the PDC insert

Figure C.4 demonstrates the spectra for other elements (oxygen, calcium, iron, potassium) along the interface of the PDC sample.

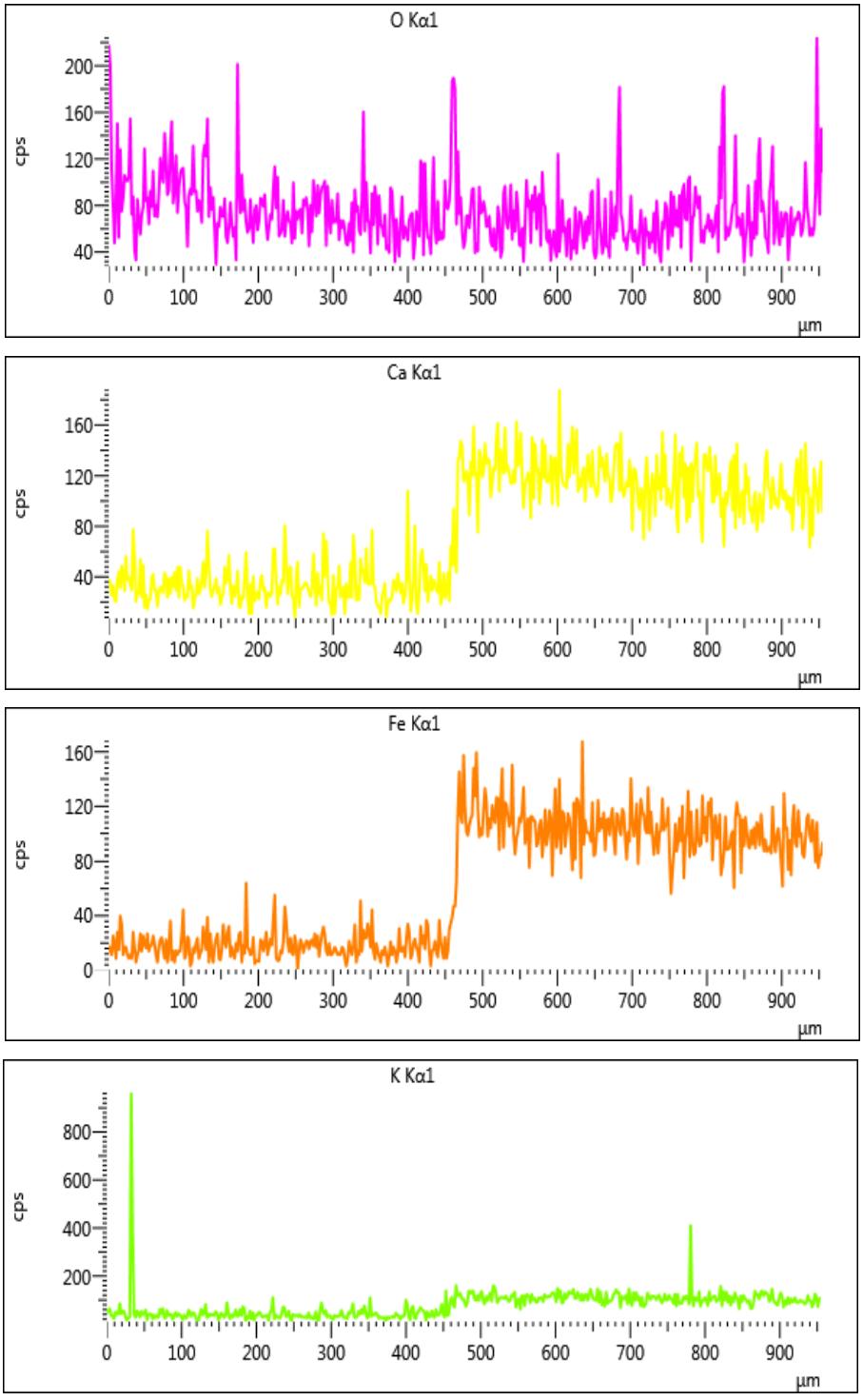

Figure C. 4 Energy dispersive spectroscopy maps for other minerals form the PDC insert

Appendix-D (Further Figures of Chapter Five)

Figures D.1 and D.2 show the micro-scratch testing with applied loads of 100 and 300 N respectively on the substrate layer of sample M1313 using Vickers indenter.

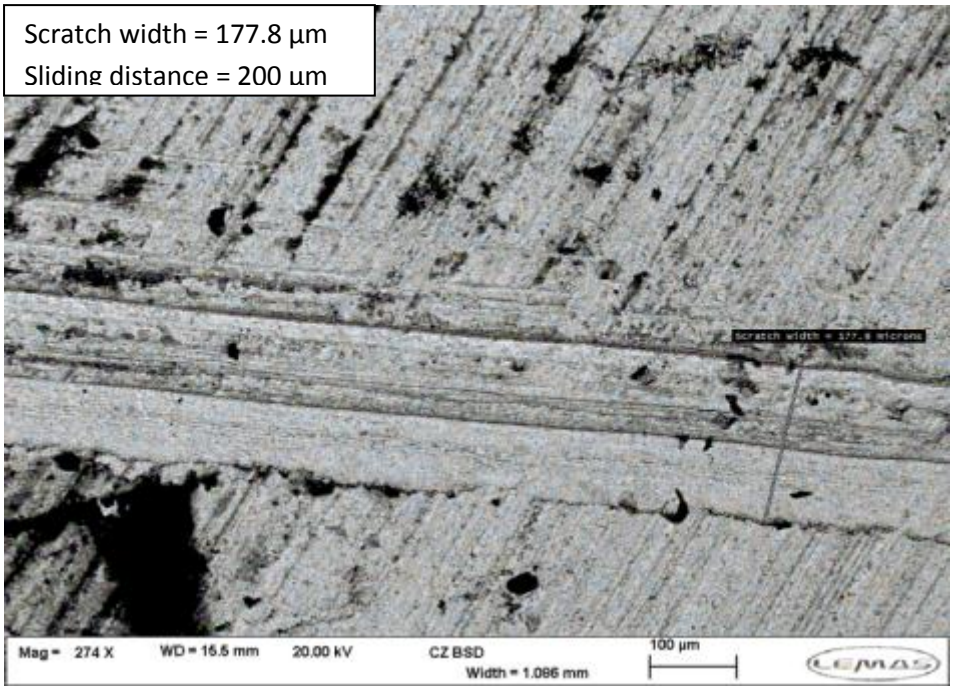

Figure D. 1 Micro-scratch obtained when applying 100 N on the tungsten-carbide layer of the sample M1313

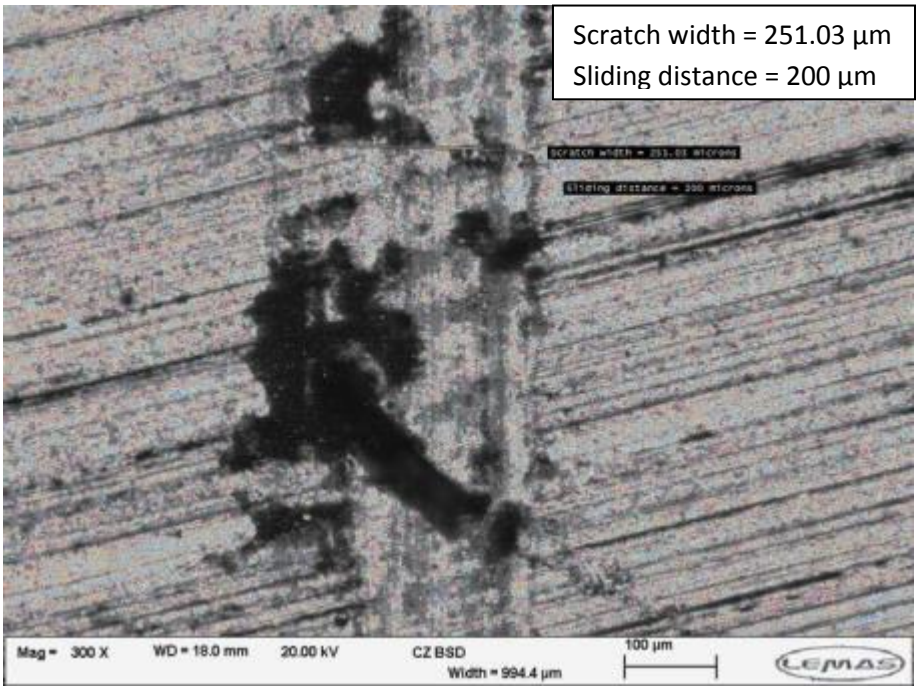

Figure D. 2 Micro-scratch produced when applying 300 N on the substrate layer of the sample M1313 with Vickers indenter

Figures D.3 and D.4 illustrate the micro-scratch testing with applied loads of 10 and 15 N respectively on the diamond layer of sample M1313 using Vickers indenter.

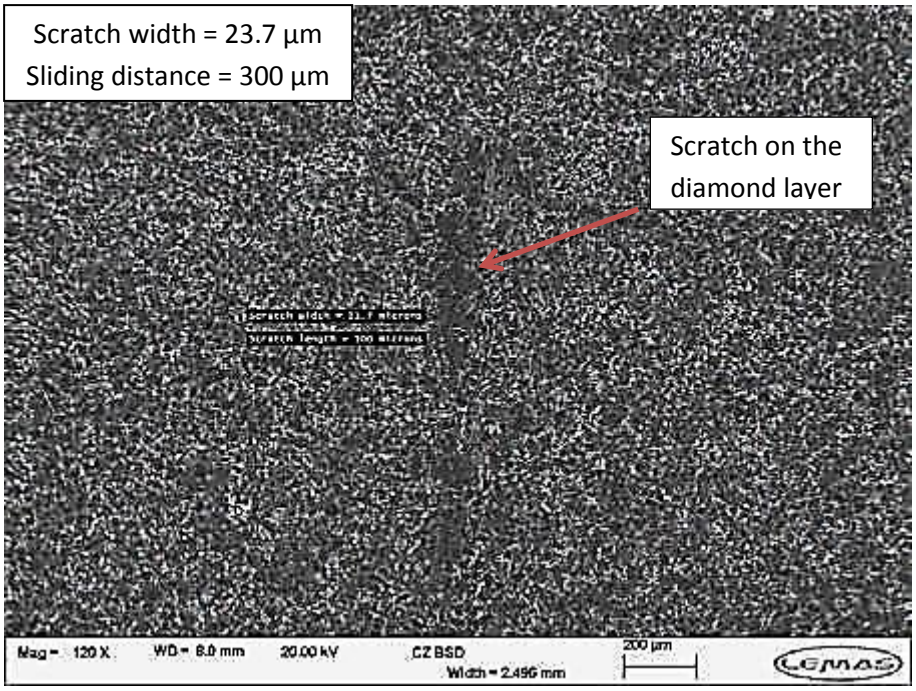

Figure D. 3 Scratch obtained after applying 10 N on the diamond layer on the sample M1313 using Vickers indenter

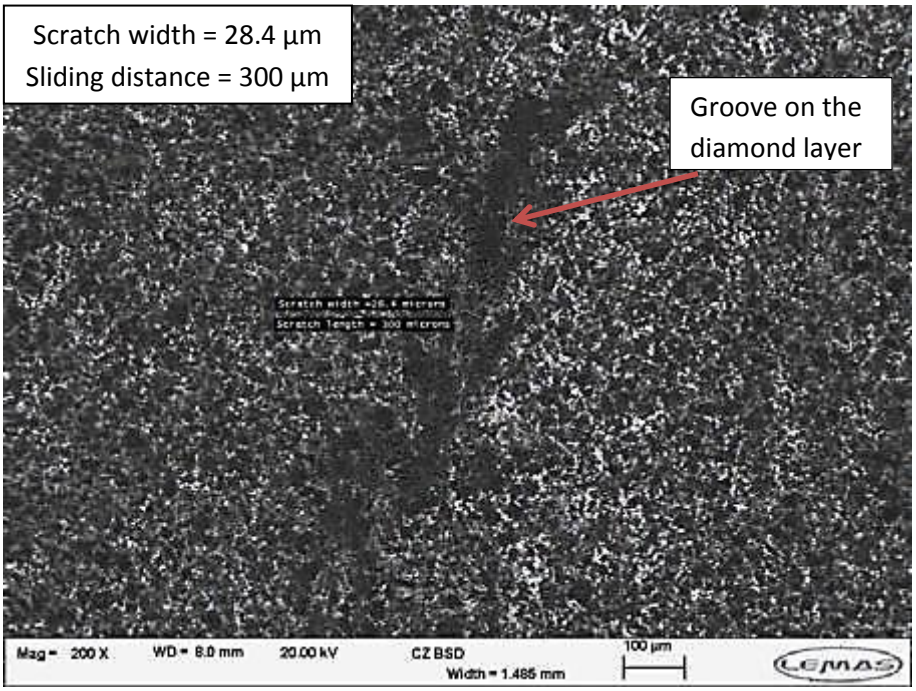

Figure D. 4 Scratch produced after applying 15 N on the diamond layer of the sample M1313 using Vickers indenter

Figures D.5 and D.6 show the micro-scratch testing on the substrate layer of sample K1908 using a spheroconical indenter at loads of 100 and 200 N respectively.

Figure D. 5 Scratch obtained on the substrate layer of the sample K1908 at load 100 N using spheroconical indenter

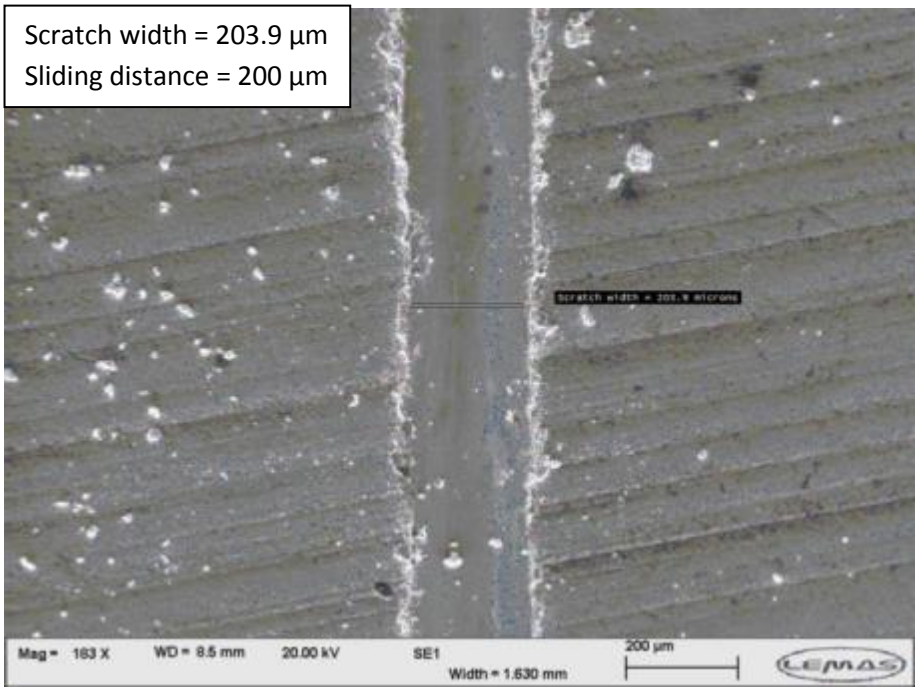

Figure D. 6 Scratch obtained on the WC-Co layer of the sample K1908 at load 200 N using spheroconical indenter

Figures D.7 and D.8 show the micro-scratch testing with applied loads of 25 and 75 N respectively on the substrate layer of sample K1908 using a spheroconical indenter.

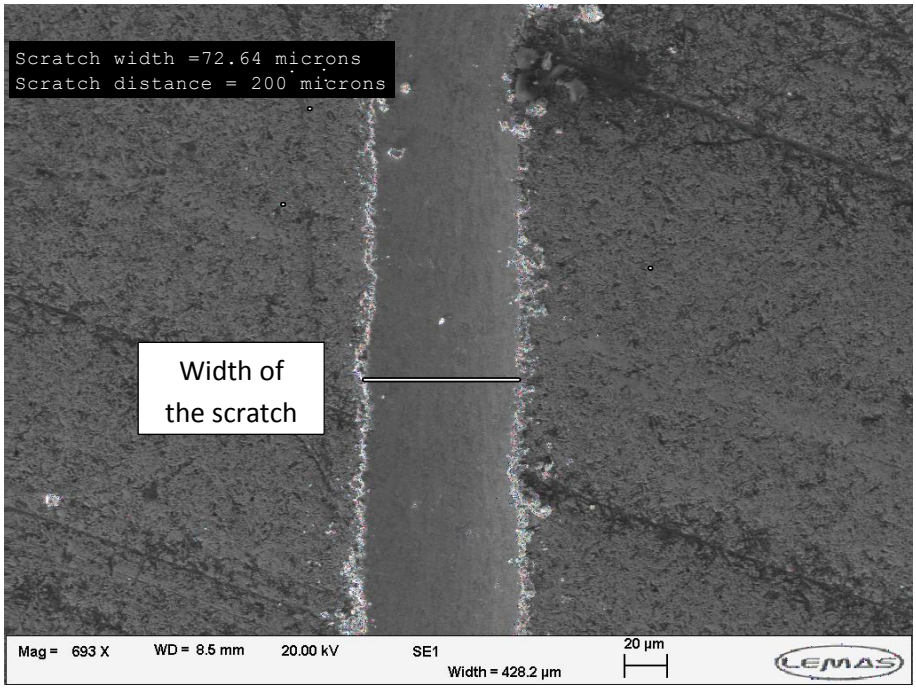

Figure D. 7 Groove obtained on the substrate layer of sample K1908 at load 25 N using spheroconical indenter

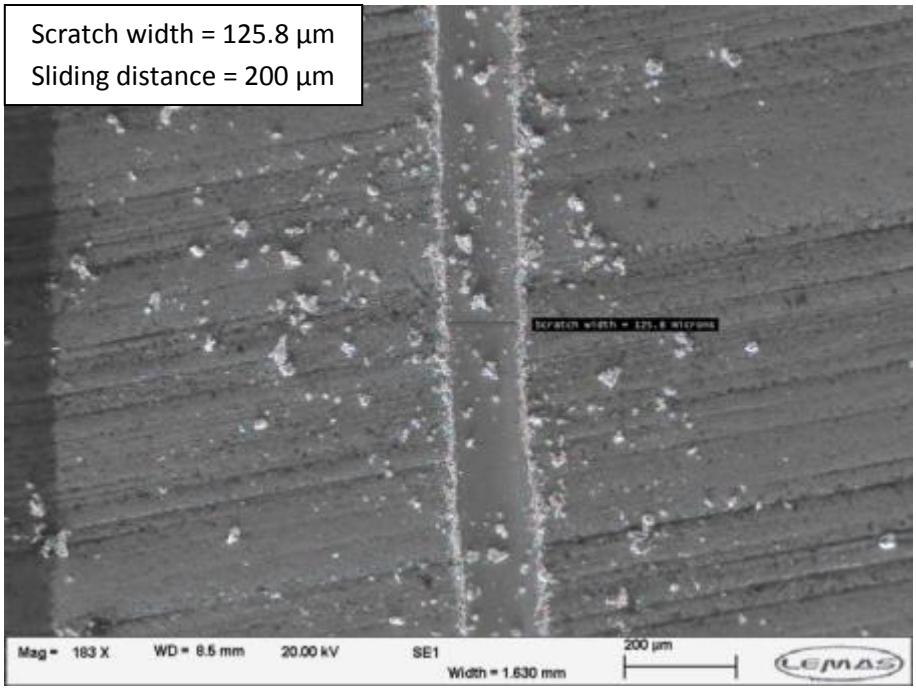

Figure D. 8 Groove obtained on the substrate layer of sample K1908 at load 75 N using spheroconical indenter

Figures D.9 and D.10 show the micro-scratch testing with applied loads of 50 and 65 N respectively on the substrate layer of sample M1313 using a spheroconical indenter.

Figure D. 9 Groove obtained when applying 50 N on the WC-Co layer of sample M1313 using spheroconical indenter

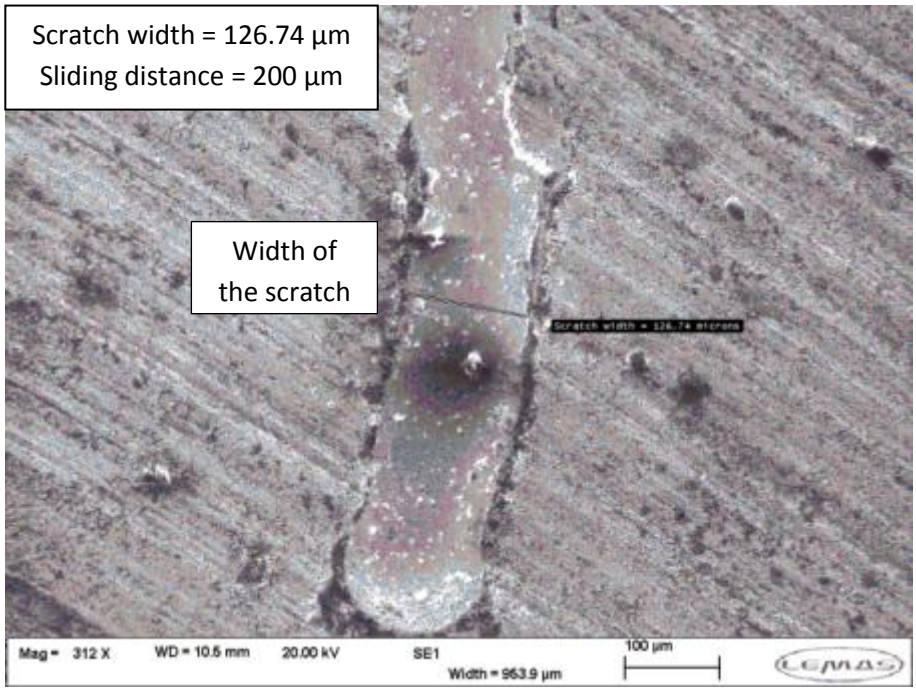

Figure D. 10 Scratch obtained when applying 65 N on the substrate layer of sample M1313 using spheroconical indenter

Figures D.11 and D.12 show the micro-scratch testing with applied loads of 20 and 10 N respectively on the diamond layer of sample K1908 using a spheroconical indenter.

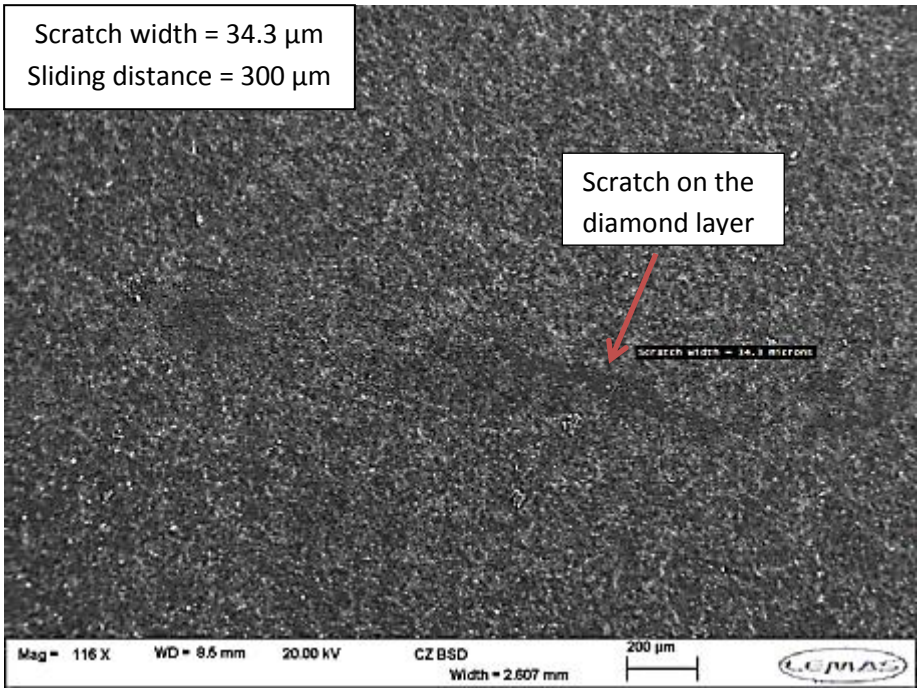

Figure D. 11 Scratch obtained when applying 20 N on the diamond layer of sample K1908 using spheroconical indenter

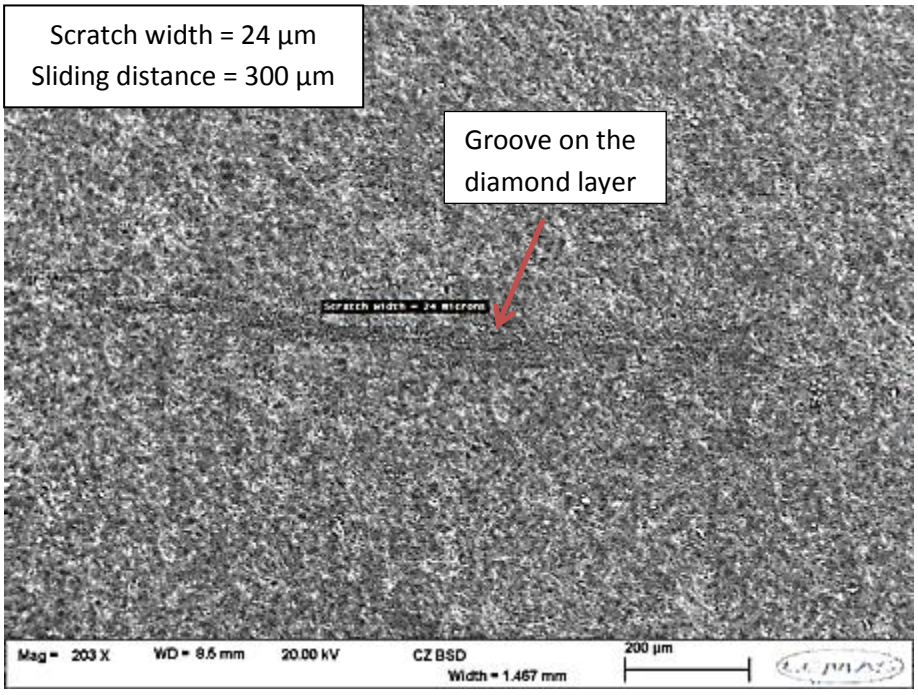

Figure D. 12 Scratch obtained when applying 10 N on the diamond layer of sample K1908 using spheroconical indenter

Figure D.13 shows the micro-scratch testing on the diamond layer of sample M1313 with applied load of 7.5 N when using a spheroconical indenter, while Figure D.14 illustrates the micro-scratching of sample K1908 with applied load of 7.5 N on the diamond layer using a spheroconical indenter.

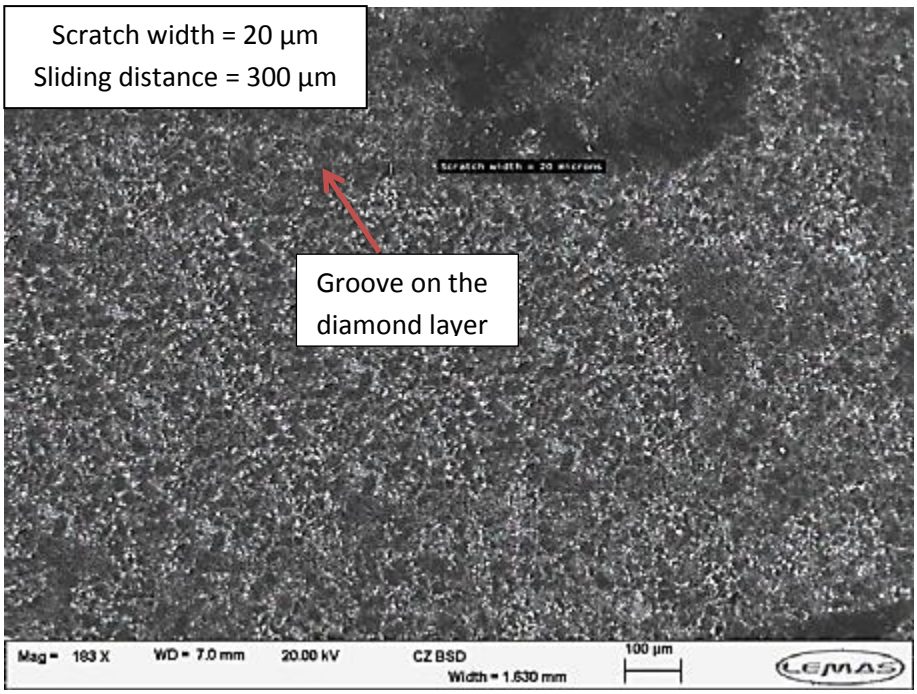

Figure D. 13 scratch obtained when applying 7.5 N on the diamond layer of sample M1313 using spheroconical indenter

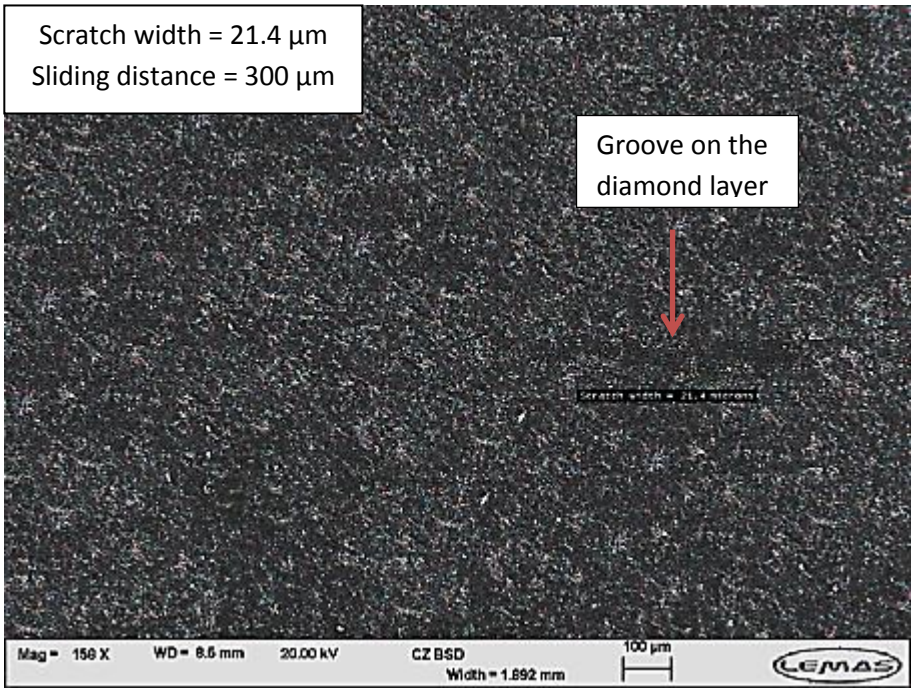

Figure D. 14 Groove produced when applying 7.5 N on the diamond layer of sample K1908 using spheroconical indenter